Interaction Properties of an Ultracold Fermi-Fermi Mixture of Dysprosium and Potassium Atoms

Elisa Soave, MSc

Doctoral thesis submitted to the faculty of
Mathematics, Computer Science and Physics
at the University of Innsbruck
in partial fulfillment of the requirements
for the degree of Doctor of Philosophy (PhD).

Innsbruck, May 2022

Supervisor:	Univ.-Prof. Dr. Rudolf Grimm
Co-Supervisors:	Univ.-Prof. Mag. Dr. Barbara Kraus
	Prof. Fabrice Gerbier

Abstract

In this thesis we consider a novel, strongly interacting degenerate Fermi-Fermi mixture of ultracold atoms. Superfluid fermionic systems are ubiquitous in nature: Neutron stars and high-Tc superconductors are just two examples of those strongly interacting systems. Given the complexity of the mechanism underling this phenomena, a proper theoretical physical description is challenging. In this regard, reaching the superfluid regime in a system of fermionic ultracold gas could further our understanding of superfluid systems. The measurements reported in this thesis are carried out on a sample of ^{40}K and ^{161}Dy. A mass imbalance of about 4 is expected to enlarge the region of the phase diagram where resonant superfluidity is predicted to appear, and make it attainable at realistic experimental conditions. From the practical point of view, the Dy-K mixture is easy to handle, and offers the advantage that the two species can be addressed independently. A thorough characterization of the mixture and its interaction properties is the first, fundamental step towards superfluidity.

In first instance, we measure the dynamic polarizability of ^{164}Dy at 1064 nm. This wavelength is of particular interest for laser trapping experiments. Our approach is based on the measurement of collective oscillations in an optical dipole trap and comparison with potassium as a reference species. We determine the scalar polarizability to be 184.4(2.4) a.u., more than three times smaller than for K. We obtain a value of 1.7(6) a.u. for the tensor polarizability.

We then bring the ^{161}Dy-^{40}K mixture in the degenerate regime. The two species are polarized in their lowest spin state. Thanks to universal dipolar scattering, dysprosium undergoes forced evaporative cooling. Potassium is sympathetically cooled via *s*-wave collisions with Dy. Based on thermalization measurements, we estimate the interspecies background scattering length to be $|a_{\mathrm{DyK}}| \simeq 62a_0$.

Resonant superfluidity requires the presence of a broad Feshbach resonance. We identify such a feature in the high magnetic-field region. In a scenario of three overlapping resonances, we consider the strongest one, centered at $B_0 \simeq 217\,\mathrm{G}$. We perform a detailed characterization of the resonance and study the behavior of the mixture at B_0. We identify several spots where the mixture is strongly interacting and has a lifetime of several hundreds of milliseconds.

Finally, we investigate the inelastic atomic losses in a degenerate spin-polarized

sample of ^{161}Dy. We measure the Feshbach spectrum in the magnetic region below 1 G, and identify as much as 44 resonance features and observe plateaus of very low losses. We perform case study on four selected resonances. We systematically measure the three-body collision rate K_3 for different conditions of temperature and magnetic-field detuning, and retrieve a behavior qualitatively similar to the one observed for p-wave scattering. We observe a strong suppression of losses with decreasing temperature already for small detunings from resonance.

The interaction properties of the system and the tunability of the population imbalance are favorable to reach the superfluid regime. A reduction of the cloud temperature will eventually locate our mixture in the region of the phase diagram where superfluidity is expected to appear.

Contents

Abstract **3**

1 Introduction **9**

2 From Ultracold Atoms to the DyK Experiment **13**
- 2.1 Ultracold atomic experiments 13
- 2.2 Ultracold fermions 15
- 2.3 Feshbach resonances 18
- 2.4 Strongly interacting Fermi gas 22
- 2.5 Strongly magnetic lanthanide atoms 28
- 2.6 Why a Dy-K mixture 30
- 2.7 Storyline of my PhD work 31

3 Accurate Determination of the Dynamical Polarizability of Dysprosium **34**
- 3.1 Introduction 35
- 3.2 Dynamical polarizability 36
- 3.3 Experimental setup 38
- 3.4 Systematic effects 39
- 3.5 Determination of the polarizability 42
- 3.6 Conclusion 43
- 3.7 Supplemental material 44
  - 3.7.1 Absence of density effect on oscillation frequency 44
  - 3.7.2 Damping of oscillations 44
  - 3.7.3 Error budget of the frequency ratio measurement 46
  - 3.7.4 Measurement of the tensor contribution 47

4 Production of a Degenerate Fermi-Fermi Mixture of Dysprosium and Potassium Atoms **49**
- 4.1 Introduction 50
- 4.2 Laser cooling and dipole trap loading 52

4.2.1 Magneto-optical traps 52
4.2.2 Sequential dipole trap loading 53
4.3 Evaporative cooling 55
4.3.1 Transfer from reservoir into main dipole trap 56
4.3.2 Evaporative cooling of a pure ^{161}Dy cloud 58
4.3.3 Evaporative cooling of the ^{161}Dy-^{40}K mixture 62
4.3.4 Effect of magnetic levitation 65
4.3.5 Interspecies scattering cross section 67
4.4 Conclusion and outlook 69
4.5 Appendix 70
4.5.1 Apparatus 70
4.5.2 Imaging of the atomic cloud 71
4.5.3 Cooling ^{40}K on the D1 line 71
4.5.4 Interspecies thermalization 73

5 Resonantly Interacting Fermi-Fermi Mixture of ^{161}Dy and ^{40}K 74
5.1 Introduction 75
5.2 Sample preparation 77
5.3 Interaction characterization 77
5.4 Hydrodynamic expansion 78
5.5 Lifetime 82
5.6 Discussion and conclusion 83
5.7 Supplemental material 84
5.7.1 Feshbach resonance scenario 84
5.7.2 Decay 93
5.7.3 Interaction-induced contraction 96

6 Low-field Feshbach resonances and three-body losses in a fermionic quantum gas of ^{161}Dy 100
6.1 Introduction 101
6.2 Low-field Feshbach Spectrum 102
6.2.1 Sample preparation 102
6.2.2 Loss Scan 103
6.3 Case Studies of Selected Resonances 105
6.3.1 Three-body decay curves and loss-rate coefficients 105
6.3.2 Dependence on magnetic-field detuning 108
6.3.3 Temperature dependence 109
6.4 Conclusion 112
6.5 Supplemental Material 113
6.5.1 Summary of the initial experimental conditions 113
6.5.2 Extraction of the loss-rate coefficient 113

6.5.3 Broadening Effects 114

7 Outlook 118

A Useful Constants and Physics Relations 122

B Additional measurements 127
B.1 Feshbach Scans for ^{161}Dy in Various Magnetic Field Regions 127
B.2 Binding energy of DyK molecules at the 217-G resonance 131
B.3 Interspecies Feshbach resonance at 53 G 132

C Linewidth Narrowing of Two DBR Lasers Through Optical Feedback and their Subsequent Phase Lock 136
C.1 Introduction 137
C.2 Linewidth reduction via optical feedback 137
  C.2.1 Experimental setup 137
  C.2.2 Linewidth reduction measurement 139
  C.2.3 Results and discussion 141
C.3 Phase lock of two DBR lasers 144
  C.3.1 Optical phase lock loop (PPL) 144
  C.3.2 Locking setup 144
  C.3.3 Results 147
C.4 Conclusions and outlook 148

Bibliography 151

A special acknowledgement 177

Acknowledgements 178

1

Introduction

In 1911, H.K. Onnes observed that the resistivity of solid mercury abruptly disappeared once the sample was brought to temperatures below 4.19 K [1]. In 1913 he named this phenomena *supraconductivity*, a name which later was substituted by the term *superconductivity* [2]. Onnes's discovery was followed by numerous experiments, which overall aimed at unraveling and better understanding the behavior of superconductors, i.e., all those materials for which, below a certain temperature (called *critical temperature,* T_c), the resistivity abruptly disappears. Despite the progress in understanding the properties of superconductors, for decades no one could explain the physical mechanisms underlying this effect. Onnes himself believed that quantum mechanics would explain the effect, but he wasn't able to develop a theory [3]. It was only in the 1950's that the Ginzburg-Landau and the Bardeen–Cooper–Schrieffer (BCS) theories were formulated (see for instance [4]). In particular, the latter provided a microscopic description of superconductivity in terms of Cooper pairs, i.e., pairs of electrons which form below a certain critical temperature, the attraction being provided by a deformation of the metallic lattice [5].

In the 1930s, twenty years after the discovery of superconductivity, another *super*-phenomenon was observed: In two independent works, Kapitza [6] and Allen and Misener [7] observed that the viscosity of ^{4}He abruptly dropped once the system was cooled below 2.17 K. Below this temperature, helium manifests frictionless flow. In 1938, F. London suggested that superfluidity in ^{4}He was related to Bose-Einstein condensation (BEC). In 1971 superfluidity was also observed in the fermionic isotope of helium, ^{3}He [8]: In this case, the frictionless flow was appearing at around 2.6 mK, three orders of magnitude lower than for ^{4}He. Superfluidity in ^{3}He was explained in terms of formation of diatomic pairs (which thus feature bosonic character), and their subsequent condensation into a BEC.

At the end of the 1950's an increasing theoretical interest was put on defining a unifying theory able to explain the pairing phenomena observed in fermionic systems for a wide range of interparticle interaction strength. Through a series of fundamental works (e.g. [9, 10, 11]) took shape what nowadays is known as the BEC-BCS crossover theory. This theory provides a theoretical description of an interacting fermionic system in terms of a modified version of the BCS wavefuntion, which undergoes a smooth crossover between the BEC regime (where diatomic molecules form and condense) and the BCS regime (where Cooper pairs form).
An important element of the BEC-BCS crossover, is the prediction of the so called resonant superfluid, which features a critical temperature T_c of the order of the system Fermi temperature T_F (in the BCS regime, the critical temperature is more than five order of magnitude lower!). Resonant superfluidity occurs where the interparticle interactions are the strongest. In this regime, the physics of the system only depends on thermodynamic quantities, and not on the details of the interaction potential. In this sense the system is said to be universal, and directly relates to other systems of strongly interacting fermions present in nature (e.g. high temperature superconductors, neutron stars, Quark-Gluon plasma).
The BEC-BCS crossover theory has been at the center of an active research activity. A theoretical description of the crossover regime poses challenges because of the lack of small parameters. The advent of ultracold atomic gases has offered to physicist an additional, unique, powerful platform where to experimentally investigate the BEC-BCS crossover model and gain a deeper insight on resonant superfluidity. The uniqueness of this platform stands on the tunability of the system parameters, in particular of the strength of the interparticle interactions.
An ultracold gas is an extremely dilute system of neutral atoms (typical density $n \approx 10^{13}\,\mathrm{cm}^{-3}$, six orders of magnitude less than air), which have been cooled to temperatures in the nanokelvin regime. At such low temperatures, the de Broglie wavelength λ_{dB} becomes comparable to the interparticle distance $l = n^{-1/3}$, and the wave nature of the atoms becomes important: Interference and quantum-statistical effects can no longer be neglected. Given the low temperatures and the dilutness of the gas, in many ultracold atom experiments the actual microscopic structure of the interaction potential can be neglected. What matters instead is the scattering amplitude, which relates to the probability for two particles to interact. The strength of the interaction can be parametrized via the so-called scattering length a. Depending if the interactions are attractive or repulsive, the scattering length can be negative or positive, respectively. A system is said to be weakly interacting if $|a| \ll l$, while for $|a| \gtrsim l$ the system is in the strongly interacting regime. For $|a| \to \infty$, the system is in the unitary regime, and resonant superfluidity as predicted by the BEC-BCS crossover theory is expected to occur.
One of the most amazing properties of ultracold atoms is the presence of Feshbach

(FB) resonances, which offer the possibility of controlling the interparticle interaction strength [12]. By tuning an external magnetic field, the scattering length can take any value, becoming zero in correspondence of the so called resonance zero crossing and diverging at the resonance center ($a \to \pm\infty$).
Because of the high degree of control that experimentalists have over lots of the system parameters (temperature, interaction strength, density, etc...), ultracold gases of fermionic atoms have been demonstrated to be a powerful platform where to investigate the BEC-BCS crossover theory. Its first observations were done in systems of dilute Fermi gases of ^{6}Li [13, 14] and ^{40}K [15], followed over the years by numerous works, both experimental and theoretical. If, on one side, experimentalists contribute to build up a more and more complete understanding of the physics underlying superfluidity along the BEC-BCS crossover, theoreticians are pushing the limits of such a theory, and predict the existence of new phases of matter which go beyond the idea of superfluid as originally formulated.
Lots of interest has risen by the question of the superfluid stability in the presence of population imbalance. In this case, indeed, not all atoms can pair up. The resonant superfluid state has been found to be robust against spin imbalance (e.g. [16, 17]), up to a critical polarization above which the system undergoes phase separation, and the non-paired atoms are "expelled" from the superfluid core (see for instance [18]). Even more intriguing is the possibility to create an inhomogeneous superfluid, where the order parameter is periodically modulated. The existence of such a phase has been predicted separately by Fulde and Ferrel (FF, plane wave order parameter [19]) and by Larkin and Ovchinnikov (LO, standing wave, [20]). Next to phase separation and the FFLO state, the phase diagram of a polarized system also predicts the presence of a Sarma phase [21, 22]. Those phases of matter, often gathered together under the name of *exotic phases of matter*, so far remained elusive to a thorough experimental investigation, because of the too narrow phase space region where they are expected to appear [23].

The DyK (dysprosium-potassium) experiment provides a new platform where to study strongly interacting Fermi systems, and is particularly suited for the investigation of new exotic phases of matter. The novelty of our fermionic mixture resides in the mass imbalance between the two components, dysprosium being four times heavier than potassium. Theoretical works (e.g. [24, 23]) show that in the presence of mass imbalance and for a majority of light particles, the FFLO state is expected to appear in the strongly interacting regime, at temperatures $T \simeq 0.1T_F$, two orders of magnitude higher than for the mass-balanced case. More in general, the ingredient of mass imbalance is expected to enlarge the regions in the phase diagram where exotic phases are predicted to appear, making them experimentally accessible. Another important aspect of working with a heteronuclear mixture is the different dynamic polarizability of the two species. This opens up the possibility of engineering species-selective traps and offers an additional knob for the mixture manipulation. In [25] it has been calculated that an increased trap-frequency ratio leads to higher critical temperature for the onset of resonant superfluidity. Other mass-imbalanced fermionic mixture have already been produced, but they all feature unfavorable mass ratio or interaction properties. Our fermionic mixture is the first of its kind, being made of a lanthanide and an alkaline species. It comes with important challenges, mainly related to the highly magnetic character of dysprosium and its complicated interaction properties.

In this thesis, we report on how a strongly interacting Fermi-Fermi mixture of dysprosium and potassium has been produced and its interaction properties have been characterized. Exploiting the long-range character of Dy-Dy dipole interactions together with standard techniques well established in the ultracold atoms community, we have been able to bring the mixture into the deeply double-degenerate regime, reaching reduced temperatures as low as $\simeq 0.1\,T/T_F^{(Dy)}$ [26]. We found a suitable Feshbach resonance centered around 217 G thanks to which the interaction strength between the two species can be smoothly tuned [27]. Where the interactions are the strongest, the mixture still features a relatively long lifetime, of the order of few hundreds of milliseconds.

A huge effort is now being put on lowering the temperature of the mixture in the strongly interacting regime. This, together with technical improvements, will finally make the long-sought exotic phases experimentally accessible.

2

From Ultracold Atoms to the DyK Experiment

2.1 Ultracold atomic experiments

An ultracold gas is an extremely dilute system of neutral atoms (typical density $n \approx 10^{13}\,\mathrm{cm}^{-3}$, six orders of magnitude less than air), which have been cooled to temperatures in the nanokelvin regime. Four main length scales define the regime of the system: the interparticle distance $l = n^{-1/3}$, the thermal de Broglie wavelength λ_{dB}, the interaction range r_0 and the scattering length a [28]. The onset of quantum degeneracy is marked by $l \simeq \lambda_{\mathrm{dB}}$. Typical experimental conditions are such that $r_0 \ll \lambda_{\mathrm{dB}}$. The particles can not resolve the microscopic structure of the interaction potential, and the remaining length scale defining interaction is the scattering length a. This latter can take any value $-\infty < a < +\infty$. Such tunability is one of the greatest feature of ultracold atoms, and will be discussed in Sec. 2.3. If $a \ll l$ and $a \ll \lambda_{\mathrm{dB}}$, the system is said to be in the weakly interacting regime. For increasing a, correlations among particles become more and more important. For $a \geq l$, many-body physics enters into play. Of particular interest in the frame of this thesis is the regime where $|a| \to \infty$: The system is said to be unitary and it enters a universal regime of scale invariance, where the scattering length drops out of the problem and the only relevant remaining length scales are λ_{dB} and l.

The last century saw fervent theoretical and technical developments in the cooling and trapping of neutral atoms, which eventually led to the achievement of quantum degeneracy. In 1995, almost simultaneously the group of Cornell at JILA (on ^{87}Rb) and the one of Ketterle at MIT (on ^{27}Na) obtained the first signatures of Bose-Einstein condensation [29, 30]. Fermionic degeneracy took a bit longer to be observed, the first degenerate Fermi gases (DFG) being obtained from a sample of

^{40}K in 1999 at JILA in the group of D. Jin [31] and of ^{6}Li in 2001 in the group of R. Hulet at Rice University [32] and of C. Salomon in Paris [33].

Nowadays ultracold-atom experiments rely in a well-establish experimental protocol to efficiently bring an atomic gas into the quantum regime. A typical ultracold atom experiment usually starts with an hot atomic cloud (a hot vapour, often coming out of an effusive oven), which is laser cooled and loaded into a MOT. The cloud is then transferred into a conservative trap (magnetic or optical). Sub-Doppler cooling technique may be used to further reduce the sample temperature, before forced evaporative cooling takes place. Quantum degeneracy is typically reached within a total of twenty to thirty seconds. The experimental sequence length is mostly dictated by the MOT loading efficacy and the efficiency of the evaporation process.

The achievement of quantum degeneracy has marked a turning point in the research direction of ultracold atoms. From the end of the 1990's ultracold atoms have become a fundamental platform for quantum simulation. The high degree of control that experimentalists have over lots of the system parameters (temperature, dimensionality, interaction strength, density, etc...) allows them to use ultracold atomic systems to study a plethora of physical problems which are otherwise extremely difficult (if not even impossible) to investigate. The aforementioned high degree of control over the system parameters can be used to engineer an ultracold atomic system whose Hamiltonian is equivalent to the one relevant to the physical problem of interest. This idea of simulating one quantum system using another, more controllable one, has proven to be quite powerful. For instance, ultracold atoms can be used to investigate solid state physics problem, for which the time or length scales of interest may be experimentally inaccessible and the presence of impurities can hinder the overall scenario. Ultracold atomic systems are also an important aid for theoreticians, whose simulations often encounter the technical limits of current computers. Example of quantum simulations with ultracold atoms are for instance the study of the Bose- (or Fermi-) Hubbard model with lattice and quantum microscope experiments [34, 35, 36, 37] or the simulation of artificial Gauge fields [38, 39]. Ultracold-atom experiments have become an important tool also for the study of fundamental physics (BEC-BCS crossover [15, 40, 14], exotic phases of matter, topological phase transitions [41], reduced-dimension systems [42, 43], disordered systems ([44] and references therein), ...), metrology (atomic clocks [45], measurement of fundamental constants [46], atomic interferometry [47],...) or quantum chemistry (laser cooling of polyatomic molecules [48, 49], ultracold molecule assembly [50], ultracold reaction control [51], ...).

Despite the fact that the experiments are pursuing different goals, they (almost) all start with the production of a degenerate gas in a relatively tight volume. The measurements are often then performed in a different trap geometry (lattice, dimensionally reduced traps, etc..), engineered on purpose for the specific experiment. It is often required a manipulation of the interatomic interactions, which is possible for instance as soon as a Feshbach resonance is present. The actual investigation of the sample involves a wide spectrum of (often standard) experimental techniques (loss spectroscopy, radio-frequency spectroscopy, lifetime measurements, Rabi oscillations measurements, thermalization measurements, etc...). No matter which experiment is performed, all the information are inferred from the atomic cloud properties (position, density distribution, dimensions...), which in turn are obtained from a picture of the cloud. The picture can be taken by absorption or by fluorescence, *in situ* (i.e., in the trap) or after expansion in time of flight (TOF, i.e., after being released from the trap).

2.2 Ultracold fermions

Bosons and fermions are the basic constituents of matter, the first being characterized by an integer spin quantum number while the second by a half integer one. Such an apparently simple difference between bosonic and fermionic particles has profound consequences on their physics, the two requiring two different quantum statistical descriptions (Bose-Einstein statistics the first, Fermi-Dirac statistics the second). Justified by the fact that bosons are not relevant in the frame of this thesis, in this section I will restrict the discussion to fermionic systems only.

The fermionic wave function is antisymmetric under particle interchange. This has the important consequence that fermions obey the Pauli exclusion principle, i.e., two identical particles can not occupy the same quantum state. At low temperatures, where a quantum-statistical treatment is necessary to describe the system, the Pauli principle dramatically changes the thermodynamics of a fermionic system. The occupancy $f(\varepsilon)$ of a quantum state with energy ε is given by the Fermi-Dirac (FD) distribution:

$$f(\varepsilon) = \frac{1}{\frac{1}{\zeta}\exp(\varepsilon/k_{\mathrm{B}}T) + 1}, \tag{2.1}$$

where T is the temperature of the gas, $\zeta = \exp(\mu/k_{\mathrm{B}}T)$ is the fugacity and μ is the chemical potential. A new energy scale, the Fermi energy E_F, is introduced. It coincides with the chemical potential at zero temperature $\mu(T = 0) = E_F$, and defines the Fermi temperature $T_F = E_F/k_B$. A fermionic system is said degenerate if the ratio T/T_F is below 1. For a non-homogeneous gas one can define a local chemical potential: $\mu(\mathbf{r}) = \mu(\mathbf{r} = 0) - V_t(\mathbf{r})$, $V_t(\mathbf{r})$ being the confining potential. From here, the local analogous of the other thermodynamic quantities can be derived. In the presence of harmonic confinement the global Fermi energy is commonly defined as $E_F = \hbar\bar{\omega}(6N)^{1/3}$, $\bar{\omega}$ being the geometrically averaged trap

frequency.
According to the Pauli principle, it can only be $0 < f(\varepsilon) < 1$. In particular, at zero temperature we have that $f(\varepsilon \leq E_F) = 1$ and $f(\varepsilon > E_F) = 0$. In contrast with a Bose system, the ground state of a Fermi system is characterized by particles that can not accumulate in the lowest energy state and are therefore forced to pile up in the different energy levels. It follows that a degenerate Fermi gas always has a finite energy and a finite pressure, even at zero temperature. It is important to remark that Bose-Einstein condensation is a phase transition, characterized by symmetry breaking (the gauge invariance). Instead cooling a fermionic system leads to a crossover into the degenerate regime: All symmetries are preserved, the behavior of the system smoothly changing at temperatures below T_F, where quantum statistics becomes more and more important.
The various thermodynamic quantities can be obtained by properly averaging over the density of states $g(\varepsilon)$ and the mean occupation number $f(\varepsilon)$. Upon integration, most of the thermodynamic quantities are expressed in terms of the polylogarithm function of order n, $\mathrm{Li}_n(-\zeta)$ [52]. Restricting the discussion to a three-dimensional harmonically trapped gas[1], we have for instance, that the level of degeneracy is given by the reduced temperature $T/T_F = -(6\mathrm{Li}_3(-\zeta))^{-1/3}$, while the density distribution reads

$$n(\mathbf{r}) = -\frac{(k_\mathrm{B}Tm)^{3/2}}{(2\pi)^{3/2}\hbar^3}\mathrm{Li}_{3/2}\left(-\zeta \mathrm{e}^{-\frac{U(\mathbf{r})}{k_\mathrm{B}T}}\right). \tag{2.2}$$

The spatial and the momentum distribution for $T < T_F$ deviate from a Gaussian profile and in the limit $T \to 0$ they can be described respectively with the expressions $n(\mathbf{r}) \propto (1 - (r/R_\mathrm{TF})^2)^{3/2}$ and $n(\mathbf{p}) \propto (1 - (p/p_F^{(0)})^2)^{3/2}$, as first measured in [31]. Here $R_F = \sqrt{2E_F/(m\omega^2)}$ is the Fermi radius and $p_F^{(0)} = \sqrt{2mE_F}$ is the Fermi momentum at the center of the trap. The total energy of a fermionic system is $U = 3k_\mathrm{B}TN\frac{\mathrm{Li}_4(-\zeta)}{\mathrm{Li}_3(-\zeta)}$, which in the degenerate regime exceeds the classical counterpart $U_{cl} = 3k_\mathrm{B}TN$ [31]. It follows that for $T \to 0$ the gas becomes incompressible, the pressure P approaching a fixed finite value. The effect of the Fermi pressure is clearly visible in the size of a degenerate atomic cloud, which shrinks with temperature slower than what happens in a bosonic gas, and only weakly depends on T for $T/T_F \lesssim 0.5$ [32].
The Pauli principle not only affects the thermodynamic properties of fermions, but also the collision properties. Given the antisimmetry of the fermionic wavefunction, only scattering in odd partial waves is allowed. This, together with the fact that at low temperatures collisions in non-zero partial waves are kinetically suppressed, has the important consequence that in an ultracold gas of identical fermions both elastic and inelastic scattering are basically absent.

---

[1] For a three-dimensional harmonically trapped gas, $g(\varepsilon) = \varepsilon^2/(2(\hbar\bar{\omega})^3)$.

Pioneering works on ultracold fermionic gas have been carried on on samples of ^{40}K or ^{6}Li. One of the main technical limitations that experimentalists had to overcome was the fact that a polarized Fermi gas can not be evaporatively cooled because rethermalization (elastic) collisions are kinetically suppressed. The group in JILA bypassed the problem by creating a spin mixture of two Zeeman substates of ^{40}K ($|f, m_f\rangle = |9/2, 9/2\rangle$ and $|f, m_f\rangle = |9/2, 7/2\rangle$). s-wave collisions among two different spin states are allowed, and the mixture could undergo forced evaporation. A different method was suggested in [53], and led to the first DFG of ^{6}Li in 2001 in the group of Hulet and the one of Salomon. In this case, the sample was a Bose-Fermi mixture of ^{7}Li and ^{6}Li. The fermions were sympathetically cooled by the evaporatively cooled bosons[2]. Employing a Bose-Fermi mixture has the important advantage that lower temperatures can be reached for the fermionic component. Indeed, in [31] was observed that the cooling efficiency decreased once the gas was sufficiently quantum degenerate, because rethermalization collisions were inhibited by the Pauli blocking. In contrast, in the lithium experiment the presence of the bosons helped minimizing this effect. Moreover, the fact that ^{6}Li was sympathetically cooled rather than evaporated prevented from atomic losses. The quantum properties of a degenerate Fermi gas were thoroughly investigated by the group in JILA, and a comprehensive summary of their results is reported in the thesis of B. DeMarco [52].

Other than ^{40}K and ^{6}Li, by now several additional fermionic species have been brought to degeneracy: ^{53}Cr [55], ^{87}Sr [56], ^{173}Yb [57], ^{171}Yb [58],^{3}He* [59], ^{161}Dy [60] and ^{167}Er [61]. In the frame of this thesis, the last two deserve particular attention. Dysprosium and erbium feature a high magnetic moment, and their interactions are governed by the dipolar force. As will be discussed in Sec. 2.5, the highly magnetic character strongly affect the scattering properties of those atoms. One of the main consequence is the fact that a spin polarized single species fermionic gas of Dy or Er can be evaporatively cooled, rethermalization among particles being possible thanks to universal dipolar scattering [60, 61, 62].

The possibility of tuning the interaction strength between particles thanks to Feshbach resonances marked a turning point in the field of ultracold Fermi gases. Fermi-Fermi mixtures of two spin states or two atomic species become a fundamental platform where to investigate fermionic superfluidity and test important theories such as the BEC-BCS crossover. In those systems three-body losses are suppressed because of the Pauli principle. This leads to a great stability of the gas, even in the strongly interacting regime. Strongly interacting Fermi gases are at the core of the DyK experiment, and they will be briefly discussed in Sec. 2.4.

---

[2] A similar method was used in Florence, where they evaporated ^{87}Rb and sympathetically cooled ^{40}K to $\simeq 0.3$ of its Fermi temperature [54].

2.3 Feshbach resonances

In this section I will recall few of the basic concepts about magnetic Feshbach resonances. Feshbach resonances are at the core of many ultracold atom experiments. The topic is extremely wide and rich, and it has been treated in several textbooks, reviews and articles. In this section, I will mostly follow Sakurai's textbook [63] and the review article from Chin et al. [12].

Interaction (and so scattering) between two particles can be formally rewritten as the scattering, in the relative coordinates frame, of a single particle from a potential $V(\mathbf{r})$, whose range is given by r_0. Let's assume that the initial state of the system is the one of a free particle with kinetic energy $E = \hbar^2 k^2/m$, traveling along the $\hat{x}$ direction, whose wave function is a plane wave $\psi_i(\mathbf{r}) \propto \mathrm{e}^{ikx}$. We assume that the scattering event will not affect the internal state of the system. The wave function of the final state, i.e., after the scattering process, will be the sum of the original plane wave plus a spherical wave with amplitude $f(\mathbf{k}', \mathbf{k})$:

$$\psi_f(\mathbf{r}) \xrightarrow{r \gg r_0} A \left(\mathrm{e}^{ikx} + f(\mathbf{k}', \mathbf{k}) \frac{\mathrm{e}^{ikr}}{r} \right). \tag{2.3}$$

The prefactor A accounts for renormalization constants; $\mathbf{k}'$ is the k-vector propagating along $\mathbf{r}$. The amplitude $f(\mathbf{k}', \mathbf{k})$ is referred to as the scattering amplitude. From the Lippman-Schwinger equation it follows that $f(\mathbf{k}', \mathbf{k}) \simeq \langle \mathbf{k}' | V | \psi_i \rangle$. The differential cross section directly follows from the scattering amplitude, being $d\sigma/d\Omega = |f(\mathbf{k}', \mathbf{k})|^2$.

So far we have considered the incoming wave function being an eigenstate of the linear momentum, $|\mathbf{k}\rangle$. It can be demonstrated that also the so called spherical wave states $|E, l, m\rangle$ form a diagonal basis for the free-particle Hamiltonian (E, l, m are respectively the relative kinetic energy, the orbital angular momentum and its projection along the quantization axis). In position space, those states are given by $\langle \mathbf{r} | E, l, m \rangle = c_l j_l(kr) Y_l^m(\hat{\mathbf{r}})$, where $c_l \propto i^l \sqrt{k}$, $j_l(kr)$ are the spherical Bessel functions of order l and $Y_l^m(\hat{\mathbf{r}})$ are the spherical harmonics. A plane wave can be written as a sum over the various l and m contributions. With some algebra it can be shown that $\mathrm{e}^{ikx} \simeq \sum_l c_l j_l(kr) P_l(\hat{\mathbf{k}} \cdot \hat{\mathbf{r}})$ (see for instance [63]). The Legendre polynomials of order l, $P_l(\phi)$, have been introduced. In this new basis, at large distances from the scatterer the initial state is a sum of incoming and outgoing spherical waves [3]. The scattering amplitude can be decomposed in spherical waves

---

[3] The limit for $x \to \infty$ of the spherical Bessel functions is

$$j_l(x) \xrightarrow{x \to \infty} \frac{\mathrm{e}^{i(kr - l\pi/2)} - \mathrm{e}^{-i(kr - l\pi/2)}}{2ix}.$$

too, and reads:

$$f(\mathbf{k}',\mathbf{k}) = \sum_{l=0}^{\infty}(2l+1)f_l(k)P_l(\hat{\mathbf{k}}\cdot\hat{\mathbf{k}}'), \tag{2.4}$$

where $f_l(k)$ is the partial-wave amplitude.
Rewriting Eq. 2.3 in the spherical waves basis gives

$$\psi_f(\mathbf{r}) \xrightarrow{r\gg r_0} \sum_{l=0}^{\infty}(2l+1)\frac{P_l(\hat{\mathbf{k}}\cdot\hat{\mathbf{k}}')}{2ik}\left[\mathrm{e}^{2i\delta_l}\frac{\mathrm{e}^{ikr}}{r} - \frac{\mathrm{e}^{-i(kr-l\pi)}}{r}\right]. \tag{2.5}$$

The scattering event leaves the incoming spherical waves unaltered, while the outgoing spherical waves get a factor $\mathrm{e}^{2i\delta_l} = 1 + 2ikf_l(k)$. The effect of the scattering process in the wave function at large distance is just a phase shift in the outgoing wave.
In the frame of ultracold atoms, we are mostly dealing with short-range, spherical potentials. The interaction between two atoms can be modeled as the sum of two contributions: a short-range repulsive one, accounting for the impenetrability of the two atoms, and a long-range attractive one, accounting for the Van der Waals interaction [64]. We are interested on the phase shift imprinted to the two-atoms wavefunction after the interaction. Since we are treating ultracold atoms, we can work in the low energy limit ($k \to 0$ and consider only s-wave scattering, $l = 0$). In this limit, the phase-shift can be parametrized by a single quantity, the scattering length a, defined as:

$$\lim_{k\to 0} k\cot\delta_0 = -\frac{1}{a}. \tag{2.6}$$

To further discuss scattering in ultracold atoms, it's important to remind that different electron spin configurations of the two interacting atoms can lead to different interaction potentials (or channels α). In the presence of more scattering channels, coupling between the channels has to be taken into account (multi-channel model). Defining the channel energy E_α, the total energy of the system will be $E_{tot} = E_\alpha + E$. Two different channels can have different total energy. Following Ref. [12], let's consider a system of two atoms ($|\psi_{at}\rangle$), far apart one from each other, with low kinetic energy ($k \to 0$), whose interaction potential is given by V_{op}, such that $V_{op}(r \to \infty) = 0$. We refer to this channel as the *open* channel. The interaction potential V_{op} is characterized by the so called background scattering length a_{bg}. We then consider a second interaction channel (close channel, V_{cl}), which has an higher internal energy. The close channel features a (bare) molecular state ($|\psi_{mol}\rangle$), with molecular energy E_{mol} quite close to zero. By tuning the magnetic field, the offset between the two channels for $r \to \infty$ can be changed by the amount $\delta\mu B$, where B is the magnetic field and where we have introduced the differential magnetic moment $\delta\mu = \mu_{cl} - \mu_{op}$, μ_{cl} and μ_{op} being the magnetic moment of the system respectively in the closed and open channel. It is thus possible to cause the molecular state to be almost degenerate with the free atoms state: The two channels can couple, the modified (dressed) states being $\left|\tilde{\psi}_{at}\right\rangle$ and $\left|\tilde{\psi}_{mol}\right\rangle$. As a consequence of the coupling, both the molecular energy and the scattering length also change. A so-called magnetic[4] Feshbach resonance arises when, for some magnetic field region, the bare molecular state gets degenerate with the asymptotic scattering state (the open channel). When this happens, the scattering length diverges.

Feshbach resonances are a powerful tool, because they allow for a modification of the interaction strength by fine tuning the magnetic field. More in general, around a single, isolated resonance, the scattering length assumes the following dependence on the magnetic field:

$$a(B) = a_{bg}\left(1 - \frac{\delta}{B - B_0}\right). \tag{2.7}$$

Here δ is the resonance width and B_0 is the center (or pole) of the resonance, i.e. where a diverges. Another important quantity is the resonance zero-crossing $B_{zc} = B_0 + \delta$, where the scattering length becomes zero.

The coupling of the two channels around a Feshbach resonance not only modifies the scattering length, but also the energy E_{mol} of the bound (molecular) state. In particular, in the universal regime, the dressed molecular state has an energy $E_b = -\hbar^2/(2ma^2)$. Recalling Eq. (2.7), this means that the binding energy around the pole of the Feshbach resonance depends quadratically on the magnetic field detuning $E_b \propto (B - B_0)^2$. Moving away from the resonance center, the molecular state becomes more and more bound. The closed channel character of the bare molecular state becomes more and more dominant, and E_b becomes linearly dependent on B.

A Feshbach resonance can be broad (strong) or narrow (weak). The difference stands in how much $\left|\tilde{\psi}_{at}\right\rangle$ and $\left|\tilde{\psi}_{mol}\right\rangle$ preserve their original character. If the near-threshold scattering and bound state have the internal structure of the scattering state, the resonance is said broad (or strong). Vice versa the resonance is said narrow (or weak) [5]. Technically speaking, a broad Feshbach resonance is often characterized by a large value of δ, making it easier to work with, given the less sensitivity to magnetic field fluctuations.

---

[4] Hereafter the term *magnetic* will be omitted, unless necessary.

[5] A useful quantity is the range parameter R^*, introduced in [65], $R^* = \frac{\hbar^2}{2m^* a_{bg}\delta\delta\mu}$. In the universal region the relation $|a| \gg R^*$ holds. Conditions for a Feshbach resonance to be broad are not necessarily a large value of δ, rather a large value for the quantity $a_{bg}\delta\delta\mu_b$, where $\delta\mu_b$ is the difference between the magnetic moment of the free atoms system and the magnetic moment of the dressed molecular state.

Near the center of a Feshbach resonance, interactions are enhanced. For an s-wave broad Feshbach resonance, the elastic cross section is given by $\sigma_{el} = 4\pi a^2/(1+k^2a^2)$ (an additional factor of 2 has to be considered for identical particles). It follows that around a Feshbach resonance, σ_{el} increases fast from its background value. In the zero temperature limit, where $k \to 0$, $\sigma_{el} = 4\pi a^2$ is a valid approximation. Where a diverges, this approximation ceases to hold and the cross section takes the value $\sigma_{el} = 4\pi/k^2$. This expression coincides with the upper bound set on the scattering amplitude by the unitarity of quantum mechanics [12]. When the scattering amplitude acquires this limit value, the system is said to be in the unitary regime. In this regime, the scattering length drops out of the problem, and the only remaining relevant length scales are the inter-particle distance and λ_{dB}.

In the vicinity of a Feshbach resonance inelastic losses are enhanced too. In an inelastic two-body process, one or both colliding atoms end up in a lower-energy internal state. The extra energy becomes available as kinetic energy, causing the atoms to escape the trap. Two-body inelastic collisions are only present in those systems where the atoms are not in their ground state. For typical experimental conditions three-body losses are thus the dominant ones. A three-body process sees the recombination of three atoms in a dimer and a free atom. The binding energy is released as kinetic energy, and the dimer plus atom escape from the trap. For bosons, the three-body recombination rate is independent of the energy of the atoms and scales as a^4 [66]. In a two-component Fermi gas, the rate is slower and linearly depends on the relative kinetic energy of two identical particle [65]. In experiments, the enhancement of both elastic and inelastic collisions are exploited respectively in thermalization and loss scans, to experimentally find, locate and characterize a Feshbach resonance (see [12] and references therein).

In the above treatment we have assumed that the atoms are interacting in s-wave collision channels. This assumption is justified by the fact that in an ultracold atomic system with dominant Van der Waals interactions, the energy of the colliding particles is usually so low that only the s-wave channel gives an actual contribution to the interaction, the other channels being kinetically suppressed. That being said, scattering can also happen in higher l-channels. Examples of systems of particles interacting in higher partial waves are gas of polarized, single species fermions, where scattering in s-wave is forbidden because of the Pauli principle, or ultracold gas featuring long-range, anisotropic interactions, where for all partial waves the phase shift is $\delta_l \propto k$, and the various channels are mixed [67, 68]. This is the case for instance of dysprosium and in general of highly magnetic atoms, and is at the base of the peculiar scattering properties of those gases. As discussed in Sec. 2.5, the coupling of different l-wave collision channels gives rise to an extremely rich Feshbach spectrum.

The aforementioned formalism of Feshbach resonances also applies to scattering in higher partial waves. In the case of a p-wave resonance, the scattering length needs to be substituted by the so-called scattering volume $V^{(p)}(B)$. In analogy with an s-wave resonance, a collision channel is characterized by a background scattering volume ($\mathrm{V}_{bg}^{(p)}$). The scattering volume diverges approaching the pole of the resonance, being $\mathrm{V}^{(p)}(B) = V_{bg}^{(p)}(1 - \delta/(B - B_0))$. Elastic and inelastic process are enhanced in vicinity of the resonance. The elastic cross section has a resonant behavior, being $\sigma_{el}^{(p)2}/((E-\delta)^2 + \hbar^2\gamma^2/4)$, where δ is the energy of the bare molecular state, and γ depends on the microscopic detail of the potential [69, 70]. In stark contrast with the s-wave resonance, where σ_{el} can be considered constant with energy (in the limit where $ak \to 0$), elastic collisions in p-wave channels are kinetically suppressed. This explains why evaporation exploiting p-wave interactions is not efficient. Also the three-body recombination rate is kinetically suppressed, in the threshold regime being $K_3 \propto E^2$ [71]. At fixed energy, the K_3 increases as $(\mathrm{V}^{(p)})^{8/3}$ [72], until it reaches the unitary limit $K_3^{max} \propto \hbar^2/(m^3E^2)$ [73].

Feshbach resonances are nowadays an ubiquitous tool in cold-atom experiments. They allow for a fine tuning of the interactions among particles, opening up the way to otherwise inaccessible physics regimes.

The first experimental observation of a Feshbach resonance in a degenerate gas was done in 1998 by the group of W. Ketterle [74]. They observed the enhancement of inelastic losses around a Feshbach resonance on a BEC of Na, and calculated the corresponding increase in the value of the scattering length. The first observation of magnetic Feshbach resonance in a fermionic spin mixture was done in 2002, by the group of D. Jin: In [75] they reported on the behavior of the elastic scattering cross section between the two lowest spin states of ^{40}K when the magnetic field was varied around the Feshbach resonance at 201 G. In 2004, the first observations of Feshbach resonances in heteronuclear mixtures were reported [76, 77].

Nowadays, many experiments are carried out in vicinity of a Feshbach resonance. The major research directions are related to the creation of BEC (or DFG) of Feshbach molecules (see for instance [78, 79, 80]), the study of impurity physics (for instance [81, 82, 83]), the investigation of few-body physics [84] and the study of Fermi mixtures in the BEC-BCS crossover, as will be discussed in Sec. 2.4. It's worthy mentioning that a steadily rising interest is also turned towards the investigation of p-wave Feshbach resonance (for instance [85, 86, 87]).

2.4 Strongly interacting Fermi gas

Under certain circumstances the energy of an interacting fermionic system can be minimized by promoting the formation of fermionic pairs. Pairing phenomena where two fermions pair up are ubiquitous in nature. The formation of Cooper pairs in superconductors or the formation of bosonic molecules are examples of such pairing phenomena. The system of paired fermions will find itself in different phase of matter, depending on several factors, in particular the temperature of the gas and the kind of interparticle interaction (symmetry, sign and strength). Ultracold Fermi gases are a great platform where to explore fermionic pairing, because of the high degree of control on the temperature of the gas and on the interactions, which can be tuned thanks to Feshbach resonances. Limiting the discussion to s-wave interactions, pairing phenomena can only be explored in fermionic mixtures, the two components being two spin states of the same species (e.g., spin mixtures of ^{6}Li and of ^{40}K), two isotopes [88] or two different atomic species (Li-K, Dy-K, Cr-Li, etc...).

When pairing happens on the attractive side of a Feshbach resonance, i.e., where the scattering length is negative, the system is said to be in the BCS regime. Here, an atom with momentum $\mathbf{k}$ pairs up with an atom with opposite momentum $-\mathbf{k}$, forming the so-called Cooper pair, which features zero momentum. The two paired atoms are correlated in momentum space. Spatially, the two atoms are quite far apart, and the pairs are overall overlapping. The formation of Cooper pairs is a many-body effect. It is energetically favorable for the system to pair atoms which are located in the vicinity of the Fermi surface. This mechanism is at the basis of low-temperature superconductivity (from which the appellation BCS regime).

On the other hand, if pairing happens on the repulsive side of the Feshbach resonance ($a > 0$), the system is said to be in the BEC regime. In this case, the two fermions pair up and create a molecule. Such a molecule can be considered as a two-body object. In contrast to the BCS case, the two atoms are correlated in space, the molecules featuring a small size. Pairing happens also on resonance. Here the pairs share some properties of the Cooper pairs and some properties of the diatomic molecules. Resonant pair formation is a subtle topic, still not fully understood (see for instance [89]).

No matter which is the nature of the interactions ($a < 0, a > 0$ or $|a| \to \infty$), if the system is cooled down below a certain critical temperature T_c, it becomes superfluid. In the BCS regime, the onset of superfluidity coincides with the formation of Cooper pairs. The critical temperature is typically few hundredths of the system Fermi temperature, and exponentially increases with the interaction strength, $T_c \propto T_F \exp\left[-\pi/(2|a|k_F)\right]$ [90]. In the BEC regime, diatomic molecules already exist at high temperature. Below T_c, they undergo condensation and form a molecular BEC, the system entering the superfluid regime. In this case, the critical temperature is the one for Bose-Einstein condensation. On resonance pairs start to form below a pairing temperature $T^* \gtrsim T_c$. The critical temperature here is much higher than in the BCS regime, with $T_c \simeq 0.17\, T_\mathrm{F}$ for an homogeneous system [91]: Such a relatively high critical temperature makes resonant superfluidity extremely appealing for experimentalists. Working on resonance also comes with the advantage of stability against collisional relaxation, as observed for instance in [92]. Indeed, in contrast to bosons, for which the three-body recombination rate grows as a^4 for large $|a|$ [93], thanks to the Pauli principle the recombination rate for a fermionic mixture scales as a^{-s}, with s close to 3 [94].

On resonance, where the scattering length diverges, the system enters the so-called unitary regime: Interactions are so strong that they become limited by the unitarity of quantum mechanics, the scattering cross sections reaching its maximum value $\sigma = 4\pi/k^2$. In the unitary regime the scattering length drops out of the problem, and the relevant remaining length scales are $n^{-1/3}$ and λ_{dB} (or, equivalently, the relevant remaining energy scales are the Fermi energy E_F and the temperature k_BT). If, on the one hand, the lack of small parameters makes theoretical calculations quite hard, on the other hand the system properties no longer depend on the atomic potential and the thermodynamic quantities hinge on T/T_F only [95, 96]. In this sense, the gas is said to enter the universal regime.The relevant thermodynamics quantities are related to the ones of a non interacting Fermi gas via a universal function of T/T_F. In the limit of $T = 0$, this universal function reduces to a universal constant (the Bertsch parameter).

It is legitimate to ask whether there is a phase transition between the three aforementioned regimes, or whether a fermionic mixture undergoes a smooth transition from one regime to the other. In his seminal work [10] A.J. Leggett demonstrated[6] a continuous transition of the zero temperature system wave function from the one of tightly bound diatomic molecules ($1/(k_Fa) \to +\infty$) to the one of Cooper pairs ($1/(k_Fa) \to -\infty$), showing that "*nothing special happens when* $1/(k_Fa) = 0$". By this meaning, the system goes smoothly from the BEC to the BCS regime through the unitary one. This concept, which nowadays we refer to as the BEC-BCS crossover, was then extended to non-zero temperatures by Nozières and Schmitt-Rink [11].

The first experimental works on strongly interacting Fermi systems were conducted on spin mixtures of ^{40}K (at JILA) and ^{6}Li (at MIT, in Innsbruck and in Paris). Early works on the strongly interacting regime ($1/(k_Fa) \lesssim 1$) focused on the expansion dynamics of the cloud [98, 99]. In particular, in [99], it was suggested that the observed inversion of the aspect ratio could also be interpreted as a signature of superfluidity. The creation of molecules starting from an ultracold Fermi gas was first demonstrated in 2003 (in potassium [100] and in lithium [101, 102, 92]). The long lifetime of the molecular sample was extremely promising in sight of the creation of a molecular BEC. The molecular condensate was eventually obtained shortly after the observation of molecules [103, 104, 13]. Observation

---

[6] A mathematical description which follows Leggett's work can be found in [97]

of pair condensation along the whole BEC-BCS crossover was reported in [15]. The momentum distribution of the pairs was measured for the whole range where $1/(k_F a) \lesssim 1$. The appearance of an energy gap in the excitation spectrum of the fermionic gas was instead investigated in [40]. The gap energy is a distinctive character of pair formation on resonance and in the BCS side. The gap energy was measured via RF spectroscopy for different temperatures, densities and coupling strength. On resonance and in the BCS regime, a double structure was detected for temperatures $T \lesssim 0.5\,T_F$. Alongside with the bare atomic component, the pair signal showed up at higher frequency. For temperature below $0.2\,T_F$ the bare atomic component disappeared, strongly suggesting that the system was in the superfluid regime. Evidence for the superfluid regime across the BEC-BCS crossover and in the strongly interacting regime has also been provided by the observation of collective modes [105, 106] and the formation of vortices upon stirring the gas [107].

The thermodynamic properties of a Fermi gas for different temperatures and interaction strength became the main subject of study of the majority of the experiments which followed. In particular, a big effort was put on the derivation of the thermodynamic quantities and the equation of state (EoS) for the unitary regime. This is of great interest, given the universal character of a strongly interacting fermionic gas: Results obtained in a table-top experiment can be extended for instance to neutron stars or to the QCD phase diagram [108]. The first measurements on the thermodynamics of strongly interacting gas concerned trap-averaged quantities, such as the heat capacity [109], the potential energy [110, 111], the trap-averaged critical temperature and the entropy [111], the Bertsch parameter [110, 17] or the sound velocity [112]. The measurement of trap-averaged quantities has two drawbacks. On one side, it makes comparison with theories developed for uniform gases difficult. On the other side, it prevents the observation of the discontinuity of certain quantities at the critical temperature, given that the critical behavior associated with the phase transition only affects the portion of the gas for which the local Fermi temperature $T_F(\mathbf{r})$ is such that $T \lesssim T_c \simeq 0.16\,T_F(\mathbf{r})$ [113]. Both limitations have been overcome in the works done in Paris [114] and at MIT [115]. In the first one, the local pressure of the gas was probed using in situ images. The EoS for an homogeneous gas was derived within the local density approximation, according to which the system can be considered locally homogeneous with local chemical potential $\mu(\mathbf{r}) = \mu(\mathbf{r}=0) - V_t(\mathbf{r})$, $V_t(\mathbf{r})$ being the trapping potential. To further benchmark their results, they integrated the EoS over the trapping potential and deduced the EoS for the harmonically trapped unitary gas. They found good agreement with previous experiments. In the Zwierlein group, experiments were performed in a cylindrically symmetric trap. Such a geometry allows for a derivation of the three dimensional density distribution via inverse Abel transformation. They were able to observe the discontinuity of the compressibility and specific heat at the critical temperature, which they measured to be $T_c = 0.167(13)T_F$.

Studies on the collective modes have been an independent check of the EoS. In [116], the first sound velocity was measured for a spin mixture of lithium. The frequencies showed a temperature dependence in good agreement with calculations based on the EoS derived by the MIT group [115]. The second sound velocity was instead measured in [117]: This was the first experimental observation of the two-component nature of a unitary Fermi gas in the superfluid regime. The two components (i.e., the superfluid and the normal one) oscillate with opposite phase, giving rise to an entropy wave whose propagation velocity is a function of the superfluid fraction.

The first experimental studies on superfluidity across the BEC-BCS crossover were all carried on a 50:50 spin mixture of either potassium or lithium and overall aimed at the experimental investigation of the T-X phase space diagram, T and X being the temperature of the gas and the interaction parameter ($X = 1/(k_F a)$), respectively. It is natural to ask what happens in the case of a polarized system. Indeed, in the case of unequal population not every atom can pair up, and the two mixture components may have different Fermi levels. The stability of the superfluid phase against population imbalance was experimentally demonstrated for instance in [16]. The presence of vortices was used as proof of the superfluid regime. The authors qualitatively observed that the higher the population imbalance, the lower the number of vortices, the less the superfluid fraction was. They were able to map out the normal-to-superfluid phase transition as a function of interaction strength and population imbalance, revealing an increasing robustness against population imbalance by going from the BCS to the BEC regime. The ingredient of population imbalance, quantified as $P = \frac{N_1 - N_2}{N_1 + N_2}$, N_i being the total atom number of the i-th species, brings in new interesting scenarios and the phase diagram of the system is predicted to become more complex. The phase diagram of a system featuring population and mass imbalance has been for instance considered in the work from Stoof and coworkers [23]. Figure 2.1 (a) shows the phase diagram of a mass-balanced unitary gas. The critical temperature of a polarized gas is expected to decrease by moving away from the unpolarized case ($P = 0$). Moreover, at high enough polarization a tricritical point[7] appears, together with a region characterized by phase separation (referred to as forbidden region in [23]). All this has been experimentally confirmed in [18].

The superfluid phase is expected to feature a crossover between the BCS phase

---

[7] According to Landau's theory of phase transitions, at a tricritical point the character of the phase transition turns from being continuous to being discontinuous. A tricritical point is associated with phase separation.

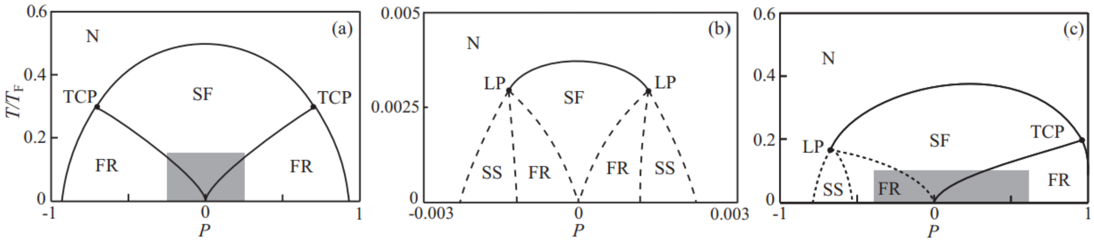

Figure 2.1: Phase diagrams of a fermionic mixture under different conditions of mass ratio and interaction strength. (a) Phase diagram for the mass-balanced case in the unitary limit ($1/k_F a = 0$). (b) Phase diagram for the mass-balanced case in the weakly interacting regime ($1/(k_F a) = -3$). (c) Phase diagram for a mass ratio 6.7 in the unitary limit. Picture adapted from [23]: the notation for the different phases of matter follows accordingly (N: Normal phase; SF: Superfluid phase; FR: Forbidden region; TCP: Tricritical point; LP: Lifshitz point; SS: Supersolid phase).

(whose excitation spectrum is gapped) to the so called Sarma phase (gapless) [21, 22]. An important aspect of polarized gas is the possibility, under certain condition, to create fermionic pairs which feature non-zero momentum. In a spin mixture, this is predicted to happen in the weakly attractive regime, at extremely low temperatures (few thousandths of the Fermi temperature, see Fig. 2.1 (b)). Such an inhomogenehous phase was predicted by Larkin and Ovchinnikov [118] and independently Fulde and Ferrell [19] (hence the name FFLO phase), and so far has been experimentally elusive because of the extremely low temperature required, which are hard to obtain in the lab. The FFLO phase is a supersolid phase, because an inhomogenehous superfluid also brakes the translation invariance. The presence of the FFLO phase in the phase diagram is accompanied by the appearance of a Lifshitz point, at which the homogeneous superfluid phase, the normal phase and the FFLO phase coexist.

Besides an imbalance in the particle densities, a fermionic mixture can also feature an imbalance between the masses of the particles. In this case, the phase diagram is no longer symmetric with respect to polarization, and different phases can build up depending if there's a majority of heavy or light particles. Mixtures featuring mass imbalance have drawn an increasing interest in the last years. Indeed, theoretical calculations show that mass imbalance enlarges the region of the phase diagram where the FFLO state is predicted to appear [24]. From Fig. 2.1 (c) it can be seen that for a unitary system with a majority of light particles, both the Lifshitz point and the FFLO phase are expected to appear at temperatures which are realistically attainable in experiments. The higher the mass ratio, the wider the range of temperatures and polarizations where the FFLO state is predicted to be [24]. Also the appearance of the Sarma phase is enhanced by mass imbalance, and is expected to appear for a majority of heavy particles [23].

2.5 Strongly magnetic lanthanide atoms

The first produced ultracold atomic systems were all featuring short-range interactions between the particles. When those systems are brought in the ultracold regime, only s-wave scattering can take place, with the important consequence that, because of the Pauli principle, interactions in fermionic systems are possible only among non-identical particles.

Recently, an increasing interest has been attracted by systems exhibiting strong dipole-dipole interactions (DDI). In contrast with the van der Waals potential, the dipole-dipole potential V_{dd} is long range ($V_{dd} \propto 1/r^3$) and anisotropic (for a polarized system, $V_{dd} \propto (1 - 3\cos^2\theta)$, θ being the angle between the orientation of the dipoles and the direction of the relative distance between the interacting particles). The main candidates to realize quantum gases with DDI are Rydberg atoms, gases of heteronuclear molecules (both characterized by an electric dipole moment) or highly magnetic atomic gas (characterized by a magnetic dipole moment). The latter are by date the easiest systems to realize and for long time they remained[8] the only ones for which degeneracy has been reached. Chromium was the first dipolar element to be Bose-Einstein condensed [119]. It has a magnetic moment $\mu_{\mathrm{Cr}} = 6\mu_{\mathrm{B}}$ (μ_{B} being the Bohr's magneton), six times higher than for alkali, and it has been the test table to observe several effects of dipolar interactions.

In the last years, lanthanide atoms have attracted the attention of atomic physicists: Some of them, indeed, feature a magnetic moment even higher than the one of chromium. The lanthanide atoms are a family of 15 elements, with atomic number ranging from 57 to 70. Ytterbium aside, they are characterized by an incomplete $4f$ shell, surrounded by two outer filled shell ($6s$ and $5s$). The unpaired electrons in the $4f$ shell give rise to a high value of the orbital angular momentum, which in turns translates into an high magnetic moment. Ytterbium, the last element of the series, makes an exception, having the $4f$ shell complete.

The first attempt to trap lanthanides was successfully done in 2004 in the group of J. Doyle [120], where they magnetically trapped dysprosium, terbium, erbium, holmium, neodymium, thulium and promethium. The atoms were thermalized with the helium buffer gas to a temperature below 2 K.

Originally the lanthanides atoms were thought not to be suitable for laser cooling, given their submerged open $4f$ shell and subsequently complex energetic level structure. In 2006 the pioneering work of McClelland showed that this was not

---

[8] Recently, a degenerate Fermi gas of KRb molecules has been produced in JILA [78].

true, and the first MOT of erbium was obtained [121]. In 2010 also Dy and Tm were loaded into a MOT, and in 2014 was the turn of Ho ([122, 123, 124]). Dysprosium, holmium, erbium and thulium have, in the order, 10, 11, 12 and 13 electrons in the $4f$ shell, which leads to magnetic moments of $9.9\mu_{\mathrm{B}}$, $8.9\mu_{\mathrm{B}}$, $6.9\mu_{\mathrm{B}}$ and $4\mu_{\mathrm{B}}$. Dy, Ho and Er [9] share similar optical transitions suitable for laser cooling. A broad transition ($\simeq 30\,\mathrm{MHz}$) in the blue follows from the excitation of one of the $6s$ electrons into the $6p$ orbital ($6s^2 \rightarrow 6s6p\,(^1\mathrm{P}^0_1)$). This is suitable for a first stage laser cooling. A similar transition, this time into the triplet state ($6s^2 \rightarrow 6s6p\,(^3\mathrm{P}^0_1)$) is responsible for the intercombination line at $\simeq 600\,\mathrm{nm}$: given its narrowness ($\simeq 150\,\mathrm{kHz}$), it is used in the MOT cooling stage to achieve MOT temperatures as low as few μK. Other important, narrow lines derive from the excitation of a $4f$ electron into the $5d$ orbital. In erbium, for instance, a second stage MOT operating in the 841 nm line, 8 kHz wide, has been used in [125] to achieve temperatures as low as 841 nK in the MOT itself. In dysprosium, the same kind of transition is responsible for the line at 741 nm. The production of a blue-detuned narrow line MOT operating on this transition has been reported in [60][10].

An important consequence of the long-range character of the dipole dipole interaction, is that in a scattering process all partial waves contribute to the scattering cross section. For low momentum k, the phase shift is $\delta_l \propto k$ for all scattering channels ($l \geq 0$) [67]. Interactions between atoms with a large orbital angular momentum are controlled by anisotropic forces which mix the different scattering channels (within the parity selection rules), with important implications in the collision properties of lanthanides gas. In first instance, the coupling of the several scattering channels results in an extremely dense Feshbach spectrum [68], as measured in several works (see for instance [126, 127]). The drawback of such an high density of Feshbach resonances is that theoretical predictions of the interaction properties are almost impossible. Additionally, manipulation of those gas becomes highly sensitive to magnetic field instabilities. A second important consequence is that the scattering cross section of identical, dipolar fermions does not vanish at low temperature. In [128] the authors derive that, in the limit of low energies, the elastic cross section can be written as $\sigma_{el} = \frac{16\pi}{45}(\frac{m\mu^2}{4\pi\hbar^2})^2 + 4\pi a^2$ and $\sigma_{el} = \frac{16\pi}{15}(\frac{m\mu^2}{4\pi\hbar^2})^2$ for scattering in even or odd partial waves, respectively. For indistinguishable particles, a factor of 2 has to be added. In other words, in the limit of low energy, the dipolar scattering assumes a universal behavior, and only depends on the strength of the dipoles and on their mass.

Quantum degeneracy has been obtained for the three most abundant bosonic iso-

---

[9] Despite those transitions are present also in Tm, to my knowledge they are not exploited in the works from the russian group.

[10] In our experiment, the 741-nm transition is used for an in-trap Doppler cooling stage performed after the MOT.

topes of dysprosium (see for instance [129, 130, 131]). Among the three, ^{162}Dy features the most favourable scattering properties to perform evaporative cooling [132]. Similarly, in 2012 ^{168}Er was brought to degeneracy for the first time [133], later followed by ^{166}Er and ^{164}Er [134, 135]. From the universality of dipolar scattering follows that elastic collisions among identical fermions are no longer suppressed. As a consequence, dipolar gas of identical fermions can undergo forced evaporative cooling, as demonstrated in [60, 61].

Degenerate gases of lanthanide atoms have risen immediately a lot of interest in the ultracold community. As a clear example of the effect of a stronger dipolar force, we mention the cases of bosonic erbium and dysprosium. Indeed, for bosons with dipolar interactions, an extended version of the Gross-Pitaevskii equation (eGPE) is required [136]. The eGPE nicely captures the physics of dipolar quantum liquids. In particular it accounts for the formation of quantum droplets, i.e. self-bound droplets of atoms [137]. Quantum droplets have been observed in Dy [138] and in Er [134]. The huge effort devoted to the study of quantum droplets lead to the observation of supersolidity, a quantum state of matter where both phase invariance and translational invariance are lost [139, 140, 141, 142].

2.6 Why a Dy-K mixture

The DyK experiment has been conceived as a new, promising platform for the exploration of exotic phases of matter in a strongly interacting Fermi gas. In a heteronuclear Fermi-Fermi mixture, the ingredient of mass imbalance is added to the tunability of interaction strength and polarization (i.e., population imbalance), with the great prospects to realize novel superfluid phases.

The decision of mixing dysprosium and potassium followed from several considerations. The choice of the two species was restricted to K, Li, He*, Cr, Sr, Dy, Er and Yb, i.e., the species that have at least one fermionic isotope for which Fermi degeneracy had already been demonstrated. Mixtures such as Dy-Er, Dy-Yb or Yb-Er were discarded, in order to have mass imbalance significantly greater than 1. On the other hand, it was clear that the mass ratio should not exceed $\simeq 13$. Indeed, it was shown by Efimov [143] that in a system of two identical fermions (A) interacting with a third particle (B), the interaction between the two distinguishable particles lead to an attractive interaction for the A-A system, which scales as $1/r^2$. If the mass ratio $m_{\mathrm{A}}/m_{\mathrm{B}}$ exceeds $\simeq 13$, this interaction is enough for the two identical fermions to overcome the centrifugal barrier, and the three particles can bind together. Near an Efimov resonance (i.e., where a near-threshold trimer forms) three-body inelastic losses are enhanced [144]. For mass ratios below $\simeq 13$, the centrifugal barrier leads to kinetic suppression of three-body recombination.

In view of this, the remaining options were Li-K, Li-Cr[11], K-Dy/Er/Yb or Cr-Dy/Er/Yb.
Any X-Cr mixture was discarded in favor of the corresponding X-K one, given the established experience in manipulating potassium shared among the other Innsbruck labs and the fact that cooling fermionic cromium is technically involved.
The realization of a collisionally stable, strongly interacting Fermi gas requires the presence of an entrance-channel dominated Feshbach resonance. Such a resonance is absent in the Feshbach spectrum of Li-K [148]. No experimental data or theoretical predictions are currently available regarding the interaction properties of the other possible combinations. Still, the dense Feshbach spectrum of Dy and Er leads to the reasonable assumption that any heteronuclear mixture with any of the two features a rich spectrum. Dysprosium has two stable fermionic isotopes (^{161}Dy and ^{163}Dy), while erbium has only one (^{167}Er). Choosing Dy in principle doubles the chances of finding a good broad interspecies Feshbach resonance.
Eventually, we decided for a mixture of dysprosium and potassium. We work with ^{161}Dy, which features an inverted hyperfine structure. For our measurements, both species are spin-polarized in the lowest hyperfine level, preventing two-body losses. The combination of ^{161}Dy and ^{40}K turned out to be a really good one, both in terms of experimental handling and scattering properties. The Dy-K mixture is indeed easy to handle. Dysprosium comes with some technical advantages. Among the others we mention the fact that, after the MOT on the 626-line, the Dy cloud is naturally polarized, and the fact that, thanks to universal dipolar scattering, evaporation of spin polarized ^{161}Dy is possible. The low-field region provides several spots where the Dy-K elastic collision properties are favorable to evaporation. In [27] we reported on the presence of a broad interspecies Feshbach feature at 217 G. Such a feature is a promising candidate where to observe exotic superfluidity. The great properties of the Dy-K mixture led us to important results, part of which are reported in this thesis.

2.7 Storyline of my PhD work

I joined the DyK team in January 2017, when the experiment was in its final building phase. Few days after my arrival, while I was still orientating myself in the new environment, the first dual fermionic MOT of Dy and K was obtained. Around May, we were able to efficiently load the two species in the dipole trap: excited times were about to start.
The first goal of the experiment was the determination of the dynamic polarizabil-

---

[11] The Li-Cr mixture is actually extremely interesting given the mass ratio $m_{\mathrm{Cr}}/m_{\mathrm{Li}} \simeq 8$. For a mass ratio $m_{\mathrm{A}}/m_{\mathrm{B}} = 8.172...$ non-Efimovian trimer states are expected to appear [145, 146]. Experimental investigation of this mixture is currently pursued in Florence [147].

ity of dysprosium at $\lambda = 1064\,\mathrm{nm}$. This wavelength is of particular interest for laser trapping experiments. By that time, there was a big discrepancy between the theoretically predicted value and the measured ones, obtained by trap frequencies measurements. Our double-species experiment was offering an elegant opportunity to settle this issue by using potassium as a reference species. Our result lies between the two available theoretical values [149, 150]. Our measurements are reported in Ch. 3.

The polarizability measurements were performed on a thermal gas of ^{40}K and the bosonic dysprosium isotope ^{164}Dy. Given that our experiment aims at the investigation of a Fermi-Fermi mixture in the unitary regime, in 2018 time had come to change to ^{161}Dy and move in that direction. In Ch. 4 is described how we can produce a deeply double-degenerate Fermi gas, reaching $T/T_F \simeq 0.2$ and $T/T_F \simeq 0.1$ for potassium and dysprosium, respectively.

It took a lot of time and patience before a suitable interspecies magnetic Feshbach resonance was found. The magnetic properties of Dy and the absence of theoretical predictions made the task quite challenging. We performed loss and thermalization scans in almost all the magnetic field range from zero to 250 G, before drawing the conclusion that the broad resonance centered at 217 G was *our* resonance. It followed a careful characterization of the resonance and study of the mixture's behavior around the resonance pole. Our findings are reported in Ch. 5.

The pursuit of superfluidity requires lower temperatures and could benefit from some technical adjustments, such as optical levitation [151], an increased trap frequency ratio [25], boxlike trapping schemes [152, 153]. Those solutions can be implemented employing light at 626 nm, where the presence of the dysprosium intercombination line provides the handle to tailor the desired optical potential. With this in mind, in spring 2020 it followed an accurate measurement of the dynamic polarizability of ^{161}Dy near its 626-nm transition [154]. For this measurement we use modulation spectroscopy in an optical lattice. This scheme relies on the same basic principle as introduced in our 2018 work, but is independent of the sign of the polarizability. Given my minor contributions to the measurements, this work has been omitted from this thesis.

An ultracold atom experiment relies on a virtually infinite number of devices, each of which could fail at any time. A breaking laser is probably one of the most annoying thing that could happen, because it often translates in repairing costs and delays. What is nice about a double species experiment, is that you can still temporarily turn your experiment in a single-specie machine. That's what happened to us in the summer 2020, when our potassium 767-nm laser system needed to be sent back to the manufacturer. We employed this time to investigate the loss properties of ^{161}Dy alone in the low magnetic field region (i.e., below 1 G). In the rich Feshbach spectrum of ^{161}Dy we identified three relatively isolated resonances

and use them as a case study for getting a better general understanding of all the others. Our findings are reported in Ch. 6.
Finally, in Ch. 7 I'll give an overview of the next steps we are planning to take in the experiment.

My PhD work has been carried on within the Doctoral Programme (Doktoratskolleg) Atoms, Light, and Molecules (DK-ALM project). Among the others, this project offered me the great opportunity to spend six months abroad in a leading research center. In agreement with my supervisor, I joined the group of Professor Martin Zwierlein at MIT (Boston). Here, supervised by Dr. C. Robens, I worked on a side project aiming to phase lock two 767 nm distributed Bragg reflector (DBR) lasers, whose linewidth was previously narrowed thanks to optical feedback. The results achieved during my six-months staying are reported in App. C.

3

Accurate Determination of the Dynamical Polarizability of Dysprosium

Published as:
C. Ravensbergen, V. Corre, E. Soave, M. Kreyer, S. Tzanova, E. Kirilov and R. Grimm
Phys. Rev. Lett. 120, 223001 (2018)

Author contribution: The author took part in the measurements and contributed to the general lab work, the interpretation and analysis of the data, and the discussions during the writing of the manuscript.

Note: With respect to the published version, section headlines have been added.

We report a measurement of the dynamical polarizability of dysprosium atoms in their electronic ground state at the optical wavelength of 1064 nm, which is of particular interest for laser trapping experiments. Our method is based on collective oscillations in an optical dipole trap, and reaches unprecedented accuracy and precision by comparison with an alkali atom (potassium) as a reference species. We obtain values of 184.4(2.4) a.u. and 1.7(6) a.u. for the scalar and tensor polarizability, respectively. Our experiments have reached a level that permits meaningful tests of current theoretical descriptions and provides valuable information for future experiments utilizing the intriguing properties of heavy lanthanide atoms.

3.1 Introduction

The dipole polarizability is a quantity of fundamental importance in light-matter interaction, as it characterizes the linear response of a neutral particle to an electric field. The polarizability is related to other important physical quantities, like the van-der-Waals dispersion coefficient, and its knowledge is of great relevance for a deep understanding of many-electron systems, for example in heavy atoms, molecules, and clusters [155]. The static polarizability characterizes the response to a constant electric field by a single real number. The dynamic polarizability (DP) describes the response to an oscillating field and is represented by a complex frequency-dependent function. Naturally, the DP is much richer and contains much more information on the properties of a particle, in particular on its resonance behavior. While various different methods have been established to measure the static polarizability with high accuracy [156, 157], measurements of dynamic polarizabilities are notoriously difficult. Accurate laser-spectroscopic methods only provide access to differential polarizabilities, whereas other methods like deflection from a laser beam suffer from the problem of characterizing the interaction region well enough.

In the realm of ultracold atoms, both the real and imaginary part of the DP play an essential role for controlling the external and internal atomic degrees of freedom. The imaginary part is related to the absorption and scattering of light. The real part gives rise to Stark shifts, which are primarily utilized for constructing optical dipole traps [158] in a wide range of different geometries. Zero crossings of the DP, which occur at tune-out wavelengths, can be used to engineer species-selective traps [159]. Optical lattice clocks operate at a so-called magic wavelength, where the differential DP between the two relevant atomic states vanishes [45]. The DP also enables coherent spin manipulation, which is the basis of many spin-orbit coupling schemes [160].

The optical manipulation of ultracold magnetic lanthanide atoms has attracted considerable interest [123, 129, 133, 60, 161, 122, 162, 138, 163]. Their exceptional magnetic properties arise from a partially filled, submerged 4f shell. They feature a very rich atomic spectrum, including narrow-line optical transitions, and a large orbital angular momentum gives rise to substantial non-scalar contributions to the polarizability. These special properties make magnetic lanthanide atoms excellent candidates to implement advanced light-matter coupling schemes, such as spin-orbit coupling [164, 165], and to realize novel regimes of quantum matter. The electronic configuration makes advanced calculations of the DP very challenging and interesting [149, 166, 150, 167]. To benchmark theoretical models, measurements are highly desirable with uncertainties on the percent level. Experimental results have been reported for dysprosium [129, 131, 168] and erbium [169], in the latter case also demonstrating the anisotropic nature of the DP. However, all these measurements have been subject to large systematic uncertainties, imposed by the methods at hand.

In this Letter, we report on the accurate determination of the real part of the dysprosium DP at a wavelength of particular interesting for cooling and trapping experiments. We utilize an idea often applied in precision metrology, performing a measurement relative to a known reference. We use potassium as a reference species, for which the DP is known on the permille level, and measure the trap frequencies of both species in the same single-beam optical dipole trap (ODT). The frequency ratio is then independent of major experimental systematics and imperfections. In a further set of experiments, we determine the tensor contribution to the DP.

3.2 Dynamical polarizability

The interaction of atoms with the electric field $\vec{E}$ of laser light is described by the Hamiltonian $H = -\frac{1}{2}\vec{E}^{\dagger}\overleftrightarrow{\alpha}\vec{E}$, where $\overleftrightarrow{\alpha}$ is the dynamical polarizability tensor operator [170]. The state-dependent energy shift is

$$U(\mathbf{r}, \omega_L) = -\frac{2\pi a_0^3}{c} I(\mathbf{r}) \tilde{\alpha}(\omega_L), \tag{3.1}$$

where ω_L is the laser frequency, $I(\mathbf{r})$ the position-dependent intensity, a_0 the Bohr radius, and c the speed of light. Here we define $\tilde{\alpha}(\omega_L)$ as a dimensionless quantity corresponding to the real part of the DP α in atomic units ($1\,\text{a.u.} = 4\pi\epsilon_0 a_0^3$, where ϵ_0 is the vacuum permittivity). For a Gaussian laser beam, the central region (trap depth $\hat{U}$) can be approximated by a harmonic potential. The corresponding radial trap frequency

$$\omega_r = \sqrt{\frac{4\hat{U}}{m w_0^2}} = \sqrt{\frac{16 a_0^3}{c} \frac{P}{w_0^4} \frac{\tilde{\alpha}(\omega_L)}{m}} \tag{3.2}$$

is determined by the laser beam parameters (power P and waist w_0) and atomic properties (polarizability $\tilde{\alpha}$ and mass m) [158].

For linearly polarized light and for atoms in a stretched state [1] we can decompose $\tilde{\alpha}$ into two contributions $\tilde{\alpha}_S$ and $\tilde{\alpha}_T$, commonly referred to as the scalar and tensor polarizability [150],

$$\tilde{\alpha}(\omega_L) = \tilde{\alpha}_S(\omega_L) + \frac{3\cos^2\theta - 1}{2}\tilde{\alpha}_T(\omega_L); \tag{3.3}$$

here θ is the angle between the polarization axis and the quantization axis, the latter being defined by the magnetic field. Note that within a hyperfine manifold $\tilde{\alpha}_S$ and $\tilde{\alpha}_T$ only depend on the wavelength.

The usual method to measure the dynamical polarizability in an ODT [129, 131, 169] is to determine the trap frequency ω_r by observing collective oscillations in a trap with a given power P and a well-defined waist w_0, and to use Eq. (3.2). A major complication arises from the strong dependence $\tilde{\alpha} \propto w_0^4$. An accurate determination of w_0 at the position of the atoms is crucial, but very difficult to achieve in practice. In addition, any aberrations from an ideal Gaussian beam are not accounted for. Moreover, a real cloud with its finite spatial extent will experience some anharmonicity, which will alter the measured oscillation frequency. The combination of these systematic problems typically limits the accuracy of such DP measurements to a few 10% [169].

The above limitations can be overcome by referencing the trap frequency of the particle of interest (or state [171]) to a species with a known polarizability [172, 173]. Figure 3.1 illustrates the situation for two species in the same optical trapping field, where different potential depths result from the different polarizabilities. Within the harmonic trap approximation, the DP of the unknown species, in our case Dy, is then obtained as

$$\tilde{\alpha}_{\mathrm{Dy}} = \tilde{\alpha}_{\mathrm{K}} \frac{m_{\mathrm{Dy}}}{m_{\mathrm{K}}} \left(\frac{\omega_{\mathrm{Dy}}}{\omega_{\mathrm{K}}}\right)^2, \tag{3.4}$$

where $\tilde{\alpha}_{\mathrm{K}}$ is the polarizability of the reference species (in our case K), and $m_{\mathrm{Dy}}/m_{\mathrm{K}}$ is the known mass ratio. Experimentally, one only has to measure the frequency ratio $\omega_{\mathrm{Dy}}/\omega_{\mathrm{K}}$, which eliminates the need to determine w_0 or P. This scheme also removes the effects of anharmonicity provided that the ratio of the temperature to the trap depth is the same for both species. In this ideal case, illustrated in Fig. 3.1, the two thermal clouds fill exactly the same region in the trap, and thus experience the same relative effect of anharmonicity. Introducing another species with a different mass may lead to a different gravitational sag and thus to a shift of

---

[1] Angular momentum projection on the quantization axis equals plus or minus the total angular momentum ($|m_J| = J$)

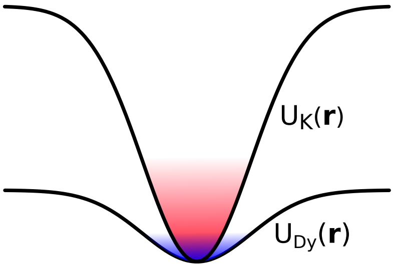

Figure 3.1: Schematic illustration of the species-dependent optical trapping potential U filled with potassium or dysprosium atoms in a beam with a Gaussian profile. Here, in the ideal case, the ratio $T/\hat{U}$ is equal for the two species, the atoms explore exactly the same region in the trap, and thus experience the same anharmonicity and beam aberrations.

the frequency ratio. This effect, however, can be suppressed by using a sufficiently deep and tight trap.

3.3 Experimental setup

In our experiments, we use the isotopes ^{164}Dy and ^{40}K, with a mass ratio $m_{\mathrm{Dy}}/m_{\mathrm{K}} = 4.102$. For trapping we use the standard near-infrared wavelength of 1064.5 nm. At this wavelength the polarizability of potassium [2] is $\tilde{\alpha}_{\mathrm{K}} = 598.7(1.1)$ [174, 175]. Based on the available theory values for Dy [149, 150], we can estimate $\tilde{\alpha}_{\mathrm{K}}/\tilde{\alpha}_{\mathrm{Dy}} \approx 3.2$ and $\omega_{\mathrm{K}}/\omega_{\mathrm{Dy}} \approx 3.6$.

We produce a thermal cloud of either ^{164}Dy or ^{40}K atoms in a single-beam ODT. For dysprosium, we employ a laser cooling and trapping scheme similar to Refs. [176, 163]. After loading the ODT and some evaporative cooling, we typically trap 10^6 atoms, spin-polarized in Zeeman substate $|J = 8, m_J = -8\rangle$, at about 8 μK. For potassium, after a sub-Doppler cooling stage [177] which also enhances ODT loading, we have 3×10^5 unpolarized atoms at $\sim$30 μK. The trapping laser (Mephisto MOPA 18 NE) operates on a single longitudinal mode, is linearly polarized, and its power is actively stabilized. All measurements reported here are performed with $P = 2.5$ W, $w_0 \approx 30\,\mu$m, and a magnetic field strength of 250 mG.

We measure the trap frequencies by exciting a center-of-mass (CoM) oscillation, the so-called sloshing or dipole mode. In a harmonic potential, this mode does not involve a compression of the cloud and the frequency is thus not affected by

---

[2] At 1064.5 nm the polarizability of potassium is without any significant tensor contribution.

the interactions within the cloud or by its quantum statistics [178]. We excite a pure radial sloshing oscillation by displacing the trap position abruptly in the vertical direction using an acousto-optic modulator. The displacement amounts to approximately $2\,\mu$m, which is smaller than the in-trap radial cloud size of about $\sigma_r = 6\,\mu$m. After a variable hold time we switch off the trap and perform standard time-of-flight (ToF) absorption imaging. The cloud position is extracted from the images by performing an one-dimensional Gaussian fit to a vertical slice taken from the central part of the elongated trap. Both species are imaged using the same optical path and camera.

A typical measurement run for both dysprosium and potassium is shown in Fig. 3.2. The magnetic field is chosen to be parallel to the polarization of the trapping light ($\theta = 0$), and therefore from Eq. (3.3) we get $\tilde{\alpha} = \tilde{\alpha}_S + \tilde{\alpha}_T$. We fit the oscillations with an exponentially damped sine wave to extract the frequency ω^{fit} and the damping time τ of the oscillation. The two species oscillate at different frequencies because of their different mass and polarizability. By relative scaling of the horizontal axes of Fig. 3.2 with the expected factor of 3.6 the oscillations exhibit a nearly identical behavior. This already confirms that the theoretical values of Refs. [149, 150] provide a good estimate for the Dy polarizability. The identical damping behavior, with $\omega^{\text{fit}}\tau$ being the same for both species, is consistent with our assumption that the main source of damping is dephasing resulting from the trap anharmonicity [3].

3.4 Systematic effects

The measured frequency ratio exhibits a residual anharmonicity effect if the ratio of temperature and trap depth is not exactly equal for both species. We take this into account by a small correction to the dysprosium oscillation frequency. For a given potassium temperature T_{K} the corresponding dysprosium temperature would be $(\tilde{\alpha}_{\text{Dy}}/\tilde{\alpha}_{\text{K}})T_{\text{K}}$. A deviation from this ideal value can be quantified by $\Delta T_{\text{Dy}} = T_{\text{Dy}} - (\tilde{\alpha}_{\text{Dy}}/\tilde{\alpha}_{\text{K}})T_{\text{K}}$. The anharmonic frequency shift depends on the slope $\beta = \mathrm{d}\omega_{\text{Dy}}/\mathrm{d}T_{\text{Dy}}$, which gives a corrected frequency ratio

$$\frac{\omega_{\text{K}}}{\omega_{\text{Dy}}} = \frac{\omega_{\text{K}}^{\text{fit}}}{\omega_{\text{Dy}}^{\text{fit}} - \beta\Delta T_{\text{Dy}}}. \tag{3.5}$$

With this correction, Eq. (3.4) allows to determine $\tilde{\alpha}_{\text{Dy}}/\tilde{\alpha}_{\text{K}}$ in an accurate way.

In order to determine β, we vary the temperature of the dysprosium atoms and measure the oscillation frequency. The temperature, determined by standard

---

[3] See Sec.3.7 for tests of the absence of density-dependent effects on frequency and damping, for the investigation of the temperature-dependence of damping, and for more information on our measurements of the tensor part of the Dy polarizability.

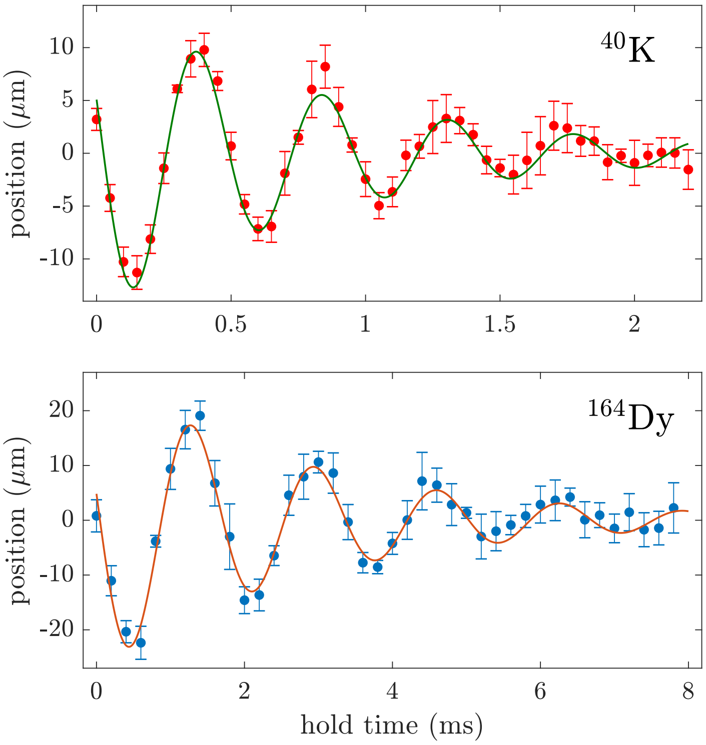

Figure 3.2: Radial sloshing mode oscillation for potassium and dysprosium. The cloud position after ToF is plotted against the hold time in the trap after the excitation. We obtain $\omega_{\mathrm{K}}^{\mathrm{fit}}/2\pi = 2060(10)$ Hz and $\omega_{\mathrm{Dy}}^{\mathrm{fit}}/2\pi = 577(2)$ Hz, $\tau_{\mathrm{K}} = 1.1(1)$ ms and $\tau_{\mathrm{Dy}} = 3.8(2)$ ms. The temperatures are $T_{\mathrm{K}} = 36(3)\,\mu$K and $T_{\mathrm{Dy}} = 8.3(2)\,\mu$K, and the ToF is 0.3 ms for K and 2 ms for Dy. Note that the time scales for K and Dy differ by a factor of 3.6. The error bars show the sample standard deviation of five individual measurements at the same hold time.

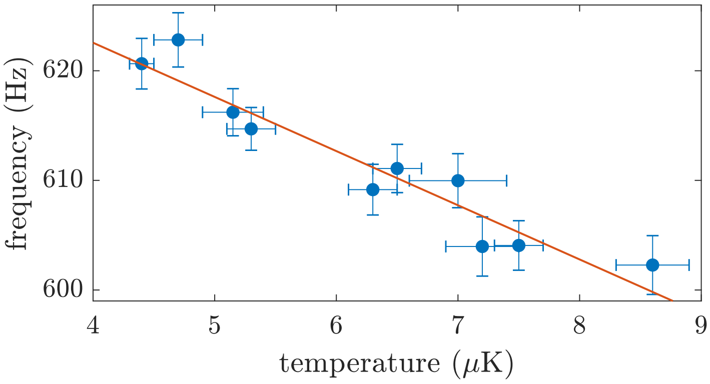

Figure 3.3: Anharmonicity effect on the trap frequency. The Dy CoM oscillation frequency is plotted as a function of the cloud temperature. The weighted linear fit takes both frequency and temperature errors into account, and yields a slope $\beta/2\pi = -5.1(7)\mathrm{Hz}/\mu\mathrm{K}$.

TOF expansion, is changed by an evaporation ramp down to a variable trap power followed by a re-compression to the standard power and a hold time for thermalization. We observe a frequency decrease with increasing temperature, as is shown in Fig. 3.3. From this set of measurements and a second one taken under similar conditions (not shown in Fig. 3.3), we obtain the combined result $\beta/2\pi = -4.5(4)$ Hz/μK. Note that the anharmonicity shifts the measured Dy frequency, for our typical temperatures and trap depth, by about 5% as compared to the harmonic approximation of Eq. (3.2).

Possible remaining systematics affecting the frequency ratio could include density-dependent interactions, the finite excitation amplitude, and the effect of gravity. We do not observe a density dependence of the oscillation frequency of Dy when varying the atom number over a wide range, confirming that the frequency shift observed in Fig. 3.3 can be fully attributed to a change in temperature. The frequency ratio should not be affected by the excitation amplitude, because, for an equal amplitude, both species are affected in the same way. In addition, we varied the excitation amplitude for a single species (Dy) and we did not observe any significant shift for the amplitude used here. The estimated gravitational frequency shift in our trap is $\sim 0.1\%$ [4], which we neglect in our analysis. Moreover, we noticed that the fitted frequency may slightly depend (on the subpercent level) on the time interval chosen for the analysis. To avoid systematic deviations in the comparison of both species, we choose the time intervals to follow the scaling factor of 3.6. With 0-2.2 ms for K and 0-8 ms for Dy, the intervals then correspond

---

[4] The relative frequency downshift caused by the gravitational sag can be approximated by: $-2(g/w_0\omega^2)^2$

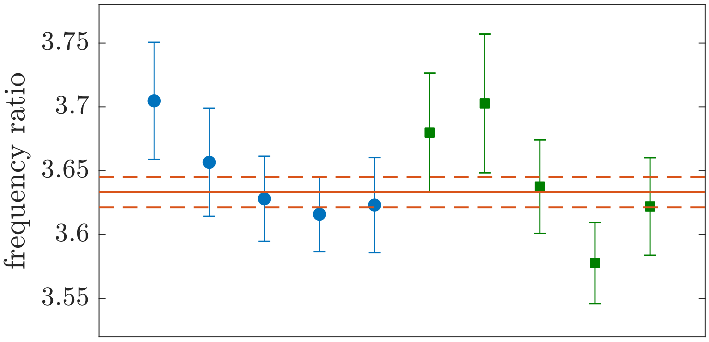

Figure 3.4: Repeated measurements of the frequency ratio $\omega_{\mathrm{K}}/\omega_{\mathrm{Dy}}$, including small anharmonicity corrections. The two symbols (blue dots and green squares) represent the data sets taken on two different days. The temperatures are $T_{\mathrm{K}} = 36(3)\,\mu$K and $T_{\mathrm{Dy}} = 8.3(2)\,\mu$K on the first day, and $T_{\mathrm{K}} = 30(2)\,\mu$K and $T_{\mathrm{Dy}} = 7.6(3)\,\mu$K on the second day. The solid line marks the weighted average $\omega_{\mathrm{K}}/\omega_{\mathrm{Dy}} = 3.632(12)$, with the dashed lines showing the corresponding statistical error range. Note that the total error is about twice larger if uncertainties in temperature and anharmonicity coefficient(not included in the error bars) are taken into account.

to about twice the respective $1/e$ damping time τ_{K} or τ_{Dy}.

3.5 Determination of the polarizability

We now turn our attention to an accurate and precise determination of the frequency ratio $\omega_{\mathrm{K}}/\omega_{\mathrm{Dy}}$. We measure the potassium and dysprosium CoM oscillation frequency, in the same trap, in an alternating fashion to eliminate possible slow drifts over time, and repeat this 10 times. The resulting frequency ratios, including small anharmonicity corrections, are shown in Fig. 3.4. The data were taken on two different days, which were one week apart, and the consistency shows the robustness of the presented method. The differential anharmonicity effect from Eq. (3.5) yields a small correction of about 1.4% and 2.2% for the frequency ratio of the two data sets. The combined result for the frequency ratio is $\omega_{\mathrm{K}}/\omega_{\mathrm{Dy}} = 3.632(22)$. Here the largest contribution to the total error comes from the uncertainties in the anharmonicity correction, which are mainly due to uncertainties in the K temperature.

In a second set of experiments, we measure the frequency ratio $\omega_{\parallel}/\omega_{\perp}$ for Dy in a magnetic field parallel and perpendicular to the polarization of the laser field. In this way, we can identify the tensor part which is expected to be more than 100 times smaller [150] than the scalar part. Here we perform in total 11 pairs of measurements, alternating the angle θ between 0 and $\pi/2$. We obtain the combined result $\omega_{\parallel}/\omega_{\perp} = 1.0070(24)$, which significantly deviates from one and thus reveals a tensor contribution.

From the measured frequency ratios and Eqs. (3.1-3.3), it is now straightforward to derive the polarizability ratios $(\tilde{\alpha}_S + \tilde{\alpha}_T)/\tilde{\alpha}_{\mathrm{K}} = 3.217(40)$ and $(\tilde{\alpha}_S + \tilde{\alpha}_T)/(\tilde{\alpha}_S - \tilde{\alpha}_T/2) = 1.014(5)$. Solving for the scalar and tensor part and using the reference value for $\tilde{\alpha}_{\mathrm{K}}$, we finally obtain $\tilde{\alpha}_S = 184.4(2.4)$ and $\tilde{\alpha}_T = 1.7(6)$.

Our result for the scalar polarizability lies between the two theoretical values of 180 a.u. [149] and 193 a.u. [150], being consistent with both of them within the corresponding error estimates of a few percent [179, 180]. For the small tensorial part, our result is consistent with the theoretical value of 1.34 a.u. [150].

3.6 Conclusion

Already in its present implementation, the experimental uncertainty of our method to determine the DP of a magnetic lanthanide atom is smaller than the uncertainties of theoretical calculations. This, in turn, means that our new result already provides a benchmark and sensitive input for refined theoretical calculations. In extension of our work, much more information on the DP can be obtained by measuring at other optical wavelengths [169], which is straightforward to be implemented experimentally. Furthermore, experimental uncertainties may be reduced considerably by using the well-defined environment of optical lattices instead of macroscopic trapping schemes. Further advanced DP measurements could provide a wealth of accurate information on the interaction of light with atoms that feature a complex electronic structure, which would go far beyond the present state of the art.

In our future experiments, we are particularly interested in mass-imbalanced Fermi-Fermi mixtures and possible new superfluid pairing regimes [181, 182, 183, 184, 185, 23, 186, 24]. For the combination of ^{161}Dy and ^{40}K and not far from our present experimental conditions, a “magic" wavelength is expected to exist where the polarizability ratio for the two species corresponds to the inverse mass ratio. An optical dipole trap operating at this particular wavelength would automatically match the Fermi surfaces of both species after deep evaporative cooling. Based on Refs. [149] and [150] for Dy and [174] for K, we would expect this wavelength to be at 982nm or 954nm, respectively, and our present measurement suggests it to be in between these two values. The precise location will be subject of further studies.

Acknowledgments

We thank M. S. Safronova for the data on the K polarizability and for useful discussions. We also thank A. Turlapov, M. Lepers, and O. Dulieu for stimulating discussions. We thank the Innsbruck Er team for kindly sharing their results prior to publication. We acknowledge support by the Austrian Science Fund (FWF) within the Doktoratskolleg ALM (W1259-N27).

3.7 Supplemental material

In Sections 3.7.1 and 3.7.2 we present measurements on Dy testing systematic effects introduced by atomic density and temperature. Section 3.7.3 provides additional information on our measurement of the tensor part of the polarizability of Dy. Section 3.7.4 reviews the different contributions to the uncertainty on our measurement of the polarizability of Dy.

3.7.1 Absence of density effect on oscillation frequency

Throughout our determination of the polarizability of Dy we assume that the frequency of the CoM oscillations is independent of the atomic density, as is expected in a harmonic potential. In this section we test this basic assumption by investigating the effect of density on our frequency measurements. We prepare samples of largely different atom number and determine the frequency for the same trap depth as used in the main text. The atom number is controlled through the MOT loading time. We use a standard (reduced) loading time of 4 s (0.2 s), resulting in a cloud of about $1.1 \times 10^6 (4.5 \times 10^5)$ atoms. We measure alternately using one loading time, then the other one, and repeat the procedure to eliminate the effect of possible slow drifts. After each individual measurement the temperature of the cloud is measured by ToF expansion. Based on these temperatures, the measured trap frequencies are corrected to account for the effect of anharmonicity of the trap, using the coefficient β defined in the main text. Note, however, that we do not observe a significant correlation between temperature and atom number. The results are presented in Figure 3.5. A linear fit gives a slope of 0.28(70)% per million of atoms, which is consistent with the absence of a density effect. This confirms our assumption of a density independence of the oscillation frequency on the level of 1% for our standard experimental condidtions.

3.7.2 Damping of oscillations

In the main text we introduce the assumption that the damping of the CoM oscillations originates essentially from the anharmonicity of the trap: Different classes

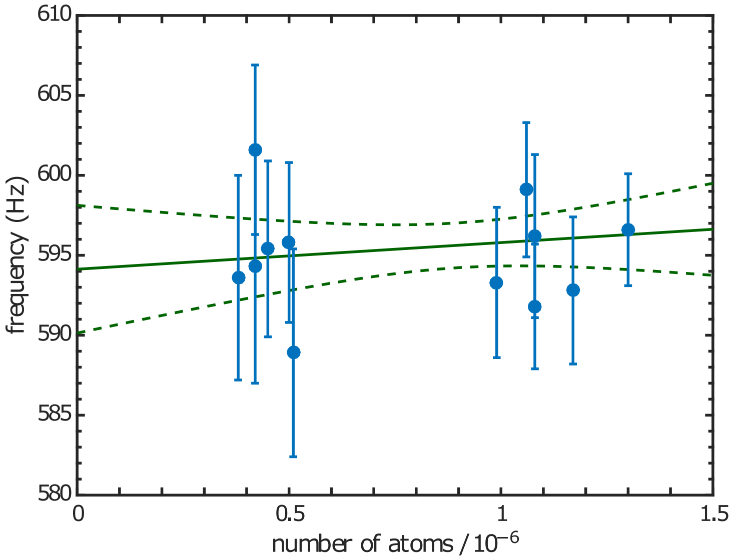

Figure 3.5: Test of the effect of atomic density on the oscillation frequency. The measured frequency is plotted against the atom number. The solid line is a linear fit, and the dashed line shows the 68% (1σ) confidence band.

of atoms explore different regions of the trap as they oscillate, hence experiencing slightly different trap frequencies and eventually dephasing. Such a behavior would mean that the CoM oscillations that we observe result from a superposition of pure single-particle oscillations. This assumption is supported by the equal damping behavior of the two species, as pointed out in the main text, and by an estimation based on our experimental settings of the collision rate of dysprosium atoms, which yields 80 s^{-1} (a similar calculation for potassium gives a collision rate of about 90 s^{-1}). Given the radial trap frequency of about 600 Hz (2 kHz for K), the radial motion in our trapped samples is far away from the hydrodynamic regime. Here we further test our assumption on the origin of the observed damping by considering the density and temperature dependence of the damping rate of the CoM oscillations.

From the analysis of the set of experiments presented in Sec. A we also obtain the damping rate of the oscillations. Its behavior as a function of atom number is plotted in Figure 3.6. A linear fit gives a slope of $+0.008(30)$ s^{-1} per million atom and thus does not show any significant density dependence on the 10% level for our standard atom number. This observation support our assumption of damping being essentially due to dephasing effects.

We now turn our attention to the study of the dependence of the damping rate on the temperature. From straightforward arguments, one expects the damping rate to be proportional to the temperature. Indeed, for small oscillation ampli-

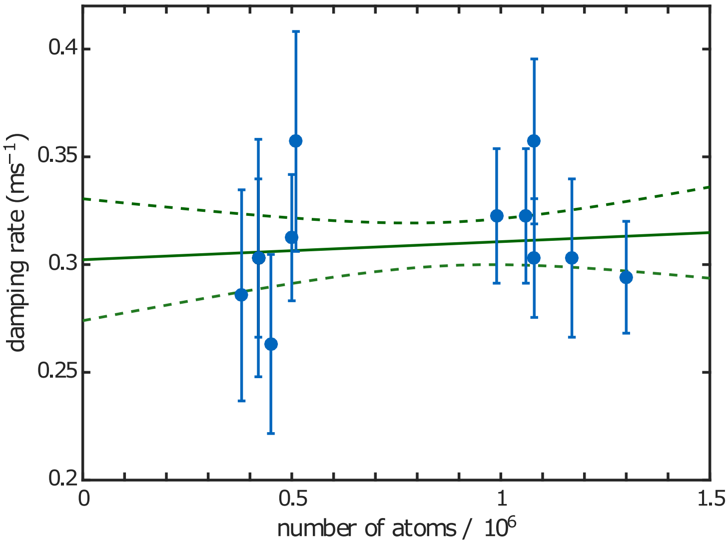

Figure 3.6: Density independence of the damping rate. The solid line is a linear fit, and the dashed lines show the 68% (1σ) confidence band.

tudes, the anharmonic frequency shift of a particle in a Gaussian potential scales linearly with its energy, such that the width in Fourier space of the CoM oscillation increases linearly with the temperature of the cloud, finally leading to a linear dependence of the damping rate on the temperature. In the main text, we present a measurement of the dependence of the frequency on the temperature of the cloud (see Figure 3 in the main text). The analysis of the corresponding oscillation data also allows us to investigate the dependence of the damping rate of the oscillations on the temperature. The results are shown in Figure 3.7. We observe an increase of the damping with temperature. A linear fit without offset gives a slope of 0.409(15) $\mathrm{ms}^{-1}\mu\mathrm{K}^{-1}$, and a reduced χ^2 of 0.96, showing that our simple model fits well to the data. This behavior also supports our interpretation on dephasing being the main source of damping.

3.7.3 Error budget of the frequency ratio measurement

We measure the trap frequency ratio in two sets of data obtained on two different days. Each set of data is corrected for the residual anharmonicity, based on the anharmonicity coefficient β and on the measured temperatures of the two species. A part of the uncertainty originates from the statistical distribution of the measured frequency ratios $\omega_\mathrm{K}/\omega_\mathrm{Dy}$. The rest of the uncertainty originates from the error in the anharmonicity correction and has five contributions: the error on the anharmonicity coefficient β, and the error on the measured temperatures of the K and Dy clouds. The respective contributions to the absolute uncertainty on

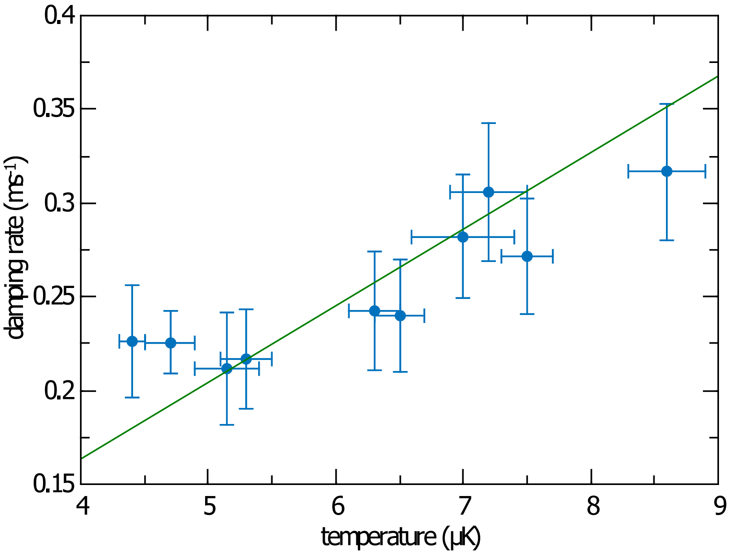

Figure 3.7: Temperature dependence of the damping time. The solid line is a linear fit without offset, with weights taking both horizontal and vertical error bars into account.

parameter	value	uncertainty in parameter	uncertainty in frequency ratio
T_{Dy} set 1	8.3 μK	0.2 μK	0.003
T_{K} set 1	7.6 μK	0.3 μK	0.004
T_{Dy} set 2	35.7 μK	3.2 μK	0.015
T_{K} set 2	30.3 μK	2.0 μK	0.008
β	-4.50 Hz/μK	0.43 Hz/μK	0.006

Table 3.1: Error budget for the measurement of $\omega_{\mathrm{K}}/\omega_{\mathrm{Dy}}$.

$\omega_{\mathrm{K}}/\omega_{\mathrm{Dy}}$ are listed in Table 3.1.

The total absolute uncertainty that results from the anharmonicity correction is 0.019, and the statistical uncertainty from the 10 combined individual measurements is 0.012. These two errors are quadratically combined, which finally yields the quoted uncertainty of 0.022.

3.7.4 Measurement of the tensor contribution

We measure oscillation frequencies for two different orientations of the magnetic field: Always being perpendicular to the propagation axis of the trapping laser, the field is either aligned with the polarization axis of the trapping laser, or per-

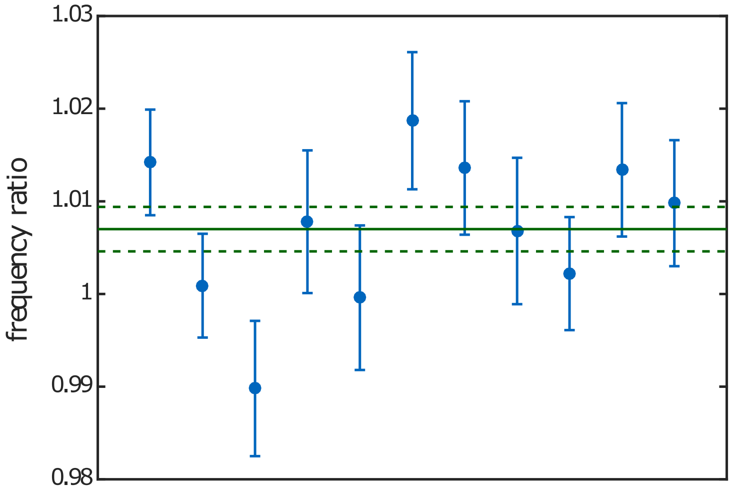

Figure 3.8: Repeated measurements of the frequency ratio $\omega_{\parallel}/\omega_{\perp}$. The first five points have been measured on one day, the remaining six ones on a second day. The solid line shows the weighted average$\omega_{\parallel}/\omega_{\perp} = 1.0070(20)$ with the dashed lines showing the corresponding statistical error range.

pendicular to it. All other parameters are kept identical. The strength of the field is in both cases 250 mG. In the latter case we take care that the spin state of the atoms adiabatically follows the rotation of the magnetic field. We measure alternately the trap frequency for one orientation of the field, then for the other one, and repeat the procedure to eliminate systematic effects from possible slow drifts. We measure in total 11 pairs of trap frequencies over two different days, which gives us 11 values for the frequency ratio, as shown in Figure 3.8. A weighted average yields $(a_s + a_t)/(a_s - a_t/2) = 1.0140(48)$.

4

Production of a Degenerate Fermi-Fermi Mixture of Dysprosium and Potassium Atoms

Published as:
C. Ravensbergen, V. Corre, E.Soave, M. Kreyer, E. Kirilov and R. Grimm
Phys. Rev. A 98, 063624 (2018)
Erratum: Phys. Rev. A 101, 059903 (2020)

Author contribution: The author took part in the measurements and contributed to the general lab work, the interpretation and analysis of the data and the discussions during the writing of the manuscript.

Note: With respect to the published version corrections have been made according to the errata.

We report on the realization of a mixture of fermionic ^{161}Dy *and fermionic* ^{40}K *where both species are deep in the quantum-degenerate regime. Both components are spin-polarized in their absolute ground states, and the low temperatures are achieved by means of evaporative cooling of the dipolar dysprosium atoms together with sympathetic cooling of the potassium atoms. We describe the trapping and cooling methods, in particular the final evaporation stage, which leads to Fermi degeneracy of both species. Analyzing cross-species thermalization we obtain an estimate of the magnitude of the inter-species s-wave scattering length at low magnetic field. We demonstrate magnetic levitation of the mixture as a tool to ensure spatial overlap of the two components. The properties of the Dy-K mixture make it a very promising candidate to explore the physics of strongly interacting mass-imbalanced Fermi-Fermi mixtures.*

4.1 Introduction

Strongly interacting systems composed of imbalanced fermions offer an increased complexity as compared to the balanced case by adding effective exchange interaction and dissimilar dispersion of the constituents. The physics emanating from new pairing mechanisms is rather enriched compared to the standard population and mass-balanced case, described by the established Bardeen-Cooper-Schrieffer (BCS) attractive interaction [187]. Appearing in various fields, such systems have been predicted to generate exotic pairing such as breached and inhomogeneous pairing, the last exhibiting a spatially varying order parameter [188]. In nuclear physics the possibility for neutron-proton correlations and Cooper pair condensation has been investigated in several contexts ranging from heavy-ion collisions to astrophysical processes [189]. Inhomogeneous superconductivity has been argued to exist for asymmetric nuclear matter in supernovae and neutron stars [190]. In quantum chromodynamics, a phenomena coined color inhomogeneous superconductivity is expected to take place [191, 192, 193, 194, 195]. Because of its ubiquity, such states of matter are also discussed and searched for in condensed matter physics, where experimentally favorable systems include heavy-fermion, organic, or high-T_c superconductors [191].

In the context of ultracold two-component Fermi gases, some exotic phases like the paradigmatic Fulde-Ferrell-Larkin-Ovchinnikov (FFLO) [19, 20, 196], Sarma [21] as well as interior [181] and exterior gap breached-pair phases [197], have been theorized. Specifically, the FFLO phase seems to be experimentally achievable in mass-imbalanced systems at unitarity, because of the higher superfluid transition temperature [23, 198, 199, 24] relative to the equal- mass case. In general the mass-imbalanced strongly interacting fermionic mixtures based on cold atoms, as a result of the generated Fermi surfaces and single-particle dispersion mismatch, exhibit a rich phase diagram, which includes a Lifshitz point and population-dependent asymmetry [184, 200, 201, 202]. Such systems can be also employed to study itinerant ferromagnetism [203], a phenomenon where microscopic understanding is still evolving [204]. As a further example, a crystalline phase of weakly bound molecules consisting of heavy and light fermions has been predicted [205], countering the intuitive expectation of a gas phase.

Fermionic mixtures of ultracold atoms are also well suited to tackle impurity physics and the polaron problem [203]. One open aspect is an impurity coupled to a non-equilibrium Fermi gas, where multicomponent cold gases are well suited to explore the non-equilibrium Anderson catastrophe and the influence of the environment on the impurity dynamics [206, 207]. Fermionic mixtures made out of different atomic species additionally allow for the use of a species-selective optical lattices [159]. This handle opens the possibility in multicomponent systems for the realization of Kondo-related physics in transport measurements [208]. It should also be emphasized that two-component Fermi gases also offer a variety of interesting few-body effects such as atom-dimer resonant scattering [209, 210] and confinement-induced Efimov resonances in systems with mixed dimensionality [211].

Up to now, the ^{40}K- ^{6}Li mixture has represented the only tunable mixture of fermionic species realized in the laboratory [212, 213, 214, 215]. The mass ratio makes this combination in principle attractive for pursuing many of the above goals. In this system, effects of strong interactions near Feshbach resonances (FR) have been observed in hydrodynamic expansion [216], in impurity physics [82, 83, 217], and in three-body interactions [210]. However, at resonant interspecies interaction, this mixture suffers from lifetime limitations owing to the narrow character of the FR [148, 218]. The width of the FR, together with Pauli suppression of few-body collisions [71, 73, 94, 219, 220, 221], is a prerequisite for achieving long lifetimes in strongly interacting fermionic atomic mixtures and weakly bound dimers made of fermionic atoms. This enhanced stability against inelastic decay has been observed in numerous experiments of both single-species [222, 99, 102, 92, 223] and recently also in dual-species experiments [224]. This facilitated the realization and exploration of numerous research avenues, including molecular Bose-Einstein condensation, BEC-BCS crossover physics, the unitary Fermi gas, and superfluid pairing [225, 226, 227].

Here, we introduce a different mass-imbalanced Fermi-Fermi mixture, namely, the dysprosium-potassium (Dy-K) mixture [1]. For creating a Fermi-Fermi mixture, a number of combinations could be selected from the variety of chemical elements

---

[1] Mixture experiments with magnetic lanthanide atoms represent a new frontier in the research field. The only other experiment reported so far has been carried out on mixtures of Er and Dy and reported quantum-degenerate Bose-Bose and Bose-Fermi mixtures [135]

that have been brought to Fermi degeneracy [59, 32, 33, 31, 55, 56, 228, 60, 61, 57]. The important criteria to adhere to are as follows: (i) mass ratio well below 13.6 to suppress Efimov-related losses [221], (ii) tunable interactions, and (iii) collisional stability [224]. Complying with these criteria narrows down the possible combinations to ^{161}Dy-^{40}K, ^{163}Dy-^{40}K, ^{167}Er-^{40}K, and ^{53}Cr-^{6}Li. We have chosen specifically the Dy-K combination, anticipating a favorable scattering spectrum, which is on one hand not chaotic, but it is conveniently dense, extrapolating from [229]. We note that, combinations utilizing a closed-shell fermion (^{171}Yb,^{173}Yb, or ^{87}Sr) in its electronic ground state with an alkali-metal atom offer only extremely narrow resonances [230, 231], and therefore are not suited for our purpose.

In this article, we present the preparation and cooling of a Fermi-Fermi mixture of ^{161}Dy and ^{40}K atoms, reaching deep quantum degeneracy for both species. In Sec. 4.2, we first summarize the laser cooling procedures that provide the starting conditions for subsequent evaporation. In Sec. 4.3, we then report our main results. We first demonstrate deep cooling of spin-polarized ^{161}Dy based on universal dipolar scattering. Then we investigate cooling of a mixture of ^{161}Dy with ^{40}K, where the K component is cooled sympathetically by thermal contact with Dy. We also demonstrate the effect of magnetic levitation as an interesting tool for future experiments, and we present a first measurement of the interspecies scattering cross section. In Sec. 4.4, we finally give a brief outlook on future steps to realize a strongly interacting, mass-imbalanced fermionic mixture.

4.2 Laser cooling and dipole trap loading

In this section, we summarize the laser-cooling steps in our experimental sequence, which prepare the starting point for subsequent evaporative cooling in an optical dipole trap. In Sec. 4.2.1 we describe the loading of dysprosium and potassium atoms into two respective magneto-optical traps (MOTs). In Sec. 4.2.2 we discuss the procedure used to transfer the atoms into a large-volume optical dipole trap, where they coexist in a mixture.

4.2.1 Magneto-optical traps

Our dysprosium preparation scheme is similar to the one described in Refs. [163, 176]. As a source of Dy atoms, we use a high-temperature effusion oven operating at about 1000 °C combined with a Zeeman slower operating on the broad line (natural linewidth of 32 MHz) at 421 nm. Dy atoms are collected in a MOT operating on the narrow ($\Gamma_{626} = 2\pi \times 135$ kHz) intercombination transition at 626 nm. Further details on the apparatus can be found in Sec. 4.5.1. The MOT uses a magnetic field gradient of about 2 G/cm along the strong vertical axis. We use 35-mm-diameter ($1/e^2$ intensity drop) beams, with an intensity of 170 $I_{\mathrm{sat},626}$ per beam (where $I_{\mathrm{sat},626} = 72$ μW cm^{-2} is the saturation intensity of the 626 nm line). The laser is detuned by a few MHz to the red of the transition [2] and subsequently spectrally broadened by a high-efficiency electro-optical modulator to increase the loading efficiency [176]. Using these parameters we typically load 2.2×10^7 atoms of ^{161}Dy atoms in 3 s. After loading, the MOT is compressed by abruptly switching off the spectral broadening and, within 170 ms, ramping the detuning closer to resonance, the power down to $I \approx 0.5$ $I_{\mathrm{sat},626}$, and the gradient of magnetic field down to 1.4 G/cm. The atoms are then held in the compressed MOT for 80 ms. During this hold time, the Dy atoms are naturally optically pumped into the stretched state $|F = 21/2, m_F = -21/2\rangle$ [163]. The temperature after the compressed MOT is approximately 8 μK.

The source of K atoms is a two-dimensional MOT in a glass cell, connected to the main chamber via a differential pumping tube, similarly to [215]. In the chamber the atoms are collected in a three-dimensional MOT operating on the D2 line at a wavelength of 767 nm. The K MOT beams combine the cooler and repumper frequencies (the latter being created by a free-space electro-optical modulator). They have an intensity of $I_{\mathrm{cool}} = 6$ $I_{\mathrm{sat},767}$ and $I_{\mathrm{rep}} = 0.3$ $I_{\mathrm{sat},767}$, and are detuned by $\delta_{\mathrm{cool}} = -4.4$ Γ_{767} and $\delta_{\mathrm{rep}} = -2.7$ Γ_{767} relative to the $F = 9/2 \rightarrow F' = 11/2$ and $F = 7/2 \rightarrow F' = 9/2$ transitions, respectively. Here $I_{\mathrm{sat},767} = 1.75$ mW cm^{-2} is the saturation intensity of the D2 line of K, and Γ_{767} its natural linewidth. The gradient of magnetic field is set to 9.6 G/cm along the strong axis. We typically load the MOT for 3 s, which gives 0.9×10^6 atoms of ^{40}K. Once loaded, the K MOT is compressed by simultaneously ramping up the gradient of magnetic field to 25 G/cm, ramping down the detunings to $\delta_{\mathrm{cool}} = -1.1$ Γ_{767} and $\delta_{\mathrm{rep}} = 0$ and the powers down to $I_{\mathrm{cool}} = 0.5$ $I_{\mathrm{sat},767}$ and $I_{\mathrm{rep}} \approx 0.01$ $I_{\mathrm{sat},767}$, all in 4 ms. At the end of the compressed MOT phase the temperature of the K cloud is 110(30) μK. We then perform gray molasses cooling on the D1 line, which allows us to lower this temperature to approximately 30 μK. Details on the gray molasses stage are given in Sec. 4.5.3.

4.2.2 Sequential dipole trap loading

The transfer of atoms from a MOT or a molasses into an optical dipole trap is a common procedure in cold-atom experiments. The optimum transfer strategy depends on the particular properties of the atomic species and on the cooling scheme applied prior to the dipole trap loading. In many dual-species experiment, however, the optimum loading conditions for both components are incompatible

---

[2] We define detunings as $\delta = \omega_{\mathrm{laser}} - \omega_{\mathrm{atom}}$, such that a red (blue) detuned laser corresponds to a negative (positive) detuning

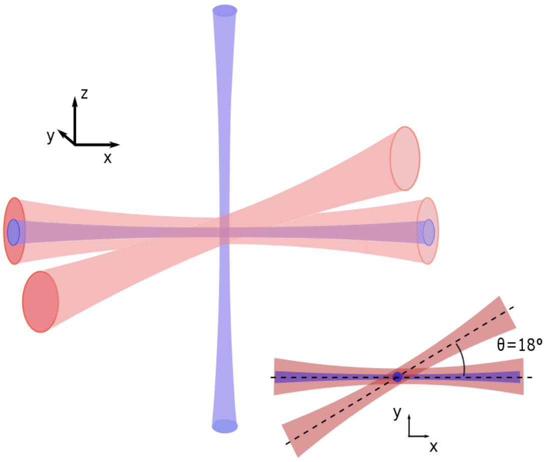

Figure 4.1: Optical dipole traps scheme. The two beams of the large volume RDT propagate in the horizontal x-y plane and intersect under an angle of 18°, while the two orthogonal beams of the CDT propagate in the x-z plane. The lower right scheme shows a view from the top.

with each other, such that a sequential loading scheme is necessary. In the case of Dy and K atoms, the main constraint is imposed by the vastly different gradient of the magnetic field required in the respective MOTs. Indeed, the larger gradient used to load K atoms would induce a strong compression of the Dy cloud, which in turn would lead to large losses. We therefore sequentially load the K atoms and then the Dy atoms into a reservoir optical dipole trap (RDT).

The RDT is created by two intersecting beams derived from a single, longitudinally multimode, fiber laser (IPG YLR-100-LP, wavelength 1070 nm) and crossing in the horizontal plane under an angle of 18°; see Fig. 4.1. The RDT is already switched on during the K-MOT stage, with a power per beam of 11.5 W, corresponding to a depth $U^{\mathrm{K}}_{\mathrm{RDT}}/k_{\mathrm{B}} = 260\ \mu$K. After compression of the K MOT (Sec. 4.2.1), the atoms are transferred into the RDT, while being cooled by the gray molasses (App. 4.5.3). We typically load 2.2×10^5 ^{40}K atoms, corresponding to a transfer efficiency of 20%, at a temperature of 33(1) μK [3].

After the gray molasses, a 0.8-ms laser pulse is applied to optically pump the atoms in the $|F = 9/2, m_F = -9/2\rangle$ state. The pulse has σ^- polarization with a small admixture of π polarization, and has frequency components resonant with the D1 transitions $F = 7/2 \rightarrow F' = 9/2$ and $F = 9/2 \rightarrow F' = 7/2$, such that the

---

[3] In the absence of dipole trap, the D1 cooling allows us to reach temperatures as low as 8(1) μK

$|F = 9/2, m_F = -9/2\rangle$ state is a dark state. During the pulse, the gradient of magnetic field is turned off and a homogeneous field of approximately 1 G is applied along the direction of the beam. The optical pumping only has a minor effect on the temperature of the cloud: We measure an increase of the temperature on the order of 1 μK. To check the polarization of the K sample we perform resonant absorption imaging at high magnetic field (155 G), where the splittings between the different $|F, m_F\rangle \rightarrow |F', m_{F'} = m_F + 1\rangle$ transitions are large compared with the natural linewidth. After the pulse we still observe approximately 10% of atoms left in $|9/2, -7/2\rangle$.

We then load the Dy MOT for 3 s, while holding the K atoms in the RDT. As we start loading Dy, the power of the RDT is increased, resulting in a depth $U_{\mathrm{RDT}}^{\mathrm{Dy}}/k_{\mathrm{B}} \approx 110\ \mu\mathrm{K}$ for Dy and $U_{\mathrm{RDT}}^{\mathrm{K}}/k_{\mathrm{B}} \approx 360\ \mu\mathrm{K}$ for K [232]. This compression increases the temperature of K to 37(2) μK. Since the Dy MOT forms below the zero of the quadrupole magnetic field, it is spatially separated from the K cloud and does not affect the lifetime of the K atoms in the dipole trap, which is measured to be 4 s. Finally, the compression of the Dy MOT (Sec. 4.2.1) moves it upward, such that it overlaps with the RDT, where Dy atoms are transferred. At this stage the central region of the RDT typically contains 4.5×10^6 Dy atoms at a temperature of 17(1) μK, corresponding to a loading efficiency of 10%, and approximately 9×10^4 K atoms at a temperature of 28(2) μK. The fact that the temperature of the K sample decreases during the 3 s hold in the RDT is also observed in the absence of Dy and is presumably an effect of plain evaporation allowed by the remaining spin polarization imperfection. We do not observe interspecies thermalization on the considered time scale at this point.

At the end of the Dy MOT stage, all resonant light is switched off and the gradient of magnetic field is set to zero. A homogeneous magnetic field of approximately 430 mG is applied along the vertical direction to define a quantization axis and to maintain the polarization of the two clouds. At this point, we do not observe any population in higher spin states of K and Dy, which we attribute to rapid intraspecies and interspecies dipolar relaxation. The conditions after the loading of both species in the RDT are summarized in Table 4.1.

4.3 Evaporative cooling

In this Section, we present our main results on evaporative cooling down to deep degeneracy of both fermionic species. We evaporatively cool fully spin-polarized Dy [60, 164] (see also related work on fermionic Er [61, 233]), relying solely on universal dipolar scattering [128]. The K component, for which the optical trap is much deeper, is cooled sympathetically. This cooling scheme is closely related to earlier experiments on the attainment of quantum degeneracy in Yb-Li mix-

	^{161}Dy	^{40}K
$\bar{\omega}/2\pi$	154(6) Hz	558(22) Hz
$U_{\mathrm{RDT}}/k_{\mathrm{B}}$	110(8) μK	360(20) μK
N	$5.3(4) \times 10^{6}$	$8.8(9) \times 10^{4}$
T	17(1) μK	28(2) μK
n_{peak}	$1.0(1) \times 10^{13}$ cm^{-3}	$5.3(9) \times 10^{11}$ cm^{-3}
PSD	$3.5(9) \times 10^{-4}$	$8(1) \times 10^{-5}$

Table 4.1: Cloud parameters after transfer into the RDT. The given parameters describe the cloud in the RDT immediately after the Dy MOT is turned off. U_{RDT} refers to the depth of the optical potential, n_{peak} to the peak density in the center of the trap, PSD to the phase-space density. The errors in n_{peak} and in the PSD result from the propagation of the errors in N and T, whereas the systematic errors in U_{RDT} and in $\bar{\omega}$ are not propagated.

tures [234, 235, 236], where the heavy lanthanide species experiences a shallower trapping potential than the light alkali-metal species. As in our work, evaporative cooling acts on the heavier species, which then cools the lighter one in a sympathetic way. The main difference to our work is the origin of elastic collisions among the heavier atoms, which in the Yb cooling scenarios result from s-wave collisions between identical bosons or non-identical fermions, and not from universal dipolar scattering between identical fermions.

We employ a sequence of two optical dipole traps. A first evaporative cooling step is performed in the RDT. Atoms are then transferred into the main dipole trap, where evaporative cooling continues. In Secs. 4.3.2 and 4.3.3, we characterize the evaporation process in two situations: We first describe the evaporation of ^{161}Dy atoms alone, and then the evaporation of the mixture. In Sec. 4.3.4 we discuss the effect of gravity and its compensation by a levitation field. Finally, in Sec. 4.3.5 we show the results of an interspecies thermalization measurement, from which we give an estimate of the inter-species s-wave scattering cross section, a quantity of primary importance in the efficiency of the simultaneous cooling of the two species.

4.3.1 Transfer from reservoir into main dipole trap

With the phase-space density reaching values in the 10^{-4} range for each species, the RDT provides favorable starting conditions for evaporative cooling. However, the large waist of the beams forming the RDT does not allow us to maintain a large enough collision rate in this trap when its power is lowered. Aside from this, as a technical issue, the RDT is created by a longitudinally multimode laser, where evaporation of Dy is known to be hindered by heating processes [131, 237]. We

	^{161}Dy	^{40}K
$\bar{\omega}/2\pi$	456(18) Hz	1460(60) Hz
$U_{\rm CDT}/k_{\rm B}$	130(5) μK	419(17) μK
$N_{\rm center}; N_{\rm arms}$	$7.9(4) \times 10^5$; $1.3(1) \times 10^6$	$2.8(2) \times 10^4$; $\sim 5 \times 10^4$
T	24(1) μK	28(1) μK
$n_{\rm peak}$	$2.7(2) \times 10^{13}$ cm^{-3}	$4.4(4) \times 10^{12}$ cm^{-3}
PSD	$6.1(9) \times 10^{-4}$	$6.6(9) \times 10^{-4}$

Table 4.2: Starting conditions for the evaporation in the CDT. $N_{\rm center}$ gives the number of atoms in the central region of the trap, while $N_{\rm arms}$ corresponds to the atom number trapped outside the region where the two beams cross, in the arms of the potential. $U_{\rm CDT}$ refers to the depth of the optical potential created by he CDT, $n_{\rm peak}$ to the peak density and PSD stands for phase-space density. As in Table 4.1, the errors in $n_{\rm peak}$ and in the PSD are obtained from the errors in N in T only.

therefore perform a two-step evaporation: After a first evaporation ramp taking place in the RDT, the atoms are transferred into a tighter crossed dipole trap (CDT), where the evaporative cooling continues.

The CDT is created by a longitudinally single-mode Nd:YAG laser (Mephisto MOPA 18 NE) at 1064 nm. The configuration of dipole traps is depicted in Fig. 4.1. One beam of the CDT overlaps in the horizontal plane with one beam of the RDT and has a waist of approximately 30 μm, while the second beam propagates along the vertical axis and has a waist around 60 μm.

During the first 20 ms after completion of the RDT loading, the power of the RDT is kept fixed while the powers in the horizontal and vertical beams of the CDT are ramped up from 0 to 1.6 and 0.7 W, respectively. This results in a depth of approximately 54 μK for Dy, and of 174 μK for K. From that point, as illustrated in Fig. 4.2, the power of the RDT is reduced in an exponential ramp to 1.6 W per beam in 100 ms, while the power in the horizontal beam of the CDT is ramped up to 3.5 W. The power in the vertical beam is kept constant during this time. At the end of these ramps, the RDT is turned off. At its full power, the CDT has a depth $U_{\rm CDT}^{\rm Dy}/k_{\rm B} = 130$ μK and the trap frequencies are $[\omega_x, \omega_y, \omega_z] = 2\pi \times [88, 1040, 1037]$ Hz for Dy. Typically, 9×10^5 Dy atoms and 3×10^4 K atoms are loaded into the CDT, with a temperature of 24(1) μK for Dy and 28(1) μK for K. The phase-space density after the transfer is on the order of 10^{-3} for both Dy and K. The cloud parameters immediately after transfer into the CDT, i.e., the starting conditions for the subsequent evaporative cooling, are summarized in Table 4.2.

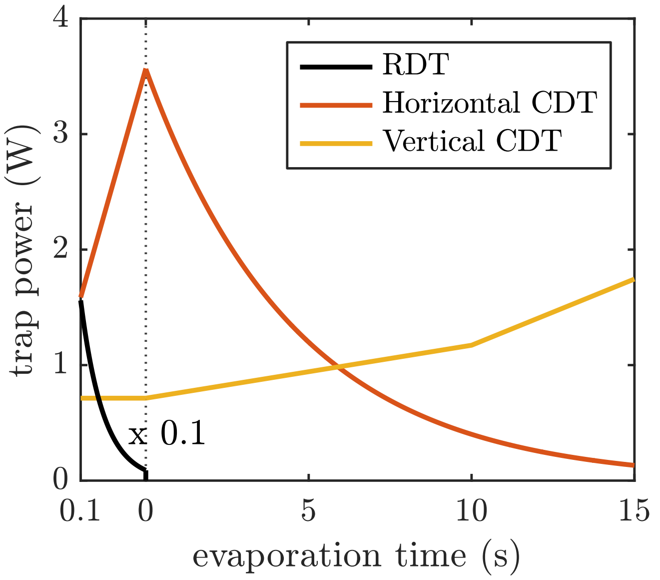

Figure 4.2: Evaporative cooling sequence. Power in the RDT (black) and in the horizontal (red or dark gray) and vertical (orange or light gray) beam of the CDT. The origin of time ($t = 0$) corresponds to the start of the evaporation in the CDT. The power in the RDT and in the horizontal beam of the CDT is decreased in exponential ramps. The sequence is identical for the pure Dy cloud and for the Dy-K mixture.

4.3.2 Evaporative cooling of a pure ^{161}Dy cloud

We now turn to the second phase of the evaporation, which is carried out in the CDT. We first consider the efficiency of the evaporative cooling of pure ^{161}Dy, i.e. in the absence of K atoms. As soon as the RDT is switched off, the evaporation ramp is started. The magnetic field is kept at 430 mG, thus avoiding crossing any major Feshbach resonance [126]. The evolution of the power in the two dipole traps is depicted in Fig. 4.2 and is optimized in terms of the final temperature ratio T/T_F achieved, where $k_\mathrm{B}T_F = \hbar\bar{\omega}\,(6N)^{1/3}$ is the Fermi temperature (in the following, we use the atom number in the central region of the CDT to calculate T_F). We adopt a standard evaporation scheme in which the power in the horizontal beam of the dipole trap is decreased while the power in the vertical one is increased [238, 239, 129, 133]. The power in the horizontal beam of the CDT is lowered in an exponential ramp to 150 mW within 15 s, while the power in the vertical beam is first increased linearly to 1.17 W within 10 s and then to 1.75 W within 5 s.

Figure 4.4 shows a time-of-flight image of the degenerate cloud obtained at the end of the evaporation ramp (a brief description of our imaging scheme is presented in Sec. 4.5.2). The two panels on the right show cuts along two orthogonal axes through the two-dimensional (2D) density profile. The solid red lines result from a fit of the density profile by a polylogarithmic function. We obtain 3.5×10^4 atoms at a temperature of 60(10) nK, corresponding to $T/T_F = 0.085(10)$. The trap depth at this point is $U = k_\mathrm{B} \times 720$ nK and the trap frequencies are $[\omega_x, \omega_y, \omega_z] = 2\pi \times [133, 248, 176]$ Hz, both calculated including the effect of gravity. The peak number density is 7×10^{13} cm^{-3}.

In Fig. 4.3 we show the evolution of the atom number in the central region of the trap, of the temperature T, and of the ratio T/T_F during the evaporation in the CDT. After approximately 10 s, we observe a change of slope in the evolution of the atom number in the central region [see Fig. 4.3(a)]. We attribute this effect to the presence of atoms in the arms of the trapping potential. At $t = 0$, around 1.3×10^6 trapped Dy atoms are present in the horizontal arms. In the first 10 s, these atoms are then preferentially evaporated, cooling also the cloud in the central region. After 10 s, the arms of the trap are found to be empty and, from that point on, the evaporation takes place in the central region of the potential only. The initial fast gain in phase-space density [PSD $\propto (T/T_F)^{-3}$] associated with the slow decrease of the atom number in the central region suggests that the atoms in the arms play an important role in the efficiency of the forced evaporative cooling.

The temperatures shown in Fig. 4.3(b) are extracted from the observed column density profiles by Gaussian fits or by polylogarithmic fits. The first ones are applied at higher temperatures, the second ones at lower temperature. The fit by a polylogarithmic profile provides two parameters: the size σ, related to the temperature T, and the fugacity ζ. The Fermi temperature is obtained from the measured atom number and the calculated averaged trap frequency. The fugacity on the other side gives direct access to $T/T_F = [-6\mathrm{Li}(-\zeta)]^{-1/3}$. The ratio T/T_F shown in Fig. 4.3(c) is obtained from the measured T and the calculated T_F. A comparison with the second method using the fugacity is presented in the inset for the lowest temperatures achieved, and shows good agreement between the two methods. The change between the Gaussian and polylogarithmic fit models happens for $T/T_F \approx 1$. The ratio T/T_F levels off after 14 s of evaporation. At this point, the trap depth is on the order of the Fermi energy $E_F = k_\mathrm{B} T_F$ and we enter the spilling regime, where efficient evaporation stops.

In Fig. 4.3(b) we compare the measured temperature T with the calculated trap depth U (where the effect of gravity is taken into account). We find that the forced evaporation is well characterized by a truncation parameter $\eta = U/k_\mathrm{B}T \approx 7$ throughout the whole evaporation process.

The trapping potential created by the CDT is deformed by gravity. In particular, the trap depth is reduced and, in the very final stage of the evaporation, the trap frequency along the vertical axis is lowered. In our scheme, after 14 s of

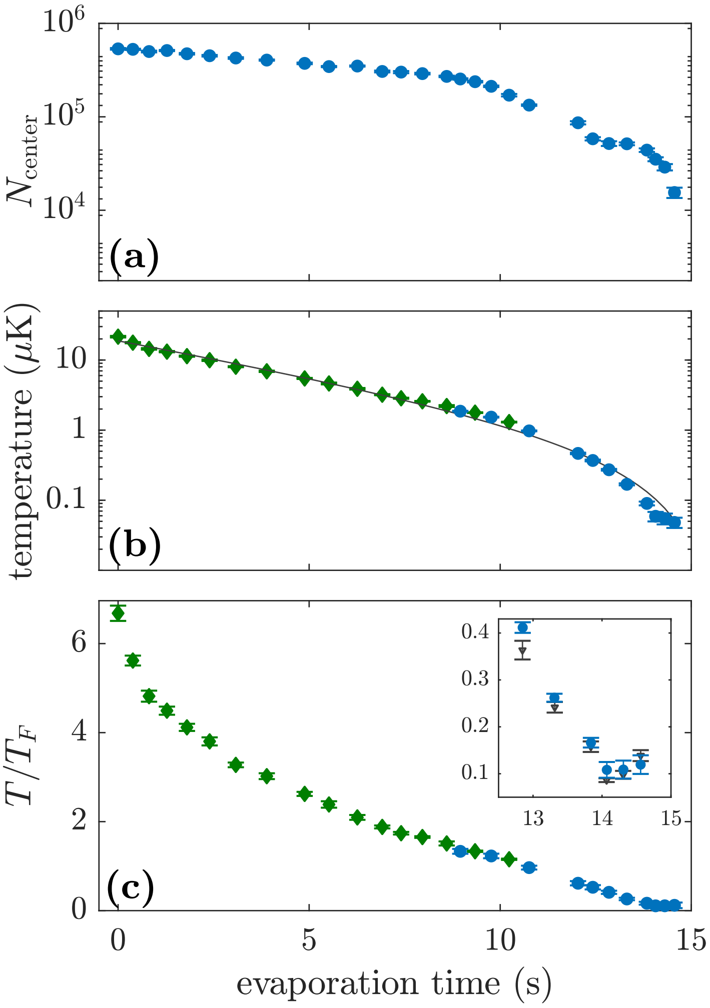

Figure 4.3: Evaporative cooling of ^{161}Dy. Atom number, temperature and temperature ratio T/T_F of the pure dysprosium cloud during the evaporation of the CDT. In (b) and (c), green diamonds show the temperature extracted from a Gaussian fit of the column density, while blue circles are extracted from a polylogarithmic fit. In (b), the solid black line shows the calculated trap depth reduced by a factor of 7. In (c) the inset shows a zoom-in on the final part of the evaporation ramp. Blue circles show the temperature ratio T/T_F obtained from the size of the polylogarithm fit, while black triangles show the ratio obtained from the fitted fugacity through the relation $T/T_F = [-6\mathrm{Li}(\zeta)]^{-1/3}$. In all figures, the error bars show the standard error derived from 10 repetitions. The time $t = 0$ refers to the beginning of the evaporation in the CDT.

evaporation, the depth of the CDT is reduced from 5.3 μK (depth without gravity) to 720 nK, and the trap frequency along the vertical axis is reduced from 210 to 176 Hz. The reduction of the trap depth is actually beneficial for the evaporative cooling, as pointed out with cesium atoms in [240]. Indeed, the reduction achieved by decreasing the laser power is inherently accompanied by a lowering of the trapping frequencies, which in turn implies a lower collision rate and a less efficient evaporative cooling. Gravity reduces the trap depth essentially without affecting the confinement strength of the trap (the lowering of the trap frequencies only appears at very low trap depth), and allows us to maintain a higher collision rate at low trap depths.

We achieved the lowest temperature $T/T_F = 0.085(10)$ after 14 s of evaporation. For longer evaporation times, the decreasing trap depth reaches the Fermi energy and we observe spilling of the dysprosium cloud. As in earlier work on evaporative cooling of fermions (see, e.g., [241]), we find that the optimal cooling is achieved just before the onset of spilling.

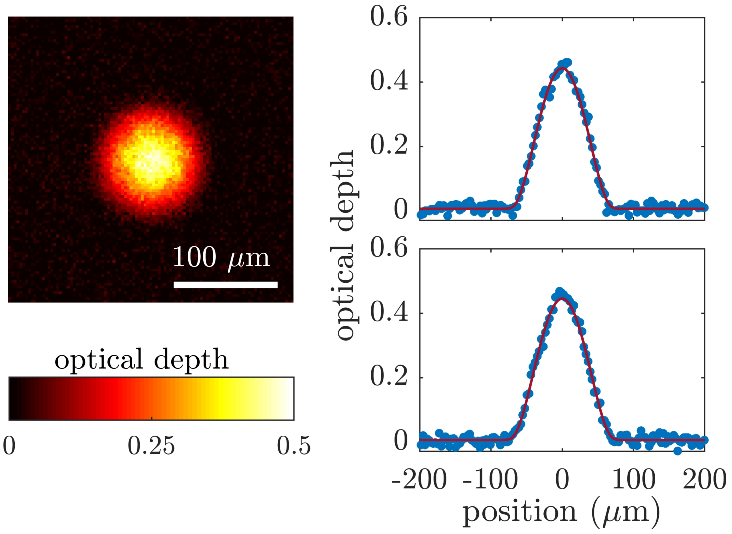

Figure 4.4: Deep evaporative cooling of pure ^{161}Dy. The density profile on the left-hand side is an average of ten absorption images of clouds of approximately 3.5×10^4 ^{161}Dy atoms taken after 14 s of evaporation in the CDT and a subsequent release from the trap (time of flight of 10 ms). The images on the right-hand side show cuts through the two-dimensional optical depth along the x and y axes. The solid lines show the corresponding profiles resulting from a two-dimensional polylogarithmic fit. From the fit we extract $T/T_F = 0.085(10)$.

4.3.3 Evaporative cooling of the ^{161}Dy-^{40}K mixture

We now characterize the combined cooling of the Fermi-Fermi mixture. Starting with both components loaded into the RDT, the experimental procedure is identical to the one described for Dy alone, as we find that it also provides the best results for the mixture, provided that the K atom number is kept small (typically, MOT loading time shorter than 3 s, resulting in a final atom number of a few 10^3). Indeed, we observe that an increase of the K atom number (achieved by extending the K MOT loading) compromises the cooling of the Dy sample. As before, the strength of the magnetic field is set to 430 mG.

We first describe the process of evaporative cooling. The atom number in the central region of the trap and the temperature of the two samples in the CDT are shown in Fig. 4.5. In these measurements, the atoms are held at fixed power during 10 ms before a time-of-flight expansion is performed. The behavior of the number of Dy atoms is essentially the same as observed in the evaporation of pure Dy, with the same change of slope after 10 s of evaporation. The number of K atoms on the other hand decreases very slowly, its final value being approximately half the initial one. Given the deep potential seen by the K atoms, we can exclude evaporation losses, and we therefore attribute the decrease in K atom number to inelastic processes.

The equality of the two temperatures seen in Fig. 4.5(b) demonstrates the efficiency of the sympathetic cooling. However, we observe that the temperature of the K sample decouples after approximately 13 s in the evaporation ramp from the temperature of the Dy component. While the temperature of the Dy follows the evolution of the trap depth, the K temperature decreases much more slowly. As a consequence of this behavior, the ratio $T_{\mathrm{K}}/T_{F,\mathrm{K}}$ essentially levels off, at a value close to 0.2. This observed decoupling is not an effect of a spatial separation of the components induced by the gravitational sag [236], as we verified by applying a levitation field that ensures full spatial overlap (see Sec. 4.3.4). This effect may indicate a relatively weak thermal coupling between the two species, which is then further reduced by Pauli blocking in the deeply degenerate regime. Further investigation is needed to understand the final limitations of our cooling scheme.

Figure 4.6 shows our final cooling results for the evaporation ramped discussed before. The absorption images were taken after 14.2 s of evaporation and a time of flight expansion of 2.5 ms for K and 7.5 ms for Dy. The lower panel shows cuts through the 2D profile, and the solid lines show the corresponding fits by a polylogarithmic function. We obtain 3.9×10^3 K atoms and 1.8×10^4 Dy atoms. At this point the two Fermi energies are calculated to be $E_{F,\mathrm{K}}/k_B = 830$ nK for K and $E_{F,\mathrm{Dy}}/k_B = 370$ nK for Dy. We measure temperatures of $T_{\mathrm{K}} = 250(10)$ nK and $T_{\mathrm{Dy}} = 45(4)$ nK, respectively, corresponding to $T/T_F = 0.30(3)$ for K and $T/T_F = 0.12(1)$ for Dy.

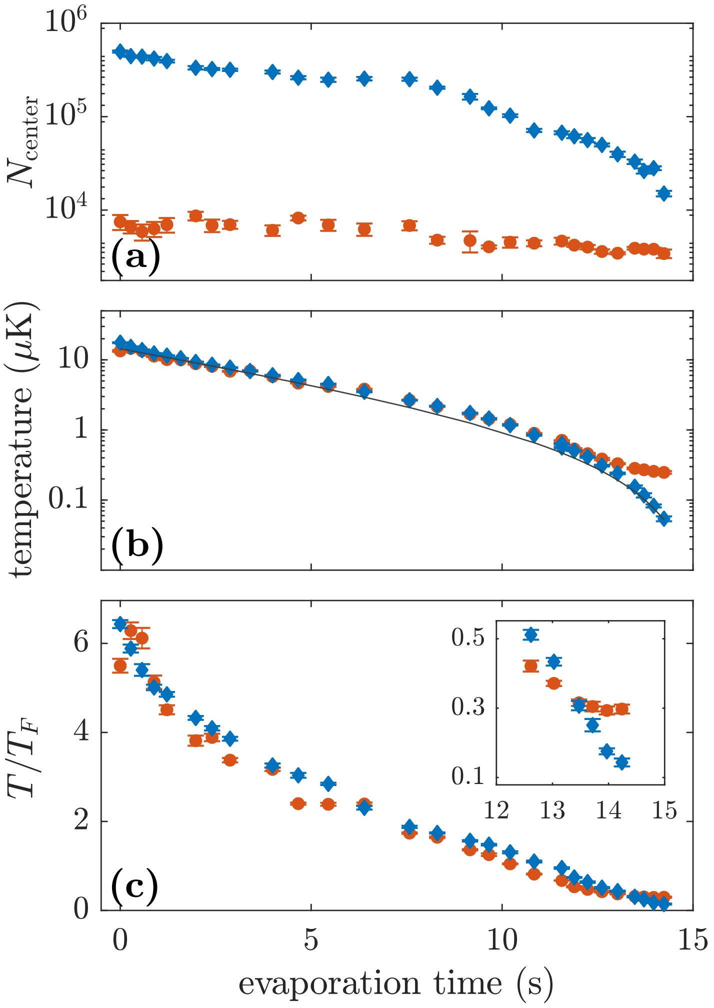

Figure 4.5: Sympathetic cooling of ^{40}K by the evaporatively cooled ^{161}Dy. Atom number, temperature and temperature ratio T/T_F of the ^{40}K (red circles) and ^{161}Dy (blue diamonds) samples during the evaporation of the CDT. As in Figure 4.3, the solid black line in (b) shows the trap depth for Dy reduced by a factor 7. The error bars show the standard error derived from ten repetitions. As in Figure 4.3, the time $t = 0$ refers to the beginning of the final ramp of the CDT.

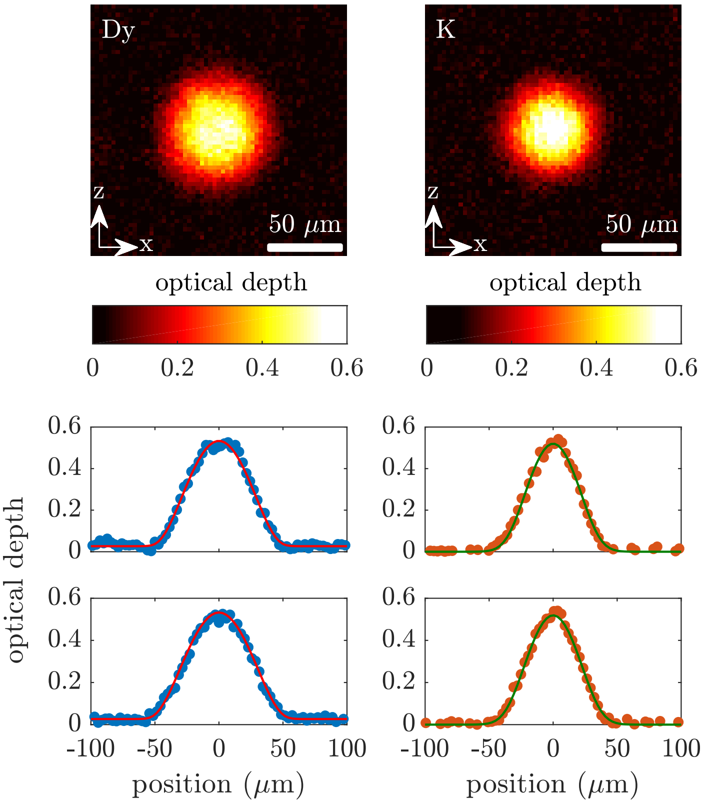

Figure 4.6: Deep cooling of the ^{161}Dy-^{40}K mixture. Density profile of a cloud of ^{161}Dy (^{40}K) atoms after a time-of-flight expansion of 7.5 ms (2.5 ms) for a ratio $T_{\mathrm{Dy}}/T_{F,\mathrm{Dy}} = 0.09(1)$ ($T_{\mathrm{K}}/T_{F,\mathrm{K}} = 0.22(2)$). Atom numbers are $N_{\mathrm{K}} = 3.96(4) \times 10^3$ and $N_{\mathrm{Dy}} = 1.8(2) \times 10^4$. The upper panel shows the averaged column density of six images obtained with resonant absorption imaging. The lower panels show cuts of the column density along the x (top) and z (bottom) axes. The solid lines are cuts of a 2D fit with a polylogarithmic function.

By varying the K MOT loading time we can control the number of ^{40}K atoms in the RDT and the resulting population ratio of the two species at the end of the evaporation. Indeed, after the transfer in the RDT, the K cloud is hotter than the Dy one and a larger number of K atoms thus represents a larger heat load for the Dy cloud, affecting its evaporation dynamics. For final number ratios $N_{\mathrm{Dy}}/N_{\mathrm{K}}$ from approximately 4 (corresponding to the situation described in Figs. 4.5 and 4.6) down to 2, we obtain similar cooling performance, with the two species as cold as $T/T_F \approx 0.2$. Then, if we further reduce the number ratio by increasing the initial number of K atoms, the K component reaches lower $T_{\mathrm{K}}/T_{F,\mathrm{K}}$ ratios at the expense of $T_{\mathrm{Dy}}/T_{F,\mathrm{Dy}}$. The absolute temperatures T_{Dy} and T_{K} achieved actually only weakly depend on the population imbalance. The main effect of the number ratio on the respective T/T_F comes from the dependence of the Fermi temperature on the atom number. In the extreme case where the Dy atom number is zero at the end of the evaporation, we achieve $T/T_F \approx 0.15$ for K.

4.3.4 Effect of magnetic levitation

Mixing two species in an optical dipole potential requires careful consideration of the effect of gravity [236]. The effect on the total potential seen by each species is twofold: its minimum is shifted in the vertical direction (referred to as gravitational sag), and its depth is reduced. Because of the different masses and polarizabilities, these two effects have different magnitudes for the two species. In our mixture, gravity has a much stronger effect on Dy than on K, because of both the larger mass and the weaker polarizability. As discussed in Sec. 4.3.2, when we reach optimum cooling results for Dy after 14 s of evaporation, the potential depth is reduced by gravity to only 14% of the optical potential depth. In contrast, the K trap depth is only reduced to 88% of the optical potential depth. At the same point, the potential seen by the Dy atoms is shifted by approximately 7 μm, which is already comparable to the size of the two clouds, while the sag experienced by the K atoms is small (around 500 nm).

When considering a single paramagnetic species, the common way to cancel the effect of gravity is to apply a gradient of magnetic field such that the spatially varying Zeeman energy creates a force opposing the gravitational force [242, 29]. The atomic cloud is then levitated. Because of their different magnetic dipole moments and masses, the strength of the gradient of magnetic field for levitation is different for two different atomic species. Yet, there exists a “magic” value of the gradient such that the gravitational sag of the two species is identical for any power of the optical dipole trap [241]. In the case of Dy and K, the much stronger dipole moment of Dy atoms brings this “magic” value (2.69 G/cm) very close to the value for the levitation of dysprosium (2.83 G/cm).

We demonstrate the effect of the levitation gradient by performing the following

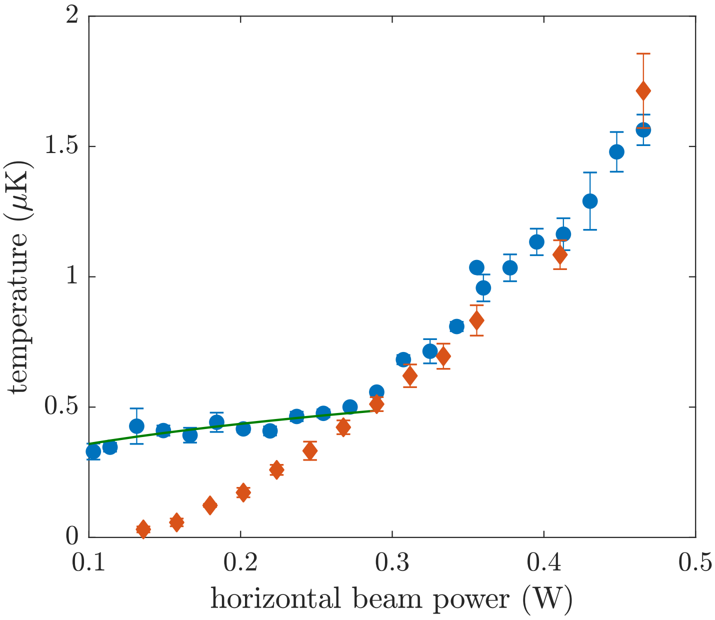

Figure 4.7: Effect of levitation on evaporative cooling. The temperature of a cloud of Dy is measured during the evaporation of the CDT in the absence of levitation (purple diamonds) and when the levitation fields are switched on below 0.3 W (blue points). The solid green line is a fit of the temperature below 0.30 W by an adiabatic cooling model assuming that the temperature for a power P_f in the trap is proportional to the average trap frequency $\bar{\omega}$ at this power: $T(P_f) = b\,\bar{\omega}(P_f)$ (see main text). The error bars show the standard error derived from six repetitions.

experiment. We evaporate dysprosium atoms in the CDT down to a given final power of the horizontal beam and turn on a levitation field when the ramp of power reaches below a threshold value set to 0.3 W. We then hold the cloud in the trap for 100 ms and finally release it for 8 ms. We extract the temperature from a polylogarithmic fit to the two-dimensional density profile. The measured temperatures are presented in Fig. 4.7. We observe that the evaporation essentially stops when the levitation is turned on, which is a consequence of the corresponding increase of the trap depth. With decreasing power, the temperature still decreases slowly. The green line in Fig. 4.7 is a fit of the temperature for final powers lower than 0.3 W by a function of the form $T(P_f) = b\,\bar{\omega}(P_f)$, where $\bar{\omega}(P_f)$ is the calculated average trap frequency for a final trap power P_f, and b is a fit parameter. The good agreement between the fit and the measured temperatures shows that the decrease of the temperature in the presence of levitation can be fully attributed to the adiabatic opening of the confinement.

Levitation is an efficient technique to ensure the spatial overlap of two species, and will be a very useful tool in further experiments investigating the physics of Fermi-Fermi mixtures, where full overlap of the two constituents is required. Yet, in our scheme, even in the absence of levitation the two species remain in thermal contact throughout the evaporation ramp, as shown by the efficiency of the sympathetic cooling. This means that we can apply the levitation after the evaporation ramp and benefit from both the positive effects of gravity on evaporative cooling and of levitation on the spatial overlap.

4.3.5 Interspecies scattering cross section

To determine the cross section for elastic collisions between ^{161}Dy and ^{40}K atoms we perform an interspecies thermalization measurement [243, 244, 245]. We interrupt the evaporation process in the CDT when the power in the horizontal beam reaches 350 mW. At this point, there are no atoms left in the arms of the CDT. Then we recompress the trap by increasing the power in the horizontal beam to 680 mW to stop plain evaporation. The two atom numbers are $N_\mathrm{K} \approx 9{\times}10^3$ and $N_\mathrm{Dy} \approx 5{\times}10^4$. The two components are in the thermal regime and their temperatures are equal, around 2 μK. The average trap frequency is $\bar{\omega} = 2\pi \times 1007$ Hz for K atoms, and the peak densities are $n_\mathrm{K} = 1.6 \times 10^{13}$ cm^{-3} and $n_\mathrm{Dy} = 1.4 \times 10^{13}$ cm^{-3}. We then suddenly displace the horizontal beam in the vertical direction using an AOM and, after a time δt, suddenly displace it back to its original position. After this sequence of two trap displacements, we hold the atoms in the CDT for a variable time and finally measure the temperature of the two components. By setting $\delta t = 2\pi/\omega_z^\mathrm{Dy}$ the energy injected in the Dy cloud by the two successive kicks ideally vanishes, while it does not for the K cloud. This kinetic energy of the K atoms is transformed after some typical time τ in thermal energy through collisions with Dy atoms. We measure this thermal energy after a variable hold time by measuring the size of the K cloud after a time of flight expansion. Following the model developed in [243] and considering the zero energy limit for elastic collisions, the total collision rate is obtained from $\Gamma_\mathrm{coll} = \sigma_\mathrm{el} v_\mathrm{rel} I$, where σ_el is the scattering cross section for elastic collisions between Dy and K atoms, v_rel is the mean relative velocity of two colliding atoms and $I = \int n_\mathrm{K} n_\mathrm{Dy} \mathrm{d}V$. The relation between the measured thermalization time τ and the total collision rate is described in Sec. 4.5.4.

Figure 4.8 shows a thermalization curve, where the measured size of the K sample is interpreted in terms of a temperature [4]. The temperatures of the two species approach each other as we hold the cloud in the trap. Because of the number ratio $N_\mathrm{Dy}/N_\mathrm{K} \approx 5$, the dominant effect is observed as a reduction of the K temperature,

---

[4] Since the ^{40}K cloud cannot thermalize by itself after the excitation, interspecies collisions are needed to reach thermal equilibrium. For shorter times, the ^{40}K cloud can therefore not be described by a temperature in a strict thermodynamic sense. Here we use an effective temperature as a measure of the cloud's kinetic energy in the center-of-mass frame.

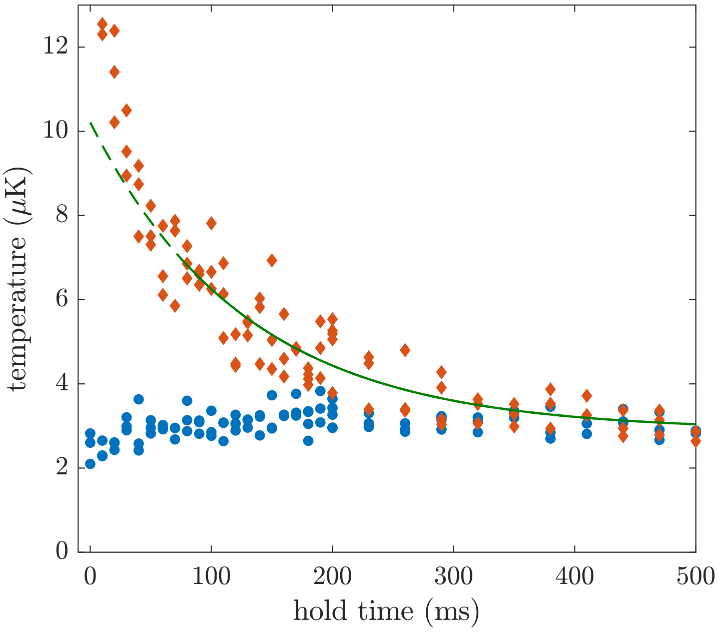

Figure 4.8: Cross-species thermalization measurement. The temperatures of the ^{40}K (red diamonds) and ^{161}Dy (blue circles) are shown versus the hold time after the species-selective heating by the trap displacements (see text). The solid green line is a fit of the temperature of the K atoms by an exponential curve for a hold time bigger than 80 ms. The dashed line extrapolates the fit.

while the Dy temperature only slightly increases. Our observation is consistent with a simple heat transfer from the K sample to the Dy one. Atom numbers of both species are constant on the time scale of the measurement.

The temperatures of the two species enter in the value of v_{rel} and of the overlap integral I; see Sec. 4.5.4. It turns out that, given the mass and polarizability ratios of Dy and K, the opposite effects of temperatures on v_{rel} and I nearly balance each other and thus lead to an almost constant value of Γ_{coll} for a temperature ratio $T_{\mathrm{K}}/T_{\mathrm{Dy}} \lesssim 2$. Since at these temperatures the elastic scattering cross section is almost constant, the measured temperatures evolve in a quasi-exponential way during the thermalization process. From an exponential fit of the temperature of K for hold times larger than 80 ms we extract a thermalization time constant of $\tau = 130$ ms. This corresponds to an elastic scattering cross section of $\sigma_{\mathrm{el}} \approx 1.4 \times 10^{-16}$ m^2, with an estimated error of 15% including all statistical and systematic errors. We calculate the cross section for elastic dipolar collisions between Dy and K atoms to be two orders of magnitude smaller than the measured cross section [5].

---

[5] The elastic dipolar cross section for interspecies collisions is obtained from $\sigma_{\mathrm{dip}} = (16/45)\pi a_D^2 + (16/15)\pi a_D^2$, where the two terms represent the contributions of even and odd

We therefore attribute the measured cross section to the contact interaction and deduce the corresponding scattering length $|a_{\mathrm{DyK}}| \approx 62$ a_0. We point out that the measured interspecies cross section is one order of magnitude smaller than the dipolar cross section for elastic collisions between identical ^{161}Dy atoms ($\sigma_{\mathrm{dip,Dy}} = 7.2 \times 10^{-16}$ m^2).

4.4 Conclusion and outlook

We have demonstrated how a deeply degenerate Fermi-Fermi mixture of ultracold ^{161}Dy and ^{40}K atoms can be efficiently produced in an optical dipole trap. The cooling process relies on the evaporation of the spin-polarized Dy component, with elastic collisions resulting from universal dipolar scattering. The K component is sympathetically cooled by elastic s-wave collisions with Dy. In this way, we have reached conditions with about 2×10^4 Dy atoms and about 5×10^3 K atoms at temperatures corresponding to ∼10% and ∼20% of the respective Fermi temperature. This represents an excellent starting point for future experiments aiming at the realization of novel quantum phases and superfluid states in mass-imbalanced fermionic mixtures.

The next challenge in our experiments will be the implementation of interspecies interaction tuning by means of magnetically tuned Feshbach resonances [12]. Although the particular interaction properties of our mixture are yet unknown, one can expect many Feshbach resonances to arise from the anisotropic electronic structure of the Dy atom [246, 68]. The key question, which we will have to answer in near-future experiments, is whether sufficiently broad Feshbach resonances exist to facilitate interaction tuning along with a suppression of inelastic losses. Reason for optimism is given by the fact that rather broad Feshbach resonances have been found in single-species experiments with Er and Dy [127, 247, 248].

If nature will be kind to us and provide us with a good handle to control interactions in the resonant regime, then the future will look very bright for novel superfluid phases in Dy-K Fermi-Fermi mixtures. A very favorable property of this mixture, as we pointed out already in Ref. [232], is the fact that the polarizability ratio of the two species in an infrared optical dipole trap nearly corresponds to the inverse mass ratio. This will allow to easily match the Fermi surfaces of both species even in the inhomogeneous environment of a harmonic trap, and to investigate pairing and superfluidity of unequal mass particles in the crossover from molecular BEC to a BCS-type regime. Moreover, our preparation naturally produces a situation with a majority of heavier atoms, which is exactly what will

---

partial waves respectively. The dipolar length a_D is given by $a_D = \mu_0 \mu_{\mathrm{K}} \mu_{\mathrm{Dy}} m_r / (4\pi\hbar^2)$. Here μ_0 is the permeability of vacuum, μ_{K} and μ_{Dy} are the magnetic dipole moments of K and Dy atoms in the relevant spin states, and m_r is the reduced mass. We calculate $\sigma_{\mathrm{dip}} = 7.2 \times 10^{-19}\mathrm{m}^2$

be needed to realize FFLO states in mass- and population-imbalanced fermionic mixtures [199, 24].

Acknowledgments

We thank S. Tzanova for her contributions in the early stage of the experiment. We acknowledge financial support by the Austrian Science Fund (FWF) within the Doktoratskolleg ALM (Grant No. W1259-N27).

4.5 Appendix

4.5.1 Apparatus

Here, we describe briefly our apparatus. We use two independent and spatially separated atomic sources for the two species, which provide collimated atomic beams in the main vacuum chamber through two different ports. As mentioned in Sec. 4.2.1, our source of Dy atoms consists of a commercial high-temperature effusion oven operating at about 1000°C combined with a Zeeman slower. The atomic flux through the Zeeman slower is increased by a transverse cooling stage applied at the exit of the oven, operating on the same broad transition as the Zeeman slower.

The K source is a two-dimensional MOT in a glass cell [249], loaded from the background pressure created by commercial isotopically enriched K dispensers (Alvatec), placed directly inside the glass cell. The glass cell is connected to the main vacuum chamber by a differential pumping tube. The two-dimensional MOT operates on the D2 line of K, and is created by two perpendicular retro-reflected elliptical laser beams and by a two-dimensional quadrupole magnetic field realized by two pairs of coils. The transversally cooled atoms are trapped around the line of zero magnetic field, forming a cigar-shaped cloud. An additional beam pushes the cloud through the differential pumping tube in the main chamber.

The K and Dy three-dimensional MOT beams are overlapped in a four fiber cluster, which distributes the light to the four MOT beam paths. The MOTs are created by two retro-reflected orthogonal beams in the horizontal plane, and by two counter-propagating vertical beams. The narrow character of the 626 nm line causes the Dy cloud to sit below the zero of the magnetic field, hence requiring the large diameter MOT beams (35 mm in our case). The laser light at 626 nm is spectrally broadened by a high-efficiency electro-optical modulator resonant at 104 kHz, which adds around 30 sidebands.

4.5.2 Imaging of the atomic cloud

The K and Dy atoms are imaged through the same imaging set-up, on a single sCMOS camera (Andor Neo), along an axis that lies in the horizontal plane (about 40° to the x axis). We use resonant absorption imaging on the D2 line of wavelength 767 nm for K, and on the broad line at 421 nm for Dy. The two probe beams are overlapped on a dichroic mirror and have σ^- polarization. The imaging sequence involves four laser pulses and one background picture: each species requires one pulse to image the atoms followed by one normalization pulse. The background picture without probe light is taken in the end of the imaging sequence. From the moment where the CDT is switched off, we wait a time corresponding to the time of flight for K, and shine the pulse imaging K atoms for 10 μs. We then wait a variable time which sets the difference between the two values for the time of flight applied to K and Dy, and shine the pulse imaging Dy atoms for 10 μs. The minimum time between the two pulses is 500 ns. The two normalization pictures are taken 40 ms after the respective pictures of the atoms. In both cases, the scattering cross section is assumed to be the resonant cross section for a two-level system.

4.5.3 Cooling ^{40}K on the D1 line

After preparation in the MOTs, the K and Dy components have very different temperatures. However, optimal efficiency of the subsequent evaporative cooling stage requires similar starting conditions for the two species. In order to reach this situation, we perform after the MOT stage sub-Doppler cooling of the K atoms in the form of a gray molasses on the D1 line. While this cooling technique has been demonstrated in free space [177], we describe here its successful implementation in the presence of our large-volume reservoir optical dipole trap (Sec. 4.2.2). In this situation, the dissipative nature of the molasses cooling improves significantly the phase-space density reached after transfer into the optical dipole trap. We account for the effect of the space-dependent light shift by ramping the laser parameters, as we describe in the following.

The laser beams creating the gray molasses are overlapped on polarizing beam splitters with the MOT beams, which fixes their polarization to circular with opposite helicity compared to the MOT beams. The cooler and repumper beams are blue-detuned relative to the $F = 9/2 \rightarrow F' = 7/2$ and $F = 7/2 \rightarrow F' = 7/2$ transitions respectively. We define Δ as the detuning of the cooling beam relative to the bare (in the absence of light shift) $9/2 \rightarrow 7/2$ line and $\delta = \omega_{\mathrm{rep}} - \omega_{\mathrm{cool}} + \omega_{\mathrm{hf}}$, where ω_{cool} is the frequency of the cooling beam, ω_{rep} is the frequency of the repumper, and ω_{hf} is the hyperfine splitting in the ground state of ^{40}K; see Fig. 4.9(a).

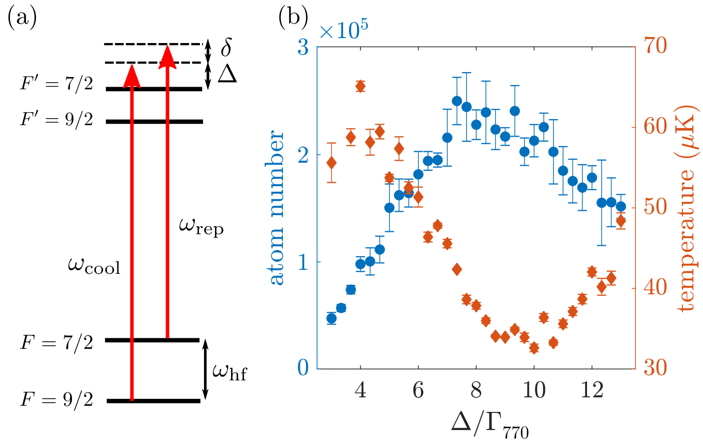

Figure 4.9: D1 cooling of ^{40}K. (a) Levels structure of the D1 transition and laser scheme. (b) Atom number and temperature at the end of the D1 cooling step in the RDT, as a function of the detuning Δ, when δ is kept to zero.

After the compression of the K MOT, the gradient of magnetic field is set to zero, and residual homogeneous magnetic fields are canceled to the level of 10 mG. The D2 light is switched off and D1 light is switched on. The RDT is turned on beforehand during the MOT and its power is kept unchanged (see Sec. 4.2.2). At this point, the cloud sits on top of the crossed RDT, though being larger.

Because the polarizability of the excited state at 1064 nm is negative, the transition is shifted to higher frequency by the ac Stark shift in the center of the trap compared to the wings of the potential. We therefore use a two-step D1 cooling scheme, in which the intensities and the detuning Δ are first kept constant and then tuned in linear ramps. During the initial capture phase of 0.6 ms, the power and detunings are kept constant at $I^{\mathrm{cool}} = 5.8\ I_{\mathrm{sat},770}$, $I^{\mathrm{rep}} = 0.11\ I_{\mathrm{sat},770}$ and $\delta = 0, \Delta = 3\ \Gamma_{770}$ (where $I_{\mathrm{sat},770} = 1.70$ mW cm^{-2} is the saturation intensity of the D1 line of K and Γ_{770} its natural linewidth), which are the parameters found to be optimal for D1 cooling in free space. In the second phase, powers are ramped down in 20 ms to $I^{\mathrm{cool}} = 0.18\ I_{\mathrm{sat}}$ and $I^{\mathrm{rep}} \approx 0.01\ I_{\mathrm{sat}}$ while the cooler and repumper are detuned further to the blue. The ramp of frequencies thus allows us to cool atoms from the outer region into the trap. Figure 4.9(b) shows the final atom number and temperature of the K cloud as the final value of Δ is varied. We achieve a temperature of 27(1) μK for a final value $\Delta = 9\ \Gamma_{770}$.

4.5.4 Interspecies thermalization

We summarize here the model developed by Mosk *et al.* [243], which describes the thermalization between two species in a harmonic trap (we assume here that the two species have the same central position). We reproduce in particular the relation between the elastic cross section σ_{el} and the thermalization time τ. First, we calculate the total collision rate $\Gamma_{\mathrm{coll}} = \sigma_{\mathrm{el}} v_{\mathrm{rel}} I$. The mean relative velocity is obtained as

$$v_{\mathrm{rel}} = \sqrt{\frac{8k_{\mathrm{B}}}{\pi}\left(\frac{T_{\mathrm{K}}}{m_{\mathrm{K}}} + \frac{T_{\mathrm{Dy}}}{m_{\mathrm{Dy}}}\right)} \; . \tag{4.1}$$

Assuming a thermal density distribution of the two components, one calculates the overlap integral

$$I = N_{\mathrm{K}} N_{\mathrm{Dy}} \bar{\omega}_{\mathrm{Dy}}^3 \left(\frac{2\pi k_{\mathrm{B}} T_{\mathrm{Dy}}}{m_{\mathrm{Dy}}}\right)^{-3/2} \left(1 + \frac{\alpha_{\mathrm{Dy}}}{\alpha_{\mathrm{K}}} \frac{T_{\mathrm{K}}}{T_{\mathrm{Dy}}}\right)^{-3/2} \; . \tag{4.2}$$

Based on the ratios of polarizabilities, masses, and temperatures, we define the quantity

$$A = \left(1 + \frac{m_{\mathrm{Dy}}}{m_{\mathrm{K}}} \frac{T_{\mathrm{K}}}{T_{\mathrm{Dy}}}\right)^{1/2} \left(1 + \frac{\alpha_{\mathrm{Dy}}}{\alpha_{\mathrm{K}}} \frac{T_{\mathrm{K}}}{T_{\mathrm{Dy}}}\right)^{-3/2} \; . \tag{4.3}$$

Combining (4.1-4.3) we deduce the collision rate

$$\Gamma_{\mathrm{coll}} = \sigma_{\mathrm{rel}} \frac{m_{\mathrm{Dy}} \bar{\omega}_{\mathrm{Dy}}^3}{\pi^2 k_{\mathrm{B}} T_{\mathrm{Dy}}} N_{\mathrm{Dy}} N_{\mathrm{K}} A \; . \tag{4.4}$$

We assume [243] that the average energy transfer during one Dy-K collision is given by $\Delta E = \xi k_{\mathrm{B}}(T_{\mathrm{K}} - T_{\mathrm{Dy}})$, where $\xi = 4 m_{\mathrm{Dy}} m_{\mathrm{K}} / (m_{\mathrm{Dy}} + m_{\mathrm{K}})^2$ accounts for the effect of the mass imbalance. Using this expression, we obtain the relation relating the collision rate Γ_{coll} and the thermalization time τ:

$$\tau^{-1} = \frac{1}{\Delta T} \frac{\mathrm{d}}{\mathrm{dt}} \Delta T = \xi \frac{N_{\mathrm{Dy}} + N_{\mathrm{K}}}{3 N_{\mathrm{Dy}} N_{\mathrm{K}}} \Gamma_{\mathrm{coll}} \; . \tag{4.5}$$

One finally finds the relation

$$\tau^{-1} = \sigma_{\mathrm{el}} \, \frac{\xi}{3\pi^2} \frac{m_{\mathrm{Dy}} \bar{\omega}_{\mathrm{Dy}}^3}{k_{\mathrm{B}} T_{\mathrm{Dy}}} \left(N_{\mathrm{Dy}} + N_{\mathrm{K}}\right) A \tag{4.6}$$

between the thermalization time and the scattering cross section. Given the mass and polarizability ratios of Dy and K [232], there is only a weak dependence of A on the temperature ratio for the range of temperatures that we consider. We calculate $A \approx 1.5$, which allows us to analyze the near-exponential thermalization curve presented in Fig. 4.8.

5

Resonantly Interacting Fermi-Fermi Mixture of ^{161}Dy and ^{40}K

Published as:
C. Ravensbergen, E.Soave, V. Corre, M. Kreyer, B. Huang (黄博), E. Kirilov and R. Grimm
Phys. Rev. Lett. 124, 203402 (2020)

Author contribution: The author took part in the measurements and contributed to the general lab work, the interpretation and analysis of the data, and the discussions during the writing of the manuscript.

Note: With respect to the published version, section headlines have been added.

We report on the realization of a Fermi-Fermi mixture of ultracold atoms that combines mass imbalance, tunability, and collisional stability. In an optically trapped sample of ^{161}*Dy and* ^{40}*K, we identify a broad Feshbach resonance centered at a magnetic field of 217 G. Hydrodynamic expansion profiles in the resonant interaction regime reveal a bimodal behavior resulting from mass imbalance. Lifetime studies on resonance show a suppression of inelastic few-body processes by orders of magnitude, which we interpret as a consequence of the fermionic nature of our system. The resonant mixture opens up intriguing perspectives for studies on novel states of strongly correlated fermions with mass imbalance.*

5.1 Introduction

Ultracold Fermi gases with resonant interactions have attracted a great deal of attention as precisely controllable model systems for quantum many-body physics [225, 226, 227]. The interest spans across many different fields, from primordial matter, neutron stars and atomic nuclei to condensed-matter systems, and in particular concerning superfluids and superconductors [188]. Corresponding experiments in ultracold Fermi gases require strong s-wave interactions, which can be realized based on Feshbach resonances [12] in two-component systems. The vast majority of experiments in this field relies on spin mixtures of fermionic atomic species, which naturally imposes equal masses. Beyond this well-established situation, theoretical work has predicted fermionic systems with mass imbalance to favor exotic interaction regimes [199]. Mass-imbalanced systems hold particular promise [198, 24] in view of superfluid states with unconventional pairing mechanisms, most notably the elusive Fulde-Ferrell-Larkin-Ovchinnikov (FFLO) state [19, 118, 196].

A key factor for experiments on resonantly interacting Fermi gases is the collisional stability that arises from a suppression of inelastic loss processes at large scattering lengths. This effect is a result of Pauli exclusion in few-body processes at ultralow energies [94, 219]. To act efficiently in an experiment, the suppression requires a broad s-wave Feshbach resonance with a sufficiently large universal range [219, 250]. For the mass-balanced case, suitable resonances exist in spin mixtures of ^{6}Li or ^{40}K, and such systems are used in many laboratories worldwide. In a mass-imbalanced fermion system, the same suppression effect can be expected [220]. However, the only s-wave tunable Fermi-Fermi system realized so far is the mixture of ^{6}Li and ^{40}K [216, 210], for which the Feshbach resonances [148, 214, 218] are too narrow to enable strong loss suppression [224].

The advent of submerged-shell lanthanide atoms in the field of ultracold quantum gases [129, 133, 60, 61] has considerably enhanced the experimental possibilities. While most of the current work focuses on interactions that result from the large

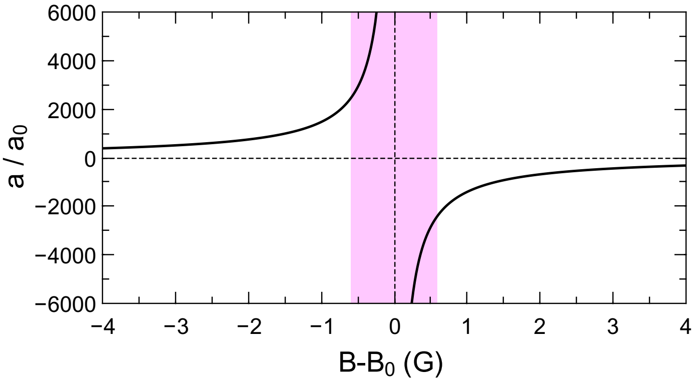

Figure 5.1: Interspecies scattering length a for ^{161}Dy-^{40}K near the broad Feshbach resonance centered at $B_0 \approx 217\,$G. The shaded region indicates the regime where a exceeds all other relevant length scales (see text).

magnetic dipole moment or the complex optical transition structure, the availability of additional fermionic atoms is of great interest in view of novel ultracold mixtures and strongly interacting systems [135, 223]. We have recently introduced the mixture of ^{161}Dy and ^{40}K [232, 26] as a candidate for realizing a collisionally stable, strongly interacting Fermi-Fermi mixture. Many narrow Feshbach resonances can be expected for such a system as a result of anisotropic interatomic interactions [246, 229]. However, the key question in view of future experiments has remained, whether suitable broad resonances would exist.

In this Letter, we report on a broad Feshbach resonance in the ^{161}Dy-^{40}K mixture with its center found near 217 G. We have identified this resonance (see Fig. 5.1) as the strongest one in a scenario of three overlapping resonances 5.7, with the other two at 200 G and 253 G. Some weak (only few mG wide) interspecies resonances do also exist in the relevant region, but they can be ignored for understanding the general structure of the broad scenario. We have characterized the three resonances by interspecies thermalization measurements, as reported in detail in 5.7. Close to the center of the strongest resonance, the tunability of the interspecies s-wave scattering length can be well approximated by

$$a = -\frac{A}{B - B_0}\, a_0\,, \tag{5.1}$$

where a_0 is Bohr's radius. Our best knowledge of the pole position and the strength parameter is $B_0 = 217.27(15)\,$G and $A = 1450(230)\,$G 5.7.

5.2 Sample preparation

The starting point of our experiments is a degenerate mixture of ^{161}Dy and ^{40}K, prepared in a crossed-beam optical dipole trap according to the procedures described in our earlier work [26]. Evaporative cooling is performed at a low magnetic field of 225 mG. Both species are in their lowest hyperfine and Zeeman substates, which excludes two-body losses. The transfer of the system into the high-field region above 200 G is challenging, because many Dy intraspecies [126, 164] and Dy-K interspecies resonances have to be crossed in a fast ramp of the magnetic field. To minimize unwanted losses, heating, and excitations of the trapped cloud we proceed in two steps. Within a few ms, we ramp up the magnetic bias field to 219.6 G [1], where the system is given a time of a few 10 ms to settle and establish thermal equilibrium. We then apply a very fast (2-ms) small-amplitude ramp to the target field, where the experiments are carried out. Throughout the whole sequence after evaporation, a magnetic levitation field is applied to compensate for the relative gravitational sag of both species [26]. In this way, we reach typical conditions of $N_{\mathrm{Dy}} = 20\,000$ and $N_{\mathrm{K}} = 8\,000$ atoms at a temperature of $T = 500\,\mathrm{nK}$ [2] in a slightly elongated trap (aspect ratio ~2) with mean oscillation frequencies of $\bar{\omega}_{\mathrm{Dy}}/2\pi = 120\,\mathrm{Hz}$ and $\bar{\omega}_{\mathrm{K}}/2\pi = 430\,\mathrm{Hz}$ [3] and depths corresponding to $3.5\,\mu\mathrm{K}$ and $10\,\mu\mathrm{K}$, respectively. With Fermi temperatures of $T_F^{\mathrm{Dy}} = 290\,\mathrm{nK}$ and $T_F^{\mathrm{K}} = 750\,\mathrm{nK}$, our experimental conditions are near-degenerate of ($T/T_F^{\mathrm{Dy}} = 1.7$ and $T/T_F^{\mathrm{K}} = 0.65$).

5.3 Interaction characterization

Interaction regimes close to resonance, where scattering is limited by unitarity [251, 252], can be discussed by comparing the scattering length with other relevant length scales. To characterize the thermal behavior we consider the inverse wave number of the relative motion $1/\bar{k}_{\mathrm{rel}} = \hbar/(m_r \bar{v}_{\mathrm{rel}})$, where $\bar{v}_{\mathrm{rel}} = \sqrt{8k_BT/(\pi m_r)}$ is the mean relative velocity and m_r denotes the reduced mass. The typical interparticle distance sets another length scale, for which we adopt a common definition for two-component Fermi gases, $d = (3\pi^2 n_{\mathrm{tot}})^{-1/3}$, where n_{tot} is the total number density of both species in the trap center. At zero temperature, d corresponds to the inverse Fermi momentum $1/k_F$. For our typical experimental parameters,

---

[1] At 219.6 G interspecies thermalization is sufficiently fast and Dy background losses show a pronounced minimum.

[2] Thermometry is based on time-of-flight images taken at high magnetic fields in regions where interspecies interactions are weak.

[3] The ratio of the trap frequencies for K and Dy is essentially determined by the mass ratio and the polarizability ratio, which results in a $\bar{\omega}_{\mathrm{K}}/\bar{\omega}_{\mathrm{Dy}} = 3.60$ [232].

we obtain similar values $1/\bar{k}_{\mathrm{rel}} \approx 2100\, a_0$ and $d \approx 2500\, a_0$, which correspond to near-degenerate conditions. The resonant interaction regime where the scattering length exceeds both scales is realized in a magnetic detuning range of roughly $\pm 0.6\,$G.

A further length scale is set by the effective range of the resonance [12] and can be characterized by the range parameter R^* as defined in Ref. [65]. For our case, the value of this parameter is presently unknown because of the yet undetermined magnetic moment of the molecular state underlying the resonance. However, by assuming reasonable values for the magnetic moment, we show in Sec. 5.7 that R^* is very likely to stay small in comparison with the large values of the scattering length in the resonant interaction regime and the other relevant length scales. We therefore assume the effective range to be negligible for the universal interaction physics in the resonant regime.

5.4 Hydrodynamic expansion

A striking effect of the resonant interspecies interaction shows up in the expansion of the mixture. In the experiments, the sample was released from the trap right after switching to the target field strength. The absorption images in the upper row of Fig. 5.2 illustrate the case of weak interactions ($a \approx -40\, a_0$), realized at $B = 235.4\,$G. Here the expansion takes place in a ballistic way and, as expected from the mass ratio, the K component expands much faster than the Dy component. In contrast, in the resonant case (images in the lower row of Fig. 5.2) both components expand with similar sizes. Evidently, the interaction between the two species slows down the expansion of the lighter species and accelerates the expansion of the heavier species. Such a behavior requires many elastic collisions [4] on the timescale of the expansion and thus can be interpreted as a hallmark of hydrodynamic behavior.

A closer inspection of the spatial profiles of the hydrodynamically expanding mixture reveals an interesting difference between the heavy and the light species; see profiles in Fig. 5.3. While the Dy cloud essentially keeps its near-Gaussian shape, the K cloud (initially about twice smaller than the Dy cloud) develops pronounced side wings. Apparently, the mixture forms a hydrodynamic core surrounded by a larger cloud of ballistically expanding lighter atoms.

To elucidate the origin of this surprising effect we have carried out a Monte-Carlo simulation [253], accounting for the classical motion and the quantum mechanically resonant collisional cross section, which is only limited by the finite rel-

---

[4] We estimate the collision rate for a K atom in the center of the Dy cloud by considering the resonant elastic scattering cross section $\sigma_{\mathrm{res}} = 4\pi/\bar{k}_{\mathrm{rel}}^2$, the Dy peak number density $\hat{n}_{\mathrm{Dy}}$, and the mean relative velocity $\bar{v}_{\mathrm{rel}}$. For our typical conditions, $\hat{n}_{\mathrm{Dy}}\sigma_{\mathrm{res}}\bar{v}_{\mathrm{rel}} \approx 10^4\,\mathrm{s}^{-1}$.

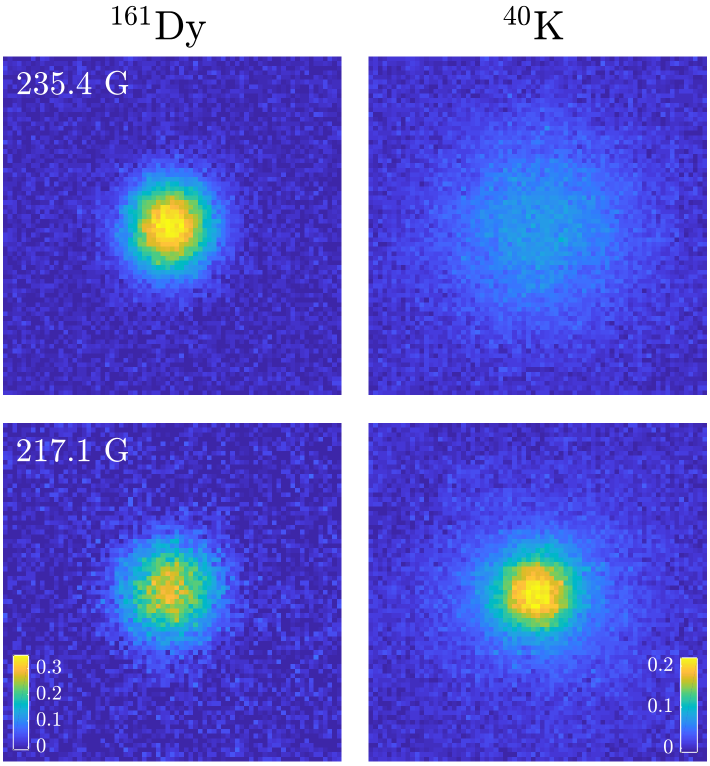

Figure 5.2: Comparison of the expansion of the mixture for weak (upper) and resonant (lower) interspecies interaction. The absorption images show the optical depth for both species (Dy left, K right) after a time of flight of 4.5 ms. The field of view of all images is 240 μm × 240 μm.

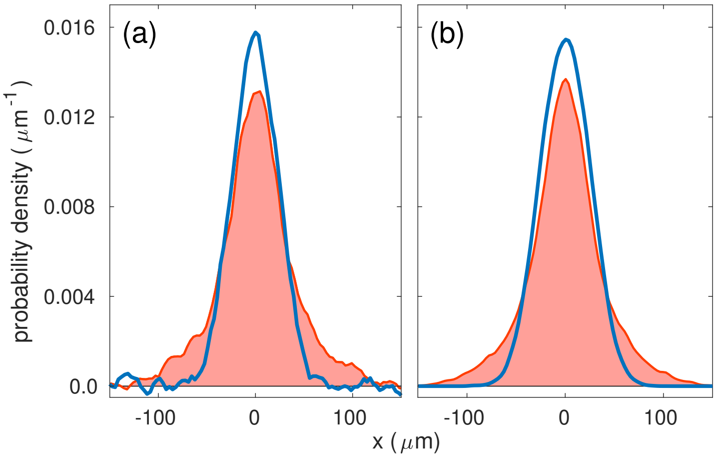

Figure 5.3: Profiles of the hydrodynamically expanding mixture for resonant interaction, (a) experimentally observed and (b) from a corresponding Monte-Carlo simulation. Shown are the probability densities of doubly-integrated profiles for both Dy (solid blue lines) and K (red curve with filling).

ative momentum of a colliding pair [251, 252]. For our near-degenerate conditions, we neglect Pauli blocking and interactions beyond two-body collisions. The simulation results in Fig. 5.3(b) reproduce the experimental profiles (a) without any free parameter. The simulation confirms our interpretation in terms of a hydrodynamic core, where both species collide with each other at a large rate, surrounded by a ballistically expanding cloud of light atoms. The physical mechanism for the formation of the latter is the faster diffusion of lighter atoms, which can leak out of the core and, in the absence of the other species, begin to move ballistically. We point out that this bimodality effect is not an experimental imperfection, but a generic feature in the hydrodynamic expansion of a mass-imbalanced mixture.

To investigate the dependence of the hydrodynamic expansion on the scattering length, we recorded two-dimensional expansion profiles (such as in Fig. 5.2) for various values of B in a 2-G wide range around the resonance center. We focus our analysis on the K profiles as they reveal the hydrodynamic core, while the Dy profiles only show a slight increase in width. As a quantitative measure we define the "central fraction" as the fraction of K atoms in a circle of particular radius. For the latter we use the $\sqrt{2}\sigma$ width of the noninteracting Dy cloud ($\sim 34\,\mu$m at a 4.5-ms time of flight). We find a marked increase of the central fraction from its non-interacting background value 0.22 to a resonant peak value of about 0.40. As a function of the magnetic detuning $B - B_0$, the central fraction shows a pronounced resonance behavior, which closely resembles a Lorentzian curve. From a fit we derive the center $B_0 = 217.04$G and a width (half width at half maximum) of 0.37 G. We finally use Eq. (5.1) with the fixed value $A = 1450$ G to convert

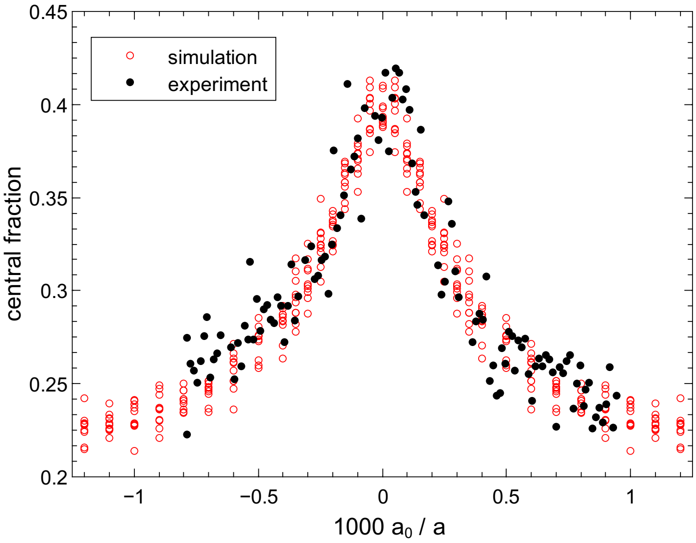

Figure 5.4: Enhancement of the central fraction of K atoms in the expanding mixture. Experimental results for the resonance behavior (filled black symbols) are shown in comparison with Monte-Carlo simulation results (red open symbols).

the magnetic detuning scale into an inverse scattering length and plot the data as shown in Fig. 5.4.

For comparison, we have also employed our Monte-Carlo approach to calculate the central fraction as a function of the scattering length. Figure 5.4 shows the simulation results (red open symbols) together with the experimental data (black closed symbols). We find that the simulation reproduces the experimental observations very well. This agreement between experiment and theory strongly supports our qualitative and quantitative understanding of both the resonance scenario and the expansion dynamics.

For a precise determination of the resonance center, measurements based on the hydrodynamic expansion can in general provide much sharper resonance features than simple thermalization [254]. While our expansion measurement yielded 217.04(1) G for the resonance center B_0, the thermalization measurement 5.7 resulted in a value of 217.27(15) G, somewhat higher and with a statistical uncertainty more than an order of magnitude larger. Whether the apparent deviation is a pure statistical effect (about 1.5 σ), whether it is caused by magnetic-field control issues [5], or whether there are unknown systematic effects behind it requires further investigation. We note that anisotropic expansion effects in our nearly spherical trap remain very weak and are barely observable. The anisotropic expansion of a

---

[5] Day-to-day fluctuations, drifts in the calibration, and residual ramping effects may cause magnetic-field uncertainties of the order of 100 mG.

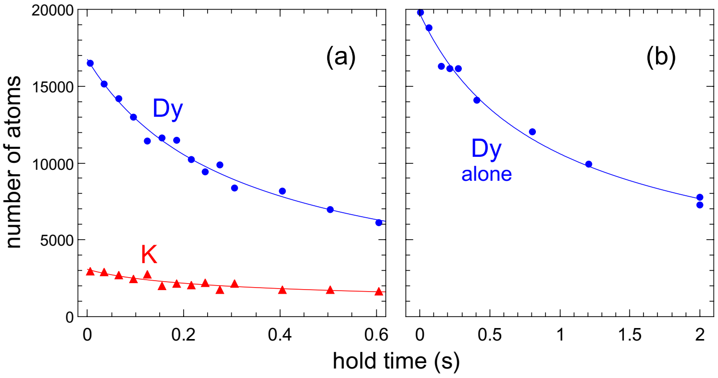

Figure 5.5: Decay of the resonant Dy-K mixture (a) in comparison with a pure Dy sample (b) at magnetic field $B = 217.5\,\mathrm{G}$, very close to the resonance pole. The solid lines show fits by a phenomenological model 5.7.

hydrodynamic, strongly interacting Fermi-Fermi system has been studied in our earlier work on a resonant ^{6}Li-^{40}K mixture [216].

5.5 Lifetime

We now turn our attention to the lifetime of the mixture in the resonance region. In general, we find the magnetic-field dependence of losses to exhibit a very complex behavior 5.7. Both Dy-K interspecies and Dy intraspecies losses show strong fluctuations with a variation of the magnetic field. A broad loss feature appears about 0.5 G below the 217-G resonance, where the scattering length is very large and positive. This feature closely resembles observations made in spin mixtures of ^{6}Li [222, 98, 255] and ^{40}K [254], which have been understood as a signature of the formation of weakly bound dimers. In addition to this broad feature, additional narrower structures appear, which make the experiment very sensitive to the particular choice of the magnetic field. Nevertheless, several good regions exist close to the center of the broad Feshbach resonance under conditions, where losses are relatively weak and s-wave scattering is deep in the unitarity-limited regime.

As an example for long lifetimes attainable in the resonance region, Figure 5.5 shows a set of measurements taken at field strength of 217.5 G, for which we estimate a large negative scattering length of $-3000\,a_0$ or even larger. We have fitted and analyzed the decay of the atom numbers following the procedures detailed in 5.7. For the number of K atoms, our data show an initial time constant of about 350 ms. If we attribute this decay completely to K-Dy-Dy (K-K-Dy) three-body processes, we obtain the upper limits of $4 \times 10^{-25}\,\mathrm{cm}^6/\mathrm{s}$ ($3 \times 10^{-25}\,\mathrm{cm}^6/\mathrm{s}$) for the event rate coefficients. These values are very small compared with other resonant three-body systems that do not involve identical fermions. In Feshbach-resonant Bose-Bose [256, 257, 258] or Bose-Fermi mixtures [259, 260, 261, 262, 263], event rate coefficients have been measured exceeding $10^{-23}\,\mathrm{cm}^6/\mathrm{s}$, i.e. at least two orders of magnitude more. In preliminary experiments [264] on Bose-Fermi mixtures of Dy-K (bosonic isotope ^{162}Dy), we have also observed a dramatic increase of resonant three-body losses by orders of magnitude. We attribute the low values of the three-body rate coefficients and thus the long lifetimes in our Fermi-Fermi system to the Pauli suppression of inelastic losses [94, 219, 220].

The decay of the Dy component in the mixture, displayed in Fig. 5.5(a) by the blue data points and the corresponding fit curve, shows a peculiar behavior. Since we find that about 10 times more Dy atoms are lost as compared to K atoms, three-body interspecies collisions may only explain a small fraction of Dy losses. As Figure 5.5(b) shows, Dy alone exhibits losses even without K being present, but much weaker. Interpreting these losses as Dy intraspecies losses, gives values for the event rate coefficient of $3.4 \times 10^{-25}\,\mathrm{cm}^6/\mathrm{s}$ in the presence of K, but only $0.8 \times 10^{-25}\,\mathrm{cm}^6/\mathrm{s}$ without K 5.7. These observations point to an unknown mechanism, in which K atoms somehow catalyze the decay of Dy without directly participating in the loss processes. A possible mechanism may be due to elastic collisions with K atoms causing residual evaporation. We tested this in our experiments by recompressing the trap, but did not observe significant changes in the observed loss behavior. Another hypothesis is based on a spatial contraction (density increase) of the Dy cloud caused by strong interaction effects with K atoms. Considering the zero-temperature limit, we have developed a model 5.7 for such an effect, but its applicability is questionable at the temperatures of our present experiments. The explanation of the mysterious enhancement of Dy losses induced by K remains a task for future experiments.

5.6 Discussion and conclusion

Already our present experiments, carried out near quantum degeneracy ($T/T_F^{\mathrm{K}} \approx 0.65$), demonstrate that mass imbalance can make a qualitative difference in the physical behavior of a strongly interacting fermion mixture. The bimodality observed in the hydrodynamic expansion profile of the lighter component is seemingly similar to observations in population-imbalanced spin mixtures near the superfluid phase transition [265]. However, while in the latter case bimodality signals superfluidity, the reason is a different one in our case. Detailed understanding of the expansion dynamics of a Fermi-Fermi mixture in different classical and quantum regimes is thus essential for interpreting the expansion profiles in future work aiming at superfluid regimes.

For reaching lower temperatures and deeper degeneracy, work is in progress to eliminate heating in the transfer from low to high magnetic fields and to implement an additional evaporative cooling stage that takes advantage of the large elastic scattering cross section close to the resonance. The experimental challenge is to realize similar degeneracy conditions near the 217 G resonance as we have achieved at a low magnetic field [26]. With some improvements, conditions for superfluid regimes seem to be attainable. To give an example, a Lifshitz point [198, 23] in the phase diagram, where zero momentum pairs become unstable, may be expected at a temperature corresponding to about 15% of the Fermi temperature of the heavy species [6].

In conclusion, we have shown that the ^{161}Dy-^{40}K mixture possesses a broad Feshbach resonance offering favorable conditions for experiments on strongly interacting fermion systems with mass imbalance. In particular, the system features a substantial suppression of inelastic losses near resonance, which is a key requirement for many experiments. Novel interaction regimes, including unconventional superfluid phases, seem to be in reach.

Acknowledgments

We acknowledge support by the Austrian Science Fund (FWF) within project P32153-N36 and within the Doktoratskolleg ALM (W1259-N27). We thank D. Petrov for enlightening discussions on fermionic suppression effects. We furthermore thank the members of the ultracold atom groups in Innsbruck for many stimulating discussions and for sharing technological know how.

5.7 Supplemental material

5.7.1 Feshbach resonance scenario

To date, no theoretical model is available that would describe the scattering properties of our Dy-K mixture. Our experimental characterization in the region of interest therefore relies on a combination of various observables, like the positions of resonance poles and zero crossings, and measurements of the interspecies thermalization time. Our basic model assumption is a scenario of three partially overlapping s-wave Feshbach resonances.

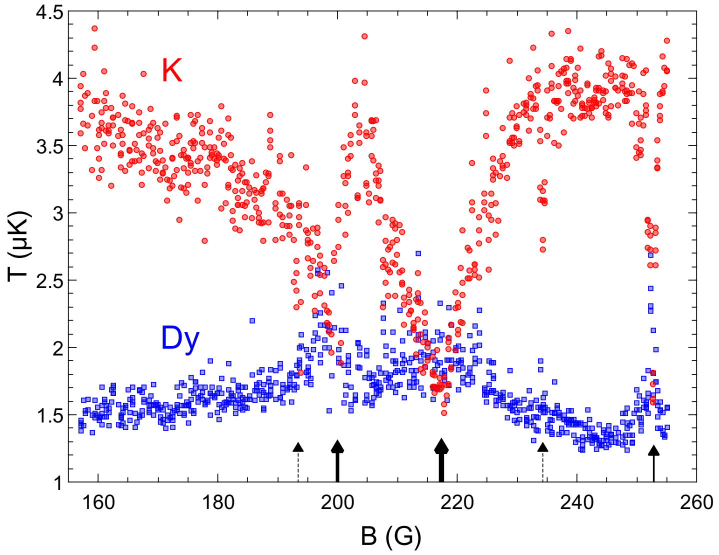

Figure 5.6: Thermalization scan revealing magnetic-field dependent resonances in interspecies elastic scattering. The mixture is initially prepared in a non-equilibrium situation, where the ^{161}Dy component (1.3 μK) is much colder than the ^{40}K component (4 μK). Within a short hold time of 50 ms, interspecies thermalization is observed. Fast thermalization is found to reach essentially equal temperatures at three points (solid arrows), which reveals the existence of three relatively broad Feshbach resonances. Indications of further, much narrower resonances are observed as well (two examples marked by dashed arrows). The broadest resonance, centered near 217 G is the one of main interest for the creation of strongly interacting Fermi-Fermi systems.

Wide-range thermalization scan

Figure 5.6 shows a thermalization scan over the wide magnetic field range from 155 to 255 G. After evaporatively cooling the mixture at low magnetic fields down to a temperature of about 1.3 μK, a short period (60 ms) of species-selective parametric heating by trap power modulation was applied to increase the temperature of the 1.4×10^4 K atoms to about 4 μK, leaving the temperature of the 2.9×10^4 Dy atoms essentially unchanged. For carrying out the measurements in the high-field region, we then quickly (within 12 ms) ramped up the magnetic field to the variable target field, where (partial) thermalization took place. After a hold time of 50 ms, the magnetic field was quickly (within 1 ms) ramped to 235.4 G. At this field, chosen for thermometry, the interspecies interaction is very weak and the sample expands ballistically after release from the trap. Temperatures were measured by standard time-of-flight imaging.

The thermalization scan reveals a scenario dominated by three broad Feshbach resonances, at the centers of which very fast interspecies heat exchange occurs and the temperatures become nearly equal. The corresponding positions are located near 200, 217, and 253 G (see solid arrows in Fig. 5.6). While the first resonance (near 200 G) is quite strong and has considerable overlap with the 217-G resonance (second resonance), the third resonance (near 253 G) is clearly weaker and well separated from the two other ones. Further, much narrower resonances exist (dashed arrows), with negligible effect on the overall scenario. The resonance near 217 G is the strongest one and thus the feature of main interest in our present work.

Model of three overlapping resonances

The magnetic-field dependence of the scattering length in a scenario of overlapping Feshbach resonances, assuming a constant background a_{bg}, can be represented by the product formula [266, 267]

$$a(B) = a_{\mathrm{bg}} \prod_{i=1}^{n} \frac{B - c_i}{B - p_i}\,, \tag{5.2}$$

where the parameters p_i and c_i denote the positions of the poles and zero crossings, respectively. A straightforward transformation gives the equivalent sum formula [267]

$$a(B) = a_{\mathrm{bg}} \left(1 - \sum_{i=1}^{n} \frac{\delta_i}{B - p_i}\right) \tag{5.3}$$

---

[6] Note that in Ref. [198] temperatures are given in units of a reduced Fermi temperature, which at the Lifshitz point is a factor of 3.4 higher than the Fermi temperature of the heavy species.

with

$$\delta_i = (c_i - p_i) \prod_{j \neq i}^{n} \frac{c_j - p_i}{p_j - p_i} \,. \tag{5.4}$$

A practical advantage of the product formula is that it explicitly contains the positions c_i of the zero crossings, which are often good observables in an experiment [268, 269]. An advantage of the sum formula is that the parameters δ_i provide a measure for the relative strengths of the different resonance contributions. In the case of a single, isolated resonance $\delta_1 = c_1 - p_1$ corresponds to the common definition [12] of the Feshbach resonance width.

Determination of poles and zero crossings

The poles (zero crossings) associated with Feshbach resonances can be identified as points of fastests (slowest) thermalization in scans like the one shown in Fig. 5.6. We have carried out further scans with higher resolution in narrower magnetic field ranges near the resonance centers, and obtained values $p_1 = 200.1(2)$ G and $p_2 = 217.27(15)$ G for the poles of the two broadest resonances. Here, because of the fast thermalization, we used short hold times of 50 ms (15 ms) for the determination of p_1 (p_2).

For the observation of zero crossings, close to which thermalization is very slow, long hold times are favorable. In a scan with a hold time of 1.2 s, we determined the position $c_1 = 203.0(2)$ G for the zero crossing between the poles p_1 and p_2.

The third resonance (near 253 G) is found in a region where the local background scattering length is very small. This is a consequence of the near cancellation of the global background scattering length a_{bg} by the effect of the two broad resonances. While the pole position p_3 can be determined in a straightforward way from the point of fastest thermalization, a determination of the two zero crossings c_2 and c_3 solely based on the observation of thermalization minima turns out to be rather inaccurate. We therefore investigated thermalization in a wide range covering c_2, p_3, and c_3 and analyzed the resulting data based on the model introduced in Ref. [243] and applied to our mixture in [26] (see also Sec. 5.7.1).

The model is based on the assumption of thermalization described by an exponential decrease of the temperature difference with increasing hold time, with a relaxation rate being proportional to the elastic scattering cross section and thus being proportional to $a^2(B)$. The temperature difference $\Delta T = T_{\mathrm{K}} - T_{\mathrm{Dy}}$ can then be written as a function of the magnetic field strength,

$$\Delta T(B) = \Delta T_0 \exp\left[-C a^2(B)\right] \,, \tag{5.5}$$

where ΔT_0 is the initial temperature difference. The parameter C is proportional to the hold time and further determined by a combination of the experimental parameters, as described in Refs. [243, 26].

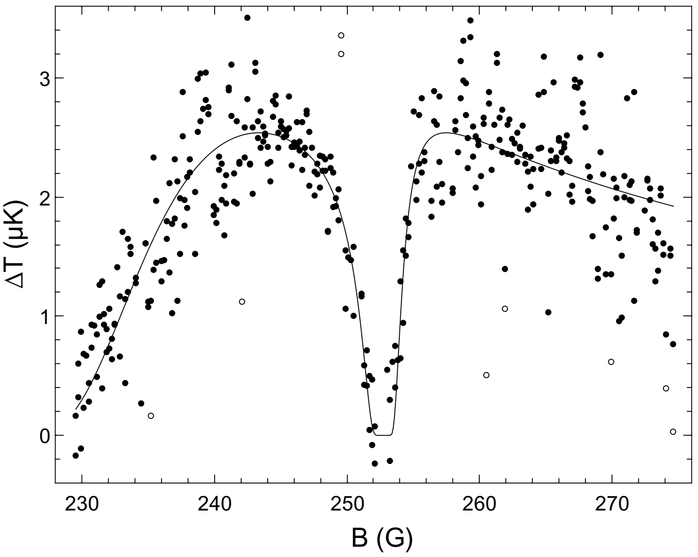

Figure 5.7: Thermalization scan in the region of the third resonance. The temperature difference ΔT was measured for a long hold time of 1.2 s. The solid line represents a fit based on the thermalization model described in the text, from which we obtain the pole position (minimum of ΔT) and the positions of the two neighboring zero crossings (maxima). Note that we have applied a rejection algorithm based on repeated application of Chauvenet's criterion [270] to reduce the effect of outliers and barely resolved narrow Feshbach on the fit. This removed 17 data points (open symbols) of in total 393 data points and resulted in very robust parameter values.

i	p_i (G)	c_i (G)	δ_i (G)
1	200.1(2)	203.0(2)	7.9(7)
2	217.27(15)	243.4(4)	24.6(6)
3	252.79(8)	257.5(4)	1.2(1)

Table 5.1: Parameters characterizing the scenario of three overlapping resonances. The given 1σ uncertainties include the fit errors and estimates for model-dependent errors. Additional magnetic-field uncertainties from the calibration and from day-to-day fluctuations are estimated on the order of 0.1 G.

The measurements in Fig. 5.7 were taken in a wide range between 229 and 275 G under similar initial conditions as in Fig. 5.6, but with a much longer hold time of 1.2 s. Thermometry was performed in the same way as in Fig. 5.6. We fitted the data based on the thermalization model [Eq. (5.5)] and the product formula [Eq. (5.2)] for $a(B)$. The parameters p_1, p_2, and c_1 were fixed to their separately determined values (see above discussion). The fit (solid curve in Fig. 5.7) yielded the parameter values $p_3 = 252.79(8)$ G, $c_2 = 243.4(4)$ G, and $c_3 = 257.5(4)$ G.

The complete set of resonance parameters p_i and c_i for our three-resonance model is summarized in Table 5.1. Based on Eq. (5.4), we also calculated the parameters δ_i, which characterize the strengths of the resonances. The resulting values (last column) confirm that the second resonance is the strongest one. The first resonance is about three times weaker, and the third resonance is about 20 times weaker than the strongest one.

Background scattering length

Having determined the poles and zero crossings describing our three-resonance scenario, the remaining task is to determine the background scattering length a_{bg}, which is left as the only unknown quantity in Eqs. (5.2) and (5.3). For this purpose, we carried out thermalization measurements in a similar way as described in Ref. [26]. We selected magnetic field regions, where thermalization takes place on experimentally convenient timescales and which are free of narrow Feshbach resonances, and determined the absolute values $|a(B)|$ of the scattering length for nine different values of the magnetic field strength. The corresponding signs uniquely follow from our three-resonance model. In this way, we obtained the nine measured values shown in Fig. 5.8. We finally fitted Eq. (5.2) to these data points with a_{bg} being the only free parameter. This yields the value of $a_{\mathrm{bg}} = +59(3)\,a_0$, where the given uncertainty includes the fit error and the effect of the uncertainties in the resonance parameters p_i and c_i.

We estimate that systematic uncertainties in the experimental parameters (mainly uncertainties in the atom numbers and trap frequencies) and model-

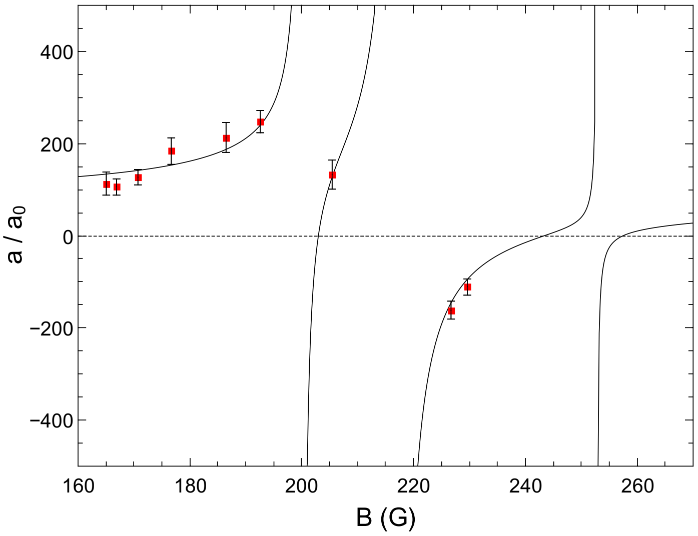

Figure 5.8: Magnetic-field dependence of the scattering length in the range of interest. The solid lines represent our model of three overlapping Feshbach resonances, with all parameters being determined experimentally. The experimental data points result from measurements of the scattering cross section by interspecies thermalization.

dependent errors result in an additional relative uncertainty of 15%, which dominates the error budget. Therefore, our final result for the background scattering length in the 200-G region is $a_{\mathrm{bg}} = +59(9)\, a_0$. It is interesting to note that our previous measurement [26], which was carried out at a low magnetic field of 430 mG, gave essentially the same value $(|a_{\mathrm{bg}}| \approx 60\, a_0)$, although the background scattering length may slowly vary with the magnetic field.

Analysis of thermalization measurements

The basic idea of our cross-species thermalization measurements to determine the Dy-K elastic scattering cross section (see example in Fig. 5.9) is the same as reported in [26], but here we have to deal with the additional complication that strong Dy losses occur during the thermalization process.

Our model was originally introduced in [243] and can be expressed in terms of a differential equation for the temperature difference $\Delta T = T_{\mathrm{K}} - T_{\mathrm{Dy}}$,

$$\frac{d}{dt}\Delta T = -\sigma_{\mathrm{el}}^2 \,\frac{\xi q}{3\pi^2}\, \frac{m_{\mathrm{Dy}}\bar{\omega}_{\mathrm{Dy}}^3}{k_{\mathrm{B}} T_{\mathrm{Dy}}} (N_{\mathrm{Dy}} + N_{\mathrm{K}})\, \Delta T, \tag{5.6}$$

where $\sigma_{\mathrm{el}} = 4\pi a^2$ is the cross section for elastic Dy-K collisions and $\xi = 4 m_{\mathrm{Dy}} m_{\mathrm{K}}/(m_{\mathrm{Dy}} + m_{\mathrm{K}})^2$ accounts for the effect of mass imbalance in the collisional energy transfer.

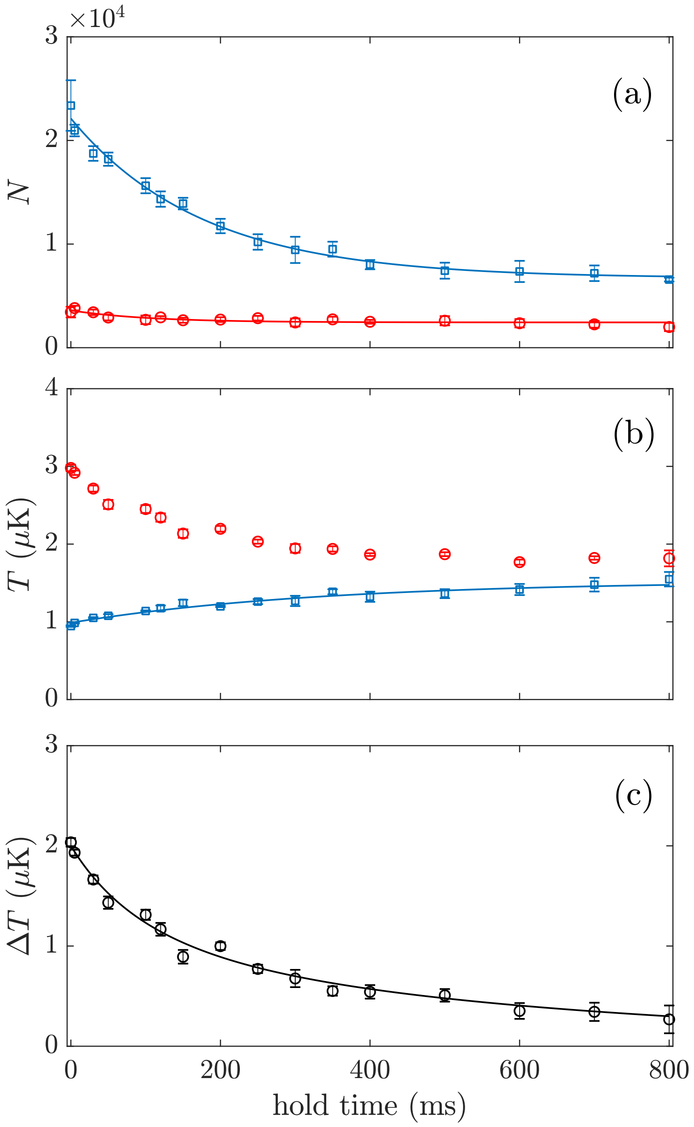

Figure 5.9: Example for cross-species thermalization ($B = 229.5\,\mathrm{G}$) and the fit analysis to extract a value for $|a|$. (a) Observed time evolution of the atom numbers N_{Dy} (blue open squares) and N_{K} (red open circles) together with fits by simple exponential functions with a constant offset. (b) Time evolution of the temperatures T_{Dy} and T_{K}; the increasing Dy temperature is again fitted by a simple heuristic model function. (c) Evolution of the temperature difference $\Delta T = T_{\mathrm{K}} - T_{\mathrm{Dy}}$ with a numerical fit based on Eq. (5.6).

The factor q depends on the ratio of polarizabilities, masses, and temperatures [26]. Under our experimental conditions, this factor can be well approximated by a constant $q = 1.45$.

A typical data set for the time evolution of the atom numbers N_{Dy}, N_{K} and the temperatures T_{Dy}, T_{K} is shown in Fig. 5.9(a) and 5.9(b). As a first step in the analysis, we independently fit the observed decay of N_{Dy}, the slow decrease of N_{K}, and the increase in T_{Dy} with simple exponential model functions, which we generally find to describe the data well. As a second step, we fit a numerical solution of Eq. (5.6) to the decreasing temperature difference ΔT, with the evolution of T_{Dy} and $N_{\mathrm{Dy}} + N_{\mathrm{K}}$ described by the fit functions obtained before. Figure 5.9(c) illustrates that the fit with the two free parameters σ_{el} and ΔT_0 matches the experimental data very well. For our specific example ($B = 229.5\,\mathrm{G}$, $\bar{\omega}_{\mathrm{Dy}}/2\pi = 180\mathrm{Hz}$), we obtain a best estimate for σ_{el} corresponding to $|a| = 87\,a_0$.

217-G resonance: Strength and universal range

For the experiments described in the main text, we are mainly interested in the interspecies scattering length near the pole of the 217-G resonance. Here, the scattering length can be well approximated by

$$a(B) = -\frac{A}{B - B_0}\,a_0\,, \tag{5.7}$$

where $B_0 = p_2 = 217.27(15)\,\mathrm{G}$ and $A = \delta_2\,a_{\mathrm{bg}}/a_0 = +1450(230)\,\mathrm{G}$.

For discussing the character of this Feshbach resonance in terms of entrance-channel or closed-channel dominated behavior [12], it is useful to introduce a characteristic length as defined by the range parameter [65]

$$R^* = \frac{\hbar^2}{2m_{\mathrm{r}}a_0\,\delta\mu\,A}\,. \tag{5.8}$$

Here $m_{\mathrm{r}} = 32.04\,\mathrm{a.m.u.}$ is the reduced mass and $\delta\mu$ the (unknown) differential magnetic moment. The universal range of a Feshbach resonance is reached if $|a| \gg R^*$, which also represents a necessary condition for a strong Pauli suppression of few-body losses [224].

The properties of the molecular states underlying our Feshbach resonances are currently unknown and require further in-depth investigation. For now, to get an idea of the universal range, we use a conservative guess for the differential magnetic moment $\delta\mu = 0.1\,\mu_{\mathrm{B}}$, where μ_{B} is Bohr's magneton. This yields $R^* \approx 300\,a_0$ as a conservative estimate for the range parameter. We thus conclude that the universality condition $|a| \gg R^*$ is rather easy to fulfill near the pole of our 217-G Feshbach resonance. We note that also the many-body condition $k_F R^* \ll 1$ for universality in a fermionic system (Fermi wave number k_F) is well fulfilled under realistic conditions.

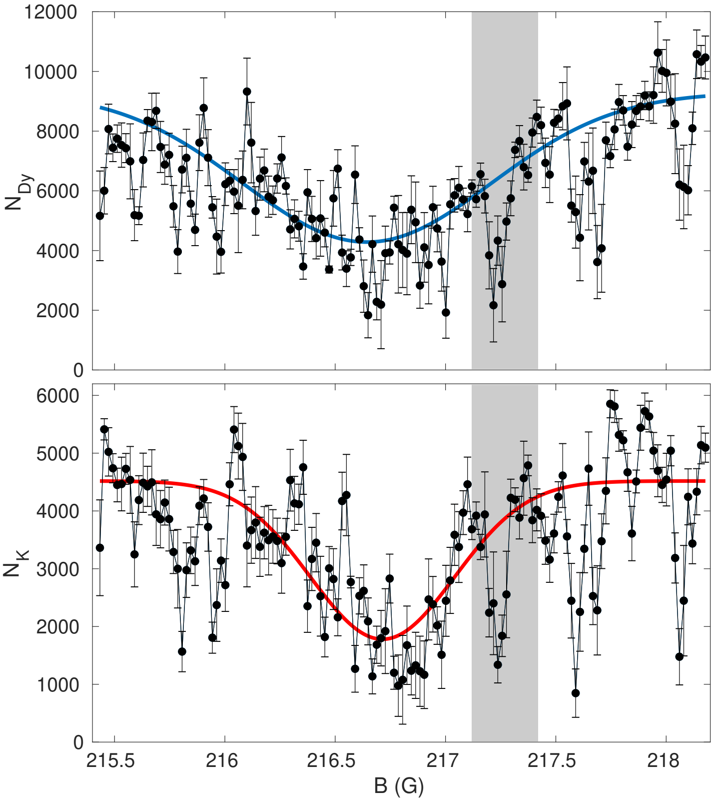

Figure 5.10: Loss scan in the resonance region. The plots show the number of Dy atoms (upper panel) and K atoms (lower panel) left in the trap ($\bar{\omega}_{\mathrm{Dy}} = 2\pi \times 130\,\mathrm{Hz}$) after a hold time of 150 ms at a fixed magnetic field. The initial atom numbers are $N_{\mathrm{Dy}} = 24\,000$ and $N_{\mathrm{K}} = 6000$, and the initial temperature is $T = 500\,\mathrm{nK}$. The solid lines are Gaussian fits to the broad loss feature, excluding narrow loss features. The shaded region indicates the 1σ-uncertainty in our knowledge of the pole position of the strong 217-G resonance.

5.7.2 Decay

Overview of losses in the resonance region

The loss scan in Fig. 5.10 presents an overview of the complex magnetic-field dependence of losses in the region of the 217-G resonance. Here the number of Dy and K atoms was recorded after a hold time of 150 ms in the trap at a constant magnetic field. Interspecies losses show up as correlated features in the loss spectra of both species.

A broad loss feature appears for both species about 0.5 G below the resonance center, where we estimate a scattering length of roughly $+3000\,a_0$. This feature resembles observations made in spin mixtures of ^{6}Li [222, 98, 255] and ^{40}K [254] and indicates the formation of weakly bound dimers, which after secondary collisions decay to deeply bound molecular states. The fact that such losses appear not at the center of the resonance, but on the side with large positive scattering length, is intrinsic to two-component fermion systems near broad Feshbach resonances with strong Pauli suppression of inelastic few-body processes.

The loss spectrum also reveals several narrow interspecies features. Some of them appear as resolved resonances, but other structures rather resemble a fluctuating background. In between features of increased losses, good regions can be identified where the lifetime exceeds 100 ms. Besides interspecies losses, we have observed intraspecies losses for Dy. This can be seen from the background atom number ($N_{\mathrm{Dy}} \approx 9500$) in Fig. 5.10, which is a factor of 2.5 below the initial atom number. These Dy losses generally show a fluctuating background behavior, as observed in [164].

From the timescale of losses (on the order of 100 ms), we conclude that recombination processes are no problem for experiments on short time scales (typically below 10 ms), such as the hydrodynamic expansion studied in the main text. For experiments on longer timescales, however, it may be important to choose good spots, where both intraspecies and Dy interspecies losses are minimized. The data of Fig. 5 in the main text were recorded on such a spot at 217.5 G.

Model for fitting decay curves

For extracting three-body rate coefficients from atom number decay curves, one has to take into account the heating of the sample [271]. Our simple model to avoid this complication is based on the initial behavior near $t = 0$, which can be characterized by the initial number $N_0 = N(t = 0)$ and the initial decay rate $1/\tau = -\dot{N}(0)/N(0)$. To extract optimum values for these parameters from a fit to the observed decay, we follow a heuristic approach based on the differential equation

$$\frac{\dot{N}}{N_0} = -\frac{1}{\tau}\left(\frac{N}{N_0}\right)^{\alpha} , \tag{5.9}$$

where the phenomenological exponent α is a fit parameter, which absorbs possible heating and other effects. We find that the solution

$$N(t) = \frac{N_0}{\sqrt[\alpha-1]{1 + (\alpha - 1)\, t/\tau}} \tag{5.10}$$

fits our loss curves for all single- and mixed-species cases very well and is thus applied to all cases discussed in the present work. The calculation of rate coefficients is then based on the values for the fit parameters N_0 and τ.

Decay of K in the mixture

Here we analyze losses of K observed in the Dy-K mixture in terms of three-body processes and extract upper limits for the corresponding rate coefficients. Three-body decay of K alone is known to be very weak and can be neglected here.

We first assume that losses are caused by processes involving one K and two Dy atoms. This leads to the loss equation

$$\dot{N}_{\mathrm{K}} = -K' \int d^3r \, n_{\mathrm{K}} n_{\mathrm{Dy}}^2 \,. \tag{5.11}$$

We approximate the number density distributions n_i ($i = $ K, Dy) in the harmonic trap (mean frequencies $\bar{\omega}_i$) by thermal Gaussian distributions with spatial widths $\sigma_i = \bar{\omega}_i^{-1}\sqrt{k_B T/m_i}$. After integration we obtain

$$\frac{\dot{N}_{\mathrm{K}}}{N_{\mathrm{K}}} = -K' \, N_{\mathrm{Dy}}^2 \left(\frac{\sigma'}{2\pi\sigma_{\mathrm{K}}\sigma_{\mathrm{Dy}}^2} \right)^3 , \tag{5.12}$$

where $\sigma' = (\sigma_{\mathrm{K}}^{-2} + 2\sigma_{\mathrm{Dy}}^{-2})^{-1/2}$.

In an analogous way, we now assume that losses are caused by processes involving two K atoms and one Dy atom (two K atoms lost per event). This leads to the loss equation

$$\dot{N}_{\mathrm{K}} = -2K'' \int d^3r \, n_{\mathrm{K}}^2 n_{\mathrm{Dy}} \,, \tag{5.13}$$

which after integration simplifies to

$$\frac{\dot{N}_{\mathrm{K}}}{N_{\mathrm{K}}} = -K'' \, N_{\mathrm{K}} N_{\mathrm{Dy}} \left(\frac{\sigma''}{2\pi\sigma_{\mathrm{K}}^2\sigma_{\mathrm{Dy}}} \right)^3 , \tag{5.14}$$

where $\sigma'' = (2\sigma_{\mathrm{K}}^{-2} + \sigma_{\mathrm{Dy}}^{-2})^{-1/2}$.

To obtain values (upper limits) for the event rate coefficients, we analyze the decay curves displayed in Fig. 5(a) in the main text. By using the above fit model, we extract values for the initial K decay time $\tau = -N_{\mathrm{K}}/\dot{N}_{\mathrm{K}} = 350(150)\,\mathrm{ms}$, the initial K atom number $N_{\mathrm{K}} = 3100(200)$, and the initial Dy atom number $N_{\mathrm{Dy}} = 16\,700(400)$. From Eqs. (5.12) and (5.14) and the experimental parameters ($\omega_{\mathrm{Dy}} = \omega_{\mathrm{K}}/3.6 = 2\pi \times 130\,\mathrm{Hz}$, $T = 540\,\mathrm{nK}$) we finally obtain

$$\begin{aligned} K' &\approx 4 \times 10^{-25}\,\mathrm{cm}^6/\mathrm{s} \\ K'' &\approx 3 \times 10^{-25}\,\mathrm{cm}^6/\mathrm{s} \end{aligned} \tag{5.15}$$

as upper limits for the interspecies three-body event rate coefficients.

Decay of Dy

Here we analyze the observed Dy decay (data shown in Fig. 5.5 of the main text) under the assumption that these losses are caused by collisions of three Dy atoms. The corresponding loss equation reads

$$\dot{N}_{\mathrm{Dy}} = -3K_3 \int d^3r \, n_{\mathrm{Dy}}^3 \,, \tag{5.16}$$

which after integration simplifies to

$$\frac{\dot{N}_{\mathrm{Dy}}}{N_{\mathrm{Dy}}} = -3K_3 \, N_{\mathrm{Dy}}^2 \left(\frac{1}{2\pi\sqrt{3}\,\sigma_{\mathrm{Dy}}^2} \right)^3 . \tag{5.17}$$

From the fit to the Dy decay shown in Fig. 5.5(a), we extract $\tau = 320(50)\,\mathrm{ms}$ and $N_{\mathrm{Dy}} = 16\,700(400)$ and obtain the value

$$K_3 = 3.4(5) \times 10^{-25}\,\mathrm{cm}^6/\mathrm{s}$$

for the event rate coefficient. Analyzing the data in Fig. 5.5(b) of the main text in the same way, with the fit yielding $\tau = 1000(150)\,\mathrm{ms}$ and $N_{\mathrm{Dy}} = 19\,700(400)$, we obtain the value

$$K_3 = 8.1(1.2) \times 10^{-26}\,\mathrm{cm}^6/\mathrm{s}\,.$$

The fact that he former value (with K present) is about four times larger cannot be explained by three-body loss events involving K atoms, as their contribution is too weak. However, our data show that K atoms somehow catalyze Dy losses. The underlying mechanism is currently not understood.

5.7.3 Interaction-induced contraction

Here we introduce a model that describes the contraction of the mixture induced by the resonant interaction in the unitarity limit under the assumption of zero temperature. The results point to a possible mechanism how the presence of K atoms can enhance three-body losses in the Dy component.

Theoretical model

We calculate the number density distributions $n_{\mathrm{Dy}}(r)$ and $n_{\mathrm{K}}(r)$ of the trapped interacting species in the Thomas-Fermi limit, in which kinetic energy terms related to density variations can be neglected and the local density approximation can be applied. This also allows us to reduce the situation to a spherical trap; the solutions can then be scaled to the real, anisotropic trap.

The functional for the total energy can be written as

$$E = \int d^3r \, (U_{\mathrm{Dy}} n_{\mathrm{Dy}} + U_{\mathrm{K}} n_{\mathrm{K}} + \epsilon_{\mathrm{Dy}} + \epsilon_{\mathrm{K}} + \epsilon_{\mathrm{int}}) \,, \tag{5.18}$$

where $U_{\mathrm{Dy}}(r) = \frac{1}{2} m_{\mathrm{Dy}} \bar{\omega}_{\mathrm{Dy}}^2 r^2$ represents the Dy trap potential and

$$\epsilon_{\mathrm{Dy}} = \frac{3}{10} (6\pi^2)^{2/3} \frac{\hbar^2}{m_{\mathrm{Dy}}} n_{\mathrm{Dy}}^{5/3} \tag{5.19}$$

denotes the kinetic energy density of Dy without interaction. For the K component, U_{K} and ϵ_{K} are defined analogously.

For the interaction energy density we use the approximation

$$\epsilon_{\mathrm{int}} = -b \times \frac{3}{10} (6\pi^2)^{2/3} \frac{\hbar^2}{2m_{\mathrm{r}}} \frac{n_{\mathrm{Dy}} n_{\mathrm{K}}}{(n_{\mathrm{Dy}}^2 + n_{\mathrm{K}}^2)^{1/6}} \,. \tag{5.20}$$

This expression was introduced in [199] to fit the equation of state of a non-superfluid mass-balanced system [272]. Remarkably, we noticed that the same expression also provides a very good fit to the equation of state for the imbalanced mixture with mass ratio 40/6, which was published in [185]. The only difference seems to be a slight difference in the optimum value of the prefactor b. While $b = 1.01$ provides an optimum fit for the mass-balanced case [199], we found the slightly higher value $b = 1.04$ for the mass-imbalanced (40/6) case. In the representation of Eq. (5.20), the interaction term seems to be nearly independent of the mass ratio. Therefore, we are confident that it can be readily applied also to our mass ratio of 161/40.

The number density distributions $n_{\mathrm{Dy}}(r)$ and $n_{\mathrm{K}}(r)$ are found by minimizing the energy functional. This is done by varying the densities with the gradient descent method under the constraint that the atom numbers N_{Dy} and N_{K} are fixed. We represent the densities on a spatial grid, of which the step size is below 10^{-3} of the typical Thomas-Fermi radius of the clouds. The number of iterations in the minimization algorithm guarantees a relative precision of 10^{-4} for number densities and derived quantities.

Density increase and loss enhancement

Figure 5.11 shows the effect of interaction for $N_{\mathrm{K}}/N_{\mathrm{Dy}} = 0.12$, which has been chosen to demonstrate that even a small fraction of K atoms can have a considerable effect. The interaction-induced contraction is clearly seen in profiles. The central Dy (K) density is increased by a factor of 1.64 (1.70). To quantify the total enhancement of three-body decay of Dy and K within the whole trap, we

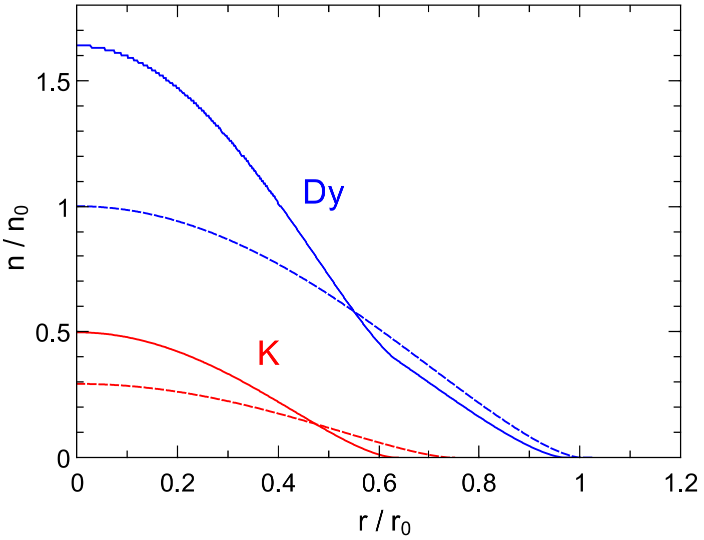

Figure 5.11: Radial density distributions for the Dy and K components, with (solid lines) and without (dashed lines) interaction for a number ratio $N_{\mathrm{K}}/N_{\mathrm{Dy}} = 0.12$. All profiles are normalized to the quantities r_0 and n_0, which represent the Thomas-Fermi radius and the central density of the non-interacting Dy component, respectively.

relate the total three-body decay rate to the case without interspecies interaction (Thomas-Fermi profile n_{TF}), and define the corresponding factors

$$\beta_i \equiv \frac{\int d^3r\, n_i^3(\mathbf{r})}{\int d^3r\, n_{\mathrm{TF},i}^3(\mathbf{r})}\,, \tag{5.21}$$

where $i = $ Dy, K. These factors can describe both the effect of attractive ($\beta > 1$) or repulsive ($\beta < 1$) interaction in the mixture, but here we focus on the case of the strong attraction on resonance. By numerical integration of the cubed density profiles of the two species we obtain $\beta_{\mathrm{Dy}} = 2.07$ and $\beta_{\mathrm{K}} = 2.85$. It is remarkable that the presence of a relatively small minority component of K can have such a large effect on the profile and thus three-body recombination rate of the majority component of Dy.

Within the assumptions of our model, the enhancement factor depends only on the atom number ratio $N_{\mathrm{K}}/N_{\mathrm{Dy}}$ and the trap frequency ratio $\bar{\omega}_{\mathrm{K}}/\bar{\omega}_{\mathrm{Dy}}$. Since, in our experiments, the latter is fixed to a value of 3.6, we can draw universal curves for β_{Dy} and β_{K} as a function of the global polarization $(N_{\mathrm{K}} - N_{\mathrm{Dy}})/(N_{\mathrm{K}} + N_{\mathrm{Dy}})$; see Fig. 5.12. The solid line that represents the Dy case shows a maximum value of about $\beta_{\mathrm{Dy}} = 4$ for a polarization of -0.7 ($N_{\mathrm{K}}/N_{\mathrm{Dy}} = 0.54$), which highlights the possible strength of the effect.

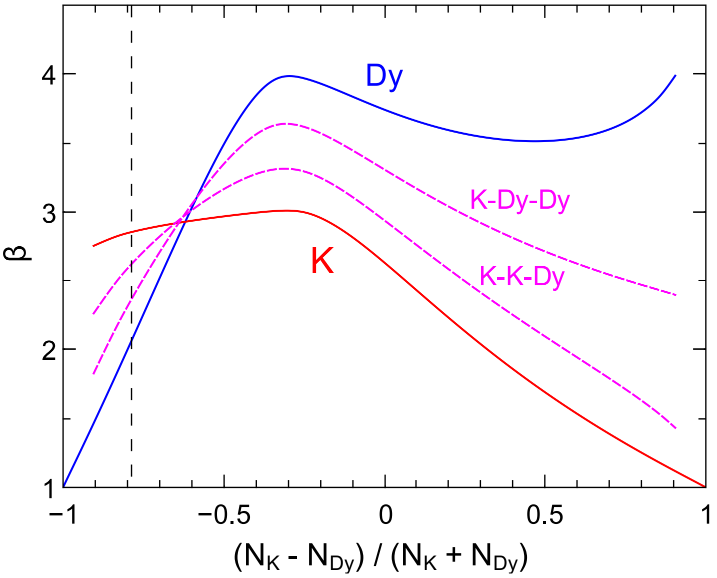

Figure 5.12: Enhancement factors for three-body recombination as a function of the global polarization. The solid curves refer to intraspecies three-body collisions of Dy and K, while the dashed curves refer to interspecies processes involving both atoms. The vertical dashed line corresponds to the situation shown in Fig. 5.11.

6

Low-field Feshbach resonances and three-body losses in a fermionic quantum gas of ^{161}Dy

Published as:
E. Soave, V. Corre, C. Ravensbergen, J. H. Han, M. Kreyer, E. Kirilov and R. Grimm
arXiv preprint: arxiv:2205.01943 (2022)

Author contribution: The author took a leading role in the process of acquiring and analyzing the data described in this publication as well as writing the manuscript.

We report on high-resolution Feshbach spectroscopy on a degenerate, spin-polarized Fermi gas of ^{161}Dy atoms, measuring three-body recombination losses at low magnetic field. For field strengths up to 1 G, we identify as much as 44 resonance features and observe plateaus of very low losses. For four selected typical resonances, we study the dependence of the three-body recombination rate coefficient on the magnetic resonance detuning and on the temperature. We observe a strong suppression of losses with decreasing temperature already for small detunings from resonance. The characterization of complex behavior of three-body losses of fermionic ^{161}Dy is important for future applications of this peculiar species in research on atomic quantum gases.

6.1 Introduction

Over the past decade, the exotic interactions of submerged-shell lanthanide atoms have tremendously boosted experimental research on ultracold quantum gases [273]. The exciting properties of such atoms result from long-range anisotropic interactions in combination with tunability of the contact interaction via magnetically controlled Feshbach resonances [12]. Prominent examples for novel states of matter created in the laboratory are quantum ferrofluids of Dy [138] and supersolids realized with both Dy and Er [140, 274, 141]. Progress has also been made with quantum-gas mixtures of different lanthanide atoms (Dy-Er) [135, 275] and mixtures of lanthanide and alkali-metal atoms (Dy-K) [26, 27], with a wide potential for future experiments on exotic states of quantum matter.

For interaction control, magnetic lanthanide atoms offer a rich spectrum of Feshbach resonances [127, 126, 164, 276], much denser as compared to alkali-metal atoms. This experimentally well-established fact is a consequence of anisotropy stemming both from the strong magnetic dipole-dipole interaction and from the van-der-Waals interaction for electronic ground states with non-zero orbital angular momentum [246, 68]. The anisotropic interaction leads to a strong mixing of different partial waves. If hyperfine structure is present, such as for the fermionic isotopes ^{161}Dy and ^{167}Er, the Feshbach spectrum is even more complex, and the blessing of tunability may turn into a curse of omnipresent three-body recombination losses.

The experiments performed with ^{161}Dy in our laboratory are motivated by the prospect to realize novel superfluid states in mass-imbalanced fermion mixtures [199, 24, 25]. In a Fermi-Fermi mixture of ^{161}Dy and ^{40}K atoms, we have recently demonstrated hydrodynamic behavior as a manifestation of strong interactions, realized on top of an interspecies Feshbach resonance [27]. Further experiments are in progress on the formation of bosonic Feshbach molecules, paired fermionic many-body states, and collective behavior of the strongly interacting mixture. In all these experiments, the Dy-Dy intraspecies Feshbach resonances and accompanying three-body losses represent a complication and appropriate strategies have to be developed to minimize unwanted effects.

Feshbach resonances in spin-polarized fermionic quantum gases result from scattering in odd partial waves. Accordingly, p-wave resonances have been observed in early experimental work [87, 86, 277] and studied theoretically [73, 70]. More recent experiments [72, 278] have provided deeper insights into the scaling laws and universal properties of three-body recombination losses near p-wave resonances. Our present situation of ^{161}Dy, however, is more complex because of the strong coupling between different partial waves and the possible interaction between different closely spaced or overlapping resonances, which makes a theoretical description very challenging. Experiments are needed to find out in how far our resonances in ^{161}Dy behave in a similar way.

In this article, we report on the experimental investigation of the ultradense Feshbach spectrum of ^{161}Dy at low magnetic field strength (up to about 1 G) with high resolution ($\sim$1 mG). To minimize the effect of finite collision energies, i.e. broadening effects and the influence of higher partial waves, we work in the deeply quantum-degenerate regime at rather low values of the Fermi energy down to a few 100 nK. In Sec. 6.2, we present the Feshbach loss spectrum, exhibiting nearly 50 loss features in a 1 G wide range. We also identify plateaus of very low losses, which can be used for efficient evaporative cooling. In Sec. 6.3, we then present case studies on four typical resonances, where we report on the dependence of the three-body rate coefficient on the magnetic detuning and the temperature of the sample. Our measurements show that even very small detunings from resonance of a few mG are sufficient to enter a regime where losses are strongly suppressed with decreasing temperature.

6.2 Low-field Feshbach Spectrum

6.2.1 Sample preparation

All our experiments begin with the production of a degenerate Fermi gas of ^{161}Dy atoms. We follow the procedures described in detail in Ref. [26]: After capturing the atoms in a magneto-optical trap (MOT) operated at the 626-nm intercombination line [176], the sample is transferred into a crossed-beam optical dipole trap (ODT), which uses near-infrared light at a wavelength of 1064 nm. Here forced evaporative cooling is performed by ramping down the trapping potential. Under optimized conditions, we obtain a sample of up to $N = 1.5 \times 10^5$ atoms in a nearly harmonic trap (geometrically averaged trap frequency $\bar{\omega} = 2\pi \times 150\,\mathrm{Hz}$) at a temperature of $T = 80\,\mathrm{nK}$. With a Fermi temperature of $T_F = \hbar\bar{\omega}(6N)^{1/3}/k_B =$

695 nK, this corresponds to deeply degenerate conditions with $T/T_F = 0.12$ and a peak number density of $\hat{n} = 1.6 \times 10^{14}\,\mathrm{cm}^{-3}$ in the center of the trap. Our sets of measurements are taken over typically many hours (sometimes even a few days), where long-term drifts may reduce the maximum atom number provided by roughly a factor of two. In a last preparation stage, the ODT is modified by replacing one of the laser beams (horizontally propagating) with a beam of larger waist. This modification provides us with more flexibility to vary the trap frequency $\bar{\omega}$ and, in particular, it allows us to realize very shallow traps to work at lower atomic number densities. For each experiment, the trap is chosen in a way to avoid residual evaporation. The particular conditions for each set of measurements are listed in App. 6.5.1.

The cloud is fully spin polarized in the lowest hyperfine Zeeman sub-level $|F, m_F\rangle = |21/2, -21/2\rangle$ as a result of optical pumping during the MOT stage [163] and subsequent rapid dipolar relaxation of residual population in higher spin states in the ODT [60]. For the fully spin-polarized sample, inelastic two-body losses are suppressed already at very low magnetic field values. The minimization of three-body losses, essential for efficient evaporative cooling, depends very sensitively on the particular magnetic field applied. Our evaporation sequence is performed at a magnetic bias field of 230 mG, which we found to work slightly better than at 430 mG, as applied in Ref. [26].

6.2.2 Loss Scan

We study the low-field Feshbach spectrum by measuring atom losses for a variable magnetic field strength [12] in the range between 0 and 1 G. After preparation of the sample in a very shallow ODT (for experimental parameters see App. 6.5.1), we ramp the magnetic field from the evaporation field to the variable target one in 20 ms. The low trap frequency of $\bar{\omega} = 2\pi \times 100\,\mathrm{Hz}$ is chosen to minimize losses induced by the magnetic field ramp. We hold the cloud for 7 s, and then release it from the ODT. An absorption image is taken after a time of flight of 10 ms.

The magnetic-field stability is essential for resolving narrow loss features. Using radio-frequency spectroscopy[1] we identified a 50-Hz ripple in the ambient magnetic field as the main source of noise, with a peak-to-peak value of 1.7 mG. Other noise sources, such as noise in the current of our coils, stay well below an estimated rms level of 1 mG.

In Fig. 6.1 we plot the remaining atom number as a function of the magnetic field. We count $\simeq 44$ loss features, which we assign to Feshbach resonances. On

---

[1] We investigate the magnetic-field stability by performing radio-frequency spectroscopy on ^{40}K. The possibility to work with potassium in the same setup follows from the fact that our apparatus is designed for mixture experiments [26, 27].

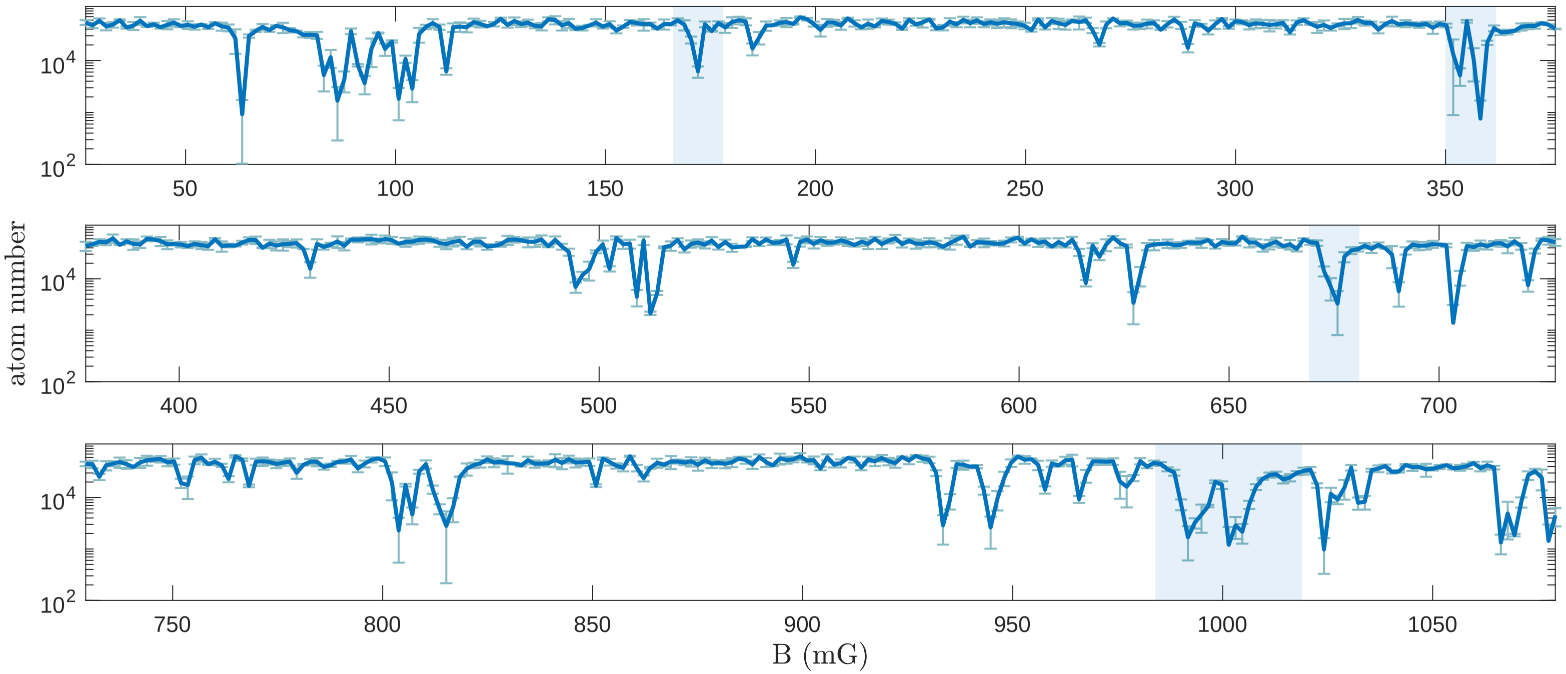

Figure 6.1: Low-field Feshbach spectrum of a degenerate sample of spin-polarized ^{161}Dy. The magnetic field is varied in steps of 1.6 mG. The error bars show the sample standard deviation of three individual measurements at the same magnetic field. We observe about 44 loss features, which we attribute to Feshbach resonances. The shaded areas correspond to the four resonances that are investigated in detail in Sec. 6.3.

.

resonance the three-body recombination rate is greatly enhanced and leads to more than a factor of 10 reduction in atom number. At these positions we also observe substantial heating (not shown). The resonances seem to mostly gather in groups, with flat, typically tens of mG wide, plateaus between them. Within these plateaus, losses are rather weak and stay within a few percent even for the long hold time of 7 s applied.

The recorded Feshbach spectrum resembles previous observations in submerged-shell lanthanide atoms (Er [127, 276], Dy [126, 164], Tm [279]), which are known to exhibit a dense and very complex resonance spectrum. In the cases of the fermionic isotopes ^{161}Dy and ^{167}Er, where hyperfine structure is present, the resonance density is extremely high. While for ^{167}Er a density of about 25 resonances per gauss has been reported in the range between 0 and 4.5 G [127], previous work on ^{161}Dy has revealed between about 10 resonances per gauss in a range between 0 and 6 G [126] and up to about 100 resonances in a 250-mG wide range near 34 G [164]. With our 44 resonances in a range between 0 and 1 G, we apparently resolve more resonances than in Ref. [126], which we attribute to our higher magnetic field resolution. We believe that a further improved magnetic field stability to well below 2 mG would reveal even more resonances and a substructure of some of our observed features. The complex spectrum of resonances may be further analyzed using statistical methods [276, 279], which is beyond the scope of the present work.

6.3 Case Studies of Selected Resonances

We now perform a systematic investigation of the K_3 coefficient as a function of the magnetic-field and the temperature for selected resonances. In Sec. 6.3.1 we first show how, from atom number decay measurements, we obtain the value of the three-body recombination coefficient K_3. In Secs. 6.3.2 and 6.3.3 we investigate the dependence of K_3 on the magnetic field and the initial temperature, respectively.

6.3.1 Three-body decay curves and loss-rate coefficients

In the absence of two-body losses, the evolution of the number of trapped atoms $N(t)$ can be modeled based on the differential equation

$$\dot{N}(t) = -\Gamma_v N(t) - 3K_3 \int d^3r\, n^3(\mathbf{r}, t), \tag{6.1}$$

where Γ_v is the one-body loss rate from collisions with rest-gas particles, and $n(\mathbf{r}, t)$ represents the number density distribution of the cloud. The quantity K_3 denotes the three-body event rate coefficient, which for a single atomic species is related to the commonly used three-body loss rate coefficient by $L_3 = 3K_3$. Note that, according to our phenomenological definition, the K_3 coefficient represents a thermal average over the distribution of collision energies in the sample, and does not represent the coefficient for a specific collision energy as used in theoretical work [71]. For our experiments we estimate a rest-gas limited lifetime as long as $1/\Gamma_v \simeq 60\,\mathrm{s}$. Given such a low one-body loss rate, Γ_v can be neglected in the analysis of near-resonance decay curves, while it is relevant for cases on the long-lived plateaus.

In Fig. 6.2 we show three typical decay curves, on resonance (a), near a resonance (b) and far away from any resonance (c). The sample is held in the ODT at a fixed magnetic field. After a variable hold time the cloud is released and the number of remaining atoms is measured by time-of-flight imaging. To analyse the decay curves and to extract values for K_3, we apply a heuristic model (for details see App. 6.5.2) to quantify the initial slope $\dot{N}(0)$. From the initial decay rate $1/\tau = -\dot{N}(0)/N(0)$ and knowledge of the experimental parameters at $t = 0$, we then calculate the resulting values for K_3. This approach, which focuses on the initial decay, avoids complications by the heating of the sample during the decay. Depending on the experimental conditions under consideration, decay times can vary from a few ms to many seconds. As an example, the measurement reported in Fig. 6.2(a) was carried out under typical experimental conditions (see App. 6.5.1) very close to the center of the 679-mG resonance, with initially about 1.2×10^5 atoms. Our fit yields an initial decay time $\tau = 22(6)\,\mathrm{ms}$, and for the three-body rate coefficient we obtain $K_3 = 4(1) \times 10^{-26}\,\mathrm{cm}^6/\mathrm{s}$. The same measurement, performed few mG detuned from the resonance at 995 mG and reported in Fig. 6.2(b), already shows a significant longer decay time ($\tau = 0.50(9)\,\mathrm{s}$). We calculate a three-body recombination coefficient value $K_3 = 7(2) \times 10^{-28}\,\mathrm{cm}^6/\mathrm{s}$, two orders of magnitude lower than on resonance.

The measurement in Fig. 6.2(c) is carried out at a magnetic field of 225 mG, on a minimum-loss plateau, and reveals a very long lifetime. To observe the effect of three-body losses we worked in tightly compressed trap with $\bar{\omega} = 2\pi \times 380\,\mathrm{Hz}$, leading to a peak-density of $\hat{n}_0 \approx 6 \times 10^{14}\,\mathrm{cm}^{-3}$, which is exceptionally high for a degenerate Fermi gas. We measure an initial decay time $\tau = 12(3)\,\mathrm{s}$, from which a value $K_3 = 5(3) \times 10^{-32}\,\mathrm{cm}^6/\mathrm{s}$ is obtained. This value is extraordinary low, which is highlighted by comparison with ^{87}Rb as a widely used bosonic species, where the K_3 coefficient has been measured to be $\sim 6 \times 10^{-30}\,\mathrm{cm}^6/\mathrm{s}$ [280, 281]. Such an extremely weak three-body decay, together with the sizeable elastic scattering cross section from dipolar collisions [128], explains why Fermi gases of submerged-shell lanthanide atoms facilitate highly efficient evaporative cooling [61, 26].

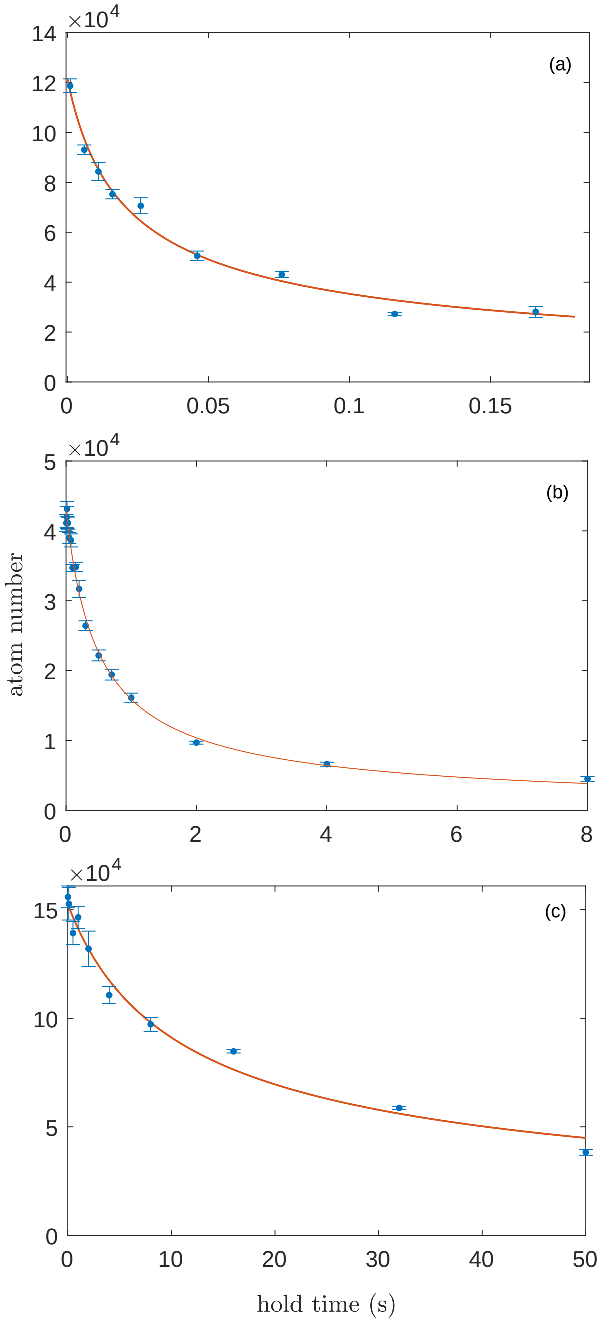

Figure 6.2: Typical decay curves. The measurements have been performed (a) on resonance at $B = 678\,\mathrm{mG}$, (b) for small detuning at $B = 989\,\mathrm{mG}$, and (c) on a minimum-loss plateau at $B = 225\,\mathrm{mG}$. The solid lines show fits by the heuristic model introduced in App. 6.5.2.

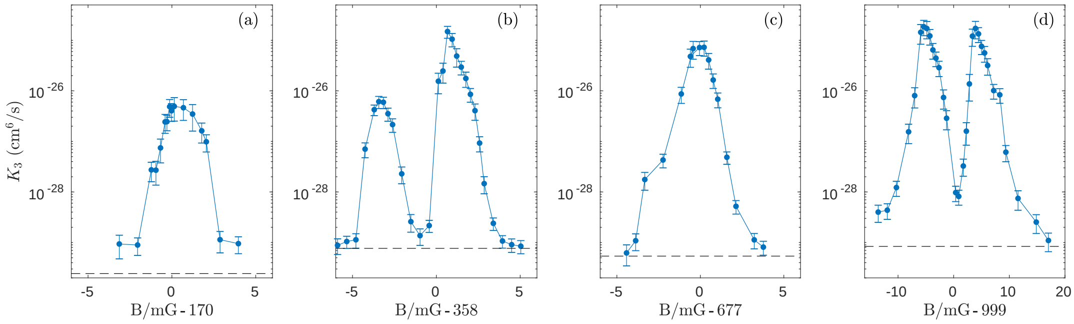

Figure 6.3: K_3 coefficient as a function of the magnetic-field, measured for the four selected resonances. Note that in (a)-(c) the full range covers 12 mG, whereas in (d) it is three times wider. Each data point is obtained from an individual decay curve as discussed in Sec. 6.3.1. The dashed lines indicate the lower limit to the measurable K_3 value, imposed by one-body losses.

6.3.2 Dependence on magnetic-field detuning

In this Section, we discuss selected loss features as typical examples for the many resonances observed in our Feshbach spectrum. We focus on three resonant features that lead to relatively strong losses in the measured Feshbach spectrum (near 358 mG, 677 mG and 999 mG, see loss scan in Fig. 6.1). For reference, we also investigate a weaker loss resonance (near 170 mG), which appears to be well isolated from other resonances. We consider their line shapes and widths by presenting measurements on the K_3 values as a function of the magnetic detuning from resonance. Here we work in the deeply degenerate regime, with $T/T_F \simeq 0.2$ at a low $T_F \simeq 400\,\mathrm{nK}$ (for details see App. 6.5.1), which minimizes line broadening stemming from the finite kinetic energy [276, 282]. Our results are displayed in Fig. 6.3(a-d). The measured values for K_3 vary over more than four orders of magnitude. Maximum values are found to exceed $10^{-25}\,\mathrm{cm}^6/\mathrm{s}$. The presence of weak one-body losses (see Sec. 6.3.1) imposes a lower limit for the measurable K_3 value, which is in the range of a few $10^{-30}\,\mathrm{cm}^6/\mathrm{s}$. This lower limit is indicated by the dashed horizontal lines in Fig. 6.3.

Figure 6.3(a) shows the resonance near 170 mG, which is the weakest of the four selected features. We observe a full width of about 3.5 mG [2]. The line shape is essentially symmetric, which may first appear surprising in view of the expected asymmetric line shapes of Feshbach resonances in higher partial waves, which usually show a sharp edge on the lower side (marking the resonance position)

---

[2] We define the width as the full magnetic field range where the K_3 value exceeds the geometric average between its maximum and minimum. This corresponds to the full width at half maximum on a logarithmic scale.

along with a tail on the upper side [282, 283, 284, 285]. We assume that the shape of the weak feature is dominated by the magnetic-field fluctuations in our experimental setup (see Sec. 6.2.2), which may affect the observed loss features in a range of a few mG. The fluctuations will smear out any narrower feature and mask the true resonance line shape (see discussion on broadening effects in App. 6.5.3). This interpretation is supported by the fact that we never observe any narrower feature. We therefore believe that the observed behavior of narrower resonances, such as the 170-mG feature, is dominated by magnetic-field fluctuations.

In Fig. 6.3(b) we show a double feature of two resonances, separated by about 4 mG. While the weaker feature near 355 mG closely resembles the one in Fig. 2(a), the stronger feature near 359 mG shows a peak value for K_3 exceeding $10^{-25}\,\mathrm{cm}^6/\mathrm{s}$, which is an order of magnitude higher. The stronger feature also shows indications of the tail expected on the upper side for such resonances. The resonance appears to be wide enough that its true structure is not fully masked by the magnetic-field fluctuations. Figure 6.3(c) shows a feature near 677 mG, which in the Feshbach scan in Fig. 6.1, appeared to be a single, relatively strong resonance. A closer investigation, however, reveals a shoulder on the lower side, which is likely to be caused by another weak overlapping resonance. On the upper side, the K_3 coefficient falls off in a way resembling the expected tail. Figure 6.3(d) finally displays our strongest observed loss feature; note the three times wider magnetic-field range. We see a double feature separated by about 10 mG. The line shapes of the two resonances correspond to the expectation of a sharper edge on the lower side and a tail on the upper side. Here, at least for these broader features, magnetic-field fluctuations do not have a substantial effect on the line shape.

6.3.3 Temperature dependence

We now turn our attention to the dependence of the K_3 coefficient on the temperature of the cloud, for different magnetic detunings from the resonance center. We vary the temperature of the cloud by interrupting the evaporation sequence in a controlled way and by adiabatically varying the final trap frequency. For these measurements, decay is observed in a 160-Hz and a 400-Hz trap, for lower and higher temperatures, respectively. The K_3 coefficient is obtained according to Eq.(6.5) or Eq.(6.4), depending on the initial T/T_F of the sample. We introduce the effective temperature $\tilde{T}$, such that the mean energy per particle is $3k_B\tilde{T}$. This definition takes into account that, for a degenerate Fermi gas, the relative momentum and thus the collision energy stay finite even at $T = 0$. In the limit of a thermal gas, $\tilde{T} = T$, while for a degenerate one we have $\tilde{T} = T\,\mathrm{Li}_4(-\zeta)/\mathrm{Li}_3(-\zeta)$ [52], where ζ is the fugacity and Li_i is the polylogarithm of order i.

Figure 6.4 reports the behavior of the K_3 value as a function of $\tilde{T}$ for three different magnetic detunings relative to the ceter of the 358-mG resonance.

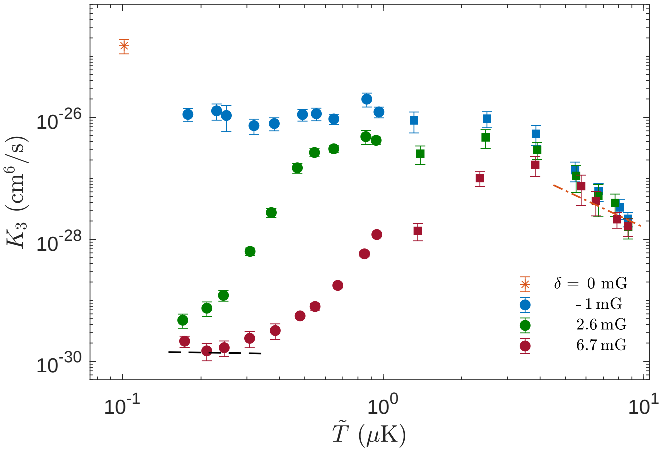

Figure 6.4: Temperature dependence of K_3, for various detunings (typical uncertainty 0.2 mG) relative to the center of the 358-mG resonance. For $\tilde{T} \lesssim 1\,\mu$K the samples have initial $T/T_F < 1$. The decay curves have been measured in a $\bar{\omega}/2\pi$ =160-Hz (circles) and 400-Hz trap (squares). As a reference, we plot the K_3 resonant peak value, corresponding to the maximum in Fig. 6.3(b). The dot-dashed line shown for $T > 5\,\mu$K indicates the T^{-2} dependence, according to Eq. (6.2), with $\zeta = 0.022$. The dashed line indicates the lower limit to the measurable K_3 value, imposed by one-body losses.

We first discuss the K_3 behavior in the high energy regime ($\tilde{T} \gtrsim 3\,\mu$K). Here the three curves decrease in a similar manner, showing no dependence on the magnetic field. Such a behavior reflects the unitarity limit for the K_3 coefficient, which was predicted and observed in several resonantly interacting systems, fermionic and bosonic ones (e.g. [286, 287, 247, 288, 72]). A non-degenerate atomic system enters the unitarity-limited regime when the thermal de Broglie wavelength $\lambda_{\mathrm{dB}} = \hbar\sqrt{2\pi/(mk_BT)}$ becomes comparable to a characteristic length associated with the resonance at a given magnetic detuning [3]. We attribute to the competition between those two length scales the fact that the larger the detuning, the higher is the temperature at which the K_3 value enters the unitary regime. In this regime the K_3 value is expected to scale as T^{-2} [73]:

$$K_3 = \zeta \frac{12\sqrt{3}\pi^2\hbar^5}{m^3(k_BT)^2}. \tag{6.2}$$

The prefactor ζ relates to the efficiency of three colliding atoms forming a dimer

---

[3] The length scale that characterizes the interaction is the scattering length a for an s-wave resonance and by $\sqrt{|V_p|k_{\mathrm{eff}}}$ in the case of p-wave Feshbach resonances. Here V_p and k_{eff} are the scattering volume and the effective range, respectively.

and a free atom, and is believed to be a non-universal (i.e. species-dependent) quantity. A fit to our data, considering only the points with $\tilde{T} > 5\,\mu$K, yields a value $\zeta = 0.022(2)$. In Ref. [278] the authors extracted a value $\zeta = 0.09$ for ^{6}Li. Those two results are about an order of magnitude below what has been observed for Bose gases, where values of $\zeta = 0.9$, 0.3, and 0.24 have been derived for ^{7}Li [286], ^{39}K [287], and ^{164}Dy [247], respectively.

We now discuss the temperature-dependence of K_3 far below the unitarity-limited regime. Figure 6.4 demonstrates that even a very small magnetic resonance detuning of a few mG can have a dramatic effect on the low-temperature behavior. The data taken at $\delta = 6.7\,$mG (typical uncertainty 0.2 mG) show a reduction of K_3 from a maximum value of the order of $10^{-27}\,\mathrm{cm}^6/\mathrm{s}$ at $\tilde{T} = 3.5\,\mu$K to a minimum of about $10^{-30}\,\mathrm{cm}^6/\mathrm{s}$ at $\tilde{T} \lesssim 200\,$nK. Note that the minimum value that we can observe is limited by one-body decay (dashed line), so that the true suppression will be even larger. A very similar behavior is observed closer to resonance at $\delta = 2.6\,$mG. Here a maximum K_3 value of $\sim 5 \times 10^{-27}\,\mathrm{cm}^6/\mathrm{s}$ is found at $\tilde{T}$ of the order of $1\,\mu$K, which is reduced by three orders of magnitude at our lowest temperature $\tilde{T} \approx 200\,$nK. The main effect of the smaller detuning appears to be a shift of the qualitatively similar behavior to lower temperatures.

These observations on the low-temperature behavior can be compared with recent experimental work studying three-body recombination on p-wave Feshbach resonances in ^{6}Li [72, 278]. For the limit of very low collision energies E_{coll}, a threshold law $K_3 \propto E_{\mathrm{coll}}^2$, as originally predicted in Ref. [73], has been observed in Ref. [72] for a thermal ($T/T_F > 1$) Fermi gas, where $K_3 \propto T^2$. This observation of threshold-law behavior required a relatively large resonance detuning. In our case, with rather small detunings, the threshold-law regime would require extremely low collision energies. This regime, however, remains inaccessible in our present experiments because of two limitations: The Fermi energy gives a lower limit to the collision energy ($\tilde{T} = T_F/4$ at $T = 0$), and one-body losses do not allow us to measure K_3 values below $\sim 10^{-30}\,\mathrm{cm}^6/\mathrm{s}$. However, beyond the threshold-law regime, we observe the same steep increase with temperature as seen in Ref. [72] for relatively large magnetic detunings. The breakdown of the threshold law has been interpreted [72] in terms of the effective range of the resonance.

The case very close to resonance (data points for $\delta = -1\,$mG in Fig. 6.4) reveals a different behavior. Here we do not observe any loss suppression with decreasing temperature. The K_3 value appears to level off at about $10^{-26}\,\mathrm{cm}^6/\mathrm{s}$. This, however, does not rule out the possibility of loss suppression at values of $\tilde{T}$ that are even lower than what we can realize experimentally in the deeply degenerate situation. The single data point shown for $\delta = 0$ at $\tilde{T} \approx 75\,$nK corresponds to the loss maximum in Fig. 6.3(b). This measurement highlights that three-body losses can be very strong on top of the resonance, suggesting no suppression at low temperatures. A similar on-resonance behavior has been observed in Refs. [278, 86], but in contrast to our work these experiments were limited to the non-degenerate case.

In the narrow detuning range of $|\delta| \lesssim 1\,\mathrm{mG}$, the interpretation of our present results is impeded by the sensitivity of the experiments to magnetic field noise (see Sec. 6.2.2 and App. 6.5.3). The on-resonance behavior of three-body recombination at ultralow collision energies, which has also been subject to recent theoretical investigations [289], thus remains a topic for future research.

6.4 Conclusion

In summary, we have carried out Feshbach spectroscopy on an optically trapped spin-polarized degenerate Fermi gas of ^{161}Dy atoms by measuring three-body recombination losses. We have focused on the range of low magnetic fields up to 1 G, scanned with a high resolution on the order of 1 mG. The ultradense loss spectrum revealed a stunning complexity with 44 resolved loss features, some of them showing up in groups and other ones appearing as isolated individual features. We also observed low-loss plateaus, which are typically a few 10 mG wide and which are free of resonances. Here very low three-body losses facilitate highly efficient evaporative cooling.

We have studied selected resonance features in more detail by measuring the three-body recombination rate coefficient K_3 upon variation of the magnetic resonance detuning and the temperature. In general, the observed behavior shows strong similarities with recent observations on p-wave Feshbach resonances [72, 278]. At higher temperatures (above a few μK) we observed the unitarity limitation of resonant three-body losses. At low temperatures in the nanokelvin range, we observed a strong suppression of losses with decreasing temperature, provided a small detuning of just a few mG is applied. Right on top of the resonance, however, three-body losses remain very strong even at the lowest temperatures we can realize.

Our work shows that in experiments employing fermionic ^{161}Dy gases special attention must be payed to choosing and controlling the magnetic field in a way to avoid detrimental effects of three-body recombination losses. For our specific applications targeting at strongly interacting fermion mixtures of ^{161}Dy and ^{40}K [27], those magnetic-field regions are of particular interest where one can combine near-resonant interspecies Dy-K interaction with low-loss regions of Dy.

Acknowledgments

We acknowledge support by the Austrian Science Fund (FWF) within Projects No. P32153-N36 and P34104-N, and within the Doktoratskolleg ALM (W1259-N27). We further acknowledge a Marie Sklodowska Curie fellowship awarded to J.H.H. by the European Union (project SIMIS, Grant Agreement No. 894429). We thank the members of the ultracold atom groups in Innsbruck for many stimulating discussions and for sharing technological know how.

6.5 Supplemental Material

6.5.1 Summary of the initial experimental conditions

In Table 6.1, we report the experimental conditions under which the measurements reported in Figs. 6.1, 6.2, 6.3 and 6.5 have been carried out. For the measurement in Fig. 6.4, where the value of K_3 as a function of the $\tilde{T}$ is reported, the different temperatures have been achieved by interrupting the evaporation in a controlled way. This unavoidably has led to initial experimental conditions which vary over a wide range. The initial atom number ranges from 5×10^4 to 1×10^6. The coldest samples have $T/T_F \simeq 0.18$ and peak densities $\hat{n} \simeq\ 1 \times 10^{14}\,\mathrm{cm}^{-3}$.

6.5.2 Extraction of the loss-rate coefficient

Here we summarize our method to extract values for the three-body rate coefficient K_3 from the decay curves. Basically the same procedures have been applied in Ref. [27].

The particles that are more likely to collide and leave the trap are the ones in the center of the trap, with highest density and lowest potential energy. Therefore losses are accompanied by heating of the cloud, which is known as antievaporation heating in the thermal case [290] or hole heating in the case of a degenerate Fermi gas [291]. As a consequence the shape of the density distribution $n(\mathbf{r}, t)$ changes with time. Taking a time-dependent temperature $T(t)$ into account, Eq. (6.1) leads to a set of coupled differential equations (see for instance [290]). We circumvent this complication by focusing on the initial decay rate $1/\tau = -\dot{N}(0)/N(0)$, where $N(0)$ and $\dot{N}(0)$ represent the atomic number and its time derivative, respectively, both at $t = 0$. For the initial decay and thus the decay time τ only the initial number density distribution $n_0(\mathbf{r}) = n(\mathbf{r}, t = 0)$ is relevant.

Neglecting one-body losses and considering only the initial part of the decay, Eq.(6.1) leads to

$$K_3 = -\frac{N(0)}{3\tau}\left(\int d^3r\, n_0^3(\mathbf{r})\right)^{-1}. \tag{6.3}$$

For the limit of a thermal (Gaussian) distribution [290], the integration results in

$$K_3 = \sqrt{3}\frac{T_0^3}{\tau N_0^2}\left(\frac{2\pi k_B}{m\bar{\omega}^2}\right)^3 . \tag{6.4}$$

Here $\hbar$ is the reduced Planck constant, k_B is the Boltzmann constant, m is the atomic mass, and T_0 is the initial temperature of the sample. For the number density distribution of a degenerate Fermi gas, we find

$$K_3 = \frac{3\pi^4}{4}\frac{1}{\tau N_0}\left(\frac{\hbar}{m\bar{\omega}}\right)^3 \frac{1}{\beta(T_0/T_F)}. \tag{6.5}$$

The function $\beta(T/T_F)$ is defined as the three-body integral of a finite-temperature Fermi gas normalized to the zero-temperature case:

$$\beta(T/T_F) = \frac{\int d^3\mathbf{r}\, n^3(\mathbf{r})}{\int d^3\mathbf{r}\, n_{\mathrm{TF}}^3(\mathbf{r})}, \tag{6.6}$$

where $n(\mathbf{r})$ describes the density profiles of non-interacting fermion systems at finite temperature, and $n_{\mathrm{TF}}(\mathbf{r})$ refers to the Thomas-Fermi profile at $T = 0$. By numerical integration, we find that the function can be well approximated numerically for $x = T/T_F \lesssim 1$ by $\beta\,(x) \simeq (1 + 12.75x^2 + 31.05x^4 - 8.46x^6)^{-1}$.

In order to obtain the initial decay rate, we fit the decay curve with

$$N(t) = \frac{N_0}{\sqrt[\alpha-1]{1 + (\alpha - 1)t/\tau}}, \tag{6.7}$$

which is the solution of the differential equation $\dot{N}/N_0 = -\tau^{-1}\,(N/N_0)^\alpha$ for decay by few-body process of order α. This heuristic model allows us to access the initial time decay τ without making an assumption on the true order of the loss process. The fit parameter α absorbs the order n of the recombination process together with effects from heating. The initial atom number N_0 is also derived from the fit, whereas the initial temperature T_0 is measured separately. The value of K_3 is finally obtained from Eq. (6.4) or Eq. (6.5).

6.5.3 Broadening Effects

When dealing with a Feshbach spectrum dense of narrow resonances, it is important to understand and possibly eliminate potential broadening effects. In our system, we identify two sources of broadening: magnetic levitation and magnetic field noise. In experiments where a decrease of the trapping frequencies leads to a trapping potential not deep enough to hold atoms against gravity, magnetic field

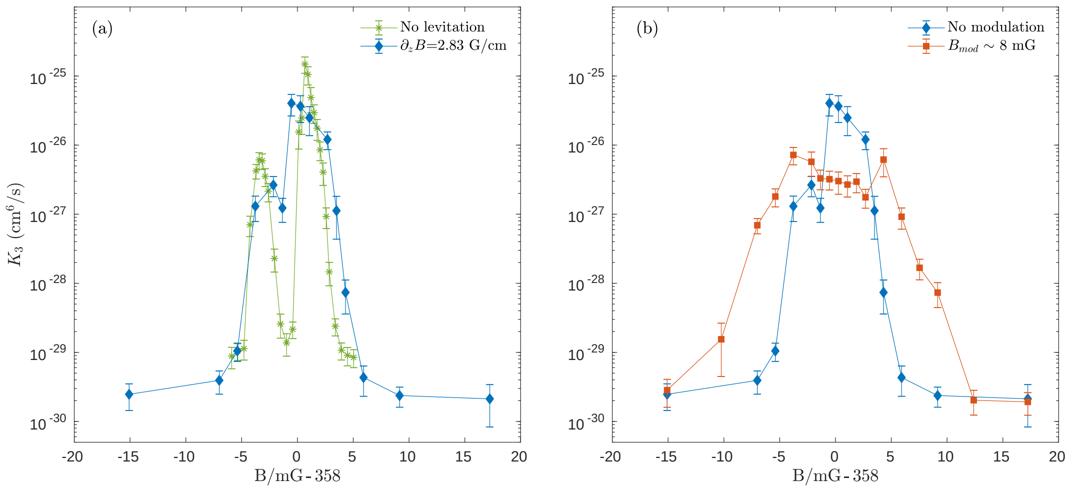

Figure 6.5: Effect of magnetic field broadening. The K_3 value is plotted versus the magnetic field, in the region around 358 mG. (a) Effect of the magnetic field gradient used for levitating Dy. (b) Effect of a sinusoidal magnetic field modulation, with a frequency of 600 Hz and an peak-to-peak amplitude of 8 mG.

levitation is often used to cancel (or reduce) the gravitational sag [242]. However, the presence of a magnetic field gradient introduces an inhomogeneity of the magnetic field along the vertical extent of the cloud. Assuming full levitation for dysprosium ($\partial_z B = 2.83\,\mathrm{G/cm}$) and a typical Thomas-Fermi radius $\sim$10 μm, our atomic sample is subjected to a magnetic-field variation of $\sim$6 mG over the trap volume. In Fig. 6.5(a) we demonstrate the effect of levitation broadening on the K_3 coefficient. We work at the 358-mG resonance. If no gradient is applied we can resolve a double-peak structure. The two features have a full width of about 2 mG, with peak values of $6(3) \times 10^{-27}$ and $1.5(4) \times 10^{-25}$ cm^6/s, respectively. The presence of the magnetic field gradient reduces the resolution and the two peaks almost merge into a single feature 7.7-mG wide. We can still distinguish two local maxima, whose values are reduced with respect to the no-levitation case. In view of this broadening effect, we decided to carry out all measurements reported in the main text without magnetic levitation. To achieve low enough trap frequencies in the shallow trap where the atoms are transferred at the end of the evaporation, we employ the second ODT stage with an increased waist of the horizontal trapping beam, as mentioned in Sec. 6.2.1. Such a trap geometry allows us to reach low trapping frequencies without too much sacrificing the trap depth.

In another set of measurements, we investigate the effect of magnetic field fluctuations. We artificially introduce noise into the system by adding a sinusoidal magnetic field modulation to the bias field. We chose a modulation frequency of 600 Hz, i.e. faster than the trap frequencies, but still slow enough to avoid technical complications. We then measure decay curves for different modulation strengths and magnetic field detunings. In Fig. 6.5(b) we report the obtained K_3 values versus magnetic field detunings for 10-mG peak to peak modulation. As a reference, we plot the K_3 profile measured in the absence of artificial noise. The modulation results in a broadening of the feature and consequent loss of field resolution. The peak value decreases and the curve flattens off.

Regardless of the source of broadening, a magnetic-field inhomogeneity (in time and space) has an averaging effect on the K_3 coefficient, and leads to a broadening and weakening of the narrow loss features characterizing the dysprosium Feshbach spectrum.

Table 6.1: Experimental parameters for the different sets of measurements: geometrically averaged trap frequency $\bar{\omega}$, atom number N, temperature T, Fermi temperature T_F, reduced temperature T/T_F, the function $\beta(x)$ according to Eq. (6.6), and the peak density $\hat{n}$. All quantities represent the initial values after preparation (at $t = 0$).

Figure	$\bar{\omega}/2\pi$(Hz)	N	T (nK)	T_F (nK)	T/T_F	$\beta(T/T_F)$	$\hat{n}$ (cm^{-3})
Fig. 6.1	100	5×10^4	70	320	0.21	0.616	4.8×10^{13}
Fig. 6.2(a)	58	$1.22(4) \times 10^5$	29(3)	250	0.12	0.84	3.1×10^{13}
Fig. 6.2(b)	120	$4.3(1) \times 10^4$	83(3)	367	0.23	0.59	5.7×10^{13}
Fig. 6.2(c)	380	$1.53(3) \times 10^5$	358(8)	1.77×10^3	0.20	0.63	6×10^{14}
Fig. 6.3(a)	88	$\simeq 1.2 \times 10^5$	64	379	0.17	0.72	6×10^{13}
Fig. 6.3(b)	118	$\simeq 4 \times 10^4$	77	352	0.22	0.59	5×10^{13}
Fig. 6.3(c)	118	4 - 6×10^4	77 - 88	352 - 403	0.22	0.59	5 - 6×10^{13}
Fig. 6.3(d)	118	$\simeq 5 \times 10^4$	106	379	0.28	0.46	5.2×10^{13}
Fig. 6.5(a) green stars	118	$\simeq 4 \times 10^4$	77	352	0.22	0.59	5×10^{13}
Fig. 6.5(a,b) blue diamonds	157	4.5 - 6×10^4	86 - 126	487 - 536	0.16 - 0.26	0.50 - 0.74	0.78 - 1×10^{14}
Fig. 6.5(b) red squares	157	4 - 5.5×10^4	88 - 187	468 - 520	0.17 - 0.4	0.26 - 0.71	0.6 - 1×10^{14}

7

Outlook

Roma non fuit una die condite

In this chapter, I will discuss the near-future plans of the DyK experiment. Superfluidity and exotic phases of matter remain our long-term goal. In order to get there one has to proceed step by step, introducing new tools (e.g., new trapping potentials), understanding each single bit of the system, while technically improving the machine.

Thanks to a continuous series of improvements achieved over almost two years, by the end of 2020 we were able to approach quite closely the experimental conditions (in terms of temperature and population imbalance) at which resonant superfluidity is expected to appear. A thorough analysis of the phase diagram for a Fermi-Fermi mixture featuring mass and population imbalance has been pursued in [25]. This work is of particular relevance for us: The authors directly treat the case of the Dy-K mixture, providing us with important quantitative benchmarks for the normal to superfluid phase transition in the unitary limit, for different condition of temperature and population imbalance. Within a t-matrix approach, they performed calculations assuming both a homogeneous system and a harmonically trapped one. Population imbalance is accounted via the polarization p, defined as $p = (n_H - n_L)/(n_H + n_L)$, n_H and n_L being the densities of the heavy and light component, respectively. In the homogeneous case, the critical temperature has a maximum for a majority of light particles ($p < 0$). Such a maximum increases with the mass ratio $r_m = m_L/m_H$ and moves toward $p = 0$, until the mass-balanced case is recovered. Limiting the discussion to the Dy-K case, the maximal critical temperature (in units of $T_F^{(Dy)}$) is found for a polarization $p_{max} = -0.166$. For

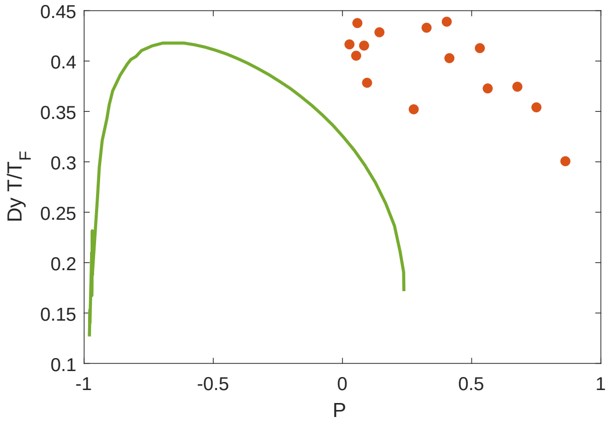

Figure 7.1: Red points: Dysprosium T/T_F as a function of the global polarization. A positive polarization P means a majority of Dy. Green line: critical temperature T_c in units of Dy T_F, as calculated in [25].

negative polarization, the critical temperature monotonically decreases. A similar trend is calculated for positive polarization. Here in addition a reentrance is expected to appear. This is associated with phase separation and the developing of the FFLO phase. These results qualitatively agree with those obtained by a mean-field approach[1] [23, 24]. For the non-homogeneous case, the authors limit the discussion to the physical conditions for which superfluidity occurs at the center of the trap. They calculate the T-P phase diagram (P being the global polarization $P = (N_H - N_L)/(N_H + N_L)$) for different trap-frequency ratio r_ω. The appearance of superfluidity is favored by the experimental conditions which promote a local density polarization $p(0) \simeq -0.1$, for which pairing is enhanced (in agreement with the findings for the homogeneous case). In Fig. 7.1, we located our results in the $P - T$ phase diagram on resonance, and compare them with the theoretical prediction for T_c from [25]. It is clear, from that comparison, that temperature-wise a lot has to be done in order to reach the superfluid regime. Still, superfluidity seems to be more easily in reach if we change our trapping strategy. Indeed Strinati and coworkers show that an increased trap frequency ratio enlarges the area in the $P - T$ phase diagram where superfluidity is expected to occur. In particular, increasing r_ω leads to an increased maximum of the critical temperature, and shifts it towards positive global polarization. So far, a majority of dysprosium is the "natural" condition for our system. 1064-nm light is used to confine the mixture, providing a trap-frequency ratio $r_\omega \simeq 3.6$ [232]. An increased value of r_ω can be obtained by means of a bichromatic trap: adding an additional beam,

---

[1] Quantitatively, the t-matrix approach gives a lower value for the critical temperature.

close detuned to a potassium line, will help to approach a trapping-frequency ratio suitable to see superfluidity.

An ongoing project is aiming to set up a box potential, which would allow us to investigate the phase diagram of the Dy-K mixture in the homogeneous case. We plan to use a DMD to produce a flat trap potential: further technical details are still unclear, and require a deeper analysis [292].

From the technical point of view, a lot of effort is put on improving the magnetic field stability in the high-field region. We recently bought a new power supply and gain an order of magnitude in B-field stability. We observed a five-fold improvement of the width of the radio-frequency absorption spectrum of K, measured around 50 G. The improved stability of the magnetic field allows for a better resolution of the Feshbach features. As a test bench, we studied the mixture behaviour around an interspecies Feshbach resonance at $\simeq 50.3\,\mathrm{G}$ whose width is $\simeq 50\,\mathrm{mG}$. We produced Dy-K Feshbach molecules by sweeping the magnetic field from the BCS to the BEC side of the resonance, and observe them in time of flight upon Stern Gerlach separation. So far, the maximum transfer efficiency is around 20%: we are confident that an improvement of the preparation protocol will lead to a higher efficiency. Such an improved magnetic field stability should lead to a better resolution of the narrow Feshbach features also in the 200 G region. In particular, we aim at the identification of low-Dy-loss plateau, i.e., B-field regions where the losses of dysprosium are almost suppressed, similarly to what observed in 6.2.2. On one side, this should go along with a better lifetime (and less heating) of the mixture[2], while on the other side could provide us with sweet spots where a second stage forced evaporation can be performed.

In Ch. 5 we provided a careful characterization of the strong DyK Feshbach resonance in the 217 G region.A direct measurement of the binding energy of the molecules as a function of the scattering length would provide valuable information on the nature of the Feshbach resonance. The plan is to perform magnetic field modulation spectroscopy [293], employing a fast coil located around the bottom viewport of the vacuum chamber. Preliminary measurements (see App. B) lead to a lower limit for the differential magnetic moment of $\delta\mu > 0.3\mu_\mathrm{B}$ (corresponding to an upper limit for the effective range $R^* < 150a_0$). The improved magnetic field stability should provide a more accurate measurement of the binding energy, and thus allow for a precise determination of the differential magnetic moment and the range parameter.

The relatively high temperature of the sample and the complicated Feshbach structure of the mixture will then be the only two remaining obstacles for the production

---

[2] The cloud is subjected to an effective field resulting from the time-averaged magnetic field fluctuations. The vicinity of narrow Feshbach resonances has thus the effect of increasing inelastic collision rates even in regions where losses or heating should be ideally suppressed.

of a DyK molecular BEC.
The hydrodynamic expansion is the main signature of resonant interspecies interactions. In order to get a deeper insight into the dynamic behaviour of our system around the resonance pole, we want to look at center of mass oscillations. An advantage of working with an heteronuclear mixture is the different dynamic polarizability of the two species. In the non-interacting limit, the two components oscillate around the trap center with their own trap frequency and their motion can be described as two decoupled harmonic oscillators. The presence of interactions introduce a friction term in the equation, proportional to the relative velocity of the two components. The system can thus be modeled as two coupled oscillators, the coupling strength being related to the strength of the interactions. On resonance we expect the two component to oscillate in phase at the same frequency. In the superfluid regime, this frequency is expected to be $\omega_l^2 = (m_{Dy}\omega_{Dy}^2 + m_K\omega_K^2)/(m_{Dy} + m_K)$ [294].

Appendix A

Useful Constants and Physics Relations

In this appendix are reported some of the physical constants, quantities and relations which have been used the most during my PhD work.

Quantity	Symbol	Value
Speed of light	c	$299\,792\,458\,\mathrm{m\,s^{-1}}$
Planck constant	h	$6.626\,070\,15 \times 10^{-34}\,\mathrm{J\,s}$
Reduced Planck constant $\left(\frac{h}{2\pi}\right)$	$\hbar$	$1.054\,571\,817... \times 10^{-34}\,\mathrm{J\,s}$
Boltzmann constant	k_B	$1.380\,649 \times 10^{-23}\,\mathrm{J\,K^{-1}}$
Bohr radius	a_0	$5.291\,772\,109\,03(80) \times 10^{-11}\,\mathrm{m}$
Bohr magneton	μ_B	$9.274\,010\,078\,3(28) \times 10^{-24}\,\mathrm{J\,T^{-1}}$
Atomic mass constant	u	$1.660\,539\,066\,60(50) \times 10^{-27}\,\mathrm{kg}$

Table A: Some of the main physical constants relevant to this thesis work.

Quantity	Value
$1\,\mathrm{G}$	$1\times10^{-4}\,\mathrm{T}$
μ_B/h	$1.399\,624\,493\,6(4)\,\mathrm{MHz\,G^{-1}}$
k_B/h	$2.083\,661\,912\,3\times10^{1}\,\mathrm{Hz\,nK^{-1}}$

Table B: Some relations among constants relevant to this thesis work.

Quantity	Symbol	Formula
Thermal de Broglie wavelength $^{(a)}$	λ_{dB}	$\sqrt{\frac{2\pi\hbar^2}{mk_BT}}$
Phase-space Density $^{(b)}$	PSD	$n\lambda_{DB}^3$
Scattering length around isolated FB resonance$^{(c)}$	a	$a_{bg}\left(1-\frac{B_{zc}-B_0}{B-B_0}\right)$
Feshbach molecule binding energy in the universal regime $^{(d)}$	E_B	$\frac{\hbar^2}{2m_ra^2}$

Table C: Some physics relations used throughout this thesis work. (a) m is the mass, T is the temperature. (b) n is the density. (c) a_{bg} is the background scattering length, B_{zc} and B_0 are respectively the Feshbach resonance's zero crossing and pole positions. (d) m_r is the reduced mass.

Quantity	Symbol	Formula
Radial trap frequency $^{(a)}$	ω_r	$\sqrt{\frac{16a_0^3}{c}\frac{P}{w^4}\frac{\tilde{\alpha}(\omega_L)}{m}}$
Mean trap frequency	$\bar{\omega}$	$(\omega_x\omega_y\omega_z)^{1/3}$
Harmonic oscillator length	a^i_{ho}	$\sqrt{\frac{\hbar}{m\omega_i}}$
Cloud width (Gaussian distribution)	σ_i	$\sqrt{\frac{k_BT}{m\omega_i^2}}$
Peak density (Gaussian distribution)$^{(b)}$	n_0^{cl}	$\frac{N}{(2\pi)^{3/2}\prod\sigma_i}$
Fermi energy (trapped gas)	E_F	$\hbar\bar{\omega}(6N)^{1/3}$
Fermi radius	$R_F^{(i)}$	$\sqrt{\frac{2E_F}{m\omega_i^2}}$
Peak density (Fermi-Dirac distribution)	n_0^F	$\frac{8}{\pi^2}\frac{N}{\prod R_F^i}$

Table D: Some of the main physical relations related to an harmonically trapped gas. (a) A single Gaussian beam with waist w and power P is assumed; $\tilde{\alpha}(\omega_L)$ is the dynamic polarizability at frequency ω_L in atomic units. (d) N is the number of particles.

Symbol	Mass number A	Atomic mass	Natural abundance	Electronic structure	Nuclear spin I	stretched ground state $\lvert f; m_f\rangle$
${}^{40}_{19}\mathrm{K}$	40	$m_K \simeq$ $6.636 \times 10^{-26}\,\mathrm{kg}$	0.011 %	$[\mathrm{Ar}]4\mathrm{s}^1$	4	$\left\lvert \frac{9}{2}; -\frac{9}{2}\right\rangle$
${}^{161}_{66}\mathrm{Dy}$	161	$m_{Dy} \simeq$ $2.6723 \times 10^{-25}\,\mathrm{kg}$	18.88 %	$[\mathrm{Xe}]4\mathrm{f}^{10}6\mathrm{s}^2$	5/2	$\left\lvert \frac{21}{2}; -\frac{21}{2}\right\rangle$

Table E: Properties of ${}^{40}_{19}\mathrm{K}$ and ${}^{161}_{66}\mathrm{Dy}$.

Wavelength (nm) λ	Lifetime (s) τ	Natural linewidth (Hz) $\Gamma/2\pi$	Doppler temperature (μK) T_D	Saturation intensity (mW/cm^2) I_{sat}
770.107 919 192(123)	2.672×10^{-8}	5.96×10^{6}	145	1.70
766.700 674 872(173)	2.637×10^{-8}	6.04×10^{6}	145	1.75

Table F: Transition lines of ^{40}K relevant to this thesis.[295]

Wavelength (nm) λ	Lifetime (s) τ	Natural linewidth (Hz) $\Gamma/2\pi$	Doppler temperature (K) T_D	Saturation intensity (mW/cm^2) I_{sat}
421.172	$4.9(1) \times 10^{-9}$	$3.21(8) \times 10^{7}$	$7.7(2) \times 10^{-6}$	$5.6(1) \times 10^{1}$
625.909	$1.15(6) \times 10^{-6}$	$1.38(7) \times 10^{5}$	$3.3(2) \times 10^{-6}$	$7.4(4) \times 10^{-2}$
740.965	$8.94(9) \times 10^{-5}$	$1.78(2) \times 10^{3}$	$4.27(4) \times 10^{-8}$	$5.72(6) \times 10^{-4}$

Table G: Transition lines of ^{161}Dy relevant to this thesis. Values are taken or calculated from [296, 297, 154].

Appendix B

Additional measurements

I report here additional measurements that have been performed during my PhD work, and which may be of interest for the DyK experiments in the future.

B.1 Feshbach Scans for ^{161}Dy in Various Magnetic Field Regions

In Figs. B.1, B.2 and B.3 we report the ^{161}Dy Feshbach scans for various magnetic field regions. The atoms are in the ultracold regime, and polarized in the lowest Zeeman substate. After producing a degenerate sample of Dy, the magnetic field is ramped in 10 ms to the target field, where the atoms are held for a variable hold time, in presence of magnetic levitation. We release the cloud from the trap and let it expand at the field. Eventually the remaining number of atoms is recorded. As expected, we observe an enormous number of loss features, which we attribute to the presence of Feshbach resonances. We suspect that lots of the features are actually the combination of more narrower Feshbach resonances, whose width is below our resolution power. As suggested in [276], such an ultra-dense spectrum suggests that the the system may be in the Ericson regime, where the mean resonance width exceeds the mean spacing of the resonances [164, 298].

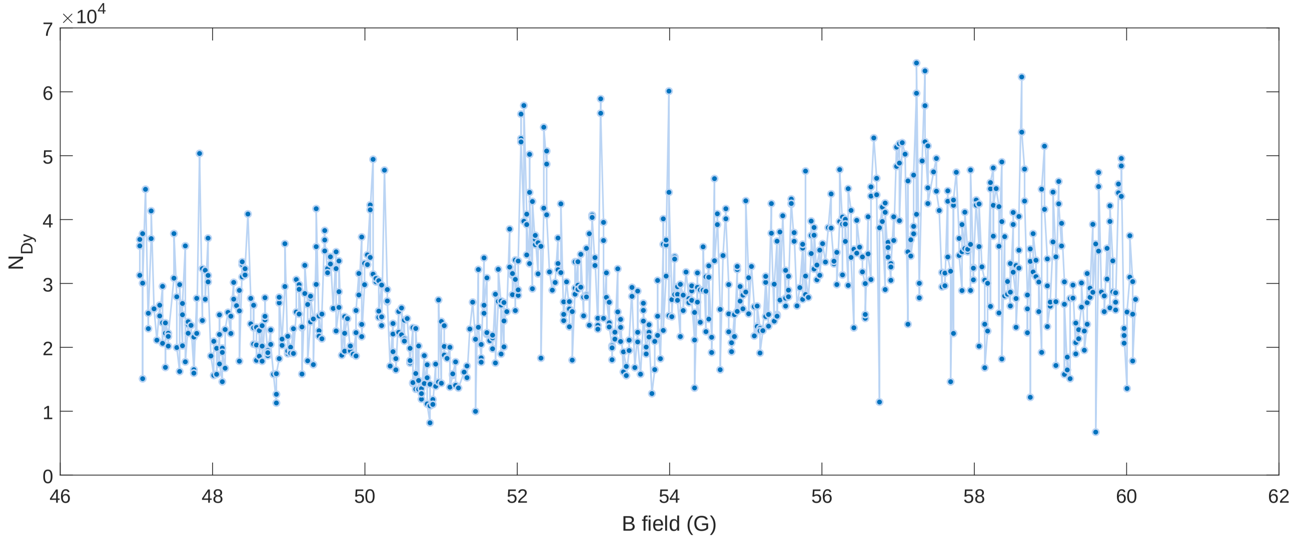

Figure B.1: Feshbach scan for the magnetic field region relevant to the investigation of the DyK mixture in the 50 G region. The atoms are held for 500 ms in a $\bar{\omega} = 2\pi \times 85\,\mathrm{Hz}$ trap.

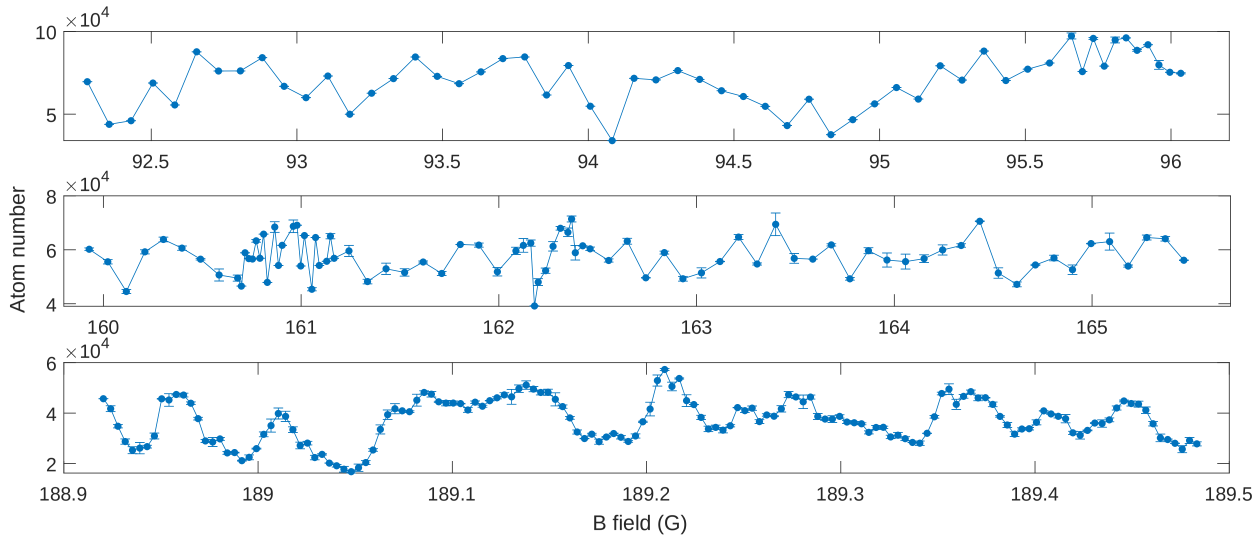

Figure B.2: Feshbach scans for selected magnetic field regions. The atoms are held in a $\bar{\omega} = 2\pi \times 45\,\mathrm{Hz}$ trap for 400 ms (panel (a) and (b)) and for 2 s (panel (c)).

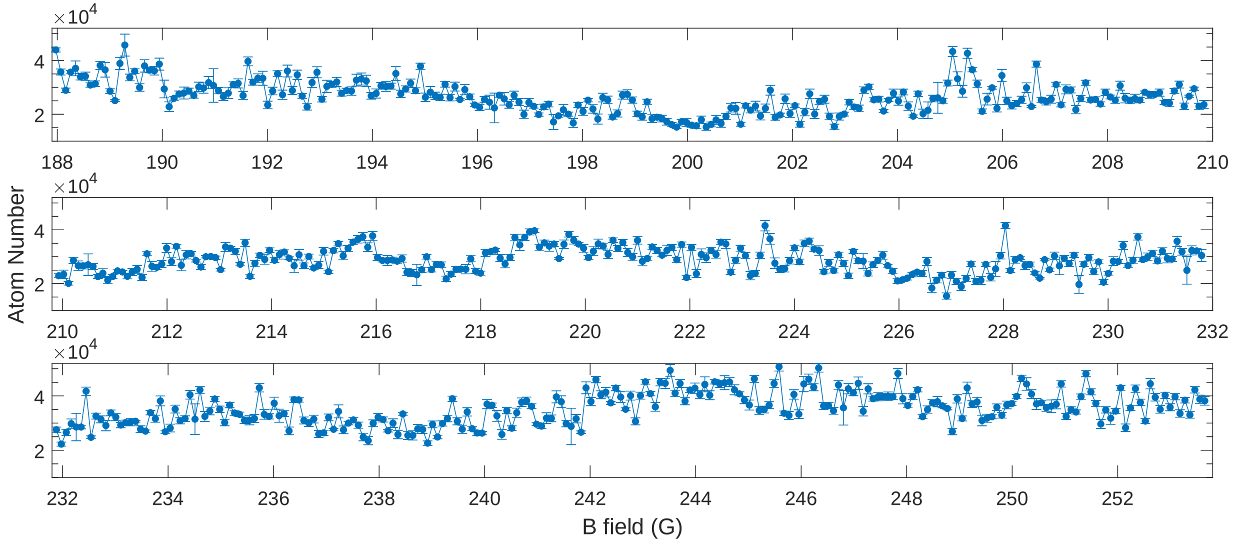

Figure B.3: Feshbach scan for the magnetic field region relevant to the investigation of the DyK mixture in the resonantly interacting regime. The pole of the interspecies resonance of interest is located around 217 G. The atoms are held for 600 ms in a $\bar{\omega} = 2\pi \times 128\,\mathrm{Hz}$ trap.

B.2 Binding energy of DyK molecules at the 217-G resonance

In Fig. B.4 we report a preliminary measurement of the binding energy of DyK molecules at the 217-G resonance. After a preparation phase at 204 G, the B-field is ramp to the target field. Here we associate the molecules by a sinusoidal modulation of the magnetic field around the bias field [293, 263]. The magnetic field is modulated by means of a coil located around the bottom viewport. The modulation has an amplitude of 500 to 700 mG, and is kept on for a duration between 300 and 700 ms. When the modulation frequency is close to the molecular binding energy we observe losses. The strength of the loss signal is quite variable (we lose from 50 to 10% of the atoms), and sometimes it is only visible for one of the two species. We can only measure the binding energy in a magnetic field range of about 1 G.

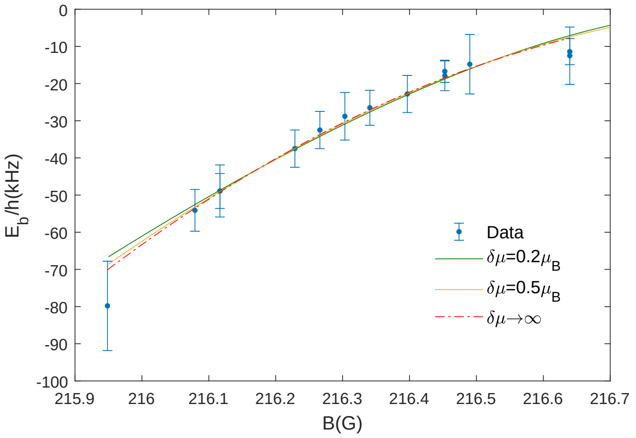

Figure B.4: Binding energy of the 217-G Feshbach molecules measured via wiggling spectroscopy (blue points). The lines are fit to the data using Eq. B.1, for different values of $\delta\mu$.

To fit our results we use the relation [263]

$$E_b = -\frac{(\delta\mu A)^2 m_r}{2\hbar^2}\left(\sqrt{1 - 2\frac{\hbar^2}{m_r\delta\mu A^2}(B - B_0)} - 1\right), \tag{B.1}$$

where m_r, A and B_0 are the reduced mass, the strength parameter and the resonance center, respectively. The effective range R^* relates to A and to the differential magnetic moment $\delta\mu$:

$$R^* = \frac{\hbar^2}{2m_r\delta\mu A}. \tag{B.2}$$

We first fit the data considering the limit $\delta\mu \to \infty$. Eq.(B.1) reduces to $E_b = -\hbar^2/(2m_r)(B - B_0)^2/(a_0 A)^2$. From the fit we obtain $B_0 = 216.98(3)\,\mathrm{G}$ (in agreement with our findings in [27]) and $A = 930(40)\,\mathrm{G}$ (2.2 standard deviations away from what reported in [27]). We then fit again the data using a fixed finite value for $\delta\mu$. We repeat this procedure for different values of the differential magnetic moment, and observe a significant deviation from the data for $\delta\mu < 0.3\mu_B$. This allows us to set a lower bound to the differential magnetic moment $\delta\mu > 0.3\mu_B$, which gives an upper bound for the range parameter $R^* < 150a_0$. Even though a more accurate quantitative analysis will require additional investigation, this measurement confirms that the interspecies Feshbach resonance at 217 G is a strong resonance.

B.3 Interspecies Feshbach resonance at 53 G

In this section we report on a preliminary investigation of the Feshbach properties of the mixture in the 53 G region. Reaching this magnetic-field region implies crossing less Feshbach features, resulting in less loss and heating. Given the presence of a broad Feshbach feature, we considered a deeper investigation worthy. We proceed similarly to what is reported in 5.

Figure B.5 shows a thermalization scan over the B-field region between 50 and 58 G. The sample is brought to degeneracy at low field, and then undergoes 100 ms of species-selective parametric heating. The temperature of potassium is increased by amplitude modulation of the optical dipole trap. Given the different dynamic polarizability, the dysprosium temperature is left unaffected. The cloud is then transferred into the high field region and is held at the target field for 35 ms, in a $\bar{\omega} = 2\pi \times 114\,\mathrm{Hz}$ trap. We perform a 1-ms ramp to a field $B_{imag} = 56\,\mathrm{G}$, where the DyK interactions are weak. We wait 3 ms and then release the cloud for imaging. We identify a main feature around 53 G, at the center of which fast thermalization between Dy and K happens, causing the potassium temperature to decrease. Unfortunately, this main feature is embedded by several narrow resonances which makes difficult a manipulation of the mixture in this region.

In order to identify the resonantly interacting region, we observe the expansion dynamics of the mixture, in the presence of interactions. After a preparation stage at 56 G, the magnetic field is rapidly (in 0.5 ms) decreased to the target value. The mixture is held there for 5 ms, released from the trap and let expand in free fall. In correspondence of the resonance center we observe a shrinking of the potassium cloud (see Fig. B.6), which we attribute to the hydrodynamic expansion of the sample, in line with the observations made in our previous work [27].

In Fig. B.7 the hydrodynamic expansion in the presence of strong interactions is probed differently. The experimental sequence is identical as for the previous

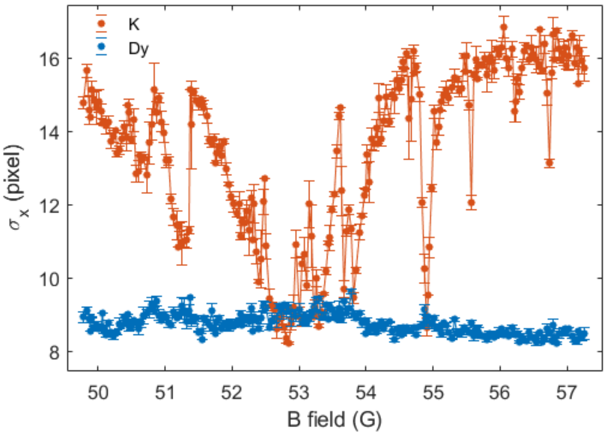

Figure B.5: Thermalization scan revealing interspecies Feshbach resonances through an enhancement of the elastic scattering. The temperature of the two cloud components are reported in terms of the cloud extension after time of flight.

measurement, except for the expansion phase. For this set of measurements, the cloud is let expand in presence of a magnetic field gradient. Given the different magnetic moments and masses, the sum of the magnetic force and the gravitational one points downwards (i.e., parallel to the gravitational acceleration g) for K and upwards (i.e., antiparallel to g) for Dy. The effect of the strong interactions appears as an upwards shift of the K cloud: indeed, potassium is dragged by dysprosium and its fall is slowed down. In correspondence of narrow resonances or for intermediate interaction strength, the almost-hydrodynamic expansion results in a tail (pointing upward) for the potassium cloud.

Despite the high density of narrow features surrounding the resonance pole, we could find good spots where the mixture is long-lived. In Fig. B.8 (top) we report the loss scan in the region around the resonance pole: the hydrodynamic expansion scan is plotted again (bottom), as a reference. The mixture is held for 150 ms in a $\bar{\omega} = 2\pi \times 30\,\text{Hz}$ trap. The overall decrease in atom number that we observe in potassium is a measurement artefact. We measure the lifetime of the mixture for some magnetic field values around the pole (see table in Fig. B.8). In the low-loss plateau the measured lifetimes are of few hundreds of milliseconds. In contrast, where the losses are more pronounced, the lifetime is as short as few tens of milliseconds.

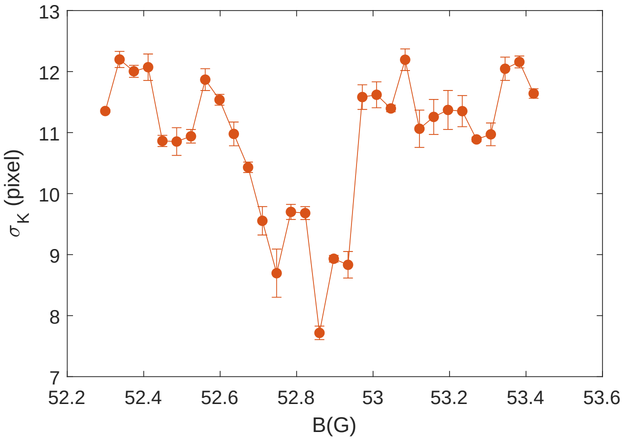

Figure B.6: Expansion of the cloud in the presence of interactions. A shrinking of the potassium cloud is taken as a signature of hydrodynamic expansion, happening in correspondence of strong interactions.

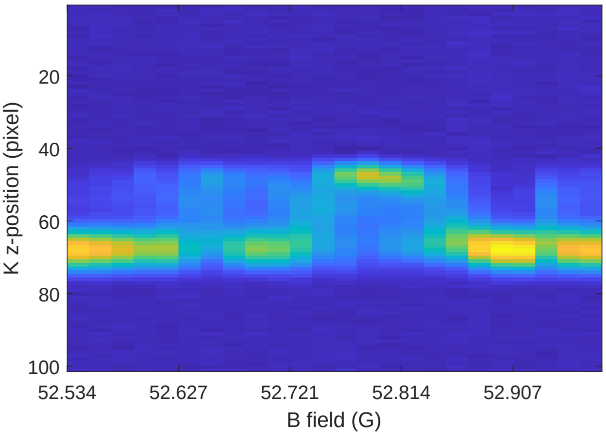

Figure B.7: Expansion of the cloud in the presence of interactions and a B-field gradient. In correspondence of strong interactions, the potassium cloud is dragged by dysprosium, which experiences a stronger magnetic force and thus a reduced acceleration along gravity.

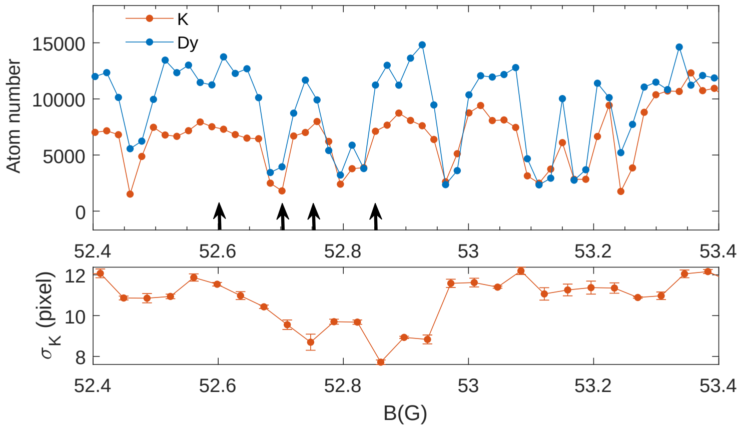

B(G)	τ_{Dy}	τ_K
52.608	1.3(2) s	4(1) s
52.693	$6(3) \times 10^1$ ms	30(6) ms
52.749	$7(1) \times 10^2$ ms	1.3(2) s
52.851	$39(5) \times 10^1$ ms	1.8(4) s

Figure B.8: Loss scan (top) of the mixture in the B-field region around the pole of the resonance at 52.8 G. The arrows are located at the magnetic fields where the lifetime has been measured (see table). The hydrodynamic scan (bottom) is reported as reference.

Appendix C

Linewidth Narrowing of Two DBR Lasers Through Optical Feedback and their Subsequent Phase Lock

Note on this project My PhD work was carried on within the Doctoral Programme (Doktoratskolleg) Atoms, Light, and Molecules (DK-ALM project). Among the others, this project offered me the great opportunity to spend six months abroad in a leading research center. In agreement with my supervisor, I joined the group of Professor Martin Zwierlein at MIT (Boston). Here, supervised by Dr. C. Robens, I worked on a side project aiming to phase lock two 767 nm distributed Bragg reflector (DBR) lasers, whose linewidth was previously narrowed thanks to optical feedback. During the last two months of my staying I have been joined by the newly enrolled PhD student Alexander Yu Chuang, who has taken over the project after my departure.
I report here the results achieved during my six-months staying, and briefly mention how the project has developed afterwards.

C.1 Introduction

Initially, the main goal of my side project was the implementation of a setup for the excitation of Raman transitions in potassium, to be used eventually in the main experiment. Being a two-photons process, high coherence between the two beams has to be ensured. Such a high coherence can be obtained either using a single laser, whose output is then suitably splitted in two beams, the frequency of each of which is then properly shifted; or using two (or more) sources and making them as much coherent as possible. The first option is by far the one that guarantees the best coherence. The second option has a less straightforward implementation, since it requires the implementations of an optical phase lock loop, to phase lock the two lasers, but comes with the nice advantage of more flexibility on the choice of the offset frequency. We decide to proceed with the second option, and phase lock two DBR lasers. It became immediately clear that given the typical linewidths of DBR and distributed feedback (DFB) lasers ($\Delta\nu_0 \simeq 1\,\mathrm{MHz}$), the achievement of a good coherence would have required a feedback bandwidth of $\simeq 10\,\mathrm{MHz}$, higher than what we could do. We thus concentrated our energies in looking for a robust method for narrowing the two lasers linewidth. Inspired by the work done in the Vuletics lab at MIT [299], we worked on narrowing the linewidth of a DBR diode employing an external cavity more than 1 m long. Such a length is possible thanks to the employment of an optical fiber. The light that is injected back into the diode acts as optical feedback, which leads to a reduction of the laser linewidth provided that the injected light stays within a well defined power-range. In Sec. C.2 this part of the project is reported: I briefly depict the setup used and characterize and discuss the effect of the optical feedback on the laser linewidth. In Sec. C.3 I instead describe how to phase lock the two lasers after their linewidth had been narrowed.

C.2 Linewidth reduction via optical feedback

C.2.1 Experimental setup

We use two DBR lasers whose wavelength is centered around 767 nm. Their nominal linewidth is $\Delta\nu_0 \simeq 1\,\mathrm{MHz}$. The maximum output power is around 45 mW. Each laser is driven by a current controller (Thorlabs, LDC 205C). A current filter cleans the noise from the controller and allows for current modulation thanks to an extra port where a modulation signal can be capacitive coupled (C-coupled) to the driving source: this port will be used for fast phase lock (see Sec. C.3.2). The diode temperature is stabilized around room temperature using a standard temperature controller (Thorlabs TED200C). The optical setup is sketched in Fig. C.1:

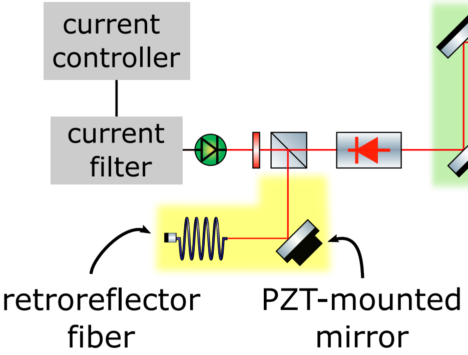

Figure C.1: Optical setup for the linewidth narrowing: the yellow shaded area constitutes the actual optical feedback path; the green one is currently used for diagnostic. The light is split between the two parts thanks to a system of half-waveplate plus PBS. An optical isolator is placed between the PBS and the diagnostic setup, in order to avoid unwanted and uncontrolled back-reflections.

it is similar to the one described in [299]. Immediately after a collimating lens, a waveplate and a polarizer beam splitter (PBS) are placed to pick up the desired amount of light for the optical feedback path: the rest of the light is used here for the characterization of the linewidth, whereas in the future will be sent to the atoms.

A polarization maintaining (PM) retroreflector fiber (Thorlabs, P5-780PMR-P01-1) constitutes the main part of the optical feedback path. It is a regular PM fiber, whose one end has a retroreflector connector: the ferrule at this end has a silver coating, which provides a nominal reflectivity of more than 98%. The other end has a standard FC/APC connector. The fiber is wrapped in foam, in order to improve the thermal and mechanical stability. Light is coupled into the fiber through a mirror mounted on a piezoelectric transducer (PZT): this allows us to fine tuning the cavity length, without compromising the fiber coupling. In front of the fiber, a half waveplate ensures that the light polarization is correctly aligned with the fiber axes. An aperture is placed in order to block undesired backreflections from the optics and the fiber tip. The optical feedback path can be considered as an external cavity for the laser, whose optical length is given by 30 cm in free space (from the diode facet to the fiber tip) plus the length of the fiber (1 m or 0.5 m, depending on the measurement) times the refractive index of the fiber, that we assume to be $n \simeq 1.45$.

In the context of this work, the rest of the light is used to evaluate the effect of the optical feedback on the laser linewidth. It can be shown [300] that the laser linewidth $\Delta\nu$ (i.e. the full width at half maximum (FWHM) of the power spectral density $S_E(\nu)$ of the electric field) is related to the frequency noise spectral density $S_N(f)$ through the relation:

$$S_E(\nu) = 2\int_0^{\infty} dt|E_0|^2 \mathrm{e}^{-i(\nu-\nu_0)t} e^{-2\int_0^{\infty} S_N(f)\frac{\sin(\pi f t)^2}{f^2}df}, \tag{C.1}$$

where E_0 is the amplitude of the electric field and ν_0 its central frequency. This integral does not have an analytic solution, even though it can be solved for trivial cases such as white frequency noise ($S_N(f) = h_0$, with h_0 a flat noise density given in $\mathrm{Hz}^2/\mathrm{Hz}$), which leads to a Lorentzian line shape with a width FWHM$= \pi h_0$. In Ref. [301] an approximate formula is derived for evaluating the linewidth of a laser featuring arbitrary noise spectral density. Their starting point is the observation that noise components in the high modulation index area (i.e., with a spectral density higher than their Fourier frequency $S_N(f) > f$) contributes to the central part of the laser line shape and so to the linewidth, whereas the low modulation index noise components contribute mostly to the wings. With good approximation, they conclude the laser linewidth to be:

$$\Delta\nu = \sqrt{8\ln(2)\cdot A} \tag{C.2}$$

where $A = \int_{1/T_0}^{\infty} S_N(f)\mathrm{d}f$, T_0 being the measurement duration. Hence, from a measurement of the frequency noise spectral density the laser linewidth can be retrieved.

Measuring $S_N(f)$ requires a filter (*optical frequency discriminator*), that converts frequency (what we are interested on) into power (what we can actually measure). Spectroscopic cells or Fabry Perot (FP) cavities are examples of those frequency discriminatores. In our case, the latter is employed [302]. The cavity is tuned such that the central frequency of the laser is located on the side of a transmission peak: doing so, the laser frequency fluctuations are converted into transmission amplitude fluctuations. The FP cavity has a free spectral range FSR = 500 MHz and a linewidth $\Delta\nu_{\mathrm{FP}} = 9\,\mathrm{MHz}$. One of the two cavity mirror is mounted on a PZT: in order to guarantee a stable frequency/power conversion we lock the cavity to the flank of the transmitted signal, which is recorded by a 10 MHz bandwidth photodiode. The lock has a BW of roughly 5 kHz, so that modulation components measured for frequency above 5 kHz directly reflects the intrinsic frequency noise spectral density of the laser. The signal used for the analysis is derived from the same photodiode used for the lock.

C.2.2 Linewidth reduction measurement

Conversion from amplitude fluctuations to frequency fluctuations requires a careful calibration of the frequency discriminator. Moreover, it could happen that the

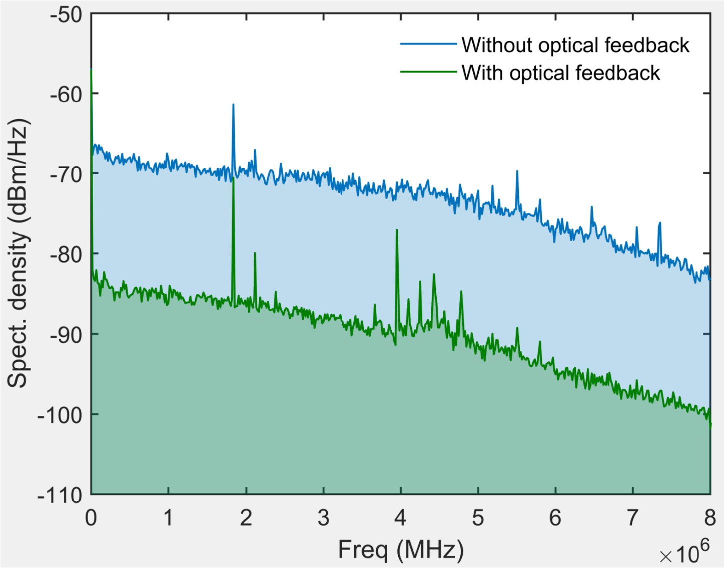

Figure C.2: Typical measurement of the linewidth reduction. The frequency spectral density of the laser is measured with and without optical feedback, by looking at the amplitude fluctuations of the transmitted light from the Fabry Perot cavity. The linewidth reduction is then deduced according to Eq.(C.3).

exact position of the laser central frequency relative to the central position of the transmission peak drifts over time. For the purpose of this work, we are interested on measuring the linewidth reduction, rather than the absolute linewidth of the laser: motivated by this, we decide to measure directly the linewidth reduction $\zeta_\nu = \frac{\Delta\nu_{of}}{\Delta\nu_{fr}}$, where $\Delta\nu_{of(fr)}$ is the linewidth of the laser with optical feedback (free running). Recalling the approximate formula for the linewidth Eq. (C.2) we obtain the simple expression

$$\zeta_\nu = \frac{\sqrt{A_{of}}}{\sqrt{A_{fr}}}. \tag{C.3}$$

Doing this, we get rid of possible systematic errors deriving from the calibration. A typical measurement is shown in Fig. C.2: the amplitude modulation is measured with a spectrum analyser. For each measurement, the noise spectra with and without optical feedback are recorded one after each other. The integrals of the recorded traces are numerically calculated and the ratio of the two is then taken, according to Eq. (C.3).

C.2.3 Results and discussion

The linewidth reduction is expected to depend on the power and phase of the optical feedback field, as well as on the length of the optical feedback path [303, 304, 299].

In a first set of measurements, we verify the dependence of the linewidth reduction on the feedback power. Keeping fix the total output power of the laser, we vary the amount of light sent to the feedback path by means of the PBS used to split the light between the two main path [1]. We can distinguish three different regimes: for really low feedback power (below 0.1% of the laser output power), we do not observe any linewidth reduction; for feedback powers between 0.1 and 2%, the linewidth decreases with the feedback power until it reaches a stable plateau; for higher feedback power, the laser becomes unstable and runs multimode [2].

We focus our attention on the central regime, where the laser is stable and where we observe a linewidth reduction. In Fig. C.3 the ratio of the linewidth with and without optical power ζ_ν as a function of the relative feedback power is reported for three different values of the total laser power. The measurements were repeated using the 1-m fiber (total optical path of 1.75 m), the 0.5-m fiber (optical path of 1.025 m), and in free space[3] (optical path of 0.4 m). For each setup (i.e., cavity length), the three sets of data share the same behavior, showing no dependency on the total power of the laser. The linewidth reduction reaches the same asymptotic value, which only depends on the length of the cavity. However, the onset of the instability region depends on the total power: the higher the total power, the wider is the plateau where the laser is stable and the linewidth ratio keeps the asymptotic value.

This kind of dependency on the optical feedback power can be naively understood if we think about the optical feedback path as a standard external cavity: varying the amount of relative power that is sent to the path is equivalent to change the finesse of the cavity; this in turn translates in a narrowing of the cavity modes and thus of the laser linewidth. A more accurate description has been reported in [303], where the laser is described in terms of classical variables: the complex electric field $E(t, x)$ and the number of carriers $N(t)$. The author derives a system of langevin rate equations that nicely predict semiconductor laser behavior. The effect of the optical feedback is described introducing the additional term $\kappa E(t-\tau_0)$

---

[1] The power in the optical feedback path is measured right at the front tip of the fiber. We calibrate the fiber coupling efficiency placing a quarter waveplate in front of the fiber and measuring the power right after the PBS used to split the light between feedback and main path. Still, this is only a crude estimate of the actual power that is going back into the laser chip

[2] We qualitatively observe those features letting the FP cavity unlocked and scanning its PZT: varying the feedback power, we clearly see that the transmitted peak gets narrower and narrower, up to the point where the laser becomes multimode and several peaks appear.

[3] We just replace the fiber with a flat mirror.

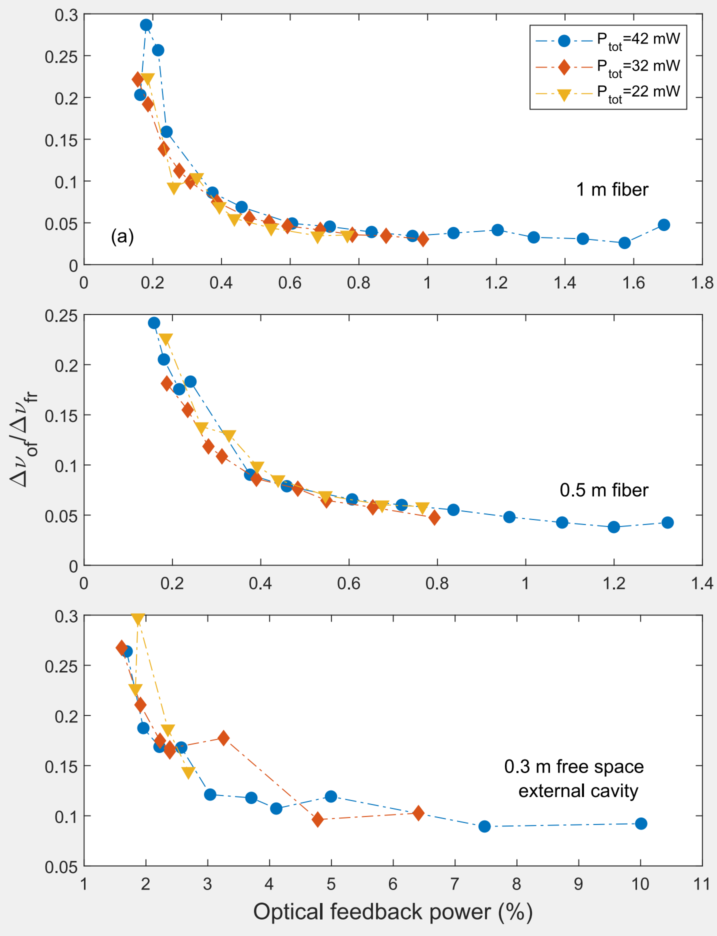

Figure C.3: Linewidth reduction as a function of the relative optical feedback power, for three different setups. For each of them, the linewidth reduction have been measured with the laser outputing a total power of 42, 32 and 22 mW (blue circles, red diamonds, yellow triangles).

.

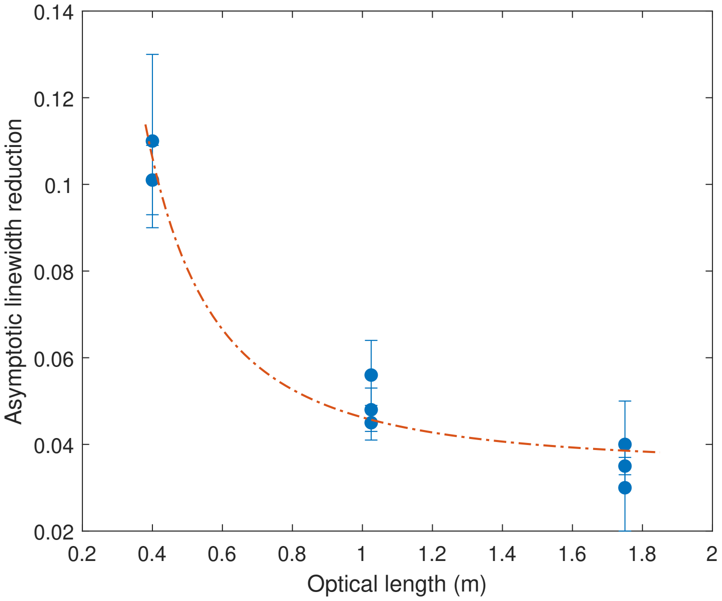

Figure C.4: Asympthotic linewidth reduction as a function of the cavity optical length. The data show an hyperbolic trend, in agreement with the $1/L^2$ behavior predicted in [303]. The line is a $1/L^2$ fit to the data.

in the equation for $\dot{E}(t)$. Here κ is the feedback parameter and is proportional to $\sqrt{P_{\text{rel}}}$ where P_{rel} is the power fraction traveling in the optical feedback path; τ_0 is the delay with which the field travels back into the laser chip. From his derivation follows that the laser linewidth in the presence of optical feedback is expected to be:

$$\Delta\nu_{of} = \frac{\Delta\nu_{fr}}{(1 + \kappa\tau_0 \cdot f(\omega\tau_0))^2}, \tag{C.4}$$

where $f(\omega\tau_0)$ is a trigonometric function of the phase of the injected field, and its value is of the order of few units.

For $\kappa\tau_0 \ll 1$, the optical feedback is not strong enough and the linewidth does not change. For $\kappa\tau_0 \gg 1$, the author predicts that the linewidth narrowing saturates, and becomes proportional to $1/L^2$, where L is the length of the optical feedback path.

We verify the $1/L^2$ dependency: in Fig. C.4 we report the asymptotic values of ζ_ν, as a function of the effective length of the optical feedback path. We indeed observe a trend that is in agreement with the predictions in [303]. It is interesting to note that in [303] is also predicted that a variation of the feedback power induces a shift in the frequency of the laser: we indeed observe this, even though a quantitative analysis of this phenomena goes beyond the purpose of this work.

C.3 Phase lock of two DBR lasers

C.3.1 Optical phase lock loop (PPL)

Phase locking is used to transfer the phase and frequency of a certain signal to a given tunable source. In general, the first signal comes from a weak, but usually highly precise source (master), while the tunable source (slave) is less precise but more powerful. If phase locking is achieved, the two sources are synchronized. Phase locking of electrical signal was first introduced at the beginning of the last century by professor D.Robertson to synchronize the bell Great George in the new Wills Memorial Building (Bristol) with a telegraph pulse coming from the Greenwchich observatory once a day[305]. Nowadays, phase locking is widely used for synchronization purposes not only with clocks, but also (and mainly) in communication, in microprocessors, in science in general. Laser synchronization is obviously not an exception, and it is usually referred to as optical phase locking. When two laser sources are phase locked, the two electric fields are coherent over time ranges which depend on the goodness of the lock. It is important to highlight that this does not necessarily imply that the linewidths of the two lasers gets narrower: the phase noise and frequency spectral densities of the master source are imprinted on the slave source. If the master source has a narrow linewidth, then the slave source inherits a narrower linewidth.

In an optical phase lock scheme, one may desire to perfectly phase lock one laser to the other or to add a frequency offset between the two. In the latter case, the synchronization is done between the two lasers beat note and a local oscillator.

C.3.2 Locking setup

We stabilize the frequency difference between the two DBR lasers exploiting the technique of optical phase lock loop (OPLL) [306, 307].

The basic elements of a PLL is a phase-frequency discriminator (PFD), which compares the phase and frequency of the two input signals and produces the error signal. We use a digital PFD, as introduced by Prevedelli and coworkers in [306]. The basic concept of this circuit is reported in Fig. C.5(a): the two signals are first digitalized[4] and then fed into the phase-frequency detector[5]. Through a system of two D-flip flop, the PFD compares the two signals: when they are unequal in phase or frequency, it will output a stream of pulses. A charge pump mechanism allows for a digital to analog conversion, producing the error signal that, for relatively small phase differences, has a linear dependence on the phase difference.

---

[4] Each signal is turned into a square wave by means of the fast comparator AD96687

[5] MC100EP140

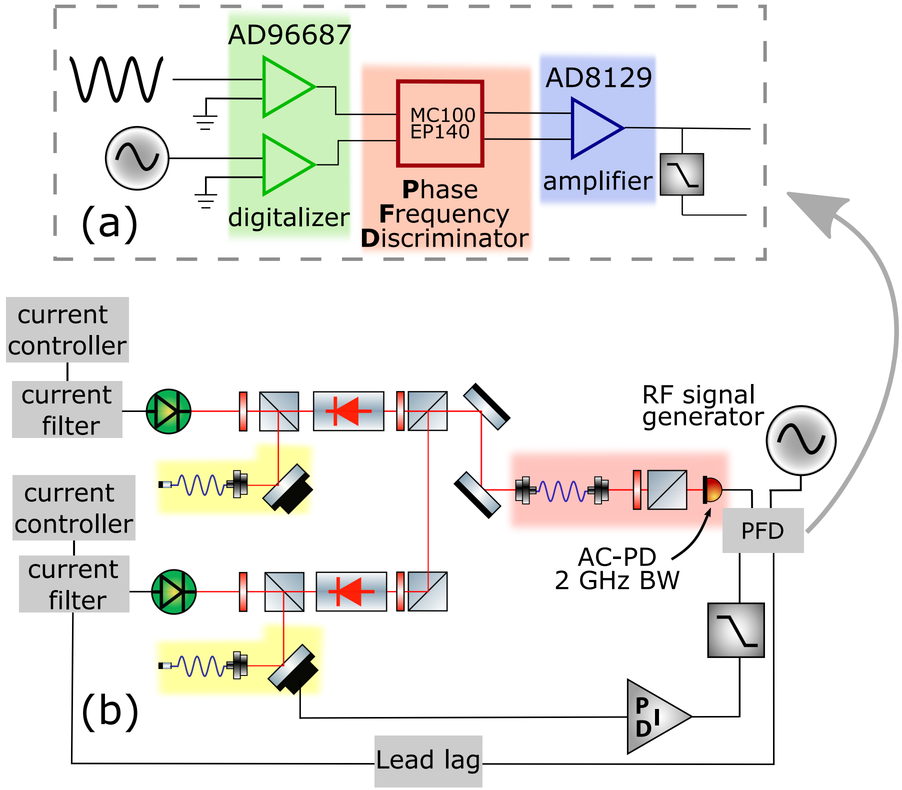

Figure C.5: (a) Simplified schematic of the phase frequency discriminator used in the expeiment; (b) optical setup for the OPLL of the two DBR lasers, upon linewidth narrowing via optical feedback. The red shaded area indicates where the beat note signal is obtained, while the two yellow areas points to the optical feedback setup.

Eventually, the error signal is split into two parts, one of which is low pass filtered and acts in the slow feedback loop. The non-filtered signal directly modulates the current.

An overview of the whole setup is sketched in Fig. C.5(b). We aim to phase lock the two lasers with a certain frequency offset. In this case, the two signals that are sent to the PFD are the beat note signal of the two lasers and the signal produced by a local oscillator. The beat note signal is obtained by coupling the two beams into the same fiber, the transmitted field being then recorded by a fast AC-coupled photodiode with 2-GHz bandwidth. The recorded signal is partially sent to a spectrum analyzer, for diagnostic. Our local oscillator is a common signal generator: for this measurements, we used an RF signal at 80 MHz. In principle, any frequency difference could work. The main limitations are the bandwidth of the AC-coupled photodiode and that of the frequency-phase comparator. The PFD

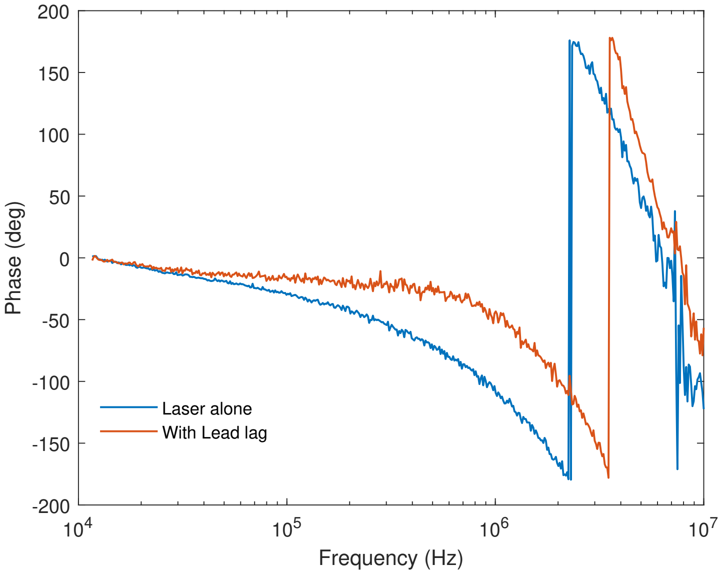

h

Figure C.6: Effect of the lead lag on the phase response of the laser. The laser current was modulated with the output of the network analyser, and the frequency fluctuation read from the Fabry Perot was input back to the network analyser.

employed in this work can compare signals that are up to 2 GHz apart. Phase lock for higher frequency offset can be achieved upon down conversion of the beat note signal to a frequency within a suitable range. The 80-MHz signal and the beat note one are input to the PFD, where they are compared and an error signal is produced. The low filtered error signal is sent to a PID box, featuring a bandwidth of 20 kHz. The box drives the PZT mirror in front of the retroreflector fiber in the optical feedback path. The "fast" (non filtered) error signal is instead sent directly to the diode itself: the signal is C-coupled to the driving current in the current filter.

The lead lag A lead lag is added in order to widen the useful bandwidth of the lock. Indeed, due to a thermal effect, semiconductor lasers show a resonance at frequencies between 500 kHz and 1.5 MHz, which causes the phase of the diode frequency modulation response to go through -90° [308, 309]. The role of the lead lag is to shift this pole towards higher frequencies. Figure C.6 shows the effect of the lead lag on the phase response of the laser to a frequency modulation. The measurement has been performed using a network analyser: the input signal is directly fed to the diode, while the frequency response is read from the amplitude fluctuations of the signal transmitted from the FP cavity.

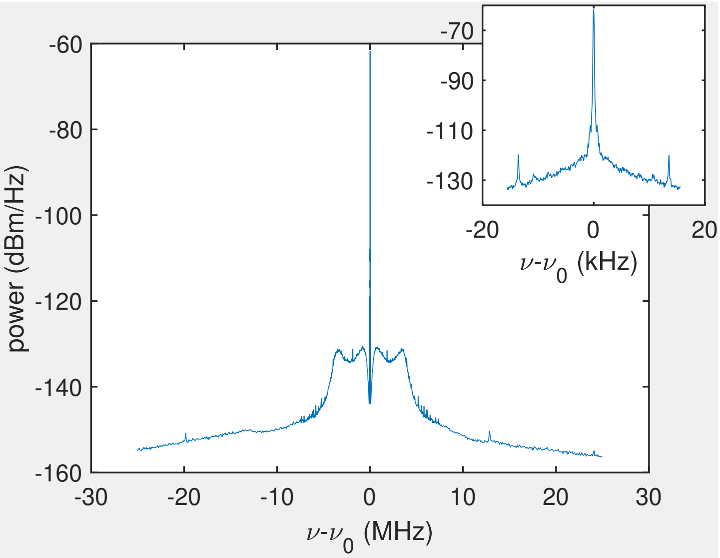

Figure C.7: Beat note signal of the two phase locked DBR lasers upon narrowing of their linewidth. The power density as a function of the detuning from the reference frequency ν_0 (here 80 MHz) is shown. Depending on the detuning range, different resolutions have been used. Data have been then merged together upon proper renormalization. The inset show the data relative to the central peak, taken with 100 Hz resolution.

C.3.3 Results

We quantify the goodness of the phase lock by looking at the spectrum of the beat note signal. The data reported in Fig. C.7 show a sidebands suppression of more than 50 dB. Data are taken with different resolution bandwidth, in order to maximize the accuracy of the measurement.

A more quantitative analysis can be done by measuring the RMS phase fluctuations of the beat note signal, quantified through $\langle \varphi^2 \rangle$. It can be demonstrated that the ratio η of the power in the carrier over the total power is given by [306, 310]:

$$\eta = \frac{P_{carr}}{P_{tot}} = \frac{P(0)}{\int_{-\infty}^{\infty} P(\nu) d\nu} \xrightarrow{\langle \varphi^2 \rangle \ll 1} \exp(-\langle \varphi^2 \rangle) \tag{C.5}$$

The RMS phase fluctuations $\langle \varphi^2 \rangle$ can be accessed through a quadrature measurement. The beat note signal and the one from the local oscillator are both split into two signals and then combined together two-by-two (see Fig. C.8(a)). In one case the two signals are just directly mixed, whereas in the other case a $\frac{\pi}{2}$-phase is added before mixing[6]. We thus obtain two signals that are in quadrature. In particular, filtering out the high frequency component, the two signals read:

$$Q(t) \propto \sin(\Delta\omega(t) \cdot t + \varphi(t)) \tag{C.6}$$

$$I(t) \propto \cos(\Delta\omega(t) \cdot t + \varphi(t)). \tag{C.7}$$

When the two lasers are phase locked, we can safely set $\Delta\omega(t) = 0$: $\varphi(t)$ is then given by the angle subtending the arc drawn by $Q(t)$ and $I(t)$ (see the inset in Fig. C.8(b)). We record the time trace for $Q(t)$ and $I(t)$, and then consider $\varphi(t) = \arctan(Q(t)/I(t))$. A typical data set is reported in the histogram in Fig. C.8(a). In this case we obtain $\langle\varphi^2\rangle = 51^2\,\mathrm{mrad}^2$, which according to Eq. C.3.3 corresponds to $\eta = 99.73\%$.
The lock is stable over time (the two lasers stay locked for hours), and has a capture range of more than 10 MHz.

C.4 Conclusions and outlook

In the frame of this project, we have demonstrated how it is possible to narrow the linewidth of a DBR laser via optical feedback. The effect of the optical feedback depends on $\sqrt{P_{rel}}$, where P_{rel} is the relative power injected into the optical feedback path. Still, if P_{rel} exceeds a certain value, the laser enters into an instability region and becomes multimode. We verified that the linewidth reduction ζ_ν scales as $1/L^2$, where L is the length of the optical feedback path.
Thanks to the line narrowing of the two lasers, it has been possible to phase lock them, imprinting a frequency shift of 80 MHz between the two: the beat note signal shows a sideband suppression of more than 50 dB.

After my departure, the project evolved with the building of a compact box which could contain the laser and the optics and retroreflector fiber needed for the optical feedback. This also guarantees a better mechanical and thermal isolation. The concept of phase locking upon linewidth narrowing has than be extended to two lasers at 1064 nm. Low noise, stable 1064 nm lasers are of great interest to seed high power fiber amplifiers which will inherit the noise properties from the seed laser. Lower noise directly results in lower heating rates on the atoms that are trapped in the potentials created by such lasers.

---

[6] The $\frac{\pi}{2}$-phase is obtained thanks to a proper choice of the cable length.

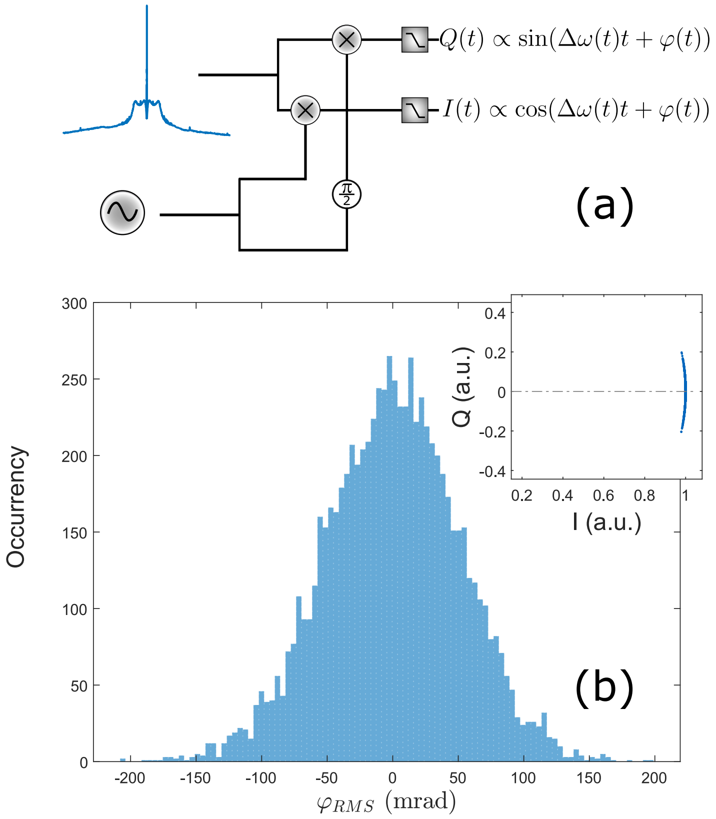

Figure C.8: (a) Sketch of the quadrature measurement described in the text. The beat note signal and the local oscillator one are split in two parts, recombined then two-by-two. The two mixed signal are phase-shifted by $\frac{\pi}{2}$. (b) Histogram and *xy* plot (in the inset) of the RMS variation of the phase fluctuations between the two lasers, as obtained from the quadrature measurement. We obtain $\langle\varphi^2\rangle = 51^2\,\mathrm{mrad}^2$, which corresponds to 99.73% of the total power concentrated in the carrier.

Bibliography

[1] H. K. Onnes, *On the sudden rate at which the resistance of mercury disappears*, Koninklijke Nederlandsche Akademie van Wetenschappen 14 (1912) (cit. on p. 9).

[2] S. Blundell, *Superconductivity. A very short introduction*. 2009 (cit. on p. 9).

[3] APA, *April 1911: Onnes Begins work on Superconductivity*. 2007 (cit. on p. 9).

[4] G. Grosso and G. Parravicini, *Solid State Physics*. 2000 (cit. on p. 9).

[5] J. Bardeen, L. N. Cooper, and J. R. Schrieffer, *Microscopic Theory of Superconductivity*, Phys. Rev. 106 (1957) (cit. on p. 9).

[6] P. Kapitza, *Viscosity of liquid helium below the λ-point*, Nature 141 (1938) (cit. on p. 9).

[7] J. F. Allen and A. Misener, *Flow of liquid helium II*, Nature 141 (1938) (cit. on p. 9).

[8] D. D. Osheroff, R. C. Richardson, and D. M. Lee, *Evidence for a New Phase of Solid* He^3, Phys. Rev. Lett. 28 (1972) (cit. on p. 9).

[9] D. M. Eagles, *Possible Pairing without Superconductivity at Low Carrier Concentrations in Bulk and Thin-Film Superconducting Semiconductors*, Phys. Rev. 186 (1969) (cit. on p. 10).

[10] A. J. Leggett, *Diatomic Molecules and Cooper Pairs*, *Modern Trends in the Theory of Condensed Matter*. Ed. by Springer-Verlag. Berlin, 1980 (cit. on pp. 10, 24).

[11] P Nozieres and S Schmitt-Rink, *Bose condensation in an attractive fermion gas: From weak to strong coupling superconductivity*, J. Low Temp. Phys.; (United States) (May 1985) (cit. on pp. 10, 24).

[12] C. Chin, R. Grimm, P. S. Julienne, and E. Tiesinga, *Feshbach resonances in ultracold gases*, Rev. Mod. Phys. 82 (2010) (cit. on pp. 11, 18, 19, 21, 69, 75, 78, 87, 92, 101, 103).

[13] M. Bartenstein, A. Altmeyer, S. Riedl, S. Jochim, C. Chin, J. Hecker Denschlag, and R. Grimm, *Crossover from a Molecular Bose-Einstein Condensate to a Degenerate Fermi Gas*, Phys. Rev. Lett. 92 (2004) (cit. on pp. 11, 24).

[14] T. Bourdel, L. Khaykovich, J. Cubizolles, J. Zhang, F. Chevy, M. Teichmann, L. Tarruell, S. J. J. M. F. Kokkelmans, and C. Salomon, *Experimental Study of the BEC-BCS Crossover Region in Lithium 6*, Phys. Rev. Lett. 93 (2004) (cit. on pp. 11, 14).

[15] C. A. Regal, M. Greiner, and D. S. Jin, *Observation of Resonance Condensation of Fermionic Atom Pairs*, Phys. Rev. Lett. 92 (2004) (cit. on pp. 11, 14, 25).

[16] M. W. Zwierlein, A. Schirotzek, C. H. Schunck, and W. Ketterle, *Fermionic superfluidity with imbalanced spin populations*, Science 311 (2006) (cit. on pp. 11, 26).

[17] G. B. Partridge, W. Li, R. I. Kamar, Y. Liao, and R. G. Hulet, *Pairing and phase separation in a polarized Fermi gas*, Science 311 (2006) (cit. on pp. 11, 25).

[18] Y. Shin, C. H. Schunck, A. Schirotzek, and W. Ketterle, *Phase diagram of a two-component Fermi gas with resonant interactions*, Nature (London) 451 (2008) (cit. on pp. 11, 26).

[19] P. Fulde and R. A. Ferrell, *Superconductivity in a Strong Spin-Exchange Field*, Phys. Rev. 135 (1964) (cit. on pp. 11, 27, 50, 75).

[20] A. I. Larkin and Y. N. Ovchinnikov, *Inhomogeneous state of superconductors*, Sov. Phys. JETP 20 (1965) (cit. on pp. 11, 50).

[21] G Sarma, *On the influence of a uniform exchange field acting on the spins of the conduction electrons in a superconductor*, J. Phys. Chem. Solids 24 (1963) (cit. on pp. 11, 27, 50).

[22] K. B. Gubbels, M. W. J. Romans, and H. T. C. Stoof, *Sarma Phase in Trapped Unbalanced Fermi Gases*, Phys. Rev. Lett. 97 (2006) (cit. on pp. 11, 27).

[23] J. E. Baarsma, K. B. Gubbels, and H. T. C. Stoof, *Population and mass imbalance in atomic Fermi gases*, Phys. Rev. A 82 (2010) (cit. on pp. 11, 26, 27, 28, 43, 50, 84, 119).

[24] J. Wang, Y. Che, L. Zhang, and Q. Chen, *Enhancement effect of mass imbalance on Fulde-Ferrell-Larkin-Ovchinnikov type of pairing in Fermi-Fermi mixtures of ultracold quantum gases*, Sci. Rep. 7 (2017) (cit. on pp. 11, 27, 28, 43, 50, 70, 75, 101, 119).

[25] M. Pini, P. Pieri, R. Grimm, and G. C. Strinati, *Beyond-mean-field description of a trapped unitary Fermi gas with mass and population imbalance*, Phys. Rev. A 103 (2021) (cit. on pp. 12, 32, 101, 118, 119).

[26] C. Ravensbergen, V. Corre, E. Soave, M. Kreyer, E. Kirilov, and R. Grimm, *Production of a degenerate Fermi-Fermi mixture of dysprosium and potassium atoms*, Phys. Rev. A 98 (2018) (cit. on pp. 12, 76, 77, 84, 87, 89, 90, 92, 101, 102, 103, 106).

[27] C. Ravensbergen, E. Soave, V. Corre, M. Kreyer, B. Huang, E. Kirilov, and R. Grimm, *Resonantly Interacting Fermi-Fermi Mixture of* ^{161}Dy *and* ^{40}K, Phys. Rev. Lett. 124 (2020) (cit. on pp. 12, 31, 101, 103, 112, 113, 132).

[28] R. Grimm, *Quantum Gases at Very Large Scattering Length (Part I)* . 2017. (Visited on 12/28/2021) (cit. on p. 13).

[29] M. H. Anderson, J. R. Ensher, M. R. Matthews, C. E. Wieman, and E. A. Cornell, *Observation of Bose-Einstein Condensation in a Dilute Atomic Vapor*, Science 269 (1995) (cit. on pp. 13, 65).

[30] K. B. Davis, M. O. Mewes, M. R. Andrews, N. J. van Druten, D. S. Durfee, D. M. Kurn, and W. Ketterle, *Bose-Einstein Condensation in a Gas of Sodium Atoms*, Phys. Rev. Lett. 75 (1995) (cit. on p. 13).

[31] B. DeMarco and D. S. Jin, *Onset of Fermi Degeneracy in a Trapped Atomic Gas*, Science 285 (1999) (cit. on pp. 14, 16, 17, 52).

[32] A. G. Truscott, K. E. Strecker, W. I. McAlexander, G. B. Partridge, and R. G. Hulet, *Observation of Fermi Pressure in a Gas of Trapped Atoms*, Science 291 (2001) (cit. on pp. 14, 16, 52).

[33] F. Schreck, L. Khaykovich, K. L. Corwin, G. Ferrari, T. Bourdel, J. Cubizolles, and C. Salomon, *Quasipure Bose-Einstein Condensate Immersed in a Fermi Sea*, Phys. Rev. Lett. 87 (2001) (cit. on pp. 14, 52).

[34] M. Greiner, O. Mandel, T. Esslinger, T. W. Hänsch, and I. Bloch, *Quantum phase transition from a superfluid to a Mott insulator in a gas of ultracold atoms*, Nature 415 (2002) (cit. on p. 14).

[35] M. Köhl, H. Moritz, T. Stöferle, K. Günter, and T. Esslinger, *Fermionic Atoms in a Three Dimensional Optical Lattice: Observing Fermi Surfaces, Dynamics, and Interactions*, Phys. Rev. Lett. 94 (2005) (cit. on p. 14).

[36] W. S. Bakr, J. I. Gillen, A. Peng, S. Fölling, and M. Greiner, *A quantum gas microscope for detecting single atoms in a Hubbard-regime optical lattice*, Nature 462 (2009) (cit. on p. 14).

[37] L. W. Cheuk, M. A. Nichols, M. Okan, T. Gersdorf, V. V. Ramasesh, W. S. Bakr, T. Lompe, and M. W. Zwierlein, *Quantum-Gas Microscope for Fermionic Atoms*, Phys. Rev. Lett. 114 (2015) (cit. on p. 14).

[38] Y.-J. Lin, R. L. Compton, K. Jiménez-García, J. V. Porto, and I. B. Spielman, *Synthetic magnetic fields for ultracold neutral atoms*, Nature 462 (2009) (cit. on p. 14).

[39] M. Aidelsburger, M. Atala, S. Nascimbène, S. Trotzky, Y.-A. Chen, and I. Bloch, *Experimental Realization of Strong Effective Magnetic Fields in an Optical Lattice*, Phys. Rev. Lett. 107 (2011) (cit. on p. 14).

[40] C. Chin, M. Bartenstein, A. Altmeyer, S. Riedl, S. Jochim, J. H. Denschlag, and R. Grimm, *Observation of the Pairing Gap in a Strongly Interacting Fermi Gas*, Science 305 (2004) (cit. on pp. 14, 25).

[41] N. R. Cooper, J. Dalibard, and I. B. Spielman, *Topological bands for ultracold atoms*, Rev. Mod. Phys. 91 (2019) (cit. on p. 14).

[42] B. Paredes, A. Widera, V. Murg, O. Mandel, S. Fölling, I. Cirac, G. V. Shlyapnikov, T. W. Hänsch, and I. Bloch, *Tonks–Girardeau gas of ultracold atoms in an optical lattice*, Nature 429 (2004) (cit. on p. 14).

[43] Z. Hadzibabic, P. Krüger, M. Cheneau, B. Battelier, and J. Dalibard, *Berezinskii–Kosterlitz–Thouless crossover in a trapped atomic gas*, Nature 441 (2006) (cit. on p. 14).

[44] L. Sanchez-Palencia and M. Lewenstein, *Disordered quantum gases under control*, Nature 6 (2010) (cit. on p. 14).

[45] A. D. Ludlow, M. M. Boyd, J. Ye, E. Peik, and P. O. Schmidt, *Optical atomic clocks*, Rev. Mod. Phys. 87 (2015) (cit. on pp. 14, 35).

[46] P. Cladé, E. de Mirandes, M. Cadoret, S. Guellati-Khélifa, C. Schwob, F. Nez, L. Julien, and F. Biraben, *Determination of the Fine Structure Constant Based on Bloch Oscillations of Ultracold Atoms in a Vertical Optical Lattice*, Phys. Rev. Lett. 96 (2006) (cit. on p. 14).

[47] J. B. Fixler, G. T. Foster, J. M. McGuirk, and M. A. Kasevich, *Atom Interferometer Measurement of the Newtonian Constant of Gravity*, Science 315 (2007) (cit. on p. 14).

[48] J. F. Barry, D. J. McCarron, E. B. Norrgard, M. H. Steinecker, and D. DeMille, *Magneto-optical trapping of a diatomic molecule*, Nature 512 (2014) (cit. on p. 14).

[49] L. W. Cheuk, L. Anderegg, B. L. Augenbraun, Y. Bao, S. Burchesky, W. Ketterle, and J. M. Doyle, *Λ-Enhanced Imaging of Molecules in an Optical Trap*, Phys. Rev. Lett. 121 (2018) (cit. on p. 14).

[50] L. R. Liu, J. D. Hood, Y. Yu, J. T. Zhang, K. Wang, Y.-W. Lin, T. Rosenband, and K.-K. Ni, *Molecular Assembly of Ground-State Cooled Single Atoms*, Phys. Rev. X 9 (2019) (cit. on p. 14).

[51] Y. Liu, M.-G. Hu, M. A. Nichols, D. Yang, D. Xie, H. Guo, and K.-K. Ni, *Precision test of statistical dynamics with state-to-state ultracold chemistry*, Nature 593 (2021) (cit. on p. 14).

[52] B. DeMarco, *Quantum Behavior of an Atomic Fermi Gas*. PhD thesis. University of Colorado, 2001 (cit. on pp. 16, 17, 109).

[53] F. A. van Abeelen, B. J. Verhaar, and A. J. Moerdijk, *Sympathetic cooling of* ^{6}Li *atoms*, Phys. Rev. A 55 (1997) (cit. on p. 17).

[54] G. Roati, F. Riboli, G. Modugno, and M. Inguscio, *Fermi-Bose Quantum Degenerate* ^{40}K–^{87}Rb *Mixture with Attractive Interaction*, Phys. Rev. Lett. 89 (2002) (cit. on p. 17).

[55] B. Naylor, A. Reigue, E. Maréchal, O. Gorceix, B. Laburthe-Tolra, and L. Vernac, *Chromium dipolar Fermi sea*, Phys. Rev. A 91 (2015) (cit. on pp. 17, 52).

[56] B. J. DeSalvo, M. Yan, P. G. Mickelson, Y. N. Martinez de Escobar, and T. C. Killian, *Degenerate Fermi Gas of* ^{87}Sr, Phys. Rev. Lett. 105 (2010) (cit. on pp. 17, 52).

[57] T. Fukuhara, Y. Takasu, M. Kumakura, and Y. Takahashi, *Degenerate Fermi Gases of Ytterbium*, Phys. Rev. Lett. 98 (2007) (cit. on pp. 17, 52).

[58] T. Fukuhara, Y. Takasu, S. Sugawa, and Y. Takahashi, *Quantum Degenerate Fermi Gases of Ytterbium Atoms*, J. Low Temp. Phys. 148 (2007) (cit. on p. 17).

[59] J. M. McNamara, T. Jeltes, A. S. Tychkov, W. Hogervorst, and W. Vassen, *Degenerate Bose-Fermi Mixture of Metastable Atoms*, Phys. Rev. Lett. 97 (2006) (cit. on pp. 17, 52).

[60] M. Lu, N. Q. Burdick, and B. L. Lev, *Quantum Degenerate Dipolar Fermi Gas*, Phys. Rev. Lett. 108 (2012) (cit. on pp. 17, 29, 30, 35, 52, 55, 75, 103).

[61] K. Aikawa, A. Frisch, M. Mark, S. Baier, R. Grimm, and F. Ferlaino, *Reaching Fermi Degeneracy via Universal Dipolar Scattering*, Phys. Rev. Lett. 112 (2014) (cit. on pp. 17, 30, 52, 55, 75, 106).

[62] S. Hensler, J. Werner, A. Griesmaier, P. Schmidt, A. Görlitz, T. Pfau, S. Giovanazzi, and K. Rzażewski, *Dipolar relaxation in an ultra-cold gas of magnetically trapped chromium atoms*, Appl. Phys. B 77 (2003) (cit. on p. 17).

[63] J. J. Sakurai and J. J. Napolitano, *Modern Quantum Mechanics*. 2014 (cit. on p. 18).

[64] M. Lepers and O. Dulieu, *Long-range Interactions Between Ultracold Atoms and Molecules*, *Cold Chemistry*. 2017 (cit. on p. 19).

[65] D. S. Petrov, *Three-Boson Problem near a Narrow Feshbach Resonance*, Phys. Rev. Lett. 93 (2004) (cit. on pp. 20, 21, 78, 92).

[66] P. F. Bedaque, E. Braaten, and H.-W. Hammer, *Three-body Recombination in Bose Gases with Large Scattering Length*, Phys. Rev. Lett. 85 (2000) (cit. on p. 21).

[67] M. A. Baranov, M. Dalmonte, G. Pupillo, and P. Zoller, *Condensed matter theory of dipolar quantum gases*, Chem. Rev. 112 (2012) (cit. on pp. 21, 29).

[68] S. Kotochigova, *Controlling interactions between highly magnetic atoms with Feshbach resonances*, Rep. Prog. Phys. 77 (2014) (cit. on pp. 21, 29, 69, 101).

[69] V Gurarie and L Radzihovsky, *Resonantly paired fermionic superfluids*, Ann. Phys. 322 (2007) (cit. on p. 22).

[70] F. Chevy, E. G. M. van Kempen, T. Bourdel, J. Zhang, L. Khaykovich, M. Teichmann, L. Tarruell, S. J. J. M. F. Kokkelmans, and C. Salomon, *Resonant scattering properties close to a p-wave Feshbach resonance*, Phys. Rev. A 71, 062710 (2005) (cit. on pp. 22, 102).

[71] B. D. Esry, C. H. Greene, and H. Suno, *Threshold laws for three-body recombination*, Phys. Rev. A 65 (2001) (cit. on pp. 22, 51, 106).

[72] J. Yoshida, T. Saito, M. Waseem, K. Hattori, and T. Mukaiyama, *Scaling Law for Three-Body Collisions of Identical Fermions with p-Wave Interactions*, Phys. Rev. Lett. 120 (2018) (cit. on pp. 22, 102, 110, 111, 112).

[73] H. Suno, B. D. Esry, and C. H. Greene, *Recombination of Three Ultracold Fermionic Atoms*, Phys. Rev. Lett. 90 (2003) (cit. on pp. 22, 51, 102, 110, 111).

[74] S. Inouye, M. R. Andrews, J. Stenger, H.-J. Miesner, D. M. Stamper-Kurn, and W. Ketterle, *Observation of Feshbach resonances in a Bose–Einstein condensate*, Nature 392 (1998) (cit. on p. 22).

[75] T. Loftus, C. A. Regal, C. Ticknor, J. L. Bohn, and D. S. Jin, *Resonant Control of Elastic Collisions in an Optically Trapped Fermi Gas of Atoms*, Phys. Rev. Lett. 88 (2002) (cit. on p. 22).

[76] C. A. Stan, M. W. Zwierlein, C. H. Schunck, S. M. F. Raupach, and W. Ketterle, *Observation of Feshbach Resonances between Two Different Atomic Species*, Phys. Rev. Lett. 93 (2004) (cit. on p. 22).

[77] S. Inouye, J. Goldwin, M. L. Olsen, C. Ticknor, J. L. Bohn, and D. S. Jin, *Observation of Heteronuclear Feshbach Resonances in a Mixture of Bosons and Fermions*, Phys. Rev. Lett. 93, 183201 (2004) (cit. on p. 22).

[78] L. De Marco, G. Valtolina, K. Matsuda, W. G. Tobias, J. P. Covey, and J. Ye, *A degenerate Fermi gas of polar molecules*, Science 363 (2019) (cit. on pp. 22, 28).

[79] S Jochim, M Bartenstein, A Altmeyer, G Hendl, S Riedl, C Chin, J. H. Denschlag, and R Grimm, *Bose-Einstein Condensation of Molecules*, Science (2003) (cit. on p. 22).

[80] K. Xu, T. Mukaiyama, J. Abo-Shaeer, J. K. Chin, D. Miller, and W. Ketterle, *Formation of quantum-degenerate sodium molecules*, Phys. Rev. Lett. 91 (2003) (cit. on p. 22).

[81] A. Schirotzek, C.-H. Wu, A. Sommer, and M. W. Zwierlein, *Observation of Fermi Polarons in a Tunable Fermi Liquid of Ultracold Atoms*, Phys. Rev. Lett. 102 (2009) (cit. on p. 22).

[82] C. Kohstall, M. Zaccanti, M. Jag, A. Trenkwalder, P. Massignan, G. M. Bruun, F. Schreck, and R. Grimm, *Metastability and coherence of repulsive polarons in a strongly interacting Fermi mixture*, Nature 485 (2012) (cit. on pp. 22, 51).

[83] M. Cetina, M. Jag, R. S. Lous, J. T. M. Walraven, R. Grimm, R. S. Christensen, and G. M. Bruun, *Decoherence of Impurities in a Fermi Sea of Ultracold Atoms*, Phys. Rev. Lett. 115 (2015) (cit. on pp. 22, 51).

[84] T. Kraemer, M. Mark, P. Waldburger, J. G. Danzl, C. Chin, B. Engeser, A. D. Lange, K. Pilch, A. Jaakkola, H.-C. Nägerl, et al., *Evidence for Efimov quantum states in an ultracold gas of caesium atoms*, Nature 440 (2006) (cit. on p. 22).

[85] J. Yoshida, T. Saito, M. Waseem, K. Hattori, and T. Mukaiyama, *Scaling Law for Three-Body Collisions of Identical Fermions with p-Wave Interactions*, Phys. Rev. Lett. 120 (2018) (cit. on p. 22).

[86] J. Zhang, E. G. M. van Kempen, T. Bourdel, L. Khaykovich, J. Cubizolles, F. Chevy, M. Teichmann, L. Tarruell, S. J. J. M. F. Kokkelmans, and C. Salomon, *P-wave Feshbach resonances of ultracold* ^{6}Li, Phys. Rev. A 70 (2004) (cit. on pp. 22, 102, 112).

[87] C. A. Regal, C. Ticknor, J. L. Bohn, and D. S. Jin, *Tuning p-Wave Interactions in an Ultracold Fermi Gas of Atoms*, Phys. Rev. Lett. 90 (2003) (cit. on pp. 22, 102).

[88] S. Taie, Y. Takasu, S. Sugawa, R. Yamazaki, T. Tsujimoto, R. Murakami, and Y. Takahashi, *Realization of a* $\mathrm{SU}(2) \times \mathrm{SU}(6)$ *System of Fermions in a Cold Atomic Gas*, Phys. Rev. Lett. 105 (2010) (cit. on p. 23).

[89] Q. Chen, J. Stajic, S. Tan, and K. Levin, *BCS–BEC crossover: From high temperature superconductors to ultracold superfluids*, Phys. Rep. 412 (2005) (cit. on p. 23).

[90] M. Holland, S. J. J. M. F. Kokkelmans, M. L. Chiofalo, and R. Walser, *Resonance Superfluidity in a Quantum Degenerate Fermi Gas*, Phys. Rev. Lett. 87 (2001) (cit. on p. 23).

[91] R. Haussmann, W. Rantner, S. Cerrito, and W. Zwerger, *Thermodynamics of the BCS-BEC crossover*, Phys. Rev. A 75 (2007) (cit. on p. 24).

[92] S. Jochim, M. Bartenstein, A. Altmeyer, G. Hendl, C. Chin, J. Hecker Denschlag, and R. Grimm, *Pure Gas of Optically Trapped Molecules Created from Fermionic Atoms*, Phys. Rev. Lett 91 (2003) (cit. on pp. 24, 51).

[93] B. D. Esry, C. H. Greene, and J. P. Burke, *Recombination of Three Atoms in the Ultracold Limit*, Phys. Rev. Lett. 83 (1999) (cit. on p. 24).

[94] D. S. Petrov, C. Salomon, and G. V. Shlyapnikov, *Weakly Bound Dimers of Fermionic Atoms*, Phys. Rev. Lett. 93 (2004) (cit. on pp. 24, 51, 75, 83).

[95] M. W. Zwierlein, *Thermodynamics of strongly interacting Fermi gases*, *Quantum Matter at Ultralow Temperatures*. Vol. 191. 2016 (cit. on p. 24).

[96] T.-L. Ho, *Universal Thermodynamics of Degenerate Quantum Gases in the Unitarity Limit*, Phys. Rev. Lett. 92 (2004) (cit. on p. 24).

[97] W. Ketterle and M. W. Zwierlein, *Making, probing and understanding ultracold Fermi gases*, La Rivista del Nuovo Cimento 31 (2008) (cit. on p. 24).

[98] T. Bourdel, J. Cubizolles, L. Khaykovich, K. M. F. Magalhães, S. J. J. M. F. Kokkelmans, G. V. Shlyapnikov, and C. Salomon, *Measurement of the Interaction Energy near a Feshbach Resonance in a* ^{6}*Li Fermi Gas*, Phys. Rev. Lett. 91 (2003) (cit. on pp. 24, 82, 94).

[99] K. M. O'Hara, S. L. Hemmer, M. E. Gehm, S. R. Granade, and J. E. Thomas, *Observation of a Strongly Interacting Degenerate Fermi Gas of Atoms*, Science 298 (2002) (cit. on pp. 24, 51).

[100] C. A. Regal, C. Ticknor, J. L. Bohn, and D. S. Jin, *Creation of ultracold molecules from a Fermi gas of atoms*, Nature 424 (2003) (cit. on p. 24).

[101] K. E. Strecker, G. B. Partridge, and R. G. Hulet, *Conversion of an Atomic Fermi Gas to a Long-Lived Molecular Bose Gas*, Phys. Rev. Lett. 91 (2003) (cit. on p. 24).

[102] J. Cubizolles, T. Bourdel, S. J. J. M. F. Kokkelmans, G. V. Shlyapnikov, and C. Salomon, *Production of Long-Lived Ultracold* Li_2 *Molecules from a Fermi Gas*, Phys. Rev. Lett. 91 (2003) (cit. on pp. 24, 51).

[103] M. Greiner, C. A. Regal, and D. S. Jin, *Emergence of a molecular Bose–Einstein condensate from a Fermi gas*, Nature 426 (2003) (cit. on p. 24).

[104] M. W. Zwierlein, C. A. Stan, C. H. Schunck, S. M. F. Raupach, S. Gupta, Z. Hadzibabic, and W. Ketterle, *Observation of Bose-Einstein Condensation of Molecules*, Phys. Rev. Lett. 91 (2003) (cit. on p. 24).

[105] J. Kinast, S. L. Hemmer, M. E. Gehm, A. Turlapov, and J. E. Thomas, *Evidence for Superfluidity in a Resonantly Interacting Fermi Gas*, Phys. Rev. Lett. 92 (2004) (cit. on p. 25).

[106] M. Bartenstein, A. Altmeyer, S. Riedl, S. Jochim, C. Chin, J. H. Denschlag, and R. Grimm, *Collective Excitations of a Degenerate Gas at the BEC-BCS Crossover*, Phys. Rev. Lett. 92 (2004) (cit. on p. 25).

[107] M. W. Zwierlein, J. R. Abo-Shaeer, A. Schirotzek, C. H. Schunck, and W. Ketterle, *Vortices and superfluidity in a strongly interacting Fermi gas*, Nature 435 (2005) (cit. on p. 25).

[108] T. Schaefer and D. Teaney, *Nearly perfect fluidity: from cold atomic gases to hot quark gluon plasmas*, Rep. Prog. Phys. 72 (2009) (cit. on p. 25).

[109] J. Kinast, A. Turlapov, J. E. Thomas, Q. Chen, J. Stajic, and K. Levin, *Heat capacity of a strongly interacting Fermi gas*, Science 307 (2005) (cit. on p. 25).

[110] J. T. Stewart, J. P. Gaebler, C. A. Regal, and D. S. Jin, *Potential Energy of a* $^{40}\mathrm{K}$ *Fermi Gas in the BCS-BEC Crossover*, Phys. Rev. Lett. 97 (2006) (cit. on p. 25).

[111] L Luo, B Clancy, J Joseph, J Kinast, and J. Thomas, *Measurement of the entropy and critical temperature of a strongly interacting Fermi gas*, Phys. Rev. Lett. 98 (2007) (cit. on p. 25).

[112] J. Joseph, B. Clancy, L. Luo, J. Kinast, A. Turlapov, and J. E. Thomas, *Measurement of Sound Velocity in a Fermi Gas near a Feshbach Resonance*, Phys. Rev. Lett. 98 (2007) (cit. on p. 25).

[113] E. Burovski, N. Prokof'ev, B. Svistunov, and M. Troyer, *Critical Temperature and Thermodynamics of Attractive Fermions at Unitarity*, Phys. Rev. Lett. 96 (2006) (cit. on p. 25).

[114] S. Nascimbène, N. Navon, K. Jiang, F. Chevy, and C. Salomon, *Exploring the thermodynamics of a universal Fermi gas*, Nature 463 (2010) (cit. on p. 25).

[115] M. J. Ku, A. T. Sommer, L. W. Cheuk, and M. W. Zwierlein, *Revealing the superfluid lambda transition in the universal thermodynamics of a unitary Fermi gas*, Science 335 (2012) (cit. on pp. 25, 26).

[116] M. K. Tey, L. A. Sidorenkov, E. R. S. Guajardo, R. Grimm, M. J. H. Ku, M. W. Zwierlein, Y.-H. Hou, L. Pitaevskii, and S. Stringari, *Collective Modes in a Unitary Fermi Gas across the Superfluid Phase Transition*, Phys. Rev. Lett. 110 (2013) (cit. on p. 26).

[117] L. A. Sidorenkov, M. K. Tey, R. Grimm, Y.-H. Hou, L. Pitaevskii, and S. Stringari, *Second sound and the superfluid fraction in a Fermi gas with resonant interactions*, Nature 498 (2013) (cit. on p. 26).

[118] A. Larkin and Y. Ovchinnikov, *Nonuniform State of Superconductors*, Soviet Physics-JETP 20 (1965) (cit. on pp. 27, 75).

[119] A. Griesmaier, J. Werner, S. Hensler, J. Stuhler, and T. Pfau, *Bose-Einstein Condensation of Chromium*, Phys. Rev. Lett. 94 (2005) (cit. on p. 28).

[120] C. I. Hancox, S. C. Doret, M. T. Hummon, L. Luo, and J. M. Doyle, *Magnetic trapping of rare-earth atoms at millikelvin temperatures*, Nature 431 (2004) (cit. on p. 28).

[121] J. J. McClelland and J. L. Hanssen, *Laser Cooling without Repumping: A Magneto-Optical Trap for Erbium Atoms*, Phys. Rev. Lett. 96 (2006) (cit. on p. 29).

[122] J. Miao, J. Hostetter, G. Stratis, and M. Saffman, *Magneto-Optical Trapping of Holmium Atoms*, Phys. Rev. A 89 (2014) (cit. on pp. 29, 35).

[123] D. Sukachev, A. Sokolov, K. Chebakov, A. Akimov, S. Kanorsky, N. Kolachevsky, and V. Sorokin, *Magneto-optical trap for thulium atoms*, Phys. Rev. A 82 (2010) (cit. on pp. 29, 35).

[124] M. Lu, S. H. Youn, and B. L. Lev, *Trapping Ultracold Dysprosium: A Highly Magnetic Gas for Dipolar Physics*, Phys. Rev. Lett. 104 (2010) (cit. on p. 29).

[125] G. A. Phelps, A. Hébert, A. Krahn, S. Dickerson, F. Öztürk, S. Ebadi, L. Su, and M. Greiner, *Sub-second production of a quantum degenerate gas*, arXiv:2007.10807 (2020) (cit. on p. 29).

[126] K. Baumann, N. Q. Burdick, M. Lu, and B. L. Lev, *Observation of low-field Fano-Feshbach resonances in ultracold gases of dysprosium*, Phys. Rev. A 89 (2014) (cit. on pp. 29, 58, 77, 101, 105).

[127] A. Frisch, M. Mark, K. Aikawa, F. Ferlaino, J. L. Bohn, C. Makrides, A. Petrov, and S. Kotochigova, *Quantum chaos in ultracold collisions of gas-phase erbium atoms*, Nature 507 (2014) (cit. on pp. 29, 69, 101, 105).

[128] J. L. Bohn, M. Cavagnero, and C. Ticknor, *Quasi-universal dipolar scattering in cold and ultracold gases*, New J. Phys. 11 (2009) (cit. on pp. 29, 55, 106).

[129] M. Lu, N. Q. Burdick, S. H. Youn, and B. L. Lev, *Strongly Dipolar Bose-Einstein Condensate of Dysprosium*, Phys. Rev. Lett. 107 (2011) (cit. on pp. 30, 35, 36, 37, 58, 75).

[130] Y. Tang, N. Q. Burdick, K. Baumann, and B. L. Lev, *Bose–Einstein condensation of* ^{162}Dy *and* ^{160}Dy, New J. Phys. 17 (2015) (cit. on p. 30).

[131] T. Maier, *Interactions in a Quantum Gas of Dysprosium Atoms*. PhD thesis. University of Stuttgart, 2015 (cit. on pp. 30, 36, 37, 56).

[132] Y. Tang, A. Sykes, N. Q. Burdick, J. L. Bohn, and B. L. Lev, *s-wave scattering lengths of the strongly dipolar bosons* $^{162}\mathrm{Dy}$ *and* $^{164}\mathrm{Dy}$, Phys. Rev. A 92 (2015) (cit. on p. 30).

[133] K. Aikawa, A. Frisch, M. Mark, S. Baier, A. Rietzler, R. Grimm, and F. Ferlaino, *Bose-Einstein Condensation of Erbium*, Phys. Rev. Lett. 108 (2012) (cit. on pp. 30, 35, 58, 75).

[134] L. Chomaz, S. Baier, D. Petter, M. J. Mark, F. Wächtler, L. Santos, and F. Ferlaino, *Quantum-Fluctuation-Driven Crossover from a Dilute Bose-Einstein Condensate to a Macrodroplet in a Dipolar Quantum Fluid*, Phys. Rev. X 6 (2016) (cit. on p. 30).

[135] A. Trautmann, P. Ilzhöfer, G. Durastante, C. Politi, M. Sohmen, M. J. Mark, and F. Ferlaino, *Dipolar Quantum Mixtures of Erbium and Dysprosium Atoms*, Phys. Rev. Lett. 121 (2018) (cit. on pp. 30, 51, 76, 101).

[136] M. Wenzel, *Macroscopic States of Dipolar Quantum Gases*. PhD thesis. Universität Stuttgart, 2018 (cit. on p. 30).

[137] M. Guo and T. Pfau, *A new state of matter of quantum droplets*, Front. Phys. 16 (2021) (cit. on p. 30).

[138] H. Kadau, M. Schmitt, M. Wenzel, C. Wink, T. Maier, I. Ferrier-Barbut, and T. Pfau, *Observing the Rosensweig instability of a quantum ferrofluid*, Nature 530 (2016) (cit. on pp. 30, 35, 101).

[139] L. Tanzi, S. M. Roccuzzo, E. Lucioni, F. Famà, A. Fioretti, C. Gabbanini, G. Modugno, A. Recati, and S. Stringari, *Supersolid symmetry breaking from compressional oscillations in a dipolar quantum gas*, Nature 574 (2019) (cit. on p. 30).

[140] L. Tanzi, E. Lucioni, F. Famà, J. Catani, A. Fioretti, C. Gabbanini, R. N. Bisset, L. Santos, and G. Modugno, *Observation of a Dipolar Quantum Gas with Metastable Supersolid Properties*, Phys. Rev. Lett. 122 (2019) (cit. on pp. 30, 101).

[141] L. Chomaz, D. Petter, P. Ilzhöfer, G. Natale, A. Trautmann, C. Politi, G. Durastante, R. M. W. van Bijnen, A. Patscheider, M. Sohmen, M. J. Mark, and F. Ferlaino, *Long-Lived and Transient Supersolid Behaviors in Dipolar Quantum Gases*, Phys. Rev. X 9 (2019) (cit. on pp. 30, 101).

[142] J Hertkorn, J.-N. Schmidt, M Guo, F Böttcher, K. Ng, S. Graham, P Uerlings, H. Büchler, T Langen, M Zwierlein, et al., *Supersolidity in Two-Dimensional Trapped Dipolar Droplet Arrays*, arXiv:2103.09752 (2021) (cit. on p. 30).

[143] V Efimov, *Energy levels of three resonantly interacting particles*, Nucl. Phys. A 210 (1973) (cit. on p. 30).

[144] P. Naidon and S. Endo, *Efimov physics: a review*, Rep. Prog. Phys. 80 (2017) (cit. on p. 30).

[145] S. Endo, P. Naidon, and M. Ueda, *Crossover trimers connecting continuous and discrete scaling regimes*, Phys. Rev. A 86 (2012) (cit. on p. 31).

[146] O. I. Kartavtsev and A. V. Malykh, *Low-energy three-body dynamics in binary quantum gases*, J. Phys. B 40 (2007) (cit. on p. 31).

[147] E. Neri, A. Ciamei, C. Simonelli, I. Goti, M. Inguscio, A. Trenkwalder, and M. Zaccanti, *Realization of a cold mixture of fermionic chromium and lithium atoms*, Phys. Rev. A 101 (2020) (cit. on p. 31).

[148] E. Wille, F. M. Spiegelhalder, G. Kerner, D. Naik, A. Trenkwalder, G. Hendl, F. Schreck, R. Grimm, T. G. Tiecke, J. T. M. Walraven, S. J. J. M. F. Kokkelmans, E. Tiesinga, and P. S. Julienne, *Exploring an Ultracold Fermi-Fermi Mixture: Interspecies Feshbach Resonances and Scattering Properties of* ^{6}Li *and* ^{40}K, Phys. Rev. Lett. 100, 053201 (2008) (cit. on pp. 31, 51, 75).

[149] V. A. Dzuba, V. V. Flambaum, and B. L. Lev, *Dynamic polarizabilities and magic wavelengths for dysprosium*, Phys. Rev. A 83 (2011) (cit. on pp. 32, 36, 38, 39, 43).

[150] H Li, J.-F. Wyart, O Dulieu, S Nascimbène, and M Lepers, *Optical trapping of ultracold dysprosium atoms: transition probabilities, dynamic dipole polarizabilities and van der Waals* C_6 *coefficients*, J. Phys. B 50 (2017) (cit. on pp. 32, 36, 37, 38, 39, 42, 43).

[151] K. Shibata, H. Ikeda, R. Suzuki, and T. Hirano, *Compensation of gravity on cold atoms by a linear optical potential*, Phys. Rev. Research 2 (2020) (cit. on p. 32).

[152] Y. B. Ovchinnikov, I. Manek, and R. Grimm, *Surface Trap for Cs atoms based on Evanescent-Wave Cooling*, Phys. Rev. Lett. 79 (1997) (cit. on p. 32).

[153] B. Mukherjee, Z. Yan, P. B. Patel, Z. Hadzibabic, T. Yefsah, J. Struck, and M. W. Zwierlein, *Homogeneous Atomic Fermi Gases*, Phys. Rev. Lett. 118 (2017) (cit. on p. 32).

[154] M. Kreyer, J. H. Han, C. Ravensbergen, V. Corre, E. Soave, E. Kirilov, and R. Grimm, *Measurement of the dynamic polarizability of Dy atoms near the 626-nm intercombination line*, Phys. Rev. A 104 (2021) (cit. on pp. 32, 126).

[155] K. D. Bonin and V. V. Kresin, *Electric-dipole polarizabilities of atoms, molecules, and clusters*. 1997 (cit. on p. 35).

[156] J. Mitroy, M. S. Safronova, and C. W. Clark, *Theory and applications of atomic and ionic polarizabilities*, J. Phys. B 43 (2010) (cit. on p. 35).

[157] H. H. Stroke, *Advances in atomic, molecular, and optical physics*. Vol. 51. 2005 (cit. on p. 35).

[158] R. Grimm, M. Weidemüller, and Y. B. Ovchinnikov, *Optical dipole traps for neutral atoms*, Adv. At. Mol. Opt. Phys. 42 (2000) (cit. on pp. 35, 37).

[159] L. J. LeBlanc and J. H. Thywissen, *Species-specific optical lattices*, Phys. Rev. A 75 (2007) (cit. on pp. 35, 51).

[160] V. Galitski and I. B. Spielman, *Spin-orbit coupling in quantum gases*, Nature 494 (2013) (cit. on p. 35).

[161] K Aikawa, S Baier, A Frisch, M Mark, C Ravensbergen, and F Ferlaino, *Observation of Fermi surface deformation in a dipolar quantum gas*, Science 345 (2014) (cit. on p. 35).

[162] B. Hemmerling, G. K. Drayna, E. Chae, A. Ravi, and J. M. Doyle, *Buffer gas loaded magneto-optical traps for Yb, Tm, Er and Ho*, New J. Phys. 16 (2014) (cit. on p. 35).

[163] D. Dreon, L. Sidorenkov, C. Bouazza, W. Maineult, J. Dalibard, and S. Nascimbène, *Optical cooling and trapping of highly magnetic atoms: the benefits of a spontaneous spin polarization*, J. Phys. B 50 (2017) (cit. on pp. 35, 38, 52, 53, 103).

[164] N. Q. Burdick, Y. Tang, and B. L. Lev, *Long-Lived Spin-Orbit-Coupled Degenerate Dipolar Fermi Gas*, Phys. Rev. X 6 (2016) (cit. on pp. 36, 55, 77, 94, 101, 105, 127).

[165] X. Cui, B. Lian, T.-L. Ho, B. L. Lev, and H. Zhai, *Synthetic gauge field with highly magnetic lanthanide atoms*, Phys. Rev. A 88 (2013) (cit. on p. 36).

[166] M. Lepers, J.-F. Wyart, and O. Dulieu, *Anisotropic optical trapping of ultracold erbium atoms*, Phys. Rev. A 89 (2014) (cit. on p. 36).

[167] H. Li, J.-F. Wyart, O. Dulieu, and M. Lepers, *Anisotropic optical trapping as a manifestation of the complex electronic structure of ultracold lanthanide atoms: The example of holmium*, Phys. Rev. A 95 (2017) (cit. on p. 36).

[168] M. Schmitt, *A Self-bound Dilute Quantum Liquid of Dysprosium Atoms*. PhD thesis. University of Stuttgart, 2017 (cit. on p. 36).

[169] J. H. Becher, S. Baier, K. Aikawa, M. Lepers, J.-F. Wyart, O. Dulieu, and F. Ferlaino, *Anisotropic polarizability of erbium atoms*, Phys. Rev. A 97 (2018) (cit. on pp. 36, 37, 43).

[170] I. H. Deutsch and P. S. Jessen, *Quantum control and measurement of atomic spins in polarization spectroscopy*, Opt. Commun. 283 (2010) (cit. on p. 36).

[171] A. Khramov, A. H., W. Dowd, R. J. Roy, C. Makrides, A. Petrov, S. Kotochigova, and S. Gupta, *Ultracold Heteronuclear Mixture of Ground and Excited State Atoms*, Phys. Rev. Lett. 112 (2014) (cit. on p. 37).

[172] B. Neyenhuis, B. Yan, S. A. Moses, J. P. Covey, A. Chotia, A. Petrov, S. Kotochigova, J. Ye, and D. S. Jin, *Anisotropic Polarizability of Ultracold Polar* $^{40}\mathrm{K}^{87}\mathrm{Rb}$ *Molecules*, Phys. Rev. Lett. 109 (2012) (cit. on p. 37).

[173] J. G. Danzl, M. J. Mark, E. Haller, M. Gustavsson, R. Hart, J. Aldegunde, J. M. Hutson, and H.-C. Nägerl, *An ultracold high-density sample of rovibronic ground-state molecules in an optical lattice*, Nat. Phys. 6 (2010) (cit. on p. 37).

[174] M. S. Safronova, U. I. Safronova, and C. W. Clark, *Magic wavelengths for optical cooling and trapping of potassium*, Phys. Rev. A 87 (2013) (cit. on pp. 38, 43).

[175] M. S. Safronova. private communication (cit. on p. 38).

[176] T. Maier, H. Kadau, M. Schmitt, A. Griesmaier, and T. Pfau, *Narrow-line magneto-optical trap for dysprosium atoms*, Opt. Lett. 39 (2014) (cit. on pp. 38, 52, 53, 102).

[177] D. Fernandes, F. Sievers, N. Kretzschmar, S. Wu, C. Salomon, and F. Chevy, *Sub-Doppler laser cooling of fermionic* ^{40}K *atoms in three-dimensional gray optical molasses*, Europhys. Lett. 100 (2012) (cit. on pp. 38, 71).

[178] F. Dalfovo, S. Giorgini, L. P. Pitaevskii, and S. Stringari, *Theory of Bose-Einstein condensation in trapped gases*, Rev. Mod. Phys. 71 (1999) (cit. on p. 39).

[179] V. Flambaum and M. Dzuba. private communication (cit. on p. 43).

[180] M. Lepers and O. Dulieu. private communication (cit. on p. 43).

[181] W. V. Liu and F. Wilczek, *Interior Gap Superfluidity*, Phys. Rev. Lett. 90 (2003) (cit. on pp. 43, 50).

[182] M. Iskin and C. A. R. Sá de Melo, *Two-Species Fermion Mixtures with Population Imbalance*, Phys. Rev. Lett. 97, 100404 (2006) (cit. on p. 43).

[183] M. M. Parish, F. M. Marchetti, A. Lamacraft, and B. D. Simons, *Polarized Fermi Condensates with Unequal Masses: Tuning the Tricritical Point*, Phys. Rev. Lett. 98 (2007) (cit. on p. 43).

[184] M. A. Baranov, C. Lobo, and G. V. Shlyapnikov, *Superfluid pairing between fermions with unequal masses*, Phys. Rev. A 78 (2008) (cit. on pp. 43, 51).

[185] A. Gezerlis, S. Gandolfi, K. E. Schmidt, and J. Carlson, *Heavy-light fermion mixtures at unitarity*, Phys. Rev. Lett. 103 (2009) (cit. on pp. 43, 97).

[186] J. Braun, J. E. Drut, and D. Roscher, *Zero-Temperature Equation of State of Mass-Imbalanced Resonant Fermi Gases*, Phys. Rev. Lett. 114 (2015) (cit. on p. 43).

[187] M. Tinkham, *Introduction to Superconductivity*. 1996 (cit. on p. 50).

[188] K.-H. Bennemann and J. B. Ketterson, *Novel Superfluids: Volumes 1 and 2*. 2013, 2014 (cit. on pp. 50, 75).

[189] G. Brown and H. Bethe, *A scenario for a large number of low-mass black holes in the galaxy*, Astrophys. J. 423 (1994) (cit. on p. 50).

[190] A. Sedrakian, T. Alm, and U. Lombardo, *Superfluidity in asymmetric nuclear matter*, Phys. Rev. C 55 (1997) (cit. on p. 50).

[191] R. Casalbuoni and G. Nardulli, *Inhomogeneous superconductivity in condensed matter and QCD*, Rev. Mod. Phys. 76 (2004) (cit. on p. 50).

[192] A. Rapp, G. Zaránd, C. Honerkamp, and W. Hofstetter, *Color Superfluidity and "Baryon" Formation in Ultracold Fermions*, Phys. Rev. Lett. 98 (2007) (cit. on p. 50).

[193] F. Wilczek, *Quantum chromodynamics: Lifestyles of the small and simple*, Nat. Phys. 3 (2007) (cit. on p. 50).

[194] D. Bailin and A. Love, *Superfluidity and superconductivity in relativistic fermion systems*, Phys. Rep. 107 (1984) (cit. on p. 50).

[195] B. C. Barrois, *Superconducting quark matter*, Nucl. Phys. B 129 (1977) (cit. on p. 50).

[196] L. Radzihovsky and D. E. Sheehy, *Imbalanced Feshbach-resonant Fermi gases*, Rep. Prog. Phys. 73 (2010) (cit. on pp. 50, 75).

[197] E. Gubankova, W. V. Liu, and F. Wilczek, *Breached Pairing Superfluidity: Possible Realization in QCD*, Phys. Rev. Lett. 91 (2003) (cit. on p. 50).

[198] K. B. Gubbels, J. E. Baarsma, and H. T. C. Stoof, *Lifshitz Point in the Phase Diagram of Resonantly Interacting* ^{6}Li-^{40}**K** *Mixtures*, Phys. Rev. Lett. 103 (2009) (cit. on pp. 50, 75, 84, 86).

[199] K. Gubbels and H. Stoof, *Imbalanced Fermi gases at unitarity*, Phys. Rep. 525 (2013) (cit. on pp. 50, 70, 75, 97, 101).

[200] I. Bausmerth, A. Recati, and S. Stringari, *Chandrasekhar-Clogston limit and phase separation in Fermi mixtures at unitarity*, Phys. Rev. A 79 (2009) (cit. on p. 51).

[201] K. M. Daily and D. Blume, *Thermodynamics of the two-component Fermi gas with unequal masses at unitarity*, Phys. Rev. A 85 (2012) (cit. on p. 51).

[202] R. B. Diener and M. Randeria, *BCS-BEC crossover with unequal-mass fermions*, Phys. Rev. A 81 (2010) (cit. on p. 51).

[203] P. Massignan, M. Zaccanti, and G. M. Bruun, *Polarons, dressed molecules and itinerant ferromagnetism in ultracold Fermi gases*, Rep. Prog. Phys. 77 (2014) (cit. on p. 51).

[204] A Amico, F Scazza, G Valtolina, P. Tavares, W Ketterle, M Inguscio, G Roati, and M Zaccanti, *Time-resolved observation of competing attractive and repulsive short-range correlations in strongly interacting Fermi gases*, Phys. Rev. Lett. (2018) (cit. on p. 51).

[205] D. S. Petrov, G. E. Astrakharchik, D. J. Papoular, C. Salomon, and G. V. Shlyapnikov, *Crystalline Phase of Strongly Interacting Fermi Mixtures*, Phys. Rev. Lett. 99, 130407 (2007) (cit. on p. 51).

[206] M. Knap, A. Shashi, Y. Nishida, A. Imambekov, D. A. Abanin, and E. Demler, *Time-Dependent Impurity in Ultracold Fermions: Orthogonality Catastrophe and Beyond*, Phys. Rev. X 2 (2012) (cit. on p. 51).

[207] J.-S. You, R. Schmidt, D. Ivanov, M. Knap, and E. Demler, *Atomtronics with a spin: statistics of spin transport and non-equilibrium orthogonality catastrophe in cold quantum gases*, Phys. Rev. B 99 (2018) (cit. on p. 51).

[208] Y. Nishida, *Transport measurement of the orbital Kondo effect with ultracold atoms*, Phys. Rev. A 93 (2016) (cit. on p. 51).

[209] J. Levinsen, T. G. Tiecke, J. T. M. Walraven, and D. S. Petrov, *Atom-dimer scattering and long-lived trimers in fermionic mixtures*, Phys. Rev. Lett. 103 (2009) (cit. on p. 51).

[210] M. Jag, M. Zaccanti, M. Cetina, R. S. Lous, F. Schreck, R. Grimm, D. S. Petrov, and J. Levinsen, *Observation of a Strong Atom-Dimer Attraction in a Mass-Imbalanced Fermi-Fermi Mixture*, Phys. Rev. Lett. 112 (2014) (cit. on pp. 51, 75).

[211] Y. Nishida and S. Tan, *Confinement-induced Efimov resonances in Fermi-Fermi mixtures*, Phys. Rev. A 79 (2009) (cit. on p. 51).

[212] M. Taglieber, A.-C. Voigt, T. Aoki, T. W. Hänsch, and K. Dieckmann, *Quantum Degenerate Two-Species Fermi-Fermi Mixture Coexisting with a Bose-Einstein Condensate*, Phys. Rev. Lett. 100, 010401 (2008) (cit. on p. 51).

[213] F. M. Spiegelhalder, A. Trenkwalder, D. Naik, G. Hendl, F. Schreck, and R. Grimm, *Collisional stability of ^{40}K immersed in a strongly interacting Fermi Gas of ^{6}Li*, Phys. Rev. Lett. 103 (2009) (cit. on p. 51).

[214] T. G. Tiecke, M. R. Goosen, A. Ludewig, S. D. Gensemer, S. Kraft, S. J. J. M. F. Kokkelmans, and J. T. M. Walraven, *Broad Feshbach resonance in the ^{6}Li-^{40}K mixture*, Phys. Rev. Lett. 104 (2010) (cit. on pp. 51, 75).

[215] A. Ridinger, S. Chaudhuri, T. Salez, U. Eismann, D. R. Fernandes, K. Magalhães, D. Wilkowski, C. Salomon, and F. Chevy, *Large atom number dual-species magneto-optical trap for fermionic 6Li and ^{40}K atoms*, Eur. Phys. J. D 65 (2011) (cit. on pp. 51, 53).

[216] A. Trenkwalder, C. Kohstall, M. Zaccanti, D. Naik, A. I. Sidorov, F. Schreck, and R. Grimm, *Hydrodynamic Expansion of a Strongly Interacting Fermi-Fermi Mixture*, Phys. Rev. Lett. 106 (2011) (cit. on pp. 51, 75, 82).

[217] M. Cetina, M. Jag, R. S. Lous, I. Fritsche, J. T. M. Walraven, R. Grimm, J. Levinsen, M. M. Parish, R. Schmidt, M. Knap, and E. Demler, *Ultrafast many-body interferometry of impurities coupled to a Fermi sea*, Science 354 (2016) (cit. on p. 51).

[218] D. Naik, A. Trenkwalder, C. Kohstall, F. M. Spiegelhalder, M. Zaccanti, G. Hendl, F. Schreck, R. Grimm, T. Hanna, and P. Julienne, *Feshbach resonances in the ^{6}Li-^{40}K Fermi-Fermi mixture: Elastic versus inelastic interactions*, Eur. Phys. J. D 65 (2011) (cit. on pp. 51, 75).

[219] D. S. Petrov, C. Salomon, and G. V. Shlyapnikov, *Scattering properties of weakly bound dimers of fermionic atoms*, Phys. Rev. A 71, 012708 (2005) (cit. on pp. 51, 75, 83).

[220] D. S. Petrov, C Salomon, and G. V. Shlyapnikov, *Diatomic molecules in ultracold Fermi gases - novel composite bosons*, J. Phys. B 38 (2005) (cit. on pp. 51, 75, 83).

[221] B. Marcelis, S. J. J. M. F. Kokkelmans, G. V. Shlyapnikov, and D. S. Petrov, *Collisional properties of weakly bound heteronuclear dimers*, Phys. Rev. A 77 (2008) (cit. on pp. 51, 52).

[222] K. Dieckmann, C. A. Stan, S. Gupta, Z. Hadzibabic, C. H. Schunck, and W. Ketterle, *Decay of an Ultracold Fermionic Lithium Gas near a Feshbach Resonance*, Phys. Rev. Lett. 89 (2002) (cit. on pp. 51, 82, 94).

[223] S. Baier, D. Petter, J. H. Becher, A. Patscheider, G. Natale, L. Chomaz, M. J. Mark, and F. Ferlaino, *Realization of a Strongly Interacting Fermi Gas of Dipolar Atoms*, Phys. Rev. Lett. 121 (2018) (cit. on pp. 51, 76).

[224] M. Jag, M. Cetina, R. S. Lous, R. Grimm, J. Levinsen, and D. S. Petrov, *Lifetime of Feshbach dimers in a Fermi-Fermi mixture of ^{6}Li and ^{40}K*, Phys. Rev. A 94 (2016) (cit. on pp. 51, 52, 75, 92).

[225] L. Pitaevskii and S. Stringari, *Bose-Einstein Condensation and Superfluidity*. 2016 (cit. on pp. 51, 75).

[226] W. Zwerger, *The BCS-BEC Crossover and the Unitary Fermi Gas*. 2012 (cit. on pp. 51, 75).

[227] G. C. Strinati, P. Pieri, G. Röpke, P. Schuck, and M. Urban, *The BCS-BEC crossover: From ultra-cold Fermi gases to nuclear systems*, Phys. Rep. 738 (2018) (cit. on pp. 51, 75).

[228] M. K. Tey, S. Stellmer, R. Grimm, and F. Schreck, *Double-degenerate Bose-Fermi mixture of strontium*, Phys. Rev. A 82 (2010) (cit. on p. 52).

[229] M. L. González-Martínez, *Magnetically tunable Feshbach resonances in Li+Er*, Phys. Rev. A 92 (2015) (cit. on pp. 52, 76).

[230] P. S. Zuchowski, J. Aldegunde, and J. M. Hutson, *Ultracold RbSr molecules can be formed by magnetoassociation*, Phys. Rev. Lett. 105 (2010) (cit. on p. 52).

[231] V. Barbé, A. Ciamei, B. Pasquiou, L. Reichsöllner, F. Schreck, P. S. Żuchowski, and J. M. Hutson, *Observation of Feshbach resonances between alkali and closed-shell atoms*, Nat. Phys. 14 (2018) (cit. on p. 52).

[232] C. Ravensbergen, V. Corre, E. Soave, M. Kreyer, S. Tzanova, E. Kirilov, and R. Grimm, *Accurate Determination of the Dynamical Polarizability of Dysprosium*, Phys. Rev. Lett. 120 (2018) (cit. on pp. 55, 69, 73, 76, 77, 119).

[233] K. Aikawa, A. Frisch, M. Mark, S. Baier, R. Grimm, J. L. Bohn, D. S. Jin, G. M. Bruun, and F. Ferlaino, *Anisotropic Relaxation Dynamics in a Dipolar Fermi Gas Driven Out of Equilibrium*, Phys. Rev. Lett. 113 (2014) (cit. on p. 55).

[234] H. Hara, Y. Takasu, Y. Yamaoka, J. M. Doyle, and Y. Takahashi, *Quantum Degenerate Mixtures of Alkali and Alkaline-Earth-Like Atoms*, Phys. Rev. Lett. 106 (2011) (cit. on p. 56).

[235] A. H. Hansen, A. Khramov, W. H. Dowd, A. O. Jamison, V. V. Ivanov, and S. Gupta, *Quantum degenerate mixture of ytterbium and lithium atoms*, Phys. Rev. A 84 (2011) (cit. on p. 56).

[236] A. H. Hansen, A. Y. Khramov, W. H. Dowd, A. O. Jamison, B. Plotkin-Swing, R. J. Roy, and S. Gupta, *Production of quantum-degenerate mixtures of ytterbium and lithium with controllable interspecies overlap*, Phys. Rev. A 87 (2013) (cit. on pp. 56, 62, 65).

[237] M. Landini, S. Roy, G. Roati, A. Simoni, M. Inguscio, G. Modugno, and M. Fattori, *Direct evaporative cooling of* ^{39}K *atoms to Bose-Einstein condensation*, Phys. Rev. A 86 (2012) (cit. on p. 56).

[238] Y. Takasu, K. Maki, K. Komori, T. Takano, K. Honda, M. Kumakura, T. Yabuzaki, and Y. Takahashi, *Spin-singlet Bose-Einstein condensation of two-electron atoms*, Phys. Rev. Lett. 91 (2003) (cit. on p. 58).

[239] S. Stellmer, M. K. Tey, B. Huang, R. Grimm, and F. Schreck, *Bose-Einstein condensation of strontium*, Phys. Rev. Lett. 103 (2009) (cit. on p. 58).

[240] C.-L. Hung, X. Zhang, N. Gemelke, and C. Chin, *Accelerating evaporative cooling of atoms into Bose-Einstein condensation in optical traps*, Phys. Rev. A 78 (2008) (cit. on p. 61).

[241] R. S. Lous, I. Fritsche, M. Jag, B. Huang, and R. Grimm, *Thermometry of a deeply degenerate Fermi gas with a Bose-Einstein condensate*, Phys. Rev. A 95 (2017) (cit. on pp. 61, 65).

[242] T. Weber, J. Herbig, M. Mark, H.-C. Nägerl, and R. Grimm, *Bose-Einstein Condensation of Cesium*, Science 299 (2003) (cit. on pp. 65, 115).

[243] A. Mosk, S. Kraft, M. Mudrich, K. Singer, W. Wohlleben, R. Grimm, and M. Weidemüller, *Mixture of ultracold lithium and cesium atoms in an optical dipole trap*, Appl. Phys. B 73 (2001) (cit. on pp. 67, 73, 87, 90).

[244] S Tassy, N Nemitz, F Baumer, C Höhl, A Batär, and A Görlitz, *Sympathetic cooling in a mixture of diamagnetic and paramagnetic atoms*, J. Phys. B 43 (2010) (cit. on p. 67).

[245] A. Guttridge, S. A. Hopkins, S. L. Kemp, M. D. Frye, J. M. Hutson, and S. L. Cornish, *Interspecies thermalization in an ultracold mixture of Cs and Yb in an optical trap*, Phys. Rev. A 96 (2017) (cit. on p. 67).

[246] A. Petrov, E. Tiesinga, and S. Kotochigova, *Anisotropy Induced Feshbach Resonances in a Quantum Dipolar Gas of Highly Magnetic Atoms*, Phys. Rev. Lett. 109 (2012) (cit. on pp. 69, 76, 101).

[247] T. Maier, I. Ferrier-Barbut, H. Kadau, M. Schmitt, M. Wenzel, C. Wink, T. Pfau, K. Jachymski, and P. S. Julienne, *Broad universal Feshbach resonances in the chaotic spectrum of dysprosium atoms*, Phys. Rev. A 92 (2015) (cit. on pp. 69, 110, 111).

[248] E. Lucioni, L. Tanzi, A. Fregosi, J. Catani, S. Gozzini, M. Inguscio, A. Fioretti, C. Gabbanini, and G. Modugno, *Dysprosium dipolar Bose-Einstein condensate with broad Feshbach resonances*, Phys. Rev. A 97 (2018) (cit. on p. 69).

[249] K. Dieckmann, R. J. C. Spreeuw, M. Weidemüller, and J. T. M. Walraven, *Two-dimensional magneto-optical trap as a source of slow atoms*, Phys. Rev. A 58 (1998) (cit. on p. 70).

[250] J. Levinsen and D. Petrov, *Atom-dimer and dimer-dimer scattering in fermionic mixtures near a narrow Feshbach resonance*, Eur. Phys. J. D 65 (2011) (cit. on p. 75).

[251] M. Arndt, M. Ben Dahan, D. Guéry-Odelin, M. W. Reynolds, and J. Dalibard, *Observation of a Zero-Energy Resonance in Cs-Cs Collisions*, Phys. Rev. Lett. 79 (1997) (cit. on pp. 77, 80).

[252] M. E. Gehm, S. L. Hemmer, K. M. O'Hara, and J. E. Thomas, *Unitarity-limited elastic collision rate in a harmonically trapped Fermi gas*, Phys. Rev. A 68 (2003) (cit. on pp. 77, 80).

[253] M. Anderlini, D. Ciampini, D. Cossart, E. Courtade, M. Cristiani, C. Sias, O. Morsch, and E. Arimondo, *Model for collisions in ultracold-atom mixtures*, Phys. Rev. A 72 (2005) (cit. on p. 78).

[254] C. A. Regal, M. Greiner, and D. S. Jin, *Lifetime of Molecule-Atom Mixtures near a Feshbach Resonance in K*, Phys. Rev. Lett. 92, 083201 (2004) (cit. on pp. 81, 82, 94).

[255] S. Jochim, *Bose-Einstein Condensation of Molecules*. PhD thesis. Innsbruck University, 2004 (cit. on pp. 82, 94).

[256] G. Barontini, C. Weber, F. Rabatti, J. Catani, G. Thalhammer, M. Inguscio, and F. Minardi, *Observation of heteronuclear atomic Efimov resonances*, Phys. Rev. Lett. 103 (2009) (cit. on p. 83).

[257] R. A. W. Maier, M. Eisele, E. Tiemann, and C. Zimmermann, *Efimov Resonance and Three-Body Parameter in a Lithium-Rubidium Mixture*, Phys. Rev. Lett. 115 (2015) (cit. on p. 83).

[258] L. J. Wacker, N. B. Jørgensen, D. Birkmose, N. Winter, M. Mikkelsen, J. Sherson, N. Zinner, and J. J. Arlt, *Universal Three-Body Physics in Ultracold KRb Mixtures*, Phys. Rev. Lett. 117 (2016) (cit. on p. 83).

[259] R. S. Bloom, M.-G. Hu, T. D. Cumby, and D. S. Jin, *Tests of Universal Three-Body Physics in an Ultracold Bose-Fermi Mixture*, Phys. Rev. Lett. 111 (2013) (cit. on p. 83).

[260] R. Pires, J. Ulmanis, S. Häfner, M. Repp, A. Arias, E. D. Kuhnle, and M. Weidemüller, *Observation of Efimov Resonances in a Mixture with Extreme Mass Imbalance*, Phys. Rev. Lett. 112 (2014) (cit. on p. 83).

[261] S.-K. Tung, K. Jiménez-García, J. Johansen, C. V. Parker, and C. Chin, *Geometric Scaling of Efimov States in a* $^{6}\mathrm{Li}{-}^{133}\mathrm{Cs}$ *Mixture*, Phys. Rev. Lett. 113 (2014) (cit. on p. 83).

[262] J. Ulmanis, S. Häfner, R. Pires, F. Werner, D. S. Petrov, E. D. Kuhnle, and M. Weidemüller, *Universal three-body recombination and Efimov resonances in an ultracold Li-Cs mixture*, Phys. Rev. A 93 (2016) (cit. on p. 83).

[263] R. S. Lous, I. Fritsche, M. Jag, F. Lehmann, E. Kirilov, B. Huang, and R. Grimm, *Probing the Interface of a Phase-Separated State in a Repulsive Bose-Fermi Mixture*, Phys. Rev. Lett. 120 (2018) (cit. on pp. 83, 131).

[264] S. Tzanova, *Realization and Characterization of two Unconventional Ultracold Mixtures*. PhD thesis. Institut für Experimentalphysik, Universität Innsbruck, 2020 (cit. on p. 83).

[265] M. W. Zwierlein, A. Schirotzek, C. H. Schunck, and W. Ketterle, *Direct observation of the superfluid phase transition in ultracold Fermi gases*, Nature (London) 442 (2006) (cit. on p. 83).

[266] A. D. Lange, K. Pilch, A. Prantner, F. Ferlaino, B. Engeser, H.-C. Nägerl, R. Grimm, and C. Chin, *Determination of atomic scattering lengths from measurements of molecular binding energies near Feshbach resonances*, Phys. Rev. A 79 (2009) (cit. on p. 86).

[267] K. Jachymski and P. S. Julienne, *Analytical model of overlapping Feshbach resonances*, Phys. Rev. A 88 (2013) (cit. on p. 86).

[268] K. M. O'Hara, S. L. Hemmer, S. R. Granade, M. E. Gehm, J. E. Thomas, V. Venturi, E. Tiesinga, and C. J. Williams, *Measurement of the zero crossing in a Feshbach resonance of fermionic* ^{6}Li, Phys. Rev. A 66 (2002) (cit. on p. 87).

[269] S. Jochim, M. Bartenstein, G. Hendl, J. Hecker Denschlag, R. Grimm, A. Mosk, and W. Weidemüller, *Magnetic Field Control of Elastic Scattering in a Cold Gas of Fermionic Lithium Atoms*, Phys. Rev. Lett 89 (2002) (cit. on p. 87).

[270] J. R. Taylor, *An Introduction to Error Analysis*. Vol. 92. 1997 (cit. on p. 88).

[271] T. Weber, J. Herbig, M. Mark, H.-C. Nägerl, and R. Grimm, *Three-Body Recombination at Large Scattering Lengths in an Ultracold Atomic Gas*, Phys. Rev. Lett. 91 (2003) (cit. on p. 94).

[272] C. Lobo, A. Recati, S. Giorgini, and S. Stringari, *Normal State of a Polarized Fermi Gas at Unitarity*, Phys. Rev. Lett. 97 (2006) (cit. on p. 97).

[273] L. Chomaz, I. Ferrier-Barbut, F. Ferlaino, B. Laburthe-Tolra, B. L. Lev, and T. Pfau, *Dipolar physics: A review of experiments with magnetic quantum gases*, arXiv:2201.02672 92 (2022) (cit. on p. 101).

[274] F. Böttcher, J.-N. Schmidt, M. Wenzel, J. Hertkorn, M. Guo, T. Langen, and T. Pfau, *Transient Supersolid Properties in an Array of Dipolar Quantum Droplets*, Phys. Rev. X 9 (2019) (cit. on p. 101).

[275] C. Politi, A. Trautmann, P. Ilzhöfer, G. Durastante, M. J. Mark, M. Modugno, and F. Ferlaino, *Interspecies interactions in an ultracold dipolar mixture*, Phys. Rev. A 105 (2022) (cit. on p. 101).

[276] T. Maier, H. Kadau, M. Schmitt, M. Wenzel, I. Ferrier-Barbut, T. Pfau, A. Frisch, S. Baier, K. Aikawa, L. Chomaz, M. J. Mark, F. Ferlaino, C. Makrides, E. Tiesinga, A. Petrov, and S. Kotochigova, *Emergence of Chaotic Scattering in Ultracold Er and Dy*, Phys. Rev. X 5 (2015) (cit. on pp. 101, 105, 108, 127).

[277] C. H. Schunck, M. W. Zwierlein, C. A. Stan, S. M. F. Raupach, W. Ketterle, A. Simoni, E. Tiesinga, C. J. Williams, and P. S. Julienne, *Feshbach Resonances in Fermionic ^{6}Li*, Phys. Rev. A 71 (2005) (cit. on p. 102).

[278] M. Waseem, J. Yoshida, T. Saito, and T. Mukaiyama, *Unitarity-limited behavior of three-body collisions in a p-wave interacting Fermi gas*, Phys. Rev. A 98 (2018) (cit. on pp. 102, 111, 112).

[279] V. A. Khlebnikov, D. A. Pershin, V. V. Tsyganok, E. T. Davletov, I. S. Cojocaru, E. S. Fedorova, A. A. Buchachenko, and A. V. Akimov, *Random to Chaotic Statistic Transformation in Low-Field Fano-Feshbach Resonances of Cold Thulium Atoms*, Phys. Rev. Lett. 123 (2019) (cit. on p. 105).

[280] E. A. Burt, R. W. Ghrist, C. J. Myatt, M. J. Holland, E. A. Cornell, and C. E. Wieman, *Coherence, Correlations, and Collisions: What One Learns about Bose-Einstein Condensates from Their Decay*, Phys. Rev. Lett. 79 (1997) (cit. on p. 106).

[281] J. Söding, D. Guéry-odelin, P. Desbiolles, F. Chevy, H. Inamori, and J. Dalibard, *Three-body decay of a rubidium Bose-Einstein condensate*, Appl. Phys. B 69 (1999) (cit. on p. 106).

[282] A. Green, H. Li, J. H. See Toh, X. Tang, K. C. McCormick, M. Li, E. Tiesinga, S. Kotochigova, and S. Gupta, *Feshbach Resonances in p-Wave Three-Body Recombination within Fermi-Fermi Mixtures of Open-Shell* ^{6}Li *and Closed-Shell* ^{173}Yb *Atoms*, Phys. Rev. X 10 (2020) (cit. on pp. 108, 109).

[283] C. Ticknor, C. A. Regal, D. S. Jin, and J. L. Bohn, *Multiplet structure of Feshbach resonances in nonzero partial waves*, Phys. Rev. A 69 (2004) (cit. on p. 109).

[284] T. Nakasuji, J. Yoshida, and T. Mukaiyama, *Experimental determination of p-wave scattering parameters in ultracold* ^{6}*Li atoms*, Phys. Rev. A 88 (2013) (cit. on p. 109).

[285] J. Li, J. Liu, L. Luo, and B. Gao, *Three-Body Recombination near a Narrow Feshbach Resonance in* ^{6}Li, Phys. Rev. Lett. 120 (2018) (cit. on p. 109).

[286] B. S. Rem, A. T. Grier, I. Ferrier-Barbut, U. Eismann, T. Langen, N. Navon, L. Khaykovich, F. Werner, D. S. Petrov, F. Chevy, and C. Salomon, *Lifetime of the Bose Gas with Resonant Interactions*, Phys. Rev. Lett. 110 (2013) (cit. on pp. 110, 111).

[287] R. J. Fletcher, A. L. Gaunt, N. Navon, R. P. Smith, and Z. Hadzibabic, *Stability of a Unitary Bose Gas*, Phys. Rev. Lett. 111 (2013) (cit. on pp. 110, 111).

[288] U. Eismann, L. Khaykovich, S. Laurent, I. Ferrier-Barbut, B. S. Rem, A. T. Grier, M. Delehaye, F. Chevy, C. Salomon, L.-C. Ha, and C. Chin, *Universal Loss Dynamics in a Unitary Bose Gas*, Phys. Rev. X 6 (2016) (cit. on p. 110).

[289] M. Schmidt, H.-W. Hammer, and L. Platter, *Three-body losses of a polarized Fermi gas near a p-wave Feshbach resonance in effective field theory*, Phys. Rev. A 101 (2020) (cit. on p. 112).

[290] T. Weber, J. Herbig, M. Mark, H.-C. Nägerl, and R. Grimm, *Three-Body Recombination at Large Scattering Lengths in an Ultracold Atomic Gas*, Phys. Rev. Lett. 91 (2003) (cit. on pp. 113, 114).

[291] E. Timmermans, *Degenerate Fermion Gas Heating by Hole Creation*, Phys. Rev. Lett. 87 (2001) (cit. on p. 113).

[292] M. Kreyer, *PhD thesis, manuscript in preparation.* 2022 (cit. on p. 120).

[293] T. Maier, I. Ferrier-Barbut, H. Kadau, M. Schmitt, M. Wenzel, C. Wink, T. Pfau, K. Jachymski, and P. S. Julienne, *Broad universal Feshbach resonances in the chaotic spectrum of dysprosium atoms*, Phys. Rev. A 92 (2015) (cit. on pp. 120, 131).

[294] G. Orso, L. P. Pitaevskii, and S. Stringari, *Equilibrium and dynamics of a trapped superfluid Fermi gas with unequal masses*, Phys. Rev. A 77 (2008) (cit. on p. 121).

[295] T. G. Tiecke, *Properties of Potassium. v1.03*. 2019 (cit. on p. 126).

[296] W. C. Martin, R Zalubas, and L Hagan, *Atomic energy levels - the rare earth elements*, Phys. Rev. A 92 (1978) (cit. on p. 126).

[297] M. Lu, S. H. Youn, and B. L. Lev, *Spectroscopy of a narrow-line laser-cooling transition in atomic dysprosium*, Phys. Rev. A 83 (2011) (cit. on p. 126).

[298] M. Mayle, B. P. Ruzic, and J. L. Bohn, *Statistical aspects of ultracold resonant scattering*, Phys. Rev. A 85 (2012) (cit. on p. 127).

[299] Q. Lin, M. A. V. Camp, H. Zhang, B. Jelenković, and V. Vuletić, *Long-external-cavity distributed Bragg reflector laser with subkilohertz intrinsic linewidth*, Opt. Lett. 37 (2012) (cit. on pp. 137, 138, 141).

[300] D. S. Elliott, R. Roy, and S. J. Smith, *Extracavity laser band-shape and bandwidth modification*, Phys. Rev. A 26 (1982) (cit. on p. 138).

[301] G. Di Domenico, S. Schilt, and P. Thomann, *Simple approach to the relation between laser frequency noise and laser line shape*, Applied optics 49 (Sept. 2010) (cit. on p. 139).

[302] E. Bava, G. Galzerano, and C. Svelto, *Measurement methods of frequency noise in optical sources based on Fabry-Perot discriminators*, *Proceedings of the 1999 Joint Meeting of the European Frequency and Time Forum and the IEEE International Frequency Control Symposium (Cat. No. 99CH36313).* Vol. 2. IEEE. 1999 (cit. on p. 139).

[303] C. Henry, *Phase noise in semiconductor lasers*, J. Light. Technol. 4 (1986) (cit. on pp. 141, 143).

[304] F. Favre, D Guen, and J Simon, *Optical feedback effects upon laser diode oscillation field spectrum*, IEEE Journal of Quantum Electronics 18 (1982) (cit. on p. 141).

[305] Wikipedia contributors, *Phase-locked loop — Wikipedia, The Free Encyclopedia*. 2021 (cit. on p. 144).

[306] M. Prevedelli, T. Freegarde, and T. W. Hänsch, *Phase locking of grating-tuned diode lasers*, App. Phys. B 60 (1995) (cit. on pp. 144, 147).

[307] S. Hild, *Resolved Raman sideband cooling in a doughnut-shaped optical trap*. Institut für Angewandte Physik, Universität Bonn, 2011 (cit. on p. 144).

[308] P. Corrc, O. Girad, and I. de Faria, *On the thermal contribution to the FM response of DFB lasers: theory and experiment*, IEEE Journal of Quantum Electronics 30 (1994) (cit. on p. 146).

[309] G. Pandian and S. Dilwali, *On the thermal FM response of a semiconductor laser diode*, IEEE Photonics Technology Letters 4 (1992) (cit. on p. 146).

[310] A. Hambitzer, *Direct Synthesis of Light Polarization for State-Dependent Transport*. Institut für Angewandte Physik, Universität Bonn, 2012 (cit. on p. 147).

A special acknowledgement

I would like to use this page to address my gratitude to Rudi. Besides the great opportunity he gave me to be one of his students, I would like to thank him for the invaluable support he gave me on building my family. During my PhD both Pietro and Luisa were born: along with them came two *mutterschutz* periods, working afternoons which unavoidably stopped when the kinderkrippe closed, lots of *pflegefreistellung*... In all this, Rudi's support never waned. I never felt *considered less*, I never had the impression of unsaid complaints, I never had the feeling I should have felt guilty. I just felt myself to be a *normal* PhD student, doing her research on quantum gases.

I would also like to thank Lorenzo, who evenly shares with me the duties of parenthood, leaving me the possibility and time to pursue in my PhD work. Last but not least, a special thanks goes to Prof. Tracy Northup, who greatly supported Lorenzo (and, indirectly, me) in all this.

I wish all women in science could feel themselves to be *normal* scientists as I do, and all parents could receive from their bosses the same support as Lorenzo and I do.

Acknowledgements

Five years is a lot of time. A time full of the great people I met, the things I learned[7], the experience I gained, and the memories I collected. There are so many people to whom I would like to express my gratitude, that I will hardly manage to mention them all.

First of all, I would like to thank Rudi for giving me the opportunity to be one of his students and to work in such a stimulating environment. The meetings and the discussions in the lab have been an inestimable source of learning. His deep and broad overview of physics together with his passion for teaching have been a constant boost to my knowledge.

In these years the DyK lab has been basically a second home. I would like to thank, in order of appearance, Cornee, Slava, Emil, Vincent, Marian, Jeong Ho, Yakoov, Zhuxiong and Alberto. I am particularly grateful to Cornee for building such a complex but amazingly stable machine, teaching me how to deal with it and guiding me through my PhD. Thanks for the technical know-how you transmitted me as well as for the overall great time we had in the lab. Thanks to Emil, the (literally) massive strength of the experiment, for all the explanations, the physics discussions, the venting about everything and nothing (kids included). Thanks to Gregor and his boundless help and source of knowledge about electronics and computers. Thanks to the FeLiKx team (Bo, Rianne, Isabella, Cosetta Erich) for sharing lab hacks, experience, codes, material, and many happy moments. In particular, thanks to Isabella, who was always ready to help, active and energetic. A special thanks also goes to Christine, Verena, Heide, the administrative staff, the electronic and the mechanical workshop, as well as to the whole ultracold Innsbruck community, both at University and at IQOQI.

My PhD was carried out within the Doktoratskolleg atoms, light and molecules (DK ALM). As part of this project, I spent six months in Prof. Martin Zwierlein's group at MIT (Boston). I would like to thank him for accepting me to be part of his team and giving me such a great opportunity. I would like to thank the whole Na-K team: Zoe, Yiqi, Alex and in particular Carsten, for all the suggestions and the patient explanations. Last but not least, thanks to Lawrence, Matt and Ian for warmly welcoming me in their Boston life.

---

[7] Except for German, leider.

These last years were also made of friends, mountains, beers and dinners. I am grateful to all the people who made my life in Innsbruck so enjoyable. Thanks to Cosetta, Deborah, Elvia, Claudia and Gabriele for all the time spent together. Thanks for the pizzas, the physics discussions carried on in Italian, the inestimable trade and exchange of Italian goods as soon as someone crossed the border. A special thanks to Hombre, Martin and Milena, Lata and Manoj and Elina, Gabriel, Cristina: with you, it feels that I have a second family here in Innsbruck.

If I have reached this point, it's because of the priceless support and help of my parents and my sister, not only in the last five years, but always. In particular, I would like to thank my parents for having instilled in me a sense of curiosity and passion for knowledge. Grazie.

Thanks to Lorenzo, for his continual support, help, and his (hopefully endless) endurance. Also thanks for our physics discussions, the lab hacks, ElectroBOOM. Thanks for always being there for me.

And finally, thanks to Pietro and Luisa: you helped me put all this in the correct perspective.